UNIVERSITÉ DE GENÈVE
Département de physique nucléaire et corpusculaire

FACULTÉ DES SCIENCES
Professeur Allan CLARK

Determination of W Boson Helicity Fractions in Top Quark Decays in $p\bar{p}$ collisions at CDF RunII

and

Production of Endcap Modules for the ATLAS Silicon Tracker

THÈSE

présentée à la Faculté des sciences de l'Université de Genève
pour obtenir le grade de Docteur ès sciences, mention physique

par

Shulamit MOED

Thèse N° 3839

GENÈVE
Atelier de reproduction de la Section de physique
2007

To my grandfather

Acknowledgements

I am thankful to Prof. Allan G. Clark for giving me the possibility to have this PhD position working on ATLAS at CERN and CDF at FNAL.

I would like to thank Markus Klute and Nils Krumnack for taking part in the W helicity analysis. I would also like to thank Yoshiaki Kusakabe for his help and quick response when needed.

Big and deep thanks belong especially to Mousumi Datta, Ricardo Eusebi and Andy Hocker for their collaboration and contribution to the analysis. Their immediate availability, constant support and super-friendly attitude has made the daily work real fun. They have taught me a significant part of what I've learned while working on this analysis.

Most of all I am grateful to Doug Glenzinski for suggesting me to work together. Doug has led the analysis and followed it closely, always willing to explain everything, help and advise in the most pleasant ways. In many ways Doug set an example for me, I enjoyed every day I have worked on it and cannot imagine making a better choice.

Abstract

The thesis presented here includes two parts. The first part discusses the production of endcap modules for the ATLAS SemiConductor Tracker at the University of Geneva. The ATLAS experiment is one of the two multi-purpose experiments being built at the LHC at CERN. The University of Geneva invested extensive efforts to create an excellent and efficient module production site, in which 655 endcap outer modules were constructed. The complexity and extreme requirements for 10 years of LHC operation with a high resolution, high efficiency, low noise tracking system resulted in an extremely careful, time consuming production and quality assurance of every single module. At design luminosity about 1000 particles will pass through the tracking system each 25 ns. In addition to requiring fast tracking techniques, the high particle flux causes significant radiation damage. Therefore, modules have to be constructed within tight and accurate mechanical and electrical specifications. A description of the ATLAS experiment and the ATLAS Semiconductor tracker is presented, followed by a detailed overview of the module production at the University of Geneva.

My personal contribution to the endcap module production at the University of Geneva was taking part, together with other physicists, in selecting components to be assembled to a module, including hybrid reception tests, measuring the I-V curves of the sensors and the modules at different stages of the production, thermal cycling the modules and performing electrical readout tests as an initial quality assurance of the modules before they were shipped to CERN. An elaborated description of all of these activities is given in this thesis.

At the beginning of the production period I developed a statistics package which enabled us to monitor the rate and quality of the module production. This package was then used widely by the ATLAS SCT institutes that built endcap modules of any type, and kept being improved and updated. The production monitoring and summary using this package is shown in this thesis.

The second part of the thesis reports a measurement of the fraction of longitudinal and right-handed helicity states of W bosons in top quark decays. This measurement was done using $955 pb^{-1}$ of data collected with the CDF detector at the Tevatron, where protons and anti-protons are collided with a center-of-mass energy of 1.96 TeV. The helicity fraction measurements take advantage of the fact that the angular distribution of the W boson decay products depends on the helicity state of the W which they originate from. We analyze $t\bar{t}$ events in the 'lepton+jets' channel and look at the leptonic side of decay. We construct templates for the distribution of $\cos\theta^*$, the angle between the charged lepton and the W flight direction in the rest frame of the top quark. Using Monte

Carlo techniques, we construct probability distributions ("templates") for $\cos\theta^*$ in the case of left-handed, longitudinal and right-handed Ws and a template for our background model. We extract the W helicity fractions using an unbinned likelihood fitter based on the information of these templates. The Standard Model predicts the W helicity fractions to be about 70% longitudinal and 30% left-handed, while the fraction of right-handed W bosons in top decays is highly suppressed and vanishes when neglecting the mass of the b quark. We measure these fractions to be:

$$\text{right handed: } f_+ = -0.056 \pm 0.056 \pm 0.03$$
$$\text{longitudinal: } f_0 = 0.606 \pm 0.12 \pm 0.06$$

In the absence of an observed signal, we set an upper limit on the fractions of right-handed W bosons:

$$f_+ < 0.11 \text{ @95\% C.L}$$

In addition to measuring separately the right-handed and longitudinal W helicity fractions, a first simultaneous measurement of these two fractions was performed and is presented in this thesis. When extracting simultaneously the longitudinal and right-handed fractions we measure:

$$\text{right-handed: } f_+ = -0.06 \pm 0.10 \pm 0.03$$
$$\text{longitudinal: } f_0 = 0.74 \pm 0.25 \pm 0.06$$

The simultaneous measurement has larger statistical uncertainties, but is completely model-independent.

Both measurements provide a direct search for a V+A current, which is suppressed by the SM, but may appear in other scenarios, as well as a test of the Standard Model description of ElectroWeak Symmetry Breaking.

The results reported in this thesis are in agreement with the Standard Model. However, they still suffer from relatively large statistical uncertainties, which will reduce with the anticipated data to be delivered by the Tevatron, and soon hopefully by the LHC as well.

Résumé en Francais

Le travail de thèse présenté ici est en deux parties. La première partie traite de la production des modules pour le endcap du SemiConducteur Tracker (SCT) de ATLAS à l'Université de Genève. L'expérience ATLAS est une des deux éxperiences généralistes qui sont en contruction pour le LHC au CERN. L'Université de Genèvea investi beaucoup d'efforts pour créer un site de production de modules excellent et efficace, dans lequel 655 modules externes ont été construits pour le disque endcap du SCT. La complexité du détecteur et les conditions extrêmes durant les 10 ans d'operation du LHC à haute résolution, haute efficacité et avec un niveau de bruit très bas ont déterminé le mode de production et les tests attentioné et éxigeant de qualité de chaque module. À la luminosité envisagée, environ 1000 particules vont passer à travers le système de tracking toutes les 25 ns. En plus de nécessiter des techniques de tracking ultra-rapides, le flux élevé de particules cause d'importants dégats dus aux radiations. De ce fait, les modules doivent être construits d'après des normes strictes et précices. Une déscription du détecteur ATLAS et de son SemiConductor Tracker sont présentés dans cette thèse, suivi d'une vue détaillée de la production de modules à l'Université de Genève.

La deuxième partie de ce travail de thèse décrit une mesure de la fraction d'hélicité longitudinale et droite du boson W dans la désintégration du quark top. Cette mesure a été faite en utilisant 955 pb^{-1} de données collectées avec le détecteur de CDF au Tevatron au Fermilab, collisionneur protons anti-protons à une énergie de centre de masse de 1.96 TeV. La mesure de la fraction d'hélicité utilise le fait que la distribution angulaire des produits de la désintégration du boson W dépend de l'hélicité du W dont ils proviennent. En plus de mesurer séparement les fractions d'hélicité droites et logitudinales du W, une première mesure simultanée de ces deux fractions a été faite et est présenté dans cette thèse.

Production de modules à l'Université de Genève

L'objectif principal du détecteur d'ATLAS est la découverte de la particule de Higgs, mais un autre grand but est la découverte de nouvelles particules au-delà du Modèle Standard (SM). L'étude de la désintégration des quarks b et une mesure précise de la masse du quark top sont parmis les objectifs de l'éxperience afin de mieux comprendre le SM.

Les concepts de base considérés pour ATLAS peuvent être résumés comme suit:

- très bonne mesure éléctromagnétique pour l'identification et la mesure de l'énergie de l'éléctron et du photon, completée par une calorimétrie hermétique pour les jets et l'énergie transverse manquante (missing E_T);

- détection de traces éfficace à haute luminosité pour la mesure de la quantité de mouvement des leptons, le tagging du quark b et une identification plus élevée des éléctrons et des photons, ainsi que les τ, la reconstructions des vertex saveur lourde et la capacité à reconstruire des désintégrations de certains B à luminosité plus basse;

- mesure à haute précision des muons, avec la capacité de garantir de bonnes mesures à la luminosité la plus élevée en utilisant seulement le spectromètre à muon;

- grande acceptance en pseudo-rapidité avec une couverture angulaire azimuthale (ϕ) quasi complète;

- déclenchement et mesure de particules à bas seuil en p_T, donnant une éfficacité élevée du détecteur.

Le système de tracking du Détecteur Interne (ID) est la partie la plus interne de l'éxperience de ATLAS. En commencant par le plus petit rayon, les trois principales sous-structures sont:

- détecteur à pixels
- détecteur semiconducteur(SCT)
- détecteur à transition de radiation(TRT)

A l'éxtérieur du détecteur interne se trouvent les calorimètres (éléctromagnétiques et hadroniques) et le spéctromètre à muons. Le SCT est divisé en trois régions - une zone barrel et deux zone s endcaps. La région du barrel est composé de quatre couches cylindiques de modules de détection autour de la direction du faisceau et qui ont une couverture azimuthale totale. Les couches vont d'un rayon de 27 à 56 cm, mesurent 149 cm de long et couvrent une régi on en pseudo-rapidité jusqu'à $|\eta| < 1.0$. Chaque zone endcap est composé de 9 roues en fibre de carbone placées perpendiculair ement au faisceau: elles fournissent les mesures dans la région de $z = 80$ cm à $z = 270$ cm, avec une couverture azimuthale totale jusqu'à $|\eta| < 2.5$ et avec une demi-longueur de 279 cm. Dans les deux régions, endcap et barrel, les modules de senseurs sont disposés avec un petit recouvrement entre les modules, afin d'éviter des zones mortes dans le détecteur. Au totale, le SCT est composè de 4088 micro-strips de silicium. Les endcaps possèdent 1976 modules.

La production en masse des 1976 modules SCT endcap a débuté en 2003 dans différents sites de production à Melbourne (Australie), Manchester (UK), Freiburg et Munich (Allemagne), Nikhef (Pays Bas), Valencia (Espagne) et à l'Université de Genève. A Genève , 655 modules pour les disques éxtérieurs du SCT encaps ont ét 'e assemblés et testés. Les tests de qualité ont ensuite été effectués au CERN puis les modules furent assemblés sur les d isques à Nikhef et Liverpool (UK).

L'assemblage des modules, la métrologie est les tests de contrôle de qualité éléctriques ont été effectués selon des normes strictes de spécifications méchaniques et éléctriques propr e à la collaboration ATLAS (voire Section 1 et [13], [12]).

L'assemblage, la métrologie ainsi que le collage des modules à l'Université de Genève ont étés faits dans une salle propre. Le s tests de qualité éléctique intermédiaire ainsi que le cycle thérmique initial furent menés dans la salle grise adjacente.

Ma contribution personnelle à la production des modules à l'Université de Genève a été de prendre part, avec d'autres physiciens, à la séléction des composants utilisés dans l'assemblage des modules, comprenant les tests de réception des hybrides, les me sures des courbes I-V des senseurs et des modules à différents stades de la production, les cycles thérmiques des modules, aux tests de lecture éléctriques comme assurance de qualité initiale des modules avant de les envoyer au CERN, ainsi que d'organiser les shifts de productions pour le travail des physiciens dans la salle grise. Une déscription détaillée de ces activités est donnée dans les sections qui suivent.

Au début de la période de production j'ai dévelopé un logicie l'informatique statistique (voire Section 1) qui nous a permis de faire du monitorage du taux et de la qualité de la production de modules. Ce progiciel a été par la suite adopté par les instituts du ATLAS SCT qui ont construits des modules endcaps de tous les types et a été constamment ammelioré.

Il y a différents composants qui doivent être testés et inspectés avant d'être assemblés en modules:

Les senseurs [7, 11] les modules endcap du SCT sont des détecteurs de type p-sur-n en forme de coins, mesurant 285 μm d'épaisseur avec 768 strips pour la lecture (voire Figure 1.12). Les strips mesurent environ 6 cm de long et sont couplés de manière AC à l'éléctronique de la chaîne de lecture qui est monté sur un hybride.

Les senseurs sont lus par **12 ASICs spécifiquement crées** (ATLAS Binary Chip DMILL 'ABCD' [10]) avec 128 canaux par ASIC, montés sur l'**hybride** (Fig. 1.11), où chaque canal donne la préamplification, la mise en forme avec une constante temporelle de 25 ns, des comparateurs avec des seuils ajustables pour chaque canal, un pipeline digital de 132 cellules de pofondeur pour permettre les stockage des données pendant la décision du premier niveau du trigger, la compression de données et les tampons de lecture. De

cette manière les signaux des senseurs sont convertis en informations de hits binaires dans le front-end et les données sont transmises par liens optiques binaires.
Les paires de senseurs de silicium sont collés dos-à-dos sur une structure de support **(spine)** avec un angle steréoscopique de 40 mrad qui donne la position en deux-dimentions. La spine , le support méchanique du module, est construit en graphite pyrolytique thérmique (TPG) avec une conductivité élevée dans le plan de 1700 W/mK afin dévacuer la chaleur des déteceurs aux points de refroidissement sur le côté ou au bout des modules.

Les autres parties du module avec leurs fonctionalité méchanique sont:

1. **pad-locator** - un localisateur précis pour l'alignement des modules lors du montage.
2. **far-end washer** - donne la précision de montage dans la direction y lors de l'assemblage du module.
3. **fan-ins (pitch adapters)** - les modules endcap du SCT ont des pas différents entre les pavs dans les différents canaux du détecteur et les chips de lecture sur les hybrides. L'adaptation de ces connections est faite via une plaque de verre avec des traces en métal appelées adaptateurs de pas, ou en bref fan-ins. Le but de ces fanins est la connection éléctrique de chaque canal entre le détecteur et le chip de lecture, adaptant les différents pas des pavs. Ils forment aussi la connexion mécanique entre l'hybride et la partie du module avec le détecteur tout en restant une barrière éfficace contre le transfert de chaleur entre ces deux parties.

Un schema des composants d'un module est présenté dans la figure 0.1.
Les principales étapes de la production des modules sont les suivantes:

1. **Avant l'assemblage**:
   - Inspection visuelle des pièces mécaniques à assembler - spines, pad-locators, fain-ins, far-end washers.
   - Tests des hybrides - inspection visuelle et tests de lecture, pour vérifier la fonctionalité numérique et analogique.
   - Mesures des courbes IV des senseurs individuels en silicium à assembler.
2. **Pendant l'assemblage**:
   - Mesures IV des 4 senseurs sur le module après l'assemblage "phase 1" (collage spine-détecteurs, voire Section 2).

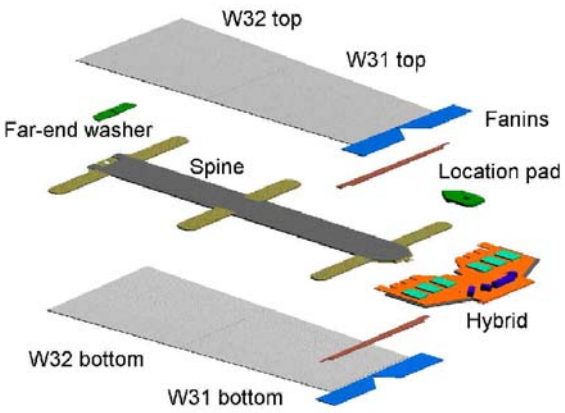

Figure 0.1 Les différents composants formant un module endcap SCT

- Mesures IV des 4 senseurs après l'assemblage "phase 2" (collage de l'hybride, voire Section 2). Cette étape a été abandonée après avoir testé suffisamment de modules pour réaliser que le collage des hybrides n'affecte pas les mesures du courrant de perte.
- Mesures IV des modules après le wire bonding.
- Prise de données métrologique pour un sous-groupe de modules.

3. **Après l'assemblage**:

   - Cycles Thérmiques
   - Métrologie - prise de données de l'alignement mécanique et du profile du module (Figure 2.3).
   - Tests de lécture éléctrique du module

Du temps et des ressources importantes ont été investis pour valider le système d'assemblage [17] afin de permettre la construction de modules fiables, respectant les normes très strictes d'alignement [18]. Les tolérances sont en rapport avec l'alignement relatif des deux détecteurs sur le côté supérieur par rapport aux détecteurs sur le côté inférieur et sont de la précision des aiguilles de montages. L'alignement des détecteurs

avant-arrière est déplacé d'un angle de 40 mrad et la tolérance acceptée est de ± 130 μrad. Une tolérance plus contraignante viens de la position moyenne du détecteur avant par rapport au détecteur sur le dos, qui doit être à moins de ± 5 μm de la valeur nominale dans l'axe y (perpendiculaire aux strips). La tolérance dans le plan du détecteur (ou axe z) est de ± 115 μ et une legère torsion de la spine peut causer des profils en dehors des normes.

Trois critères principaux sont essentiels pour le site de production de modules:

De bons résultats de mesures métrologiques, un bon comportement du courant dans les modules et finalement une chaîne de lecture satisfaisante avec un nombre minimum de canaux défectueux.

Le système d'assemblage à Genève a prouvé sa capacité à délivrer le nombre nécessaire de bons modules dans le temps préconisé par la collaboration du ATLAS SCT. Avec un rendement excellent de 97%, 655 modules endcap extérieurs ont été produits à l'Université de Genève, parmi lesquels 634 furent qualifiés pour être assemblés sur les disques qui seront utilisés dans les système de tracking de ATLAS. La vue d'ensemble de la production est donnée dans ce travail de thèse, ainsi que la présentation de la pérformance mécanique et éléctrique des modules, qui démontre clarement que l'Université de Genève a fait de son mieux pour atteindre une production de module de haute qualité, safisfaisant de manière soutenue les critères nécessaires pour l'opération des modules dans l'environnement du LHC.

Détermination des fractions d'hélicité du boson W dans la désintégration du quark top à CDF

Parmi les particules fondamentales connues, le quark top sort du lot en étant le plus lourd, sa masse étant de l'ordre de l'échelle de rupture de la symmétrie éléctrofaible (EWSB). Les particules fondamentales ont un spin. Ce degré de liberté interne joue un rôle imporant dans leurs intéractions. La connaissance de ces interactions est nécessaire pour déterminer le méchanisme de EWSM. La largeur de la désintétration tree-level' $t \to Wb$ du quark top, en utlisant le vertex général tWb peut être obtenu en considérant les amplitudes d'hélicité dans l'état final de la désintégration du quark top: il y a trois modes de désintégration $t \to Wb$, qui dépendent de la polarisation du boson W. Chaque mode est associé à une fraction, F_0, F_R (F_+) ou F_L F_-, ce qui correspond respectivement à la polarisation longitudinale, droite et gauche. Les fractions sont contraintes de satisfaire

$F_0+F_R+F_L = 1$. Le SM prédit de manière définitive les trois fractions de l'hélicité du W.

Actuellement, le seul ingrédient manquant au SM est le boson de Higgs. C'est l'agent qui cause la EWSB et des recherches au LEPII ont conclu que sa masse doit être plus élevée que 115 GeV si il existe [29]. Il est bien connu que le mécanisme de Higgs dans le SM laisse beaucoup de questions importantes non-résolues - quelle est la vrai origine de la masse des fermion? Ou quelle est l'éxplication pour une annulation importante des corrections d'ordre suppérieures à la masse du Higgs?

De ce fait, d'autres théories de la ESWB sont considérés en physique des particules. Des théories comme le Minimal Supersymmetric Standard Model ($MSSM$), le modèle Technicolor et des théories avec de nouvelles interactions du quartk top suggèrent quelques une des réponses. Mais jusqu'à présent aucune indication de leur validité n'a été trouvée.

Dans le SM, le quark top se désintègre via l'interaction faible , donc, comme tous les fermions, il a un couplage V-A qui permet au boson W de se coupler au fermions d'hélicité droite seulement. La nature V-A de l'intéraction, ainsi que la conservation de la quantité de mouvement angulaire, donne une suppression élevée de la production du boson W d'hélicité droite dans l'état final de la désintégration du top. La fraction d'hélicité droite du W deviens nulle en négligeant la masse du quark b. Observer une fraction non-nulle d'hélicité droite du boson W (au-delà des petites prédictions du SM) serait un indicateur d'un couplage V+A anormal qui suggérerait de la physique au delà du SM. Toutefois, des études du modéle éléctrofaible dans les désintégrations beta du noyeau [30], ainsi que les mesures de désintégration de processus rares tels que $b \to s\gamma$ par la collaboration CLEO [31], [32], et aussi les mesures de précision du LEP et du SLC, ont déjà testé la nature V-A de la force éléctrofaible et ont pu établir des limites fortes pour le courrant V+A. Par exemple, la mesure de seulement $b \to s\gamma$ fourni des contraintes de moins de 0.5% pour la force possible du couplage de droite tWb - ce niveau de précision ne sera pas possible à atteindre, même au LHC.

Les mesures des fractions d'hélicité du W dans les désintégrations du top fourni une recherche directe pour les couplages V+A et, avec plus de données que celles prises jusqu'à aujourd'hui, elles pourraient être utilisées comme tests de modèles au-delà de la physique du SM.

La distribution angulaire ω des produits de désintégration avec $I_3 = -1/2$ (lepton à charge, quark up ou quark strange) du boson W, dans le système de centre de masse du

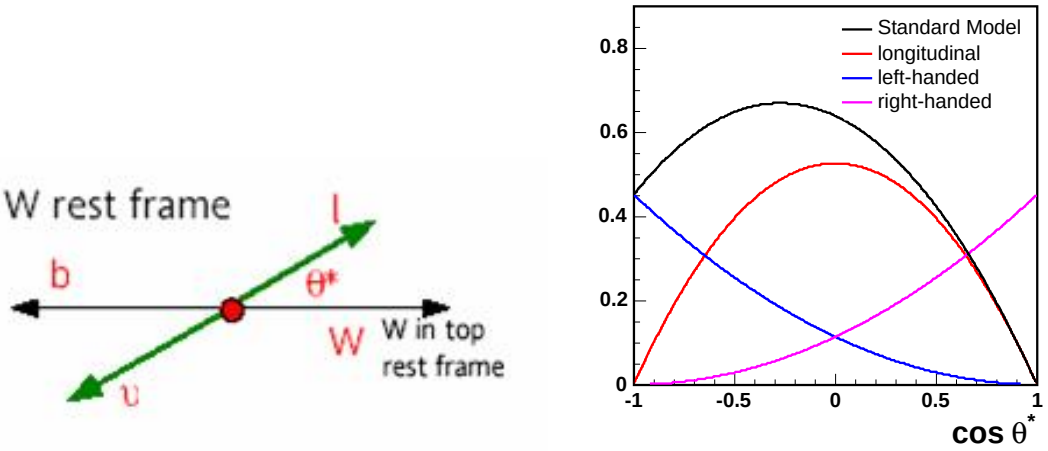

Figure 0.2 L'angle de désintégration θ^* dans la désintégration du top est défini comme d'angle entre le quark de type down provenant de la désintégration du W et la direction du quark top dans le système de centre de masse du W (gauche). La figure de droite montre la distribution angulaire $\omega(\theta^*)$ pour les désintégrations d'hélicité longitudinale, gauche et droite du boson W ainsi que la distribution attendue dans le Modèle Standard.

W, peut être exprimée en introduisant un angle θ^* par rapport à la direction de vol du W dans le système de centre de masse du quark top. La distribution angulaire a la forme générale:

$$\omega(\theta^*) = f_0 \cdot \omega_0(\theta^*) + f_- \cdot \omega_-(\theta^*) + f_+ \cdot \omega_+(\theta^*), \tag{0.1}$$

avec

$$\omega_0(\theta^*) = \frac{3}{4}(1 - \cos^2\theta^*), \tag{0.2}$$

$$\omega_-(\theta^*) = \frac{3}{8}(1 - \cos\theta^*)^2, \tag{0.3}$$

$$\omega_+(\theta^*) = \frac{3}{8}(1 + \cos\theta^*)^2. \tag{0.4}$$

La figure 0.2 illustre la définition de θ^* et montre la distribution angulaire pour des boson W d'hélicité longitudinale, droite et gauche ainsi que la distribution attendue dans le Modèle Standard. A cause des bruits de fond, les effets de reconstruction et d'acceptance la distribution de θ^* est différente de celle de $\omega(\cos\theta^*)$. Toutefois, la forme de la distribution observée de θ^* dépend de f_0, f_- et f_+ et peut donc être utilisé pour extraire les fractions de polarisation. La stratégie de la mesure présentée ici est de

reconstruire entièrement les événements $t\bar{t}$ et de déterminer la distribution en $\cos\theta^*$, puis d'utiliser une méthode de matrices afin de déterminer les fractions f_0, f_- et f_+. Nous analysons des événements $t\bar{t}$ dans le canal 'lepton + jet', où une paire de $t\bar{t}$ est produite et un des bosons W provenant de la désintégration du quark top se désintègre de manière leptonique dans un lepton chargé et un neutrino, tandis que l'autre boson W de désintègre en quarks légers qui sont détectés comme des jets dans le détecteur. Nous regardons du côté leptonique et construisons des matrices pour la distribution en $\cos\theta^*$, l'angle entre le lepton chargé et la direct ion de vol du W dans le système de centre de masse du quark top. En utilisant des simulations Monte-Carlos, nous reconstruisons des distributions de probabilité (matrices) pour $\cos\theta^*$ dans les cas d'hélicité longitudinale, gauche et droite du W ainsi que des matrices pour notre modèle du background. Nous extrayons les fractions d'hélicité du W en utilisant un programme dajustement de type maximum de vraisemblance non binn, basé sur les informations de ces matrices. Le Modèle Standard prédit que la fraction d'hélicité du W est environ 70% longitudinale et 30% gauche, tandis que la fraction d'hélicité droite est hautement diminuée et disparaît quand on néglige la masse du quark b. La mesure que ces fractions donne:

$$\text{hélicité droite: } f_+ = -0.056 \pm 0.056 \pm 0.03$$
$$\text{hélicité longitudinale: } f_0 = 0.606 \pm 0.12 \pm 0.06$$

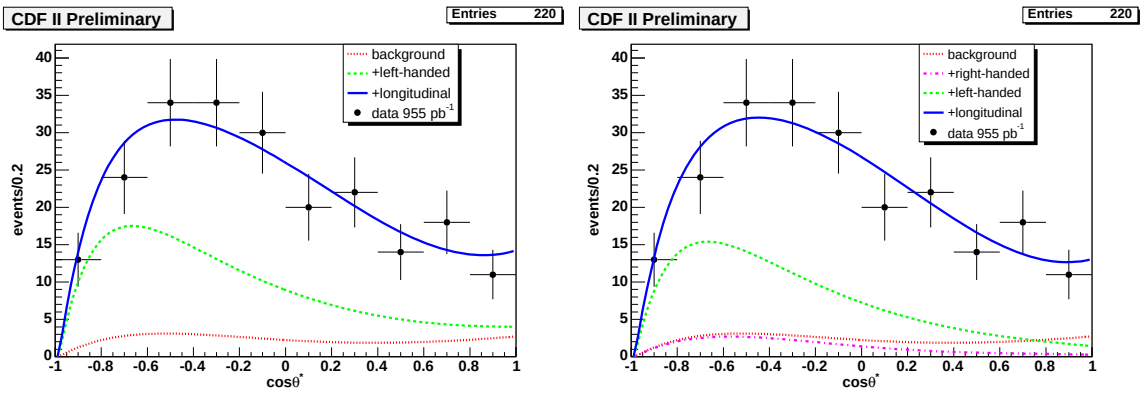

Figure 0.3 A gauche - la distribution de $\cos(\theta^*)$ observée dans les données (points) superposée avec les distributions pour le fond (ligne pointillée), fond + hélicité gauche (ligne traits-tillée) et fond + hélicité gauche + longitudinale (ligne pleine), déterminé par un ajustement pour F_0. A droite - la distribution observée $\cos(\theta^*)$ dans les données (points) superposé avec les distributions pour le fond (ligne pointillée), fond + hélicité droite (ligne tiret-point), fond + hélicité droite + hélicité gauche (ligne traits-tillée) et fond + hélicité droite + hélicité gauche + hélicité longitudinale (ligne pleine), déterminés par un ajustement pour F_+.

Les résultats des données sont montrés dans la Figure 0.3.

En plus de mesurer séparément les fractions d'hélicité droite et longitudinale du W, une première mesure simultanée de ces deux fractions a été faite et est présentée dans cette thèse. En extrayant simultanément la fraction d'hélicité droite et longitudinale, nous mesurons:

$$\text{hélicité droite: } f_+ = -0.06 \pm 0.10 \pm 0.03$$
$$\text{hélicité longitudinale: } f_0 = 0.74 \pm 0.25 \pm 0.06$$

La mesure simultanée a des erreurs statistiques plus élevé, mais est entièrement indépendante d'un modèle particulier.

Les deux mesures fournissent un recherche directe d'un courrant V+A, qui est fortement diminué dans le SM, mais peut apparaître dans d'autre scenarios, ainsi qu'un test de la déscription de la rupture de la force éléctrofaible dans le Modèle Standard.

Les résultats montrés ici sont en accord avec le Modèle Standard. Toutefois, ils souffrent encore d'erreurs statistiques relativement grands, qui seront réduits avec les données anticipée pour le Tevatron et bientôt le LHC.

Contents

Acknowledgements 4

Abstract i

Résumé en francais i

List of Tables iv

List of Figures vi

1 The ATLAS Experiment and ATLAS Silicon Tracker 1

1.1 ATLAS . . . 1

1.1.1 The ATLAS inner detector . . . 2

1.1.2 Calorimetry . . . 6

1.1.3 Muon spectrometer . . . 7

1.1.4 Trigger . . . 9

1.2 The SemiConductor Tracker . . . 10

1.2.1 Micro-strips detectors . . . 13

1.2.2 Front-end electronics . . . 15

1.3 SCT endcap modules . . . 19

1.3.1 Mechanical Description of a Module . . . 19

1.3.2 Module performance specifications and mechanical tolerances . . . 21

1.4 Physics potential of the Inner Detector . . . 23

2 Module Production at the University of Geneva 25

2.1 Production Overview . . . 25

2.2 Assembly Facilities . . . 26

2.3 Quality Assurance Along the Assembly Stages . . . 28

2.4 Assembly line . . . 28

2.5 Selection of Components . . . 30

2.6 Assembly Sequence 31
2.7 Module Production Rate 35
2.8 Metrology 35
2.8.1 The x, y survey 36
2.8.2 The z survey 37
2.9 Thermal cycling 38
2.10 Electrical readout tests of the module 42
2.11 Statistics package for ATLAS SCT module production 48
2.12 Module Classification 49
2.12.1 Summary of Production Failures 52
2.13 Module Production - Conclusion and Summary 55

3 W helicity in Top Quark Decays 57
3.1 Top Production 57
3.2 Top Quark Decay 58
3.3 Helicity of W bosons 59
3.4 W Helicity Fractions in the SM 60
3.5 Possible modifications of the W helicity fractions - beyond the SM scenarios 65

4 Experimental Design 71
4.1 FNAL - the Fermi National Accelerator Laboratory 71
4.2 Accelerator Complex 71
4.2.1 Proton Source 73
4.2.2 Antiproton Source 73
4.2.3 TEVATRON 74
4.3 The CDF II Detector 75
4.3.1 Tracking System 76
4.3.2 The Calorimetry 80
4.3.3 The Muon System 82
4.3.4 The Cherenkov Luminosity Counter 83
4.4 Data Acquisition and Trigger 83
4.5 Online Monitoring 86

5 Data Sample and Event Selection 89
5.1 Lepton+jets event selection 89
5.1.1 The data sample 89
5.2 Event Reconstruction 90
5.2.1 Electron identification 90

5.2.2 Muon Identification . . . 93
5.2.3 Jet reconstruction . . . 95
5.2.4 Missing Transverse Energy . . . 97
5.2.5 b-Tagging - Displaced Secondary Vertex algorithm . . . 97
5.3 Event Selection . . . 100
5.3.1 Triggers . . . 100
5.3.2 Offline Selection . . . 101
5.4 Top Quark Reconstruction . . . 102

6 Background **107**
6.1 Background Categories . . . 107
6.1.1 Non-W QCD . . . 108
6.1.2 Mistag . . . 111
6.1.3 W+Heavy Flavor . . . 111
6.1.4 Single top and diboson . . . 112
6.2 Summary of Background Estimate . . . 112

7 $cos\theta^*$ templates **115**
7.1 Signal samples . . . 115
7.1.1 GGWIG - a modified version of HERWIG . . . 115
7.1.2 Pythia samples . . . 116
7.1.3 GGWIG validation . . . 116
7.2 Background samples . . . 116
7.3 Constructing the Templates - Fit Parameterizations of the $\cos\theta^*$ Distributions . . . 119

8 The Likelihood Fitter **123**
8.1 The Extended Likelihood Function . . . 123
8.2 Acceptance Corrections . . . 125
8.3 Linearity Study and Expected Statistical Uncertainty . . . 128

9 Systematic Uncertainties **131**
9.0.1 Jet Energy Scale . . . 132
9.0.2 Background . . . 132
9.0.3 Initial State Radiation . . . 134
9.0.4 Final State Radiation . . . 134
9.0.5 Signal Monte Carlo . . . 134
9.0.6 Monte Carlo Statistics . . . 134

9.0.7 Acceptance Correction 134
9.0.8 Parton Distribution Functions 135
9.0.9 Instantaneous Luminosity 137
9.1 Summary of Systematic Uncertainties 137
9.2 Top Mass dependence 138

10 Results **143**
10.1 Fitting the Data - separate measurement of f_0 and f_+ 143
10.1.1 Limit on f_+ 143
10.2 First Simultaneous Measurement of f_0 and f_+ 144
10.2.1 Method 146
10.2.2 Linearity Studies 146
10.2.3 Acceptance Correction 148
10.2.4 Systematic Uncertainties 148
10.2.5 Results from the Data 150
10.3 Determination of W helicity fractions - conclusions 154

11 Summary **155**

Bibliography **157**

List of Tables

1.1 Geometrical characteristics for the SCT silicon wafers. 13

2.1 Estimated time for phase 1 and phase 2 of the module production. The maximum time takes account of problems encountered during assembly (e.g - visual inspection problems such as glue overflow). 36

2.2 Nominal values and tolerances for the 13 points used to measure the module profile. 37

2.3 Statistics of the SCT Endcap module production. 55

3.1 $t\bar{t}$ decay branching ratios for different channels. The factor of 2/3 for $q\bar{q}$ reflects the two hadronic channels and the three colors for all quarks: $2 \times 3 \times 1/9 = 2/3$ 59

5.1 Luminosity using GoodRun list v13. 90

6.1 Theoretical cross sections and errors for the electroweak and single top backgrounds, along with the theoretical cross section for $t\bar{t}$ at (m_t = 175GeV/c^2). The cross section of $Z^0 \to \tau\tau$ is obtained in the dilepton mass of $m > 30$ GeV/c^2 together with k-factor(NLO/LO) of 1.4. 113

6.2 Expected number of background events and the number of observed events in the 695 pb^{-1} data set and the scaling to the 955 pb^{-1} data set, using the selection criteria described in reference [85], including the H_T requirement and demanding at least four tight jets. 113

7.1 Summary of the Monte Carlo $t\bar{t}$ signal samples used in the analysis. . . . 116

7.2 Summary of the Monte Carlo samples used to model the background. . . 119

7.3 Summary of the resulting fit parameters used to parameterize the signal and background $\cos\theta^*$ distributions. 119

8.1 Test of the unbinned likelihood fitter using simple toy Monte Carlo pseudo-experiments constructed as described in the text. 124

8.2 Test of the unbinned likelihood fitter using pseudo-experiments constructed from tree-level Monte Carlo information as described in the text. 125
8.3 The acceptance as a function of the W-boson polarization determined using the $t\bar{t}$ GGWIG samples. These numbers are used to correct the fitted fractions $F_{0,+}$ to determine the true polarization fractions $f_{0,+}$ as described in the text. The uncertainties are statistical only. 127
8.4 The acceptance for a Standard Model $t\bar{t}$ PYTHIA sample and a mixture of $t\bar{t}$ GGWIG samples which have been weighted according to the Standard Model predictions of f_0. The row marked "leptonic" ("hadronic") utop corresponds to GGWIG samples in which the leptonic (hadronic) decaying W boson is forced to a specific helicity while the other W boson decays with SM helicity fractions. 127
8.5 Linearity tests of the unbinned likelihood fitter using realistic, fully simulated, signal-plus-background Monte Carlo pseudo-experiments. 130

9.1 The systematic uncertainties of the 20 PDF eigen-vectors for f_+ and f_0. 137
9.2 The sources of systematic uncertainty and their related estimate. The total systematic uncertainty is taken as the quadrature sum of the individual sources. 138

10.1 Results of combined fits for the longitudinal and right-handed helicity fractions in ensembles with pairs of input values (F_0, F_+). 146
10.2 The sources of systematic uncertainty and their related estimate when measuring f_+ and f_0 simultaneously. The total systematic uncertainty is taken as the quadrature sum of the individual sources. 150

List of Figures

0.1 Les différents composants formant un module endcap SCT v

0.2 L'angle de désintégration θ^* dans la désintégration du top est défini comme d'angle entre le quark de type down provenant de la désintégration du W et la direction du quark top dans le système de centre de masse du W (gauche). La figure de droite montre la distribution angulaire $\omega(\theta^*)$ pour les désintégrations d'hélicité longitudinale, gauche et droite du boson W ainsi que la distribution attendue dans le Modèle Standard. viii

0.3 A gauche - la distribution de $\cos(\theta^*)$ observée dans les données (points) superposée avec les distributions pour le fond (ligne pointillée), fond + hélicité gauche (ligne traits-tillée) et fond + hélicité gauche + longitudinale (ligne pleine), déterminé par un ajustement pour F_0. A droite - la distribution observée $\cos(\theta^*)$ dans les données (points) superposé avec les distributions pour le fond (ligne pointillée), fond + hélicité droite (ligne tiret-point), fond + hélicité droite + hélicité gauche (ligne traits-tillée) et fond + hélicité droite + hélicité gauche + hélicité longitudinale (ligne pleine), déterminés par un ajustement pour F_+. . ix

1.1 Simulated view of the ATLAS detector 2

1.2 Layout of the inner detector of ATLAS, composed of: Pixel detector, Semiconductor Tracker (SCT) and Transition Radiation Tracker (TRT). 5

1.3 3D view of the calorimetry system of ATLAS. In the central part the electromagnetic calorimeter is placed (ECAL). The outer part is formed by the hadronic calorimeter (HCAL). 8

1.4 Representation of the ATLAS trigger and trigger rates. 10

1.5 Barrel module layout 12

1.6 The three forward module layouts: from left to right, inner, middle and outer modules. 12

1.7 Schematic view of a transversal cut of a micro-strip detector. 13

1.8 Equivalent diagram of SCT micro-strip detector. 15

1.9 Block diagram of the analogue front-end circuit. 16

1.10 Schematic diagram of the analog stages of a single channel as implemented in the ABCD chips (C_F and R_F are the feedback capacitor and resistance respectively). 16

1.11 K5-300 hybrid front and back view. 18

1.12 Geometry of the Hamamatsu W31 and W32 silicon sensors used for outer modules of the SCT endcap built in Geneva. 20

1.13 The different parts composing an SCT endcap module 21

2.1 MicroVu metrology machine in the clean room. 27

2.2 The climate chamber used for thermal cycling of the module. 27

2.3 Alignment system with the xy and θ stages and the dowel pins for the referencing the detector transfer. 29

2.4 The SCT hybrid for the Endcap modules. 31

2.5 IV curves for a typical module. at the different stages the currents of the four sensors are summed to give a total current for every applied bias point. The curves obtained at the different stages are compared as well as the curve obtained for the whole module after assembly is completed. 33

2.6 Aligned detectors to be fixed on the gluing base. 33

2.7 On the left: glue dispensing while the spine is positioned on the gluing base; on the right: Gluing base with the bottom detector pair and the spine handling-frame. 34

2.8 Probe Station for detectors and module IV measurements. 34

2.9 Turning plate on which the detectors and spines are glued to the hybrid via the fan-ins. 35

2.10 Definition of the parameters describing the geometry of a standard module. black circles C1 to C4 are the measured centers of the four sensors. The dashed line through each center gives the measured orientation of each wafer. The module is describe in the database with 13 numbers: three coordinate pairs in the x, y system (mhx,mhy), (msx,msy), and (midxf, midyf), two wafer separations sepf, sepb, the angle stereo and four wafer angle a1,a2,a3,a4. Anti-clockwise is positive so in this example a1 is positive and a2,a3,a4 are all negative. 37

2.11 scheme of the 50 points measured for the module z profile on the module front (left) and back (right) side. 38

2.12 Surface gradient for the front (top) and back (bottom) sides of a typical SCT Endcap module. 39

2.13 Thickness profile along the z axis of a typical SCT Endcap module 39

2.14 On the left - 1D surface plots for a module within specified z range.The tolerance from the $z = 0$ reference plane is ± 150 μm. On the right - 1D surface plot for a module outside specified z-range. This is not a typical module. In this particular case the shims which are used to restrict the module z thickness during the detector gluing procedure were forgotten. Such errors were extremely rare during the module production. 40

2.15 On the left (right) - 1D surface plot for the front and back (top and bottom) sides for a module that went through thermal cycle without (with) applying vacuum to constrain it to the jig in the z axis. 41

2.16 A module test box made of Aluminum, with a cooling outlet and a patch card to which the power cable and the data cable are connected. 43

2.17 Scheme of the SCT DAQ system. 44

2.18 A module that passed the electrical readout tests at the University of Geneva packed in a transport box before being shipped to CERN. 44

2.19 Results of the response curve for one side (corresponding to six ABCD chips pr 768 channels) of a typical module as presented by SCTDAQ. The upper plot shows the 50% point of the s-curves for all 768 channels, obtained by scanning the threshold while keeping a fixed charge injection of 2 fC. The distribution within each of the six chips are shown to the right. The third plot from the top shows the extrapolated offset of the response curves. Finally, the lower plot shows the input noise, calculated for each channel in the usual way by taking the width of the response curve (output noise) divided by the gain, at the 2 fC injected charge point. 47

2.20 Results of the response curve test for one side (corresponding to six ABCD chips pr 768 channels) of a typical module as presented by SCTDAQ. The top row of six plots presents the chip averaged response curves: the 50 pc point of the S-curves as a function of injected charge. The gain (slope of the response curve) for each chip is shown below this. The gain is then used to convert the average output noise into an input noise value in ENC for each chip, presented in the bottom plots. 48

2.21 Summary of module metrology. The left figure shows the average z position and RMS for the front and back sides of the module: red lined indicate the specified tolerances. The figure on the right-hand side shows the mid-x and mid-y values with the specified limits and the distance between the mid-point and the hole position in (x, y) (See Figure 2.10) 50

2.22 Summary of module electrical tests. The left figure shows average noise for each module, measured in ENC, while the left figure shows average noise occupancy of the modules. 50

2.23 Average gain of the modules measured during electrical readout tests 51

2.24 Average leakage current of the modules measured during electrical readout tests 51

2.25 Summary of the module production: the number of masked channels for each module. Specifications accept modules with less than 1% (15) defective channels. 52

2.26 Number of produced modules versus date during the production period (May 2003 - June 2005) at the University of Geneva. 56

2.27 A summary of the total module production divided into the different module acceptance categories. 56

3.1 Leading order Feynman diagrams for $t\bar{t}$ production via the strong interaction: upper left - $q\bar{q} \to t\bar{t}$ s-channel, upper right - $gg \to t\bar{t}$ s-channel, lower left - $gg \to t\bar{t}$ t-channel, lower right - $gg \to t\bar{t}$ u-channel. 58

3.2 The decay angle θ^* in top decays is defined as the angle between the down-type particle from the W decay and the W boson flight direction in the top quark rest frame. 61

3.3 The plot shows the angular distribution $\omega(\theta^*)$ for longitudinal, right- and left-handed W boson decays as well as the distribution expected in the Standard Model [33]. 61

3.4 The tWb vertex includes both left (SM) and right (beyond the SM) components in the coupling. 62

3.5 Dependence of the helicity fractions F_i on the anomalous coupling in Eq. 3.27 (plots taken from reference [41]). 67

3.6 Dependence of the helicity ratios $\rho_{R,L} = \Gamma_{R,L}/\Gamma_0$ on the anomalous coupling in Eq. 3.27 (plots taken from reference [41]). 68

4.1 A schematic drawing of the Fermilab accelerator complex. the diagram shows the paths taken by protons and antiprotons at the Fermilab's five accelerators. The beam of particles begins as negative hydrogen ions at the right in the Cockcroft-Walton accelerator. They continue down the short, straight section, the Linac. As the beam of negative hydrogen ions enters the third accelerator, the circular Booster, both electrons are stripped off leaving a proton beam. The protons are injected into the Tevatron. In fixed target mode, the proton beam is extracted and sent down the Fixed Target beamline to the experimental areas. When the accelerator is run in colliding beam mode, antiprotons are collected in the triangle behind the Booster, the Antiproton Storage Rings. The antiprotons are injected into the Main Ring traveling in an opposite direction with respect to the protons. The protons and antiprotons collide inside the two detectors - CDF and Dzero (D0). 72

4.2 Elevation view of one half of the CDF II detector. 75

4.3 Longitudinal view of the CDF tracking volume. its main components are the solenoid, the central outer tracker (COT), which is a gas drift chamber, and the silicon micro-strip detectors - ISL, SVX and L00. 77

4.4 Cross section of the COT tracker. 77

4.5 An overview of the CDF SVX. 79

4.6 End view of the L00 detector 80

4.7 η and ϕ coverage of the CDF muon system. 82

4.8 Data flow schematic of the three level pipe-lined and buffered trigger system. 84

4.9 Functional block diagram of the CDF L1 and L2 trigger system. 85

4.10 Data flow after L3 triggers. 86

5.1 Cartoon showing true reconstructed secondary vertex ($L_{xy} > 0$, left) and fake one ($L_{xy} < 0$, right). 99

5.2 b-tagging efficiencies as functions of E_T(left) and η(right) of jets. Only jets which were b-quarks at the parton level are used for the calculation. Two SecVTX tagging conditions, "Tight" and "Loose" are shown. The bands associated with black lines show the total systematic uncertainty. 100

5.3 Distance between tree-level information and reconstructed object. For events with $dR > 0.4$ no correct match can be assigned. 104

5.4 The performance of the top-quark reconstruction. The left plot shows the index of the best combination in a list of combinations sorted by χ^2 for the permutation chosen as the "best match". The plot on the right shows the performance when sorting by χ^2 the list of the "best lepton-b match" combinations. 104
5.5 Reconstructed $\omega(\theta^*)$ distribution for longitudinal, right- and left-handed W boson decays (left). The absolute value of the difference between tree level value and the reconstructed value for θ^* in a Standard Model $t\bar{t}$ sample is shown in the right plot. 105

6.1 Missing E_T and lepton isolation plane divided into four sectors for non-W background estimation. 109
6.2 $\not\!\!E_T$ vs lepton isolation distributions in high-P_T electron(left) and muon(right) samples associated with at least one jet before applying SECVTX b-tagging. 109
6.3 The expected number of W+jets events with at least one SECVTX b-tagged jet and a $H_t > 200\ GeV$ cut. 114

7.1 Jet E_T distributions for events passing the selection for data together with SM signal and background. The four plots refer to the four leading jets in the event. The upper-left plot is for the leading jet, the upper-right plot for the second leading jet and the bottom plots show the E_T distribution for the third (left) and fourth (right) leading jets. 117
7.2 The left plot shows the P_T of the lepton for data in the signal region and for MC. The right plot shows the distribution of the missing E_T. 118
7.3 SM mixture of the GGWIG samples in comparison with Pythia: the P_T of the lepton (up left), E_T of the leading jet (up right), H_t (bottom left) and the $cos\theta^*$ distribution at the particle level (HEPG). 118
7.4 The reconstructed $\cos\theta^*$ distribution and the fitted parameterization for longitudinal (up-left) , right- (up-right) and left-handed (low-left) W-boson decays and for W+jets background (low-right). 120
7.5 A comparison of the parameterizations of the reconstructed $\cos\theta^*$ distributions for signal and the dominant background sources. 121

8.1 The acceptance correction necessary to determine the true polarization fraction f_0 as a function of the fitted fraction F_0. 128
8.2 Representative pull distributions for the realistic signal-plus-background pseudo-experiments constructed with $(f_0, f_+) = (0.70, 0.00)$. The top two plots are the fitted f_0 and its pull when f_+ is constrained to 0. The bottom two plots are the fitted f_+ and its pull when f_0 is constrained to 0.70. 129

9.1 The $\cos(\theta^*)$ distribution for the multi-jet sample together with a parametrization (left) and all background parametrisations (right) 133
9.2 Zero-tag sample is shown together with a fit and the background model (left). The negative-tag sample is shown together with the background model (right). 133
9.3 Systematic uncertainties for f_+ and f_0 for each of the 20 PDF eigen-vectors. . 136
9.4 $\cos^{\theta^*}$ distribution in events with different gluon fusion/$q\bar{q}$ annihilation ratios. . 138
9.5 Projection plot for the expected statistical uncertainty for measuring the right-handed and longitudinal W helicity fractions assuming no improvements or changes in the current method. 139
9.6 The measured fraction of longitudinal Ws from MC samples with different top masses 140
9.7 The difference between the measured longitudinal fraction f_0 from different top mass MC samples and the measured fraction at $M_t = 175$ GeV 140
9.8 The measured fraction of longitudinal Ws from MC samples with different top masses - results with signal events only using the full sample, but only one pseudo-experiment 141
9.9 The difference of the measured value of f_0 and the value at 175 GeV in the signal only sample. 141
9.10 The measured fraction of right-handed Ws from MC samples with different top masses. f_0 is fixed to 0.703 141
9.11 The measured fraction of right-handed Ws from signal only MC sample with different top masses. f_0 is fixed to 0.703 142
9.12 The measured fraction of right-handed Ws from signal only MC sample with different top masses. f_0 is fixed its expected value. 142
9.13 The measured fraction of right-handed Ws from MC sample with different top masses. 142

10.1 On the left - the observed $\cos(\theta^*)$ distribution in the data (points) overlaid with the background (dotted), background + left-handed (dashed), and background + left-handed + longitudinal (solid) distributions as determined by the fit for F_0. On the right - the observed $\cos(\theta^*)$ distribution in the data (points) overlaid with the background (dotted),background + right-handed (dash-dot), background + right-handed + left-handed (dashed), and background + right-handed + left-handed + longitudinal (solid) distributions as determined by the fit for F_+. . . 144
10.2 Distributions of $-2\Delta \ln \mathcal{L}$ for F_0 (left plot) and F_+ (right plot) from the fits to the data. 145
10.3 Posterior probability distribution for and 95% CL upper limit on f_+. 145

10.4 f_+ posterior probability with (blue) and without (black) folding in systematic uncertainties. 145
10.5 Standard and combined fit results as function of the input polarization fraction. The left plot shows the measured longitudinal fraction f_0 as a function of the input right-handed fraction f_+, while the input longitudinal fraction is set to $f_0 = 0.7$. The right plot shows the measured right-handed fraction as a function of the input longitudinal fraction f_0, while the input right-handed fraction is set to $f_+ = 0.0$. 147
10.6 Standard and combined fit results as function of the input polarization fraction. The plot show the measured longitudinal fraction f_0 as a function of the input longitudinal fraction, while the input right-handed fraction is set to $f_+ = 0.0$. . 147
10.7 Standard and combined fit results as function of the input polarization fraction. The plot show the measured right-handed fraction f_+ as a function of the input right-handed fraction, while the input longitudinal fraction is set to $f_0 = 0.7$. . 148
10.8 Pull distributions for F_0 (left) and F_+ (right) for the 2D fit. The upper pair is an ensemble of pseudo-experiments with SM W helicity fractions; the lower pair is an ensemble with non-SM W helicity fractions. 149
10.9 The distribution of the statistical uncertainty on F_0 (top) and F_+ (bottom), from 1000 SM pseudo-experiments. The arrows indicate the result from the CDF data. 151
10.10 The observed $\cos(\theta^*)$ distribution in the data (points) overlaid with the background (dotted),background + right-handed (dash-dot), background + right-handed + left-handed (dashed), and background + right-handed + left-handed + longitudinal (solid) distributions as determined by the fit for F_+. 151
10.11 Contours of constant ln-likelihood in the (f_+, f_0) plane from the fit to the data. The X shows the minimum of the ln-likelihood, *i.e.* our result. 152
10.12 The area of the (f_+, f_0) plane excluded by the data is shown as the hatched region. The unhatched region in the upper right is unphysical. 153

11.1 Expected statistical uncertainties for measuring the right-handed and longitudinal W fractions with larger datasets. 156

Chapter 1

The ATLAS Experiment and ATLAS Silicon Tracker

The Large Hadron Collider (LHC) is currently being built in the former LEP tunnel at CERN. The LHC tunnel is 27 km long and it is situated under the Swiss-French border in Geneva. The machine will accelerate protons to energies of 7.0 TeV, and collide them head-on to have a center of mass energy of $\sqrt{s} = 14$ TeV. Superconducting magnets of 8.33 Tesla define the trajectory of the 7 TeV protons along the LHC tunnel.

In this chapter a brief introduction of the ATLAS experiment at the LHC hadronic collider is presented, together with a more detailed description of the Semi Conductor Tracking (SCT) detector of ATLAS and its physics potential.

1.1 ATLAS

The ATLAS detector [1] is one of the two general purpose experiments being built in the LHC accelerator, optimized to be sensitive to a wide range of physics signatures. The ATLAS dimensions are 12 m of radius, 44 m length and a weight around 7000 tons.

The principal aim of ATLAS is the discovery of the Higgs particle, but a major additional goal is the search for new particles coming from theories beyond the Standard Model. The basic design considerations for ATLAS can be summarized as follows:

- very good electromagnetic calorimetry for electron and photon identification and energy measurements, complemented by hermetic jet and missing E_T ($\not{E}_T$) calorimetry;

- efficient tracking at high luminosity for lepton momentum measurements, b-quark tagging and enhanced electron and photon identification, as well as τ and heavy-

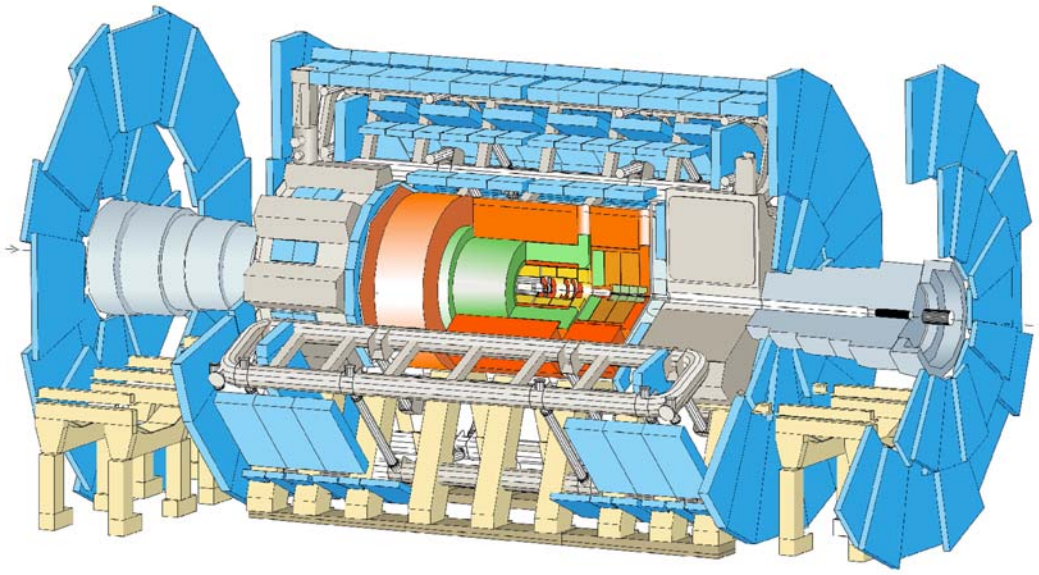

Figure 1.1 Simulated view of the ATLAS detector

flavor vertexing and reconstruction capability of some B decay final states at lower luminosity;

- high-precision muon momentum measurements, with the capability to guarantee accurate measurements at the highest luminosity using the external muon system alone;

- large acceptance in pseudorapidity with almost full azimuthal angle (ϕ) coverage;

- triggering and measurement of particles at low p_T thresholds, providing high detector efficiency.

Figure 1.1 shows the simulated view of the ATLAS detector. It is composed of three main different sub-systems, from outside to inside: the muon system, the calorimeters and the inner detector tracking. These are briefly introduced in the next section.

1.1.1 The ATLAS inner detector

The Inner Detector (ID) is a high performance tracker, that has been developed to provide efficient tracking in the severe conditions of short bunch crossing and strong radiation. It consists of several layers of position sensitive detectors of three different technologies: silicon pixel detectors, occupy the radii between 5 and 12 cm from the interaction point (for the barrel part), micro-strip detectors (SCT), cover the intermediate layers – at radial

distances of 27 to 56 cm, and a transition radiation tracker (TRT) occupies the outer layers. These subsystems are enclosed inside a solenoidal magnet with a magnetic field of 2 Tesla used for charged particle momentum measurement. The Inner Detector will cover up to $|\eta| \leq 2.5$.

The main problems for the ID will be the large occupancies and the high radiation dose. A detailed description of the ATLAS ID can be found in [1] and [2].

Figure 1.2 shows the layout of the of the Inner Detector. Starting from the smallest radii, the three main sub-structures can be summarized as follow:

- **Pixel detector**: designed to achieve high granularity and obtain vertex measurements with a high precision. Sensors are placed very close to the interaction point: the first layer has a radius of 5 cm, while the outer barrel layer is at 12.25 cm from the interaction point. Its total area is 2.3 m^2. The system provides up to three high resolution points per track.
  The layer at lowest radius (called the B-layer because of its prominent role to improve the secondary vertex resolution for b-tagging) covers the full rapidity range $|\eta| < 2.5$. Barrel layer one and two cover pseudo-rapidities $|\eta| < 1.7$ and three endcap disks are used to provide space points in the forward regions $1.7 < |\eta| < 2.5$. Each layer is equipped with modules of 60.8 mm length and 16.4 mm width, each one composed of a silicon n^+n diode segmented in pixels of dimensions 50×400 μm^2 with around 46,000 bump connections.
  Charged particles traversing the diode deposit a small ionization signal. By applying a reverse bias voltage the liberated carriers drift to the segmented readout plane of the detector. Each pixel is bump-bonded to a readout channel in the front-end chips that are mounted on the diode. The total number of channels is 140 million.

- **Semiconductor Tracker (SCT)**: intermediate layers of the ATLAS Inner Detector. It provides four three-dimensional space-points on tracks at radial distances[1] in the range 27 cm to 56 cm. The total number of barrel SCT modules is 2112, and the total number of endcap modules is 1976. Good spatial resolution is required to provide a precise transverse momentum measurement in the bending direction of the 2 T magnetic field of the ID solenoid. For a detailed description see Section 1.2.

- **Transition Radiation Tracker (TRT)**: placed in the outermost part of the Inner Detector, from 56 cm of radius to 115 cm. The pseudorapidity coverage of the TRT

[1]The ATLAS geometry is best described in terms of a cylindrical coordinate system with its origin at the interaction point and its z-axis parallel to the beam line.

is $|\eta| < 2.$, with the barrel region covering $|\eta| < 0.7$. Averaged over the full pseudo-rapidity range, 36 hits per track are generated. The TRT is composed of several hundred thousand straw tubes (50000 in the barrel part, each divided in two at the center in order to reduce the occupancy, and 320000 in the endcap). The total number of channels in the TRT is $425,000$. Each of these straws is a 4 mm diameter cylindrical tube. The inner surface of each straw is covered in aluminium, and acts as high voltage cathode. In the middle of the straw lies an anode wire made of gold-plated tungsten, from which the signal is read out. The straws are filled with a gas mixture of 70% Xe, 27% CO_2 and 3% O_2. The potential difference between the wire and the straw is used to collect the charge liberated by the passage of charged particles through the gas. The resolution expected with this structure is 170 μm.

The straws are also embedded in a medium with an abruptly varying refractive index. Transition radiation is produced when a relativistic particle traverses an inhomogeneous medium, in particular the boundary between materials of different electrical properties. The intensity of transition radiation is roughly proportional to the particle energy $I = m/\sqrt{1-\beta^2}$, where m and $\beta = v/c$ are respectively the mass and the velocity of the particle. Thus transition radiation allows the identification of highly relativistic particles. Electron/hadron discrimination is possible for momenta higher than ~ 1 GeV/c. Transition radiation is emitted in the X-ray regime, *i.e.* between 10 and 30 KeV and the resulting photons are collimated in the forward direction. These allow the detector to discriminate tracking hits (ionization inside straws), which pass a lower threshold, from transition radiation hits, with a bigger one.

The three subsystems composing the ID provide 7 high precision measurements (3 pixels and 4 SCT) and ~ 36 measurements in the TRT. The whole ID is confined inside a 2T solenoidal field bending the charged particles. Using the measured space-points, the helical trajectory of the track is reconstructed. With simulations of the inner tracker response to minimum ionizing particles (MIP) the expected resolution of the helix parameters gives a momentum resolution[2][2]:

$$\sigma\left(\frac{1}{p_T}\right) = 0.36 \oplus \frac{13}{p_T\sqrt{\sin\theta}} \qquad (\mathrm{TeV}^{-1}) \tag{1.1}$$

where θ is the polar angle and p_T transverse momentum in GeV. The parameters that give

[2]The numbers quoted here are based on the atlas TDR, and might change and deteriorate due to the additional material that has been added to the detector.

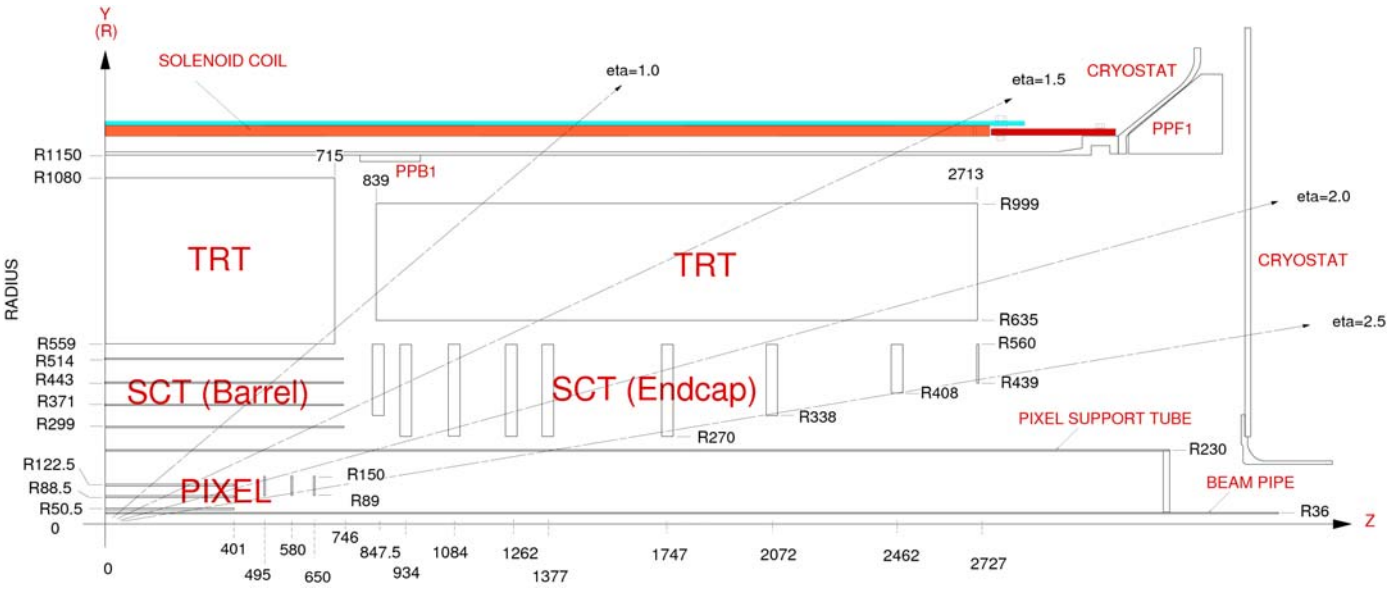

Figure 1.2 Layout of the inner detector of ATLAS, composed of: Pixel detector, Semiconductor Tracker (SCT) and Transition Radiation Tracker (TRT).

the track direction are azimuthal angle, ϕ, and polar angle, θ. The Z axis of the system is defined by the beam axis. The other helix parameters correspond to the longitudinal (z_0) and the transversal (d_0) impact parameters. The expected resolution in the transverse impact parameter is:

$$\sigma(d_0) = 11 \oplus \frac{73}{p_T\sqrt{\sin\theta}} \quad (\mu m) \tag{1.2}$$

The resolutions come from different sources. In particular, for particles with $p_T < 36$ GeV (most of the tracks in B-physics are in this range), effects related to multiple scattering in the detector material dominate the p_T resolution. Particles change their trajectory due to Coulomb interactions with material, degrading not only the p_T resolution but also the angular resolution. Scattering also dominates the resolution in the transverse impact parameter, d_0, for $p_T < 6$ GeV. In addition to these processes, electron bremsstrahlung contributes to the resolution deterioration.

An essential goal of the ID is to maintain high tracking efficiency. In the range $|\eta| < 2.5$, the acceptance region for high precision physics, > 95 % of the minimum ionizing particles (MIPs) with $p_T > 5\ GeV$ are expected to be reconstructed. The probability to reconstruct fake tracks should be less than 1 %. These requirements are relaxed slightly in the vicinity of the high p_T candidates. Nevertheless, the efficiency can be reduced, degrading the detector performance, because of low energy particle absorptions in the material. To avoid these effects, the material composing the ID should be kept as low as possible. This has been partially fulfilled with a careful design of the active detectors and

by the use of low Z-materials (such as aluminium for the power cables, and carbon-fiber for support structures), although an increase of material in the whole range of η values has occurred with respect to the initial ID Technical Design Report.

1.1.2 Calorimetry

The ATLAS calorimeter system [3] is designed to measure the energy (and $\theta - \phi$ direction) of particles and jets formed in the pp collisions. The energy measurement of calorimeters is based on the formation of a shower, a cascade of particles, when a relativistic particle transverse dense matter. The energy resolution for the calorimeters is dominated by the stochastic or sampling term which decreases with $1/\sqrt{E}$.

Electrons and photons create a shower through pair production, $\gamma \to e^+e^-$ and $e \to e\gamma$ (bremsstrahlung) in the electric field of the nucleus. The energy loss for a given material is characterized by the radiation length X_0. The lateral development of the shower is determined by the Moliere radius.

Hadrons produce a cascade of hadron-nucleus interactions. The longitudinal development of the shower is determined by the interaction length of the material. Hadronic showers contain a variable electromagnetic component from radiation of photons (bremsstrahlung) and π^0 decays. The shower shape of hadronic showers is more irregular than that of pure electromagnetic showers.

Since the nuclear interaction length is about an order of magnitude greater than X_0, ATLAS, as CDF and other experiments, has two different calorimetry systems: an electromagnetic (ECAL), placed in the innermost part of the system, and an hadronic calorimeter (HCAL), see Figure 1.3.

- **Electromagnetic calorimeter:** a high granularity lead/liquid argon (LAr) sampling calorimeter with a specific geometry that provides a complete hermetic ϕ symmetry. The total thickness of ECAL is around 24 to 36 radiation lengths (X_0). The sub-system has a first part acting as a *pre-shower* detector (with around 1.5 X_0), enhancing particle identification (γ, π^0, e) and providing a precise measurement of η. An excellent invariant mass resolution is needed for many physics measurements: for a 1% resolution of the W mass, the energy resolution requirement for the sampling and constant terms becomes:

$$\sigma(E) \simeq \frac{10\%}{\sqrt{E}} \oplus 1\% \tag{1.3}$$

  where the energy is expressed in GeV; the energy measurement is based on the determination of the ionization energy loss by the charged component of the shower

(electrons and positrons) in the thin (2-6 mm) gaps between the absorber plates, filled with the liquid argon. The total coverage of the ECAL extends up to $|\eta| < 4.9$.

- **Hadronic calorimeter:** it uses different technologies in each rapidity region. The barrel and *extended barrel* regions consist of steel plates which are sampled by plastic scintillator tiles. These are placed perpendicular to the beams, and are grouped into cells of approximately constant η. The structural material and iron absorber together form the return yoke for the central solenoid. In the endcap, where radiation damage would severely degrade the scintillator, a parallel-plate Cu/LAr hadronic sampling calorimeter covers $1.5 < |\eta| < 3.2$. The jet energy resolution is expected to be measured with a precision that should be adequate for the study of the physics processes of interest at the LHC. It is given by [4]:

$$\frac{\Delta E}{E} = \frac{50\%}{\sqrt{E}} \oplus 3\%, \ |\eta| < 3 \tag{1.4}$$

$$\frac{\Delta E}{E} = \frac{100\%}{\sqrt{E}} \oplus 10\%, \ 3 < |\eta| < 5 \tag{1.5}$$

where the energy E is expressed in GeV. The ATLAS calorimeter performance technical design reports present the results of detailed simulation studies of the hadronic calorimeters, showing that the energy resolution requirements of the previous equations are met by the current design. Beam tests of prototype modules have confirmed these conclusions.

1.1.3 Muon spectrometer

High-momentum final state muons are amongst the most promising and robust signatures of physics at the LHC. Many of the physics processes of interest involve the production of muons. Their identification provides an important signature for the event selection of the experiment, especially because of the high density environment of hadronic colliders. For instance, muons coming from disintegrations of heavy quarks can be identified and trigger on such events. To exploit this potential, the ATLAS collaboration has designed a high-resolution muon spectrometer with stand-alone triggering and momentum measurement capability over a wide range of transverse momentum, pseudorapidity and azimuthal angle. Muons are the only charged particles able to go through all sub-detectors and reach the detector external layers, where the muon system [5] is placed.

The muon system consists of muon detectors and toroidal magnets. The magnet system for the muon chambers is composed of eight superconducting air-coils in the

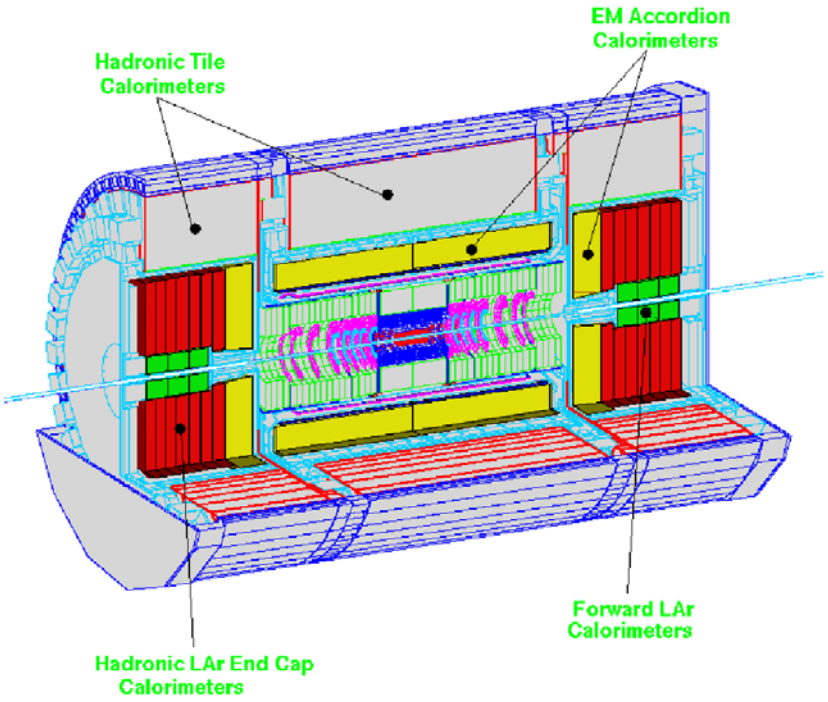

Figure 1.3 3D view of the calorimetry system of ATLAS. In the central part the electromagnetic calorimeter is placed (ECAL). The outer part is formed by the hadronic calorimeter (HCAL).

barrel region and eight in each endcap. The magnet generates a toroidal magnetic field, that is 3.9 Tesla in the barrel part to 4.1 in the endcaps. The inner diameter of the barrel toroids is 9.4 m, the outer diameter is 19.5 m and the length is 26 m.

There are three measurement chambers or *stations* for muons in the barrel and in the endcap region, giving high precision space points for the measurement of the sagitta of the track. Over most of the pseudo-rapidity range, a measurement is made by Monitored Drift Tubes (MDT) and, for large pseudo-rapidities ($|\eta| < 2$) and close to the interaction point ($2 < |\eta| < 2.7$) by Cathode Strip Chambers (CSC). The resolutions achieved with these systems is around 80 μm and around 60 μm respectively. The final ATLAS muon reconstruction uses the combined information from the high resolution measurements in the muon spectrometer and the inner detector.

Dedicated muon detectors with fast response time and less precision will give a measurement of the p_T and trigger. The trigger chambers are Resistive Plate Chambers (RPC) in the barrel part and Thin Gap Chambers (TGC) in the forward region.

1.1.4 Trigger

ATLAS trigger and data acquisition is a technological challenge due to the large number of channels ($\sim 10^8$), the high crossing frequency (40 MHz) and the high LHC luminosity ($10^{34}\ cm^{-2}s^{-1}$). At the high luminosity of LHC a total of 10^9 interactions per second will occur, each event with a raw data size of 1 MByte. Current data storage technology limits the amount of data that can be stored to the order of 100 MB/s. This corresponds to a maximum trigger rate of $\sim$ 100 Hz. Thus it is necessary to have a very fast trigger, which is able to reduce the frequency of storage by 7 orders of magnitude, but also able to preserve all interesting events, with an open design for unknown physics channels.

The trigger is structured in three levels (LVL1, LVL2, Event Filter(EF)), see Figure 1.4. Each of the levels is more complex and slower than the previous one: the frequency achieved in each level trigger is also showed in the figure.

The Level-1 (LVL1) trigger uses information from a relatively small number of detectors[3], to achieve a fast turn-around time; it takes data each beam crossing at a frequency of 40 MHz (25 ns), having only 3 μs to reach a decision on the validity of the event. This leaves a maximum frequency for the next level of 100 KHz, that is the capacity of LVL2. During the trigger latency the data from the detector is stored locally in a pipeline. At this level, the trigger decision is based entirely on an analysis of the data from the dedicated parts: fast muons stations (Thin Gap Chambers and Resistive Plate Chambers) and the calorimeter data with reduced granularity.

[3]Inner Detector is not used in this level due to the complexity of the events at high luminosity.

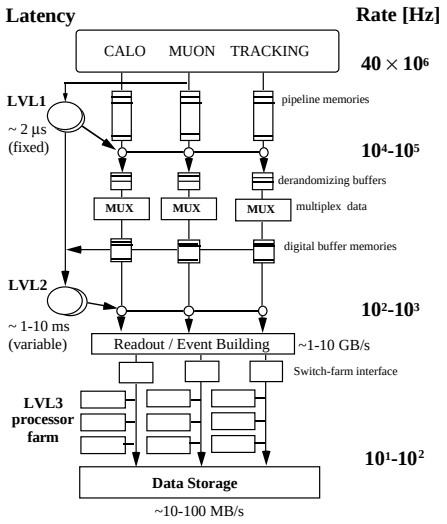

Figure 1.4 Representation of the ATLAS trigger and trigger rates.

The Level-2 (LVL2) reduces the processing frequency from 100 KHz to 1 KHz. Information from Level-1 is used to identify regions with electromagnetic clusters with high p_T, (electrons or photons), jets and muons. Thus, Level-2 has data coming from a small part of the detector, reaching a latency smaller than 10 ms.

Both the LVL1 and LVL2 algorithms as well as efficiencies and frequencies for several signal to noise rates have been evaluated with detailed physics and detector simulations. Processors used in trigger will be fully programmable. In this way, selection criteria will be able to be changed depending on the physics results.

The third stage, the EF, is placed after the event builder. At this point detailed alignment and calibration data are available. The definition of an abstract event data model allows the use of offline algorithms in the EF. A software based event reconstruction is done in PC farms at this level. Event reconstruction will not be longer than 1 s, and events will be stored for later analysis. The EF will have a storage capacity around 100 MB/s.

1.2 The SemiConductor Tracker

The Semiconductor Tracker (SCT) is one of the ATLAS Inner Detector elements which aim to track charged particles in the ATLAS experiment. The SCT is divided to three regions - one barrel and two endcap regions.

The barrel region is composed of four cylindrical layers of detection modules around the beam axis and covering the full azimuthal range. The layers extend from a radius of

27 to 56 cm, and they are 149 cm long, covering a rapidity range up to $|\eta| < 1.0$.

Each of the endcap regions is composed of 9 carbon-fiber wheels placed perpendicular to the beam: they provide measurements in the region from $z = 80$ cm to $z = 270$ cm, covering the full azimuthal range and a rapidity range up to $|\eta| < 2.5$ and with a half length of 279 cm.

In both regions, endcap and barrel, sensor modules are arranged with an overlap between modules, to avoid dead zones in the detector.

The SCT is populated with a total of 4088 silicon micro-strip detector modules. The modules are constructed from one or two pairs of micro-strip sensors (wafers) glued back-to-back with a 40 mrad stereo-angle: in this way the measurement of the particle position can be obtained as the intersection of the strips with signal (information from both sides). The assembly and gluing of the sensors should fulfill certain limits [2] to have a reliable and precise position reconstruction.

In both barrel and endcap geometries, the azimuthal angle ϕ - essential to the transverse momentum determination - is measured with a high precision. The barrel modules also provide a measurement with limited resolution in the Z coordinate along the beam axis, and the endcap modules in the radial distance R from the beam axis. In both cases the third coordinate is given by the sensor position. The barrel modules are all identical whereas the radial coverage of the end caps requires three geometrically different versions [6]. Endcap module geometries have denominations: *Inner* (in the ring closer to the beam axis), formed with a single wafer of 61.06 mm length, *Middle* and *Outer* (ring closer to TRT) with an active strip length of 121.1 mm and 116.7 mm respectively. The outer rings have 52 outer modules while middle and inner rings have 40 modules. The inner modules are composed of only 2 wafers, whereas for outer and middle 4 wafers are needed. The different layouts are shown in Figure 1.5 and 1.6. There are basic differences between the two module designs - barrel and endcap, both in the geometrical concept and in the different components.

Barrel modules are rectangular, composed of four wafers with the same size; endcap modules are wedge shaped. The readout electronics position is centered for barrel and at one end for the end caps, where the connection between strips and readout electronics is made through a pitch adapter (or 'fan-in') structure. The hybrid itself is one of the main differences between barrel and forward modules, although the same type of chips is implemented in both cases and the readout is the same (see Section 1.2.2). Each chip has 128 channels, so that six are necessary for a single module plane read-out. Chips are glued on the hybrid circuit, with analog and digital part, based on a carbon-carbon flex. Different versions of the endcap module hybrid were designed. The final version, called K5, is the one used for the production of endcap modules. Among the three endcap

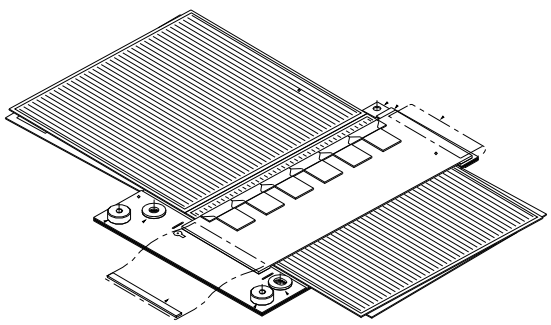

Figure 1.5 Barrel module layout

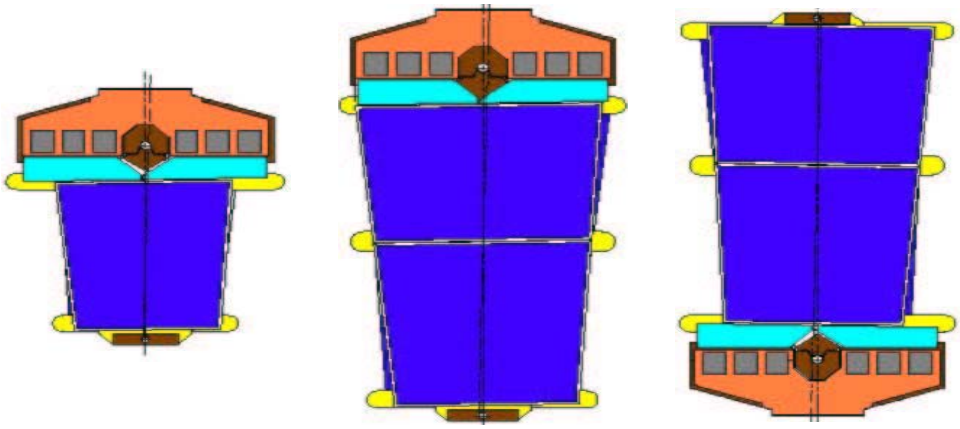

Figure 1.6 The three forward module layouts: from left to right, inner, middle and outer modules.

geometries, few main differences exist. The electronics is situated in the narrower region of the wedge for the outers and in the opposite side for middle and inner modules. As mentioned, the inner module is composed of only two silicon wafers.

All the silicon sensors are of 285 μm thick n-type material with a resistivity of 4-8 k Ω·cm. Each sensor has 768 active micro-strips formed by implanting p^+ material. The strips on the barrel sensors have a pitch of 80 μm, while the strip pitch on endcap modules varies from 54.4 to 94.8 μm with the fan geometry. A detailed description of the sensors is given in [7]. Table 1.1 shows values for angles between strips and pitch for endcap and barrel wafers.

The SCT will use around 20000 silicon wafers, 10900 rectangular in the barrel and 8700 wedge shaped in the endcap. In total 6 different geometries are used, 5 of them in the endcap (two geometries for the outer, two for the middle and one for the inner). The dimensions of wafers vary from 38 cm^2 to 42 cm^2. The next section explains the general

performance of the micro-strip detectors.

Wafer type	Pitch
Barrel	80 μm
Forward Outer	0.161 mrad
Inner, Middle	0.209 mrad

Table 1.1 Geometrical characteristics for the SCT silicon wafers.

1.2.1 Micro-strips detectors

Historically, the first operative micro-strip detector was built by the CERN-MUNICH group in the 1970s for the study of short live particles in hadronic interactions. Since then, these detectors have become essential for most experiments in particle physics [8].

The basic device of a micro-strip detector is the so called "reverse biased pn junction" (diode): Figure 1.7 shows a sketch of a transverse cut. At the bottom of the device a metal layer (aluminium) is deposited to make electrical contact for the biasing of the device. The highly doped n-type part over the metal is placed to prevent depleted zone to reach the bottom and to guarantee a good ohmic contact. Thus, the bulk is composed of an n-type semiconductor material and p-type strips implemented in it. Over all an insulator material (usually SiO_2) is placed, to protect the silicon of the wafer. Aluminium is deposited on the p-type zones over the insulator and it is used to connect the pn-junction to the electronics and collect the charge.

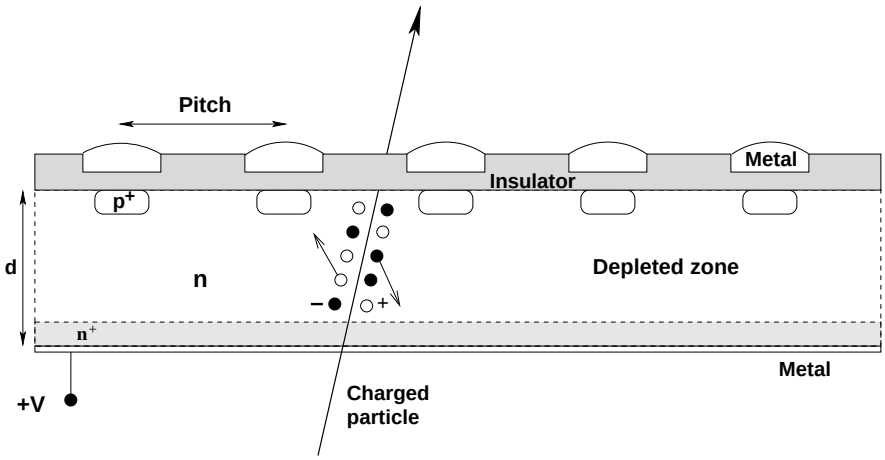

Figure 1.7 Schematic view of a transversal cut of a micro-strip detector.

Silicon micro-strip detectors are basically a set of reverse biased diodes or more precisely a set of parallel pn-junction strips separated by a small distance. The reverse-biased

pn-junction generates a region without free carriers, called the depleted zone. When a charged particle passes through the depleted zone, it creates electron-hole pairs by ionization. The initial ionization is limited to a cylinder of radius around 1 μm, of electron-hole pair produced uniformly along the particle trajectory. The generated pairs drift in the electric field originated by the applied bias: if the *pn* detector is fully depleted, the passage of a charged particle creates about 20,000 electron-hole pairs, the holes drifting to the strips p^+ and the electrons to the backplane. During the drift, spatial distribution of the cloud of carriers is dominated by diffusion, while the contribution due to the repulsion between carriers of the same type is insignificant. The resulting width of the cloud for a typical device is small, around 10 μm for a 280 μm thick detector at room temperature and biased at 50 V. The width can be calculated as [9]: $\sigma = \sqrt{2\frac{\kappa T}{q}\mu t}$, where κ is the Boltzmann constant, T is temperature, q is electron charge, μ is carrier mobility and t is the charge collecting time. Using this approximation, the spatial distribution of the drifting carriers is the same for electrons and holes. The typical full deposited charge collected in a readout strip is about 4 fC. The signal produced is proportional to deposited energy, so it increases with the width of the depleted region. The bias needed to fully deplete a *pn* junction is:

$$V_d = \frac{q}{2\epsilon_s} N_D d^2 = \frac{d^2}{2\epsilon_s \mu_e \rho} \tag{1.6}$$

where N_D is the donor (substrate) concentration, d is the thickness of the wafer and ρ is the resistivity of the less doped zone (substrate). ϵ_s is the dielectric constant of silicon and μ_e is the electron mobility.

The signal collected on the strips gives the particle crossing point. Thus, the separation between strips or pitch, p, determines the resolution of such devices. Equation 1.7 show the expected resolution for a micro-strip device with binary readout, as in the case of SCT.

$$< \Delta x^2 >= \frac{1}{p} \int_{-\frac{p}{2}}^{\frac{p}{2}} x^2 dx = \frac{p^2}{12} \tag{1.7}$$

Considering the ATLAS case for barrel modules with a constant pitch of 80 μm, a resolution $\sigma \sim 23$ μm is obtained

There are many advantages using a semiconductor as the detecting medium, for instance:

- reduced ionization energy: only 3.6 eV are needed to create an electron-hole pair, compared to 5 eV to ionize solid insulator and 30 eV to ionize gas;

- the energy loss per unit length is large due to the high density (2.33 g/cm^3): thus, sensors can be very thin and produce a clear signal;

- despite the density, electron and holes can move almost freely and very fast. Charge from carriers can be collected in less than 20 ns;
- electronics can be integrated inside or very close to the detector.

1.2.2 Front-end electronics

A signal of 4 fC is the typical deposited charge in the silicon, and external amplification is in general needed before further processing of the signal. The read-out electronics is located very close to the silicon sensors to avoid loss of noise performance and large input capacitance due to long cabling.

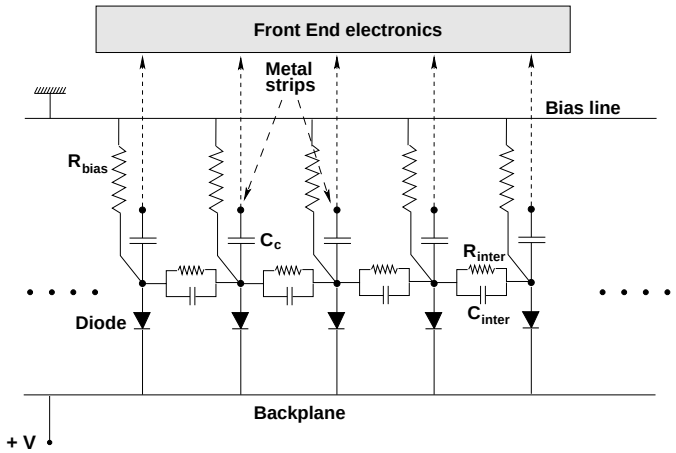

Figure 1.8 Equivalent diagram of SCT micro-strip detector.

A silicon *pn* micro-strip detector can be represented with a simplified equivalent diagram as in Figure 1.8. The bias resistance, R_{bias}, is a poly-silicon resistance situated between the bias line and the front-end electronics. The main goal of the R_{bias} is to ensure a low current in the electronics. The value is chosen to have a small contribution to electronics noise. C_{inter} and R_{inter} are the inter-strip capacity and resistance. C_{inter} has the largest contribution to the load capacitance C_{load}, where the load capacitance is the equivalent capacity of the p strip and it is the capacity seen by the readout electronics connected to the strip. C_{load} is responsible for most of the electronic noise, being dominant when increasing the strip length. The impact of C_load on the signal/noise ratio depends on the peaking time of the shaping (short time = high noise). A small peaking time is of course needed for LHC applications. . Micro-strip detectors can have DC-coupling or AC-coupling. In the direct coupling or DC, the readout electronics is connected directly to the p^+n junction of the strip, whereas in AC coupling, a capacitor (C_c) is placed after the junction. For the SCT detectors, AC-coupling has been chosen.

The p^+ implant is AC coupled to a metalized strip on the sensor surface, which is connected to a channel of the readout electronics. The coupling capacitance C_c has a value around 20 pF/cm. AC-coupling between the strips and the electronics prevents current generated in the reverse-biased diode (leakage current) from entering the electronics.

The SCT front-end integrated circuit - the radiation-hard ABCD3T [10] - has 128 channels. The ABCD3T is the final design of the single chip implementation of binary read out architecture, with radiation-hard DMILL technology. The ABCD integrates the analog and digital functionalities in a single chip: the front end circuit, discriminator, binary pipeline, derandomizing buffer, data compression logic and the read-out control logic. The design and performance of these chips are detailed in [10]. Figure 1.9 shows a block diagram of the chip, while the schematic of a single channel is shown in figure 1.10.

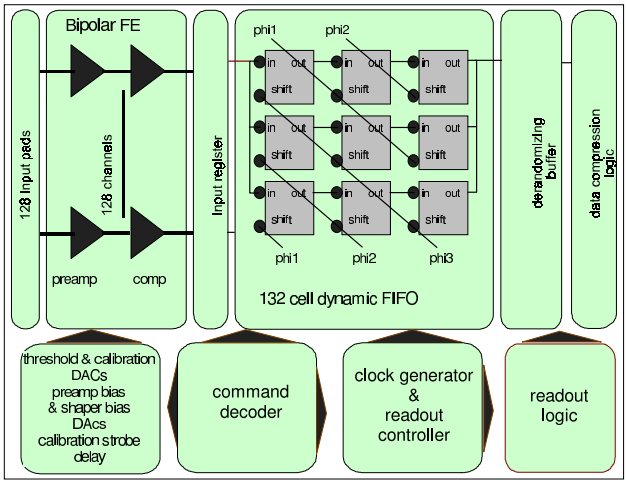

Figure 1.9 Block diagram of the analogue front-end circuit.

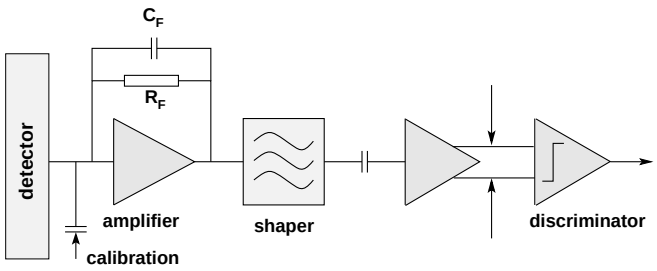

Figure 1.10 Schematic diagram of the analog stages of a single channel as implemented in the ABCD chips (C_F and R_F are the feedback capacitor and resistance respectively).

The signal coming from strips is amplified and integrated with a semi-gaussian shap-

ing. The shaper optimizes the signal to noise ratio of the front-end. The transfer function of an ideal $CR(RC)^3$ is:

$$h(t) = (\frac{t}{\tau})^3 e^{-t/\tau} \tag{1.8}$$

where τ^3 is the shaping time. The design peaking time of the shaper is 20 ns. The response of the shaper to a certain input is obtained by convoluting the time resolved input pulse with the transfer function $h(t)$, but a more realistic description of the ABCD shaper is obtained by taking into account an extra differentiation step of 150 ns. This results in a faster fall-off of the pulse tail.

In the binary readout scheme, the pulse obtained is reduced to one bit of digital information by comparing it with a selected threshold. The non-uniformity of the amplifiers is corrected at this point by adjusting a 4 bit digital-to-analogue converter (trimDAC) for each channel. This feature is implemented especially to cover the increasing spread between channels after irradiation and will be further described later.

The shaped signal is compared in the discriminator. One important feature of the ABCD discriminator is that it can be operated in two modes: level sensing (returns 1 if the signal is above the threshold) and edge sensing (1 is saved only if a transition low to high occurs). Operating the discriminator in edge sensing reduces the tail of the shaped signal, thus the probability that ghost hits appear in the consecutive beam crossing.

The resulting hit pattern is then transferred and stored into a binary pipeline (FIFO memory), 132 cells deep, until a level-1 trigger decision requires it (trigger latency $\simeq$ 3.2 μs). The output data of 3 bits (the precedent, the required bit and subsequent) is compared to a compression pattern. If the hit pattern satisfies the requirement, it is added to the data stream. Three different algorithms (or compression mode) are available:

- ANYHIT compression: $1XX \quad | \quad X1X \quad | \quad XX1$
- LEVEL compression: $X1X$
- EDGE compression: $01X$

where 1 means that a hit has been recorded in the register, 0 no hit and X could be 0 or 1. These three bit combinations are the type of patterns read out by each of the algorithms. In ANYHIT compression, channel information is considered if the signal was over threshold in any of the three bits (three different clock cycles). This mode is used for tests. In ATLAS, beam will be synchronized with trigger request. The LEVEL and EDGE compressions uses this information to provide an additional noise rejection.

The ABCD chips include an integrated calibration circuit that allows a fast and accurate characterization of the module.

To readout each strip, 6 chips are attached to each side of a module; they are mounted on a specific structure called *hybrid*. A fully assembled hybrid consists of a six layer copper-polyimide flex circuit, a substrate, SMD components (connectors, resistors, capacitors, and a thermistor), twelve ABCD3T read-out chips and one DORIC (Digital Optical Receiver Integrated Circuit) chip for the optical links[4].

The first chip on each side of the module, designed as the master chip, is responsible for the electrical transmission of data. Within the module a token passing scheme is used to control the transfer of data to the master chip for onward transmission. This scheme incorporates several redundancy options such that, should any single chip fail, the remaining chips can still be read out.

Each SCT module is connected to its own programmable low voltage and high voltage power supply channels. The power distribution system includes three patch panels and three lengths of conventional cable, the innermost section being formed by low mass power tapes to minimize the material in the tracker volume. In the endcap module the power tapes connect directly to the hybrid, on which the opto communication chips are mounted. In the barrel region the interface between the module, power tapes and optical signals is provided by a further copper/kapton flex circuit.

The final version of the endcap hybrid chosen by the SCT community is the already mentioned K5 hybrid, shown in Figure 1.11.

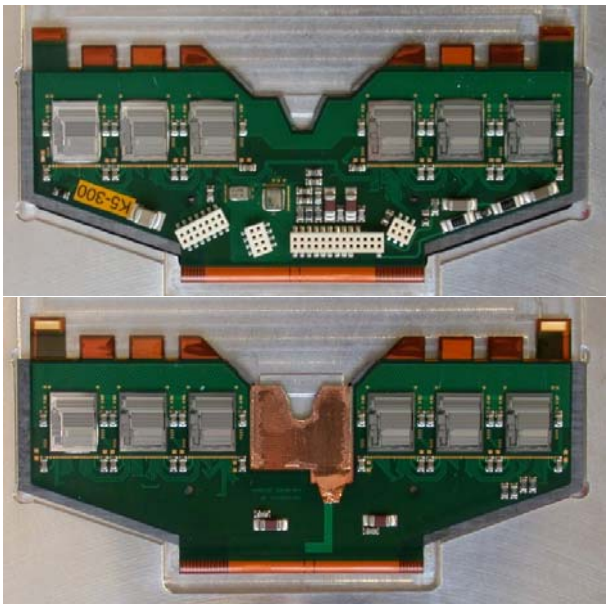

Figure 1.11 K5-300 hybrid front and back view.

[4]The SCT will be read-out and supplied with clock and control signals optically, with approximately 8000 data- and 400 control-links. These numbers come from the fact that each silicon module will require one control and two readout links.

1.3 SCT endcap modules

1.3.1 Mechanical Description of a Module

The sensors [7][11] for the SCT endcap module are wedge-shaped p-on-n detectors, 285 μm thick with 768 read-out strips (see Figure 1.12). The strips are about 6 cm long and AC-coupled to read-out electronics mounted on a hybrid.
The sensors are read out by **12 custom designed ASICs** (ATLAS Binary Chip DMILL 'ABCD' [10]) with 128 channels per ASIC mounted on the **hybrid** (Figure 1.11), where each channel provides preamplification, shaping with a time constant of 25 ns, comparators with thresholds which are trimmable for each channel, a digital pipeline which is 132 cells deep to allow for data storage while the first level trigger decision is made, data compression and readout buffers. In this way signals from the sensor are converted to binary hit information in the front-end and the data are transmitted by binary optical links.

The silicon sensor pairs are glued back-to-back on a support structure **(spine)** with a 40 mrad stereo angle providing two-dimensional position information. The spine, the module mechanical support structure, is made of thermal pyrolitic graphite (TPG) with a high in-plane thermal conductivity of 1700 W/mK in order to carry the heat from the detectors to the cooling points at the side or end of the modules. Thanks to the cooling structre, an operating design temperature of -7^oC of the wafers is expected. The spine is not present on barrel modules, and a TPG baseboard supplies the same functions. Fan-in structures are replaced by a small pitch adapter located on the hybrid.

A scheme of a module components is presented in Figure 1.13. Other parts of the module and their mechanical functionality include:

1. **The pad-locator** - a precision locator for the alignment of the module when mounted.

2. **The far-end washer** -gives the mounting precision in the y direction when mounting the module.

3. **The fan-ins (pitch adapters)** - the SCT endcap Modules have a pitch dissimilarity between pads in the different detector channels and the read-out chips located on the hybrids. The adaptation of these connections is made via a glass plate with metal tracks named pitch adapters, or in short, fan-ins. The purpose of these fan-ins is the electrical connection of every channel from the detectors to the read-out chips, adapting the different pad pitch. They also make the mechanical connection

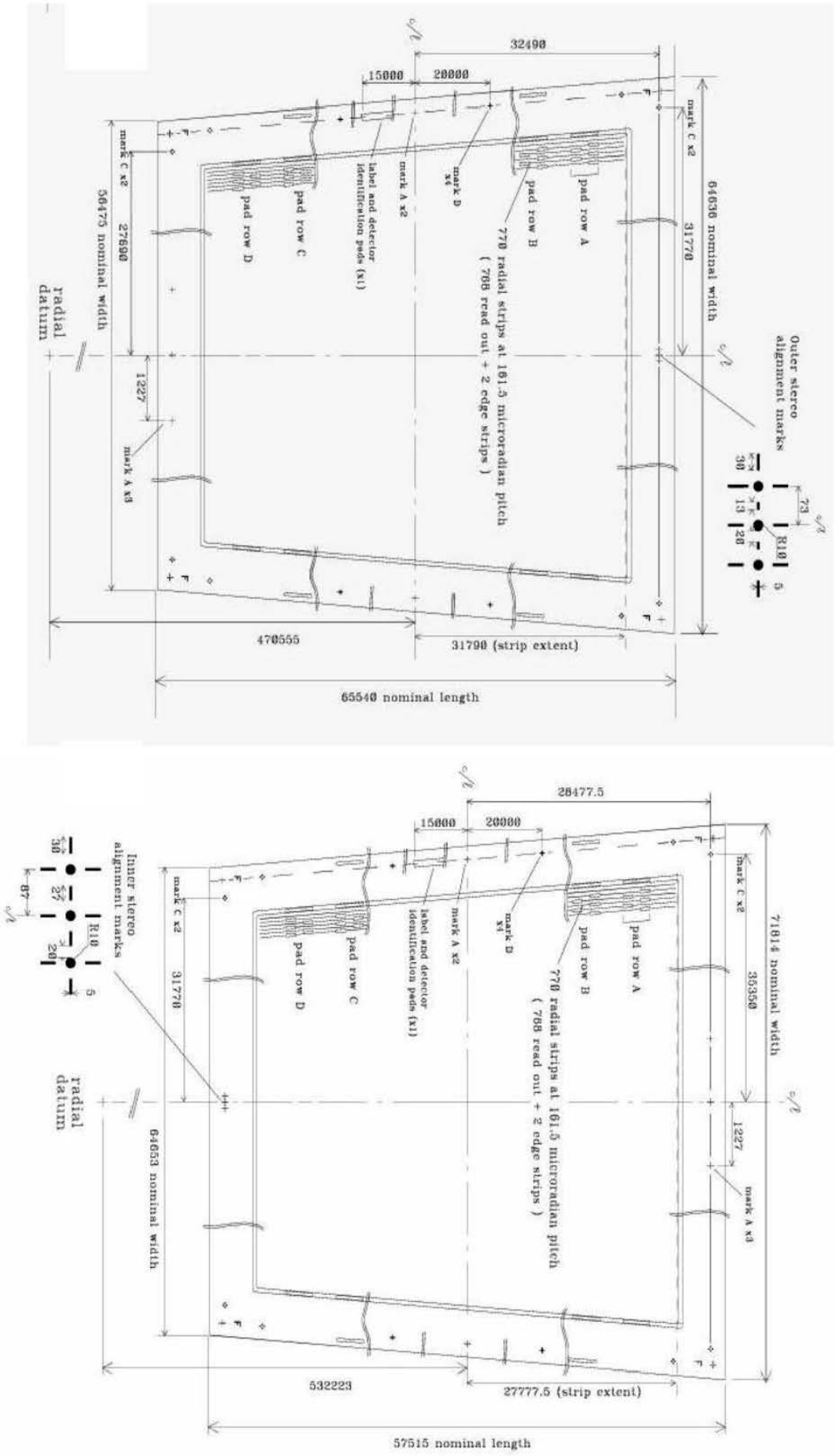

Figure 1.12 Geometry of the Hamamatsu W31 and W32 silicon sensors used for outer modules of the SCT endcap built in Geneva.

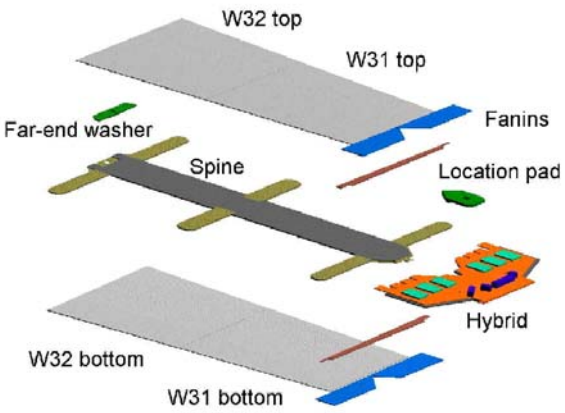

Figure 1.13 The different parts composing an SCT endcap module

between the hybrid part and the detector part of the module, while maintaining an effective barrier to heat flow between these parts.

1.3.2 Module performance specifications and mechanical tolerances

The modules of the ATLAS SCT have been designed to withstand doses of up to $2.14 \cdot 10^{14}$ n_{eq}/cm^2, normalized using the non-ionizing energy-loss (NIEL) cross-sections to the expected damage of 1MeV neutrons [2]. This motivates the following operational requirements:

- Bias voltage $< 500\,\mathrm{V}$
- Produced heat $< 7\,\mathrm{W}$ per module
- Gain - $50\,\mathrm{mV/fC}$
- Linearity - better than 5%
- Peaking time - 20 ns

- Signal charge - 3.3 fC, S/N > 10
- Noise < 1500 (1900) e^- ENC before (after) irradiation
- Noise occupancy $< 5 \cdot 10^{-4}$
- Hit efficiency $> 99\%$
- Time Walk ≤ 16 ns, and bunch crossing resolution better than 99%
- Spatial resolution $\sigma = 16\,\mu$m in $R - \phi$ and $500\,\mu$m in z-direction.

A detailed explanation for the full reasoning for those requirements can be found in [12].

1.4 Physics potential of the Inner Detector

The task of the ATLAS ID is to reconstruct tracks and vertices in the event with high efficiency, contributing, together with the calorimeter and muon systems to the electron, photon, and muon recognition, and supplying the important extra signature for short-lived particle decay vertices. It has the major role in reconstructing the primary vertex in an event. The knowledge of the very precise primary vertex position is crucial for the physics in many many channels, for e.g - $H \to \gamma\gamma$, $H \to b\bar{b}$, $B \to J/\Psi K$, $B_S \to D_s\pi$ and many more. The high granularity region made of pixels and microstrips in the ID provides a unique opportunity for the detection of B-Hadrons. B hadrons, with their relatively long lifetime, leave a signature of a secondary vertex in the detector which may be efficiently reconstructed using the SemiConductor tracker.

Reconstruction and identification of B hadrons in ATLAS is most important to many physics analyses:

- searches for the low mass Higgs boson. The decay $H \to b\bar{b}$ is predominant at $M_H < 130$ GeV. Dominant background processes for the associated WH production followed by $H \to b\bar{b}$ and a leptonic decay of the W are Wbc, Wbj and Wjj, which can be reduced using b-tagging.

- precision measurements in the top quark sector

- tests of perturbative QCD (b production, $b-\bar{b}$ production correlations, asymmetries and polarizations)

- precision measurements of B hadron properties (B_c, Λ_b) for verification of the SM or searches for its possible violations

- searches for SUSY particles which include b quarks in their decay signature

- searches for forth generation quarks

As the second part of this thesis presents a measurement of a top quark property at the Tevatron, I would like to emphasize the importance of b quark tagging using the Semi-Conductor tracker. The top quark decays almost 100% to a Wb. Therefore, identifying b quarks with high efficiency is crucial for obtaining top quark enriched samples. Various measurements of top quark properties are still limited by the size of the available samples. The measurement of the W boson helicity in top quark decays, which is presented in later chapters, shows that the determination of the helicity fractions still lacks statistical precision. This measurement relies on the ability of tagging b quarks using an algorithm for secondary vertex reconstruction with the CDF Silicon tracker. Other

examples of such measurements are precision measurement of the mass of the top quark, which is a fundamental parameter of the SM and also places constraints on the mass of the SM Higgs boson, measurements of spin correlation in $t\bar{t}$ pair production production, measurements of the top charge, etc. The top production cross-section at the LHC is about 100 times higher than the Tevatron one, leading to a production of $8 \cdot 10^6$ $t\bar{t}$ pairs per year at low luminosity. With this amount of data, many top quark property studies done with statistically limited data samples at the Tevatron, could be measured more precisely. These analyses will all rely extensively on efficient identification of b quarks and therefore an excellent tracking performance provided by the ATLAS SCT is crucial. The task of achieving good tracking performance does not end once the tracker is built. The maintenance and operation of a semiconductor tracker is a great effort, which, based on my experience as part of the silicon operation group of the CDF experiment, is very time consuming and requires expertise and dedication. An efficient and professional operation of the detector and its sub systems is as well a crucial component in obtaining high quality data samples.

Chapter 2

Module Production at the University of Geneva

2.1 Production Overview

The mass production of the 1976 SCT Endcap modules began in mid-2003 at production sites in Melbourne (Australia), Manchester (UK), Freiburg and Munich (Germany), Nikhef (The Netherlands), Valencia (Spain) and the University of Geneva. At the Geneva facility, 655 modules for the outer rings of the ATLAS SCT Endcaps were assembled and tested. The module quality assurance was subsequently made at CERN and the modules were then assembled onto the disks at Nikhef and Liverpool (UK).

The module assembly, metrology and initial electrical quality control were made on the basis of rigid collaboration-wide mechanical and electrical specifications (see Section 1.3.2 and [12, 13]).
The module assembly, module metrology and module bonding at the University of Geneva were made in a clean room environment. The intermediate electrical quality control and initial thermal cycling steps were performed in an adjacent "grey room".

My personal contribution to the endcap module production at the University of Geneva was taking part, together with other physicists, in selecting components to be assembled to a module, including hybrid reception tests, measuring the I-V curves of the sensors and the modules at different stages of the production, thermal cycling the modules and performing electrical readout tests as an initial quality assurance of the modules before they were shipped to CERN, as well as oraganizing the physicists shifts for production work in the "grey room". An elaborated description of all of these activities is given in the following sections.

At the beginning of the production period I developed a statistics package (see Section

2.11) which enabled us to monitor the rate and quality of the module production. This package was then used widely by the ATLAS SCT intitutes that built endcap modules of any type, and kept being improved and updated.

2.2 Assembly Facilities

Both the $38m^2$ clean room and the $48m^2$ grey room at the University of Geneva are equipped with a slight over-pressure air filtering system having a controlled temperature ($\pm$ 1°C) and humidity. The clean room is specified as class 10,000 (less than 10,000 particle per cubic inch for 0.5μm particle size), but throughout the production the room was measured to be better than class 1000. Air from the clean room was transfered to the grey room. When necessary, manipulations in the grey room were made in a laminar flow cabinet.

The clean room areas were equipped with the necessary furniture, machines and assembly tools:

- A MicroVu [14]. Coordinate Measuring Machine (CMM - Figure 2.1) is equipped with six miniature stages for both the detector alignment and the module metrology. Labview software was used to control the movement of all nine axes in order to automate and secure the detector alignment system. The MicroVu CMM provides an x and y travel of 14×14 inches. Using a granite table, together with air bearings and linear servo motors, a measurement repeatability of 0.5 μm is achieved with an absolute accuracy, following an optical rule calibration of approximately 1 μm.

- A robotic glue dispenser was used for spreading the araldite glue over the spine and fan-ins. The operating parameters were optimized to ensure at least a 70% glue coverage with a nominal 90μm thickness [15].

- A small custom built probe station (Figure 2.8) was used for the detector and module IV scans. LabView software enables communication with the SCT production database and a comparison of the current results with existing quality control data.

- A H&K 815 bonding machine [16] was used to bond up to three modules per day. The H&K 815 bonding machine was used to make connections between each pair of silicon sensors and from the silicon sensors to the readout electronics via pitch adapters (a total of 5000 wires per module). For this project, 25 μm bonding wire (99% aluminium and 1% silicon) was used. Excellent bonding consistency and reliability was achieved. The routine bonding time for each outer module was approximately 2.5 hours. Bond failures occasionally occurred. The most severe

Figure 2.1 MicroVu metrology machine in the clean room.

Figure 2.2 The climate chamber used for thermal cycling of the module.

problem was due to pad contamination. To avoid bad wire bonds, contaminated pads were systematically identified and cleaned before the bonding operation. All defective bonds were recorded in the SCT production database for later correlation with possible readout problems. Both the metrology and the bonding machines were located in the clean room where temperature stability was maintained.

- A climate chamber (Bia Clamatic - Figure 2.2) was used to make an initial thermal cycling of the modules in the grey room. This chamber can operate at temperatures between -40°C and +200°C. The relative humidity inside the chamber was controlled using nitrogen.

- Storage cabinets were used to maintain the sensors and completed modules at between 20% to 30% relative humidity.

2.3 Quality Assurance Along the Assembly Stages

1. **Before assembly**:

   - Visual inspection of mechanical pieces to be assembled - spines, pad-locators, fain-ins, far-end washers.
   - Hybrid tests - visual inspection and readout tests, to check digital and analog functionality.
   - Measurements of IV curves of the individual silicon sensors to be assembled.

2. **During Assembly**:

   - Visual inspection of the glue and sensors after curing
   - IV measurement of the 4 sensors on the module after assembly "phase 1" (spine-detectors gluing, see Section 2.4)
   - Wire bonding and inspection
   - IV measurement of the 4 sensors after assembly "phase 2" (hybrid gluing, see Section 2.4). This step was dropped after having tested enough modules to confirm that hybrid gluing does not affect the leakage current measurements.
   - IV measurement of the module after wire bonding.
   - Metrology survey on a module subset.

3. **After assembly**:

   - Thermal cycling
   - Metrology - survey of the mechanical alignment and profile of the module (Figure 2.3).
   - Electrical readout tests of the module

2.4 Assembly line

CERN and the University of Geneva invested significant time and resources to validate an assembly system [17] that would allow the construction of reliable electrical modules within tight alignment tolerances [18]. The tolerances concern the relative alignment of the two detectors on the top side with respect to the bottom side detectors and to the precision mounting pins. The front-to-back side detectors are shifted by 40 mrad angle and the accepted tolerance is ± 130 μrad. A much more constraining tolerance comes

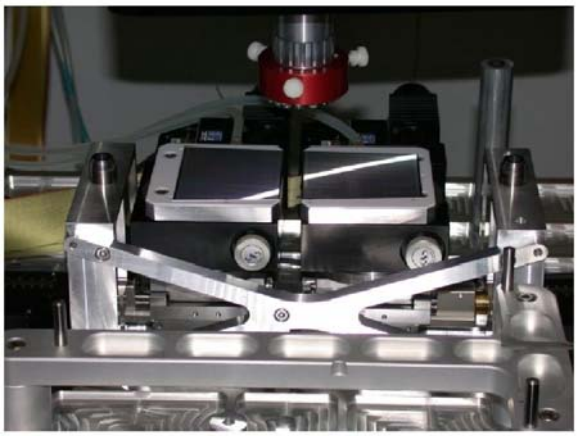

Figure 2.3 Alignment system with the xy and θ stages and the dowel pins for the referencing the detector transfer.

from the average position of the front side detectors relative to the back side detectors, which must be within ± 5 μm of the nominal value in the y axis (opposite the strips). The tolerance in the detector plane (or z axis) is ± 115 μm and original spine twisting may lead to profiles outside specifications.

Initially, when validating the procedure, a manual detector alignment tooling was developed using the principle of touching vertical dowel pins to locate two detector pairs and the spine to form an SCT outer forward module. The detectors are assembled between two vertical "reference dowels". The MicroVu machine, which is equipped with pattern recognition software and miniature $x - y - \theta$ stages is used to align the detector pairs. Vacuum detector transfer plates are used to assemble the baseline spine to the detector pairs during the gluing phase. The gluing base on which the detectors are glued to the spine has the same precise diameter dowel pins as the alignment jigs.

For ensuring a good contact between the horizontal pins and the two dowel pins, two screws are tightened in the perpendicular directions using a torque gauge screwdriver. The contact is made for the top side and back side detector transfer plates which is essential for the relative alignment between the two detector pairs and also relative to

the spine V-tongue.

A shift in the dowel pin diameters or a miss-perpendicularity in the detector alignment would be systematically wrong and a shift of several microns would then be visible. The procedure was successfully validated and metrology surveys confirmed a very good detector alignment throughout the production period.

A set of assembly jigs was developed [19] to allow the construction of reliable electrical modules within the tight mechanical alignment tolerances [13].
The assembly jigs were fabricated using Alplan, a stress free material, with the same thermal expansion coefficient (CTE) as standard aluminium.
There are two phases in the module assembly sequence:

1. Phase 1 - the spine and sensor assembly, referenced to a gluing base.

2. Phase 2 - the assembly of the hybrid with the fan-in pieces and the precision pad locator to the sensor-spine assembly.

2.5 Selection of Components

All module components to be assembled were subjected to a visual inspection and/or electrical characterization prior to assembly:

- The spine is a mechanically fragile object [20] that was visually inspected prior to assembly. The inspection verified that the aluminium nitride (AlN) V-shape was not damaged, that no damage was observable on the TPG bar, that the spine wings were not broken, that there were no openings in the insulating polymide material (especially on the TPG area) and that the aluminium high voltage HV strip for the detector bias was correctly positioned.

- The (separated) right and left fan-ins [21] were carefully examined for any chips or cracks on the cut edges, and the surfaces were checked for possible processing contamination.

- The washers are essential as reference points during the module assembly. For this reason, the quality and metrology were carefully checked; In particular the washer hole diameter was required to be 3 $mm \pm 10\ \mu m$.

- The hybrid [22] (Figure 2.4) is a flexible six layer copper/polyamide circuit laminated onto a carbon-carbon substrate that serves as a heat sink. It is equipped

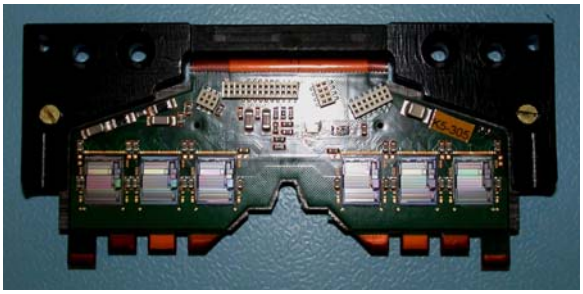

Figure 2.4 The SCT hybrid for the Endcap modules.

with SMD components and with the 12 wire-bonded ASICs. Each hybrid was initially subjected to extensive burn-in and subsequent quality assurance in Cracow. Following delivery to CERN, each hybrid was visually inspected using a 500x microscope to ensure that the ASICs were correctly wire-bonded, that the connectors were correctly placed and that there was no visual damage such as scratches or dirt on the hybrid or chips. A sequence of "confirmation" electrical tests, described in detail in 2.10 was made to confirm the digital and analog functionality.

- The testing and inspection of individual silicon sensors is extremely important, since if an electrically defective sensor is glued on the spine, the other sensors are also lost. It is also important to detect by visual inspection any potential problem on a detector. for example broken sensor edges, scratches and surface contamination. All sensors were stored in dry air following delivery. The I-V behavior of each sensor was measured up to 500 V bias in 10 V steps prior to assembly and sorted for compatibility with other sensors of the same module.

Results from each component test were stored in the SCT production database [23]. During assembly, I-V scans were also made after detector and spine gluing (Phase 1 assembly), after hybrid gluing (Phase 2 assembly) and after wire bonding (I-V measurements after hybrid gluing were discontinued later in the production). After bonding, the total current of the module was systematically compared to previous following successive assembly steps for a typical module.

All modules fabricated in Geneva used Hamamtsu sensors [11]. Their I-V behavior was very uniform, with typical leakage currents of approximately 500 nA at 500 V for the four sensors combined.

2.6 Assembly Sequence

Successive steps of the assembly procedure are described below:

1. The first sensor pair is automatically aligned using the CMM machine (Figure 2.1) and then transfered to the transfer plate. The second sensor pair is then aligned using the same automatic procedure and is transfered to its own jig.

2. After the spine is fixed into a handling frame (Figures 2.6, 2.7), Araldite 2011 glue is spread on it using the glue dispensing robot. The bottom side detector pair, the glue-spread spine and the top side detector pair are stacked on the gluing base. The detector transfer plates are screwed against the dowel pins once the spine has been correctly positioned and clamped.

3. Once the four sensors are glued to the spine an I-V measurement is made for each sensor on the probe station (Figure 2.8).

4. In the next alignment phase, the sensor-spine assembly is aligned on a turn plate jig using the V-tongue of the spine.

5. The hybrid is pre-aligned in the wishbone tool using reference pins and is located on the same jig as the sensor-spine assembly.

6. The fan-in pieces are pre-aligned with reference pins and then transferred to a jig where Araldite 2011 glue lines are added using the glue dispenser. This jig is then fixed onto the turning plate, on top of the hybrid and spine.The same step is repeated for the second fan-in pair.

7. The precision washer is vacuum placed on a specific jig and is spread with glue.

   The last four steps are made in a single operation and the module is left overnight for glue curing.

8. An I-V measurement for each sensor is made to verify the last assembly steps did not deteriorate them.

9. Wire bonding is made on both sides of the module.

10. The total current of the module is measured and compared to the expected current sum after gluing.

11. A metrology survey in x, y, z is performed on the module using the metrology frame.

All assembly steps were documented on a traveler document attached to the module during the whole production procedure, until the module is shipped to CERN for module quality assurance (a copy of the document is sent as well). The relevant information of the assembly is then inserted into the SCT database.

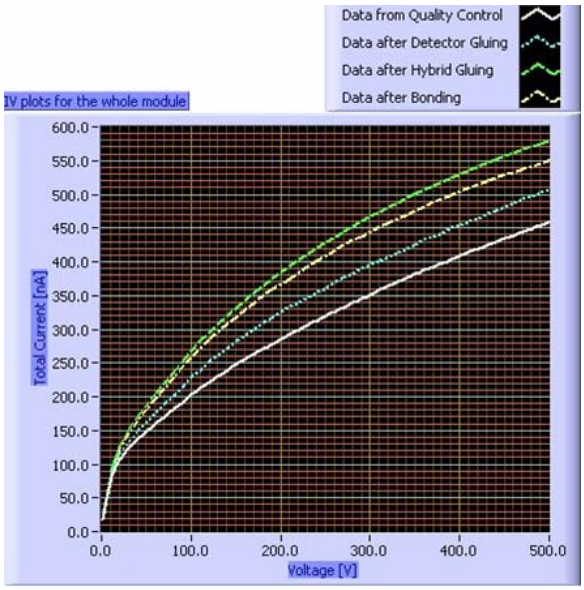

Figure 2.5 IV curves for a typical module. at the different stages the currents of the four sensors are summed to give a total current for every applied bias point. The curves obtained at the different stages are compared as well as the curve obtained for the whole module after assembly is completed.

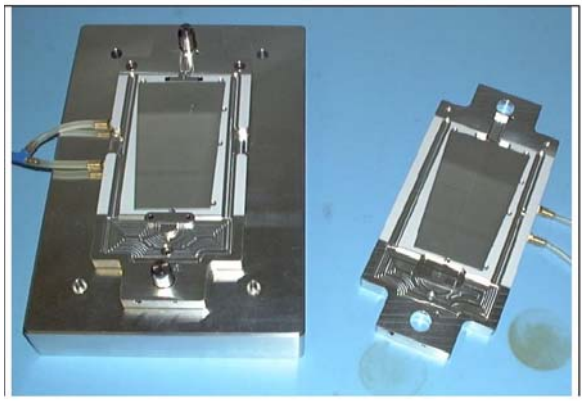

Figure 2.6 Aligned detectors to be fixed on the gluing base.

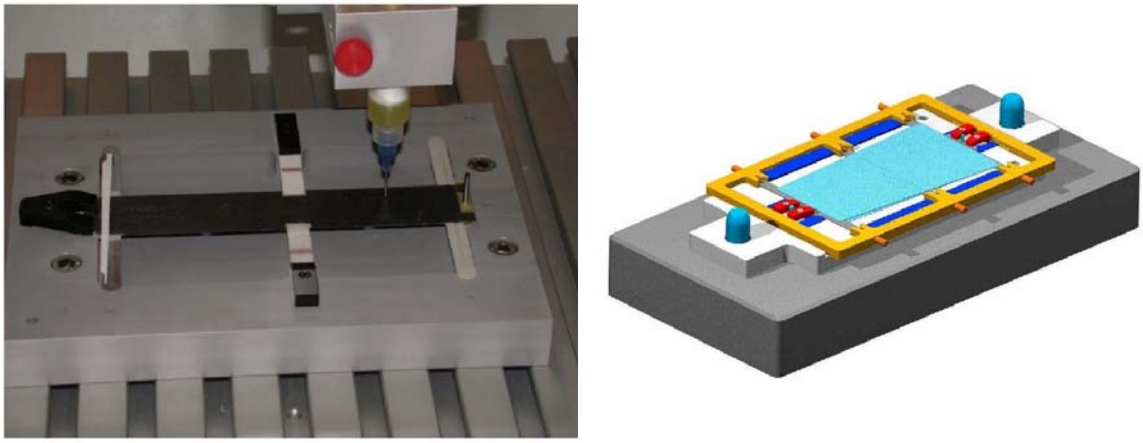

Figure 2.7 On the left: glue dispensing while the spine is positioned on the gluing base; on the right: Gluing base with the bottom detector pair and the spine handling-frame.

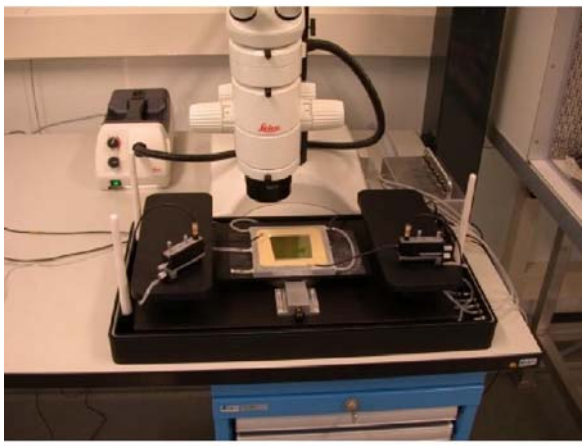

Figure 2.8 Probe Station for detectors and module IV measurements.

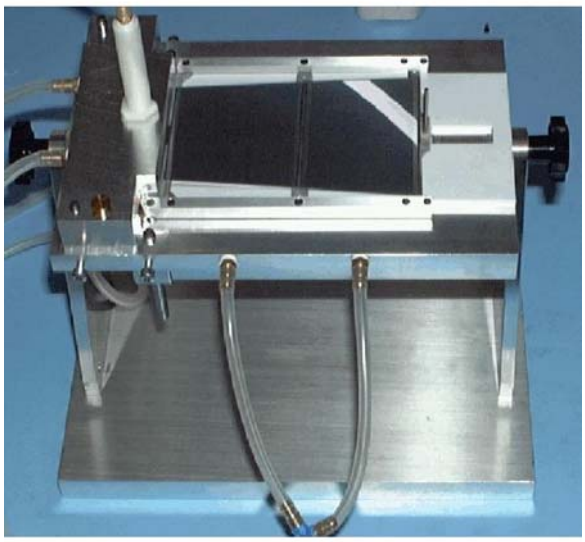

Figure 2.9 Turning plate on which the detectors and spines are glued to the hybrid via the fan-ins.

2.7 Module Production Rate

The module production rate was a key issue, because of the large number of constructed modules, the requirements for strict quality assurance and the resulting logistics. It was determined by the time needed for each production step together with the availability of infrastructure and manpower. Table 2.1 shows the time required to produce a module. Taking account of parallel operations during the assembly process, an assembly time of between 155 and 175 minutes per module could be maintained. Including the metrology and intermediate electrical quality assurance steps, an average rate of 10 modules per week was achieved.

2.8 Metrology

The MicroVu CMM machine was used for both the alignment and the subsequent module metrology.

Phase 1	Time (min, minutes)	Time (max, minutes)
Alignment	20	60
Gluing and glue preparations	30	30
Assembly on jigs	10	10
Database+traveler document entries	10	10
jigs dismounting + preparations for tests + database and traveler document + visual inspection	20	45
total	90	155
Phase 2	Time (min, minutes)	Time (max, minutes)
Assembly and glue of the spine-detector assembly, the hybrid, the precision washer and the fan-ins with glue	90	90
Dismounting the jigs + inspection + DB entry	20	40
Total	110	130
Overall total time (min)	210	285

Table 2.1 Estimated time for phase 1 and phase 2 of the module production. The maximum time takes account of problems encountered during assembly (e.g - visual inspection problems such as glue overflow).

2.8.1 The x, y survey

There are 13 parameters extracted from the x, y survey, allowing the measurement of the module x, y profile. The points measured on the back of the module need to be transformed into the same coordinate system as the front survey. The parameters are:

- mounting hole position - ("mhx, mhy"), see Figure 2.10 .
- mounting slot position - ("msx, msy"), see Figure 2.10 .
- the stereo angle of the front pair of detectors ("stereo")- defined as the angle between the line joining the two detectors and the x axis created by the hole and slot x positions. The stereo angle of the back pair is -stereo by definition. (Figure 2.10)
- mid-point between the two front detectors and the two back detectors ("midxf, midyf"), see Figure 2.10 .
- The separation between the two front detectors ("sepf") and between the two back detectors ("sepb"), see Figure 2.10.
- the orientations of the four detectors are described by the angles a1,a2,a3,a4 between their central axis and the line defining the stereo angle of that side (Figure 2.10).

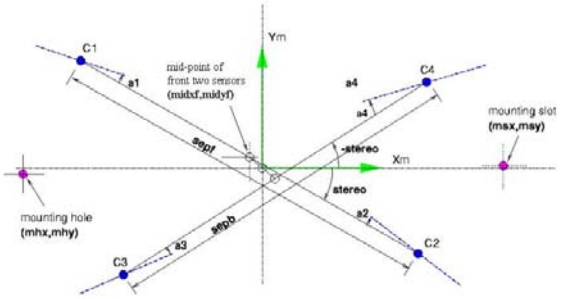

Figure 2.10 Definition of the parameters describing the geometry of a standard module. black circles C1 to C4 are the measured centers of the four sensors. The dashed line through each center gives the measured orientation of each wafer. The module is describe in the database with 13 numbers: three coordinate pairs in the x, y system (mhx,mhy), (msx,msy), and (midxf, midyf), two wafer separations sepf, sepb, the angle stereo and four wafer angle a1,a2,a3,a4. Anti-clockwise is positive so in this example a1 is positive and a2,a3,a4 are all negative.

The nominal values and tolerances of the 13 x, y parameters are summarized in table 2.2. References [24] describe how these values and tolerances are derived.

parameter	tolerance	nominal value
mhx(mm)	0.020	-78.136
mhy(mm)	0.020	0.000
msx(mm)	0.1	62.244
msy(mm)	0.020	0.000
midxf(mm)	0.010	0.000
midyf(mm)	0.005	-0.04
sepf,sepb(mm)	90	155
a1-a4(mrad)	0.13	0.00
stereo(mrad)	0.13	-20.00

Table 2.2 Nominal values and tolerances for the 13 points used to measure the module profile.

2.8.2 The z survey

The module is mounted in the survey frame and a reference plane $z = 0$ is fitted through two measured surfaces [18].

All subsequent measurements are made relative to this reference plane. A measurement of the position of 50 different points on each side of the module is done.
The measured points are each given a numerical label.
The z coordinate of each of these points is measured relative to a reference plane $z = 0$ [18]. The labeling scheme for the 100 points is indicated in Figure 2.11, the front and back sides being completely symmetric (i.e, point 1 on the front side is just opposite point

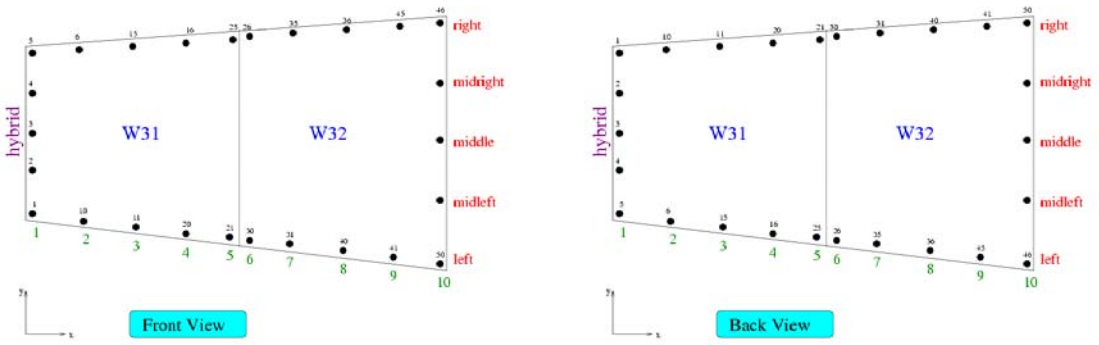

Figure 2.11 scheme of the 50 points measured for the module z profile on the module front (left) and back (right) side.

1 on the back side, what means that they should have the same x,y position). When the module is viewed from the front, the direction toward the viewer is defined to be the positive z direction. Therefore, when viewed from the back negative z is toward the viewer. For each module, metrology survey profile plots were generated and stored, example can be seen in Figures 2.12 and 2.13. The plots visualize the module surface profiles and the module thickness, allowing a powerful visual control on defects in the module structure. Plots are also available of the z-profile for a given (x, y) projection, see Figure 2.14.

2.9 Thermal cycling

When the assembly is completed the module is put through a thermal cycling (TC) in order to verify that operating over a range of different temperatures does not compromise the mechanical layout of the module and the electrical functionality. The electrically unconnected module is put in a climate chamber (Figure 2.2), supported on a jig without stress in the xy-plane but forced to be flat in the z-direction using vacuum. Applying the vacuum in the z direction was added to the TC process after few modules had been thermally cycled and a bow due to the natural bow of the spine was observed (Figure 2.15). With the vacuum it was noticed that the bowing of the module improves significantly as shown in (Figure 2.15). Over a 17 hour period the temperatures of the modules are cycled 10 times between -30° C and +35° C. A controlled flow of nitrogen is supplied to the inside of the climate chamber in order to control the dew point.

Once the thermal cycling is completed a final survey of the module profile (metrology) was made and the module profile before and after the T.C was compared. During the whole production at the University of Geneva damages or deformation of the module so

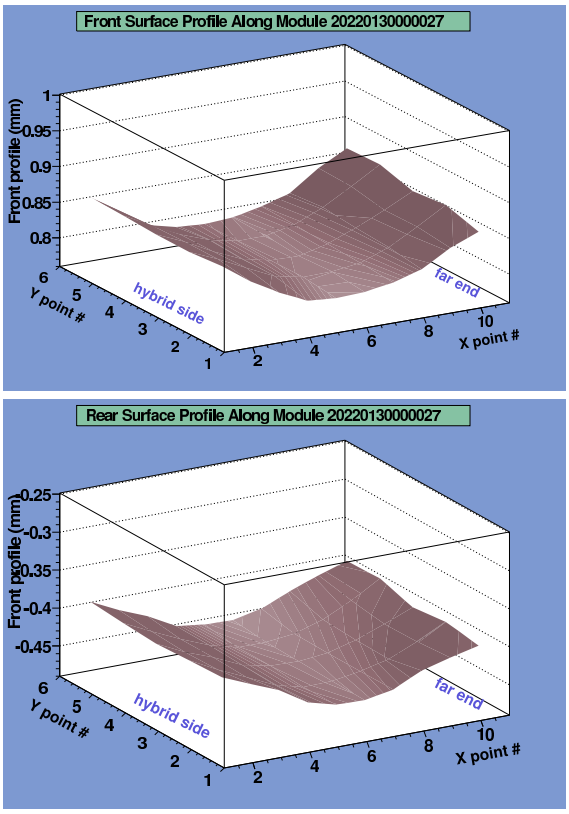

Figure 2.12 Surface gradient for the front (top) and back (bottom) sides of a typical SCT Endcap module.

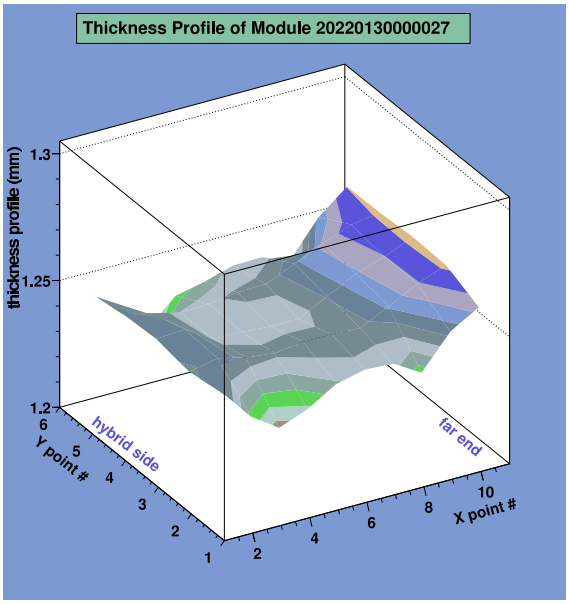

Figure 2.13 Thickness profile along the z axis of a typical SCT Endcap module

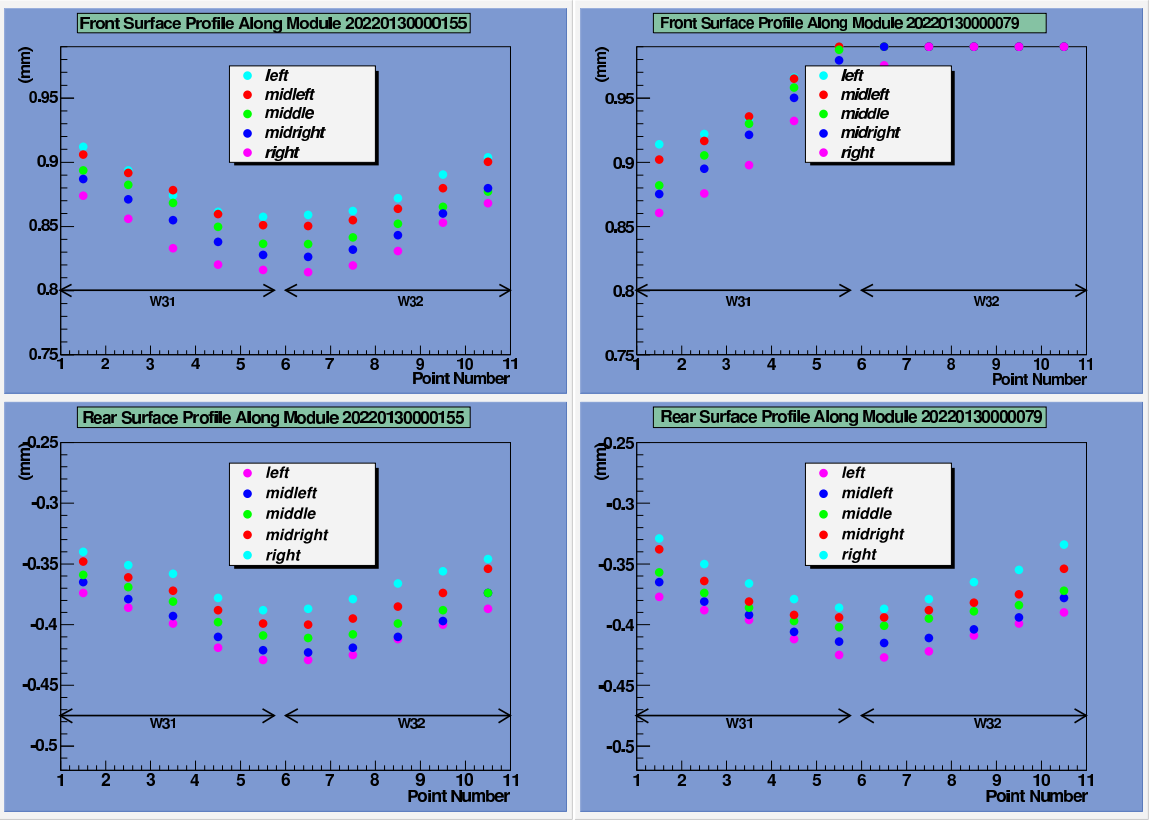

Figure 2.14 On the left - 1D surface plots for a module within specified z range.The tolerance from the $z = 0$ reference plane is ± 150 μm. On the right - 1D surface plot for a module outside specified z-range. This is not a typical module. In this particular case the shims which are used to restrict the module z thickness during the detector gluing procedure were forgotten. Such errors were extremely rare during the module production.

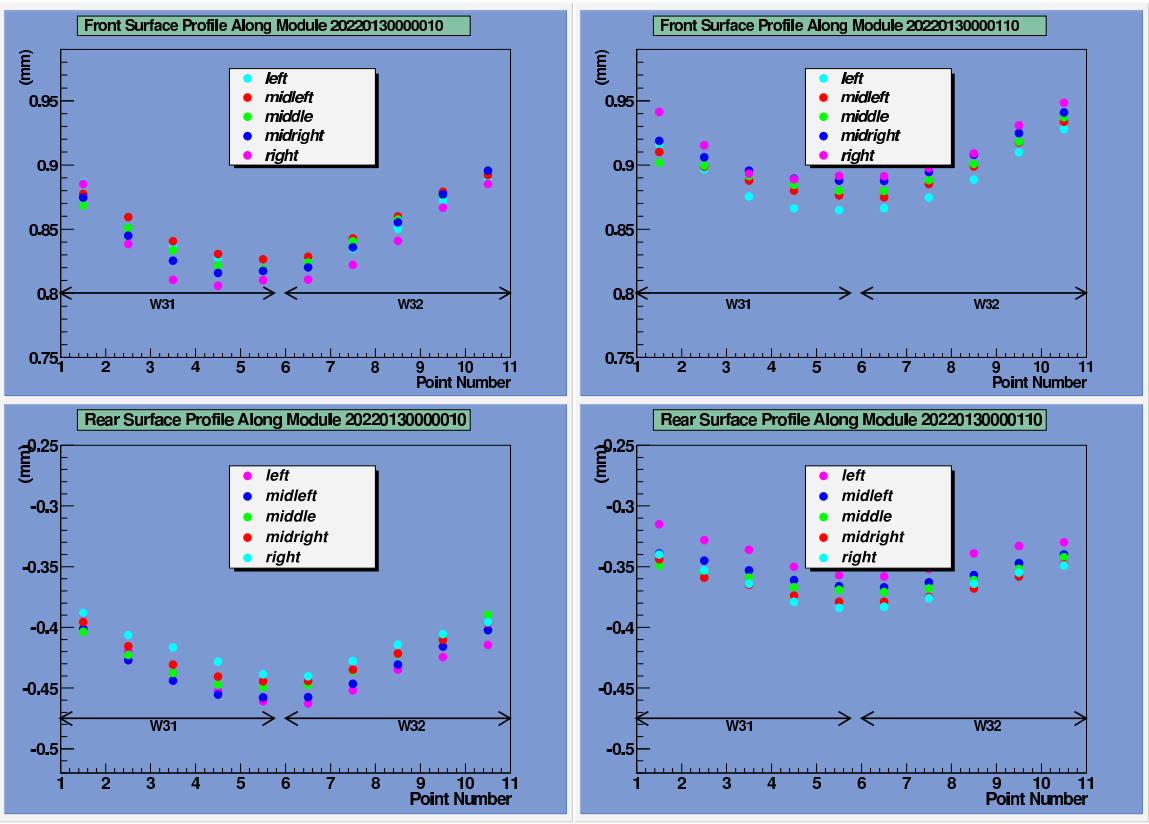

Figure 2.15 On the left (right) - 1D surface plot for the front and back (top and bottom) sides for a module that went through thermal cycle without (with) applying vacuum to constrain it to the jig in the z axis.

that it's out of mechanical specifications were never observed.

2.10 Electrical readout tests of the module

Once the thermal cycling is completed and the module passes the final survey of its profile (metrology) various electrical tests of the module are executed, that check the module electrical functionality. During production testing, a set of custom VME modules is used to read out the modules. A schematic diagram of the readout system is shown in Figure 2.17. The CLOAC MASTER module provides the system wide 40.08 MHz clock and generates fast commands such as L1A. Fast commands may be generated in response to an external trigger source or as a burst comprising a specified number of triggers at a designated frequency. However for the majority of the electrical tests performed during module production, individual triggers are generated in response to VME commands. SLOG distributes the clock and fast command signals generated by CLOAC to up to 12 detector modules. It also generates the slow command data needed to configure the detector modules. MuSTARD receives data from up to 6 detector modules, or 12 data streams, decodes the events and creates histograms. Individual events may be transferred to the host computer if more detailed analysis is required. Each SCTLV module provides low voltage power for two detector modules and reads out the NTC thermistors mounted upon the SCT modules. The companion module SCTHV provides detector bias for four detector modules at up to 500V.

The VME crate is interfaced to a PC. SCT module configuration and data acquisition is performed by the SCTDAQ software package [25]. Static libraries written in C handle the basic communication with the VME boards. Higher level functions are implemented in a small number of C++ classes, linked with the static libraries and some libraries of the ROOT framework, to form a shared library.

The test setup also includes a chiller connected to the coolant inlet of the test box. While running the electrical readout tests, the chiller temperature is set to 10° C cycling a mixture of ethanol (20%) and distilled water (80%) to keep the module from heating up to a too high temperature while applying high voltage to it. Usually the thermistors on the module indicated a module temperature between 24-32 degrees while running readout tests.

The test setup is capable of testing up to four modules at a time but usually tests of two modules only were done in parallel. The module to be tested is put inside a test box made of Aluminum (Figure 2.16). The test box has two contact points with the module, an inlet for nitrogen flow, an inlet for the cooling liquid provided by the chiller, and the patch card on which the connectors to the Kapton data cable and power cables

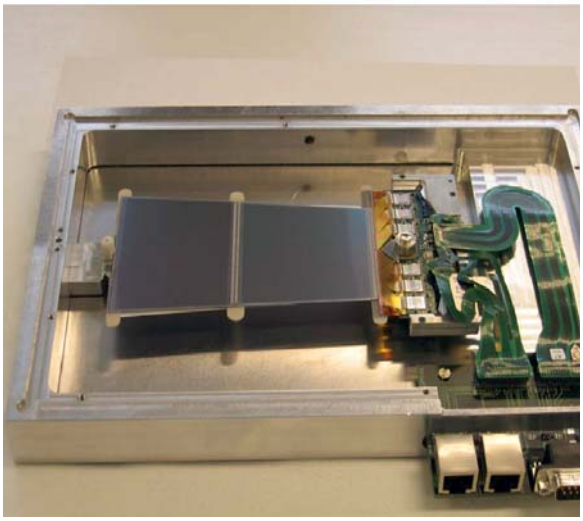

Figure 2.16 A module test box made of Aluminum, with a cooling outlet and a patch card to which the power cable and the data cable are connected.

are mounted, as well as the power cable connector.

Every module must pass the "confirmation sequence" of tests before it is packed and prepared for transport to QA at CERN, see Figure 2.18.

Each test has been designed to determine a certain set of parameters and/or to identify a number of specific defects or failure modes. The full set of measurements demonstrates the complete functionality of a module and provides measurements of all electrical parameters. Used in conjunction with the SCT database query tool, this information can be used to track points of failure and to evaluate yield statistics. As all measurements and actions performed on a detector module will be registered in the database, failures can be correlated with steps of the assembly and QA sequence.

The confirmation sequence includes the following tests:

1. **Stream Delay** (digital) - is a parameter that adjusts the relative phase between each input data stream (from a detector module) and the system clock. Its value is dominated by system considerations such as cable length; hence this test is usually performed only when setting up a readout system.

2. **Hard Reset** - The module is clocked and the power is switched on. Using an oscilloscope connected to monitor, the operator must verify that each datalink responds with CLK/2 and that, after the chips have been configured, the clock feedthrough signal stops. The analogue and digital currents are then recorded. Finally Hard Reset is issued to bring back the CLK/2 signal. This test verifies that the Clock,

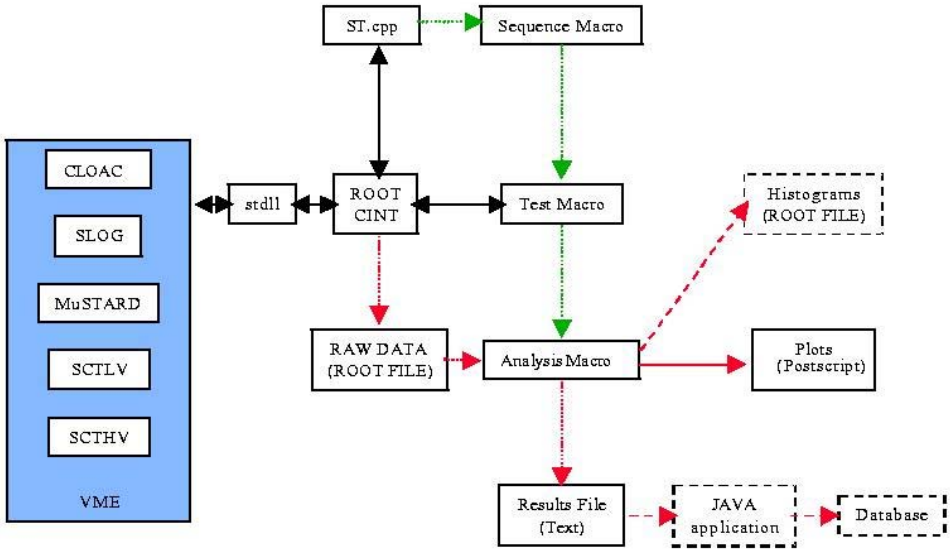

Figure 2.17 Scheme of the SCT DAQ system.

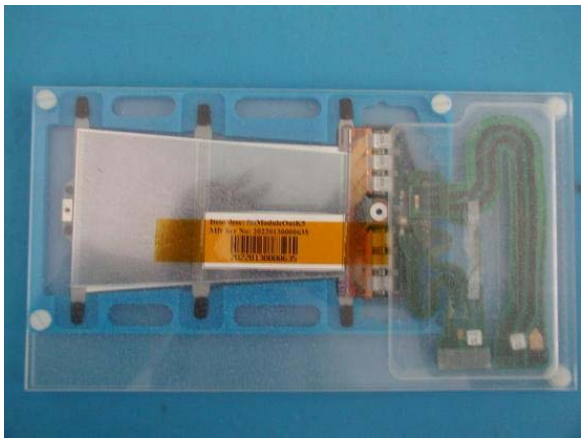

Figure 2.18 A module that passed the electrical readout tests at the University of Geneva packed in a transport box before being shipped to CERN.

Command and Hard Reset signals are received correctly, that the chips can be configured and that the current consumption is reasonable. The test will identify modules with severe failures and/or cases where devices have been connected incorrectly. Every module must pass this test without error.

3. **Redundancy test** (digital)- the chips are configured to return the contents of the Mask Register and a burst of triggers is issued for each of the Primary and Redundant Clock and Command options. Prior to each event, a different bit pattern is loaded in the Mask Register such that consecutive events are not the same. By comparing the received data with expectation it is verified that both the Primary and Redundant Clock and Command signals are received correctly and that the top address bit of each chip changes as the Clock/Command source is varied, as specified in the module design. This test will identify modules with faulty command reception or addressing errors. Modules with such defects would be considered to have failed, pending further investigation and possible rework.

4. **FullBypass test** (digital) - a trigger burst is recorded with the module programmed to each of a number of different configurations, sufficient to exercise all data/token passing links between the chips. In each case the chips are configured to return the contents of the Mask Register such that the expected data is accurately known. The test is repeated across a range of digital supply voltages to determine the minimum value of the digital supply voltage needed for the correct functionality of each of the data/token passing links. Any link that did not work at the nominal supply voltage of 4.0V, which could not be identified as being due to a missing wirebond and subsequently repaired, would cause a module defect.

5. Pipeline test (digital) - a Soft Reset command is sent to reset the pipeline followed a certain number of clock periods later by a Pulse Input Register command and L1A trigger. In this way, a known pattern is injected into a given location in the pipeline. By varying the distance between the Soft Reset and Pulse Input Register commands it can be verified that each of the eleven blocks within the pipeline is free of defects. The pipeline is scanned twice: once with all channels enabled to identify dead cells and dead channels; once with all channels disabled to identify stuck cells and stuck channels. Modules with a large number of dead or stuck cells or channels will be rejected.

6. **Strobe Delay** (analogue) - this scan is performed to determine the correct Strobe Delay setting, corresponding to the timing of the charge injection pulse, to be used during the analogue tests.

7. **Three Point Gain** - threshold scans are taken for three injected charges to facilitate a quick measurement of gain, noise and the discriminator offset. Pathological channels are categorized as FAULTY if the defect would result in the channel having a reduced but non-zero detection efficiency in ATLAS, or as LOST if the defect would result in the channel having zero efficiency: LOST: dead, stuck, unbonded or noisy channels; FAULTY: inefficient, low gain or partially bonded channels modules having any chips with abnormal gain or high noise will be rejected and put aside for potential rework, as will those with large numbers of pathological channels.
   Maximum number of defective channels should not exceed 1% per module (less than 15 channels).

8. **IV Curve** - this test records the leakage current as a function of the applied detector bias. The bias voltage is increased in discrete steps of 10 volts until the requested upper limit (500 volts) is reached. At each step of the voltage ramp the leakage current is measured.
   This measurement is usually done while flowing N_2 into the test box, in order to avoid high humidity effects.

9. **Trimming** - this procedure minimized the channel variations in the front-end response to a 1fC charge signal by applying individual corrections to the offsets in each channel, via a 4-bit DAQ.

10. **Response Curve** - this test is similar to the three point gain but employs 10 different values of injected charge in the range from 0.5 fC to 10 fC. The gain and input noise at 2 fC are then calculated by an exponential fit the response curve. Figures 2.19, 2.20 illustrate the result of a response curve test obtained from a typical module. The criteria for identification of bad channels and overall acceptance are the same as for the three point gain test.

11. **Noise Occupancy** - A threshold scan in the absence of charge injection is used to obtain the variation of ln(occupancy) as a function of the square of the threshold in fC. An alternative measurement of the noise in ENC is then obtained from the slope of this curve. Furthermore, the crucial value of the noise occupancy at 1fC threshold is obtained (giving the probability for a strip to give a hit during a bunch crossing due to noise).

12. **Time Walk** - In the final test of the module characterization the threshold is set to 1fC and a complementary error function is fitted to the falling edge of the efficiency versus the strobe delay, for injected charges in the range 1.25 to 10fC. The time

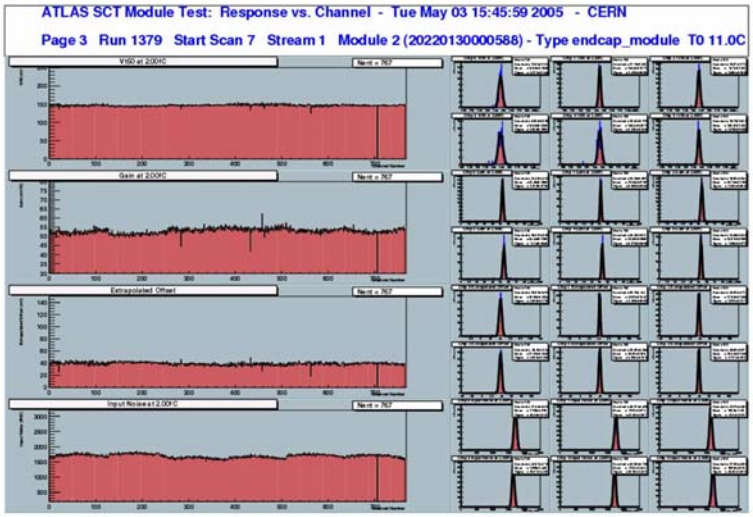

Figure 2.19 Results of the response curve for one side (corresponding to six ABCD chips pr 768 channels) of a typical module as presented by SCTDAQ. The upper plot shows the 50% point of the s-curves for all 768 channels, obtained by scanning the threshold while keeping a fixed charge injection of 2 fC. The distribution within each of the six chips are shown to the right. The third plot from the top shows the extrapolated offset of the response curves. Finally, the lower plot shows the input noise, calculated for each channel in the usual way by taking the width of the response curve (output noise) divided by the gain, at the 2 fC injected charge point.

walk is then defined as the difference between the 50% points observed for the 1.25 and 10 fC charges.

Modules that pass the tests of the confirmation sequence are then prepared to be transported to CERN for more extensive QA tests before being qualified for being mounted on the Endcap disks. The results of the confirmation tests are uploaded to the ATLAS SCT database where they are available to the whole collaboration. In addition running a perl script on the PC connected to the test setup automatically uploads a summary of the module electrical performance to the dedicated module webpage.

Photos of both sides of the completed and tested module are taken and put as well on the module webpage. In case the module had a problem or was repaired and had some rework done on it, the relevant photos are put on the module webpage next to comments and details describing the problem, repair, current status, etc.

The various activities described above are sketched below as the production flow diagram (put image).

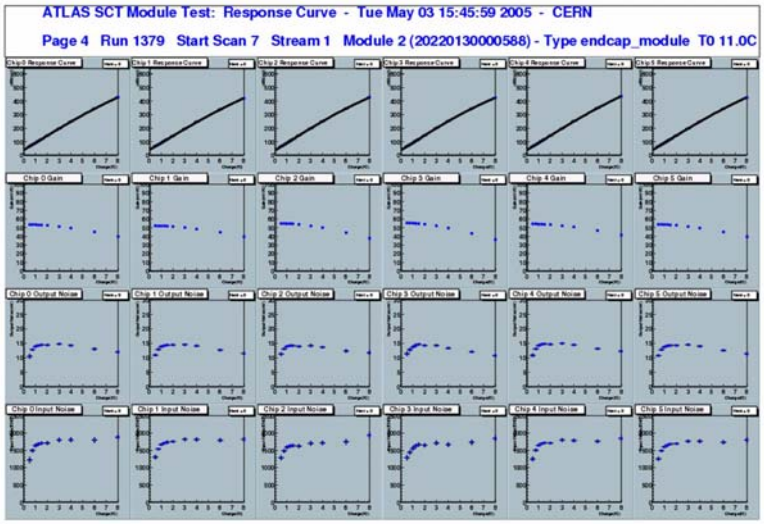

Figure 2.20 Results of the response curve test for one side (corresponding to six ABCD chips pr 768 channels) of a typical module as presented by SCTDAQ. The top row of six plots presents the chip averaged response curves: the 50 pc point of the S-curves as a function of injected charge. The gain (slope of the response curve) for each chip is shown below this. The gain is then used to convert the average output noise into an input noise value in ENC for each chip, presented in the bottom plots.

2.11 Statistics package for ATLAS SCT module production

A package providing a statistical representation of the module production status in each of the ATLAS SCT institutes was developed at the University of Geneva [26].

The representation of the module production and metrology survey is based on a query of the SCT production database. The query itself for collecting the relevant information is a Java application running on any standard CERN machine, or on computers on which the needed database software is installed. This package allows the user to define the type of modules, the manufacturer and the production period for which the data should be presented. The query produces different text files containing information about the following parameters per module:

- noise (in electrons) of each of the module chips
- the noise occupancy of each of the module chips
- the gain of each of the module chips
- module temperature readout from the thermistor mounted on the hybrid
- number of defective channels found while testing the module

- leakage currents at 150V and 350V
- metrology of module profile - z parameters and xy parameters.

In addition, the query generates for each module a list of tests for which the information was not entered to the database. This provides an easy way to identify missing tests or problems with the tests uploaded to the database.

The data that are summarized in the text files can then be processed in ROOT, using ROOT scripts that are provided as a part of the package. The ROOT application [27] visualizing the results that are summarized in the text files by providing a graphical statistical representation. It has the advantage of making the identification of measurements that are out of the specified limits easier. For each parameter that has a well defined specification the accepted specified ranges are marked on the plots, so that every entry which is an underflow or an overflow is immediately identified and the fraction of entries which are not within specifications is well noticed. This tool has been used by all the ATLAS SCT institutes, and in addition it offers the option to get a summary of the production in all the SCT institutes which produce the same type of modules. The package had been updated from time to time according to users suggestions and requests.

The following plots show the summary of the Geneva production results for some measured characteristic module values:

2.12 Module Classification

After assembly the modules are classified as:

- **Good**: if all specifications are met
- **Pass**: if the metrology measurements are within 50% tolerance and a smooth IV-curve, that does not exceed the current limit of 8 μA is obtained up to a minimum breakdown voltage of 350V (150V for CiS sensors).
- **Hold**: if electrical specifications are not met but at least a smooth IV curve is obtained up to 150V (Hamamatsu) and all chips are responding. The module is also assigned to this category if the metrology measurement identifies outliers with respect to the nominal envelope.
- **Fail**: if the module does not match any of the above categories and is not reworkable.

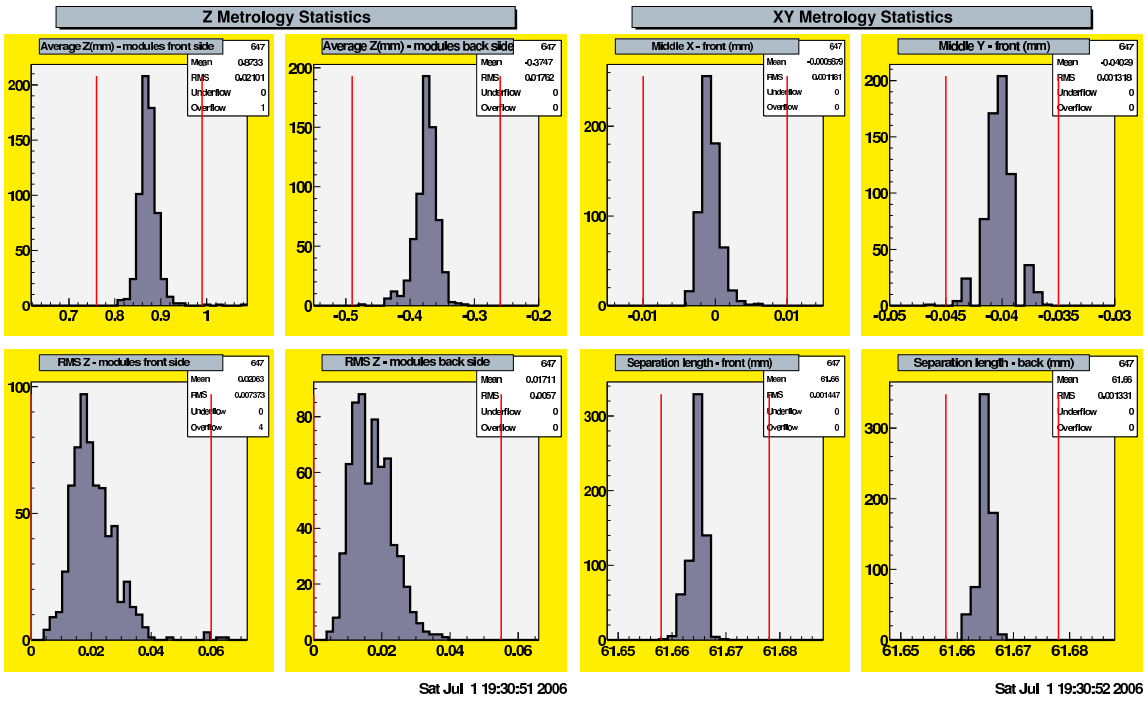

Figure 2.21 Summary of module metrology. The left figure shows the average z position and RMS for the front and back sides of the module: red lined indicate the specified tolerances. The figure on the right-hand side shows the mid-x and mid-y values with the specified limits and the distance between the mid-point and the hole position in (x, y) (See Figure 2.10)

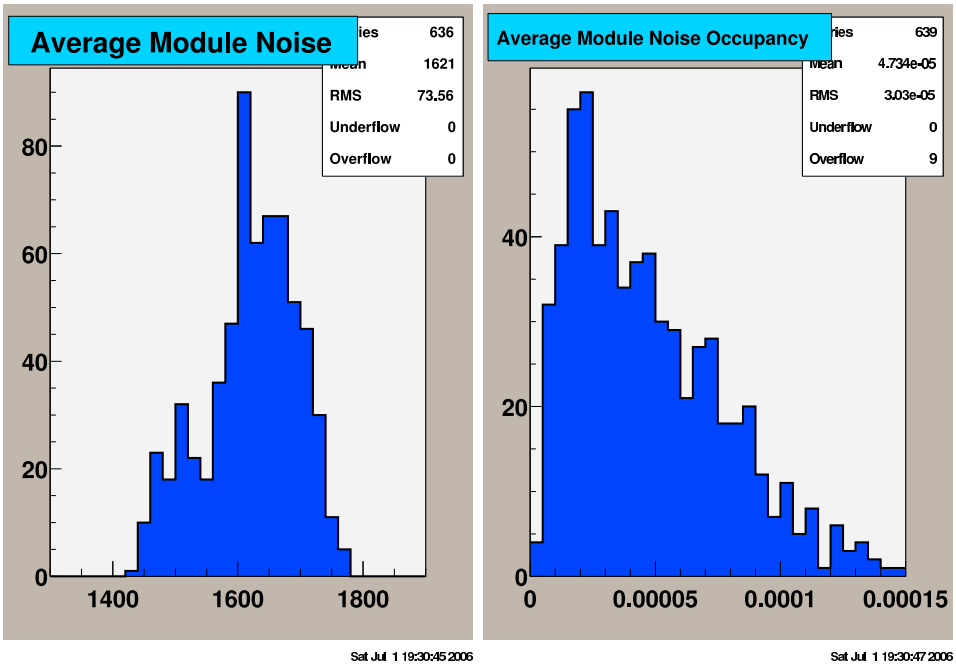

Figure 2.22 Summary of module electrical tests. The left figure shows average noise for each module, measured in ENC, while the left figure shows average noise occupancy of the modules.

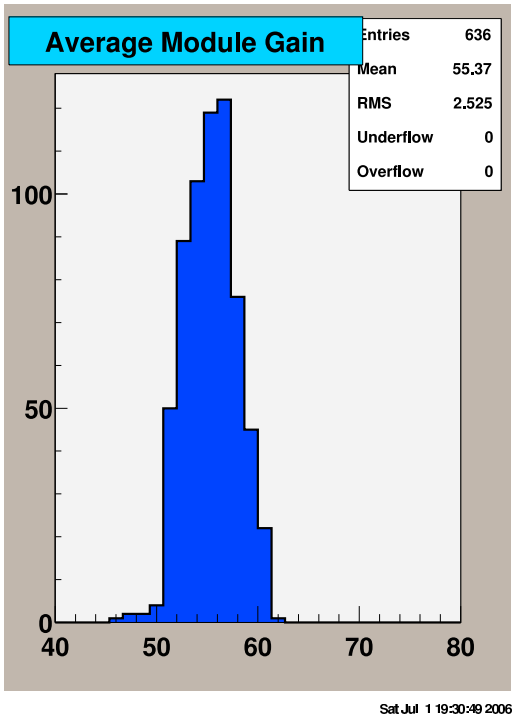

Figure 2.23 Average gain of the modules measured during electrical readout tests

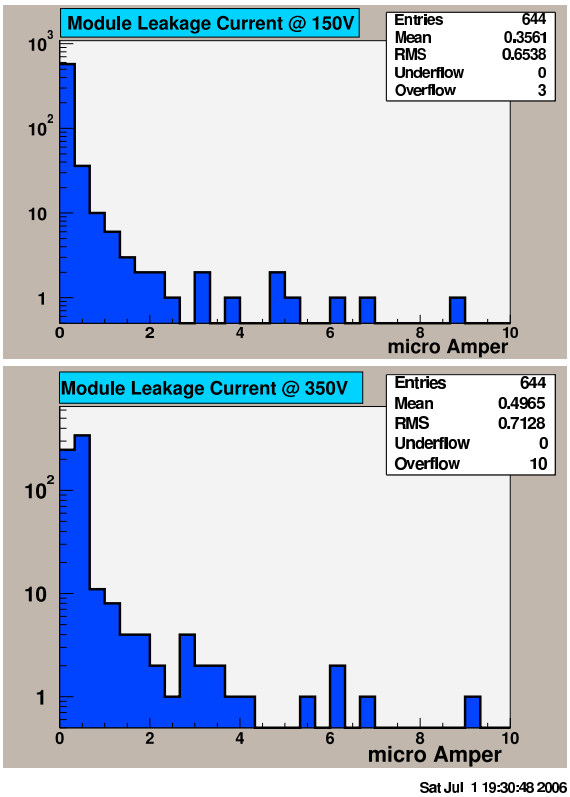

Figure 2.24 Average leakage current of the modules measured during electrical readout tests

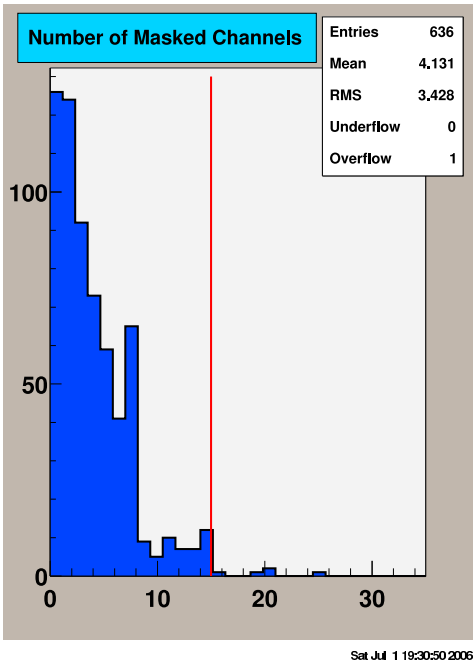

Figure 2.25 Summary of the module production: the number of masked channels for each module. Specifications accept modules with less than 1% (15) defective channels.

2.12.1 Summary of Production Failures

Although the module production at the University of Geneva was very efficient and had an excellent yield of good modules, a small fraction of the modules failed or have some defects. The problematic modules and the source for their defects are summarized below[1]:

'Hold' modules:

- Module 177 - Bonding problem on the top left fan-in. When the wire is pulled out from the source bond (on the fan-in bonding pad) to the destination bond (detector bond pad) the Al-pad delaminates. Only the inner raw is bonded and six pads cannot be reworked.

- Modules 228, 231, 233, 241, 244, 246, 248 - All of these seven modules exceed the top z profile specifications by values between 60 to 475 microns. The reason is that a longer pin which was designed to be used with the third assembly set only was used randomly with all the assembly sets. A combination of this pin and the transfer plates of the first or the second assembly set gave z profile results far outside the specified z limits.

[1]Modules produced in Geneva have serial numbers between 200220130000000 - 20220130000655, starting from module 0 consecutively to module 655.. The module numbers reported here refer to the last three digits of the module serial number.

- Module 488 - This module failed the FullByPass test. QA at CERN gave the same results, the reason is not completely understood.

Failed modules:

- Module 23 - 16 consecutive strips of the fan-ins were found opened. It is not clear when this scratch appeared but the suspicion is that it came damaged from the producer. Quite a few damaged fan-ins were identified before they were assembled.

- Module 79- metrology of ZmaxF parameter is greater by 200 microns than the specifications allow. This is caused by an operator mistake - during assembly phase 1 the shims that should restrict the z profile on the far-end side during the gluing procedure were forgotten.

- Module 106 - One of the chips (S2) of this module failed the readout tests - can not read noise during the noise occupancy test. This was already the case for this chip when tested for hybrid QA at the Cracow hybrid QA site before it was sent to Geneva. However during hybrid QA the problem was not noticed and therefore the hybrid was accepted for assembly in Geneva where the failure was identified.

- Module 134 - Left fan-in on the bottom side is broken. The crack continues all the way through the strip region. This happened during the operation of refilling some glue underneath the top fan-in. The glue needle hit the edge of the bottom fan-in and cracked it. About 20 consecutive channels are opened due to this crack.

- Module 285 - Failed readout tests. 20 consecutive defective channels were found. 8 unbonded channels and 4 partly bonded channels were identified in the tests although visual inspection of the bonds seem fine. Some unbonded channels were repaired but the readout tests still gave the same results.

- Module 359 - After assembly phase 2 a big scratch on the bottom right fan-ins was noticed, near the cooling block. This scratch was probably there before assembly. The readout tests of this modules identify 42 defective channels due to this scratch.

Aborted at phase 1:

- Module 29 - One of the detectors on the bottom side had a too high current. This detector was already problematic when tested individually. From this incident we learned not to qualify problematic detectors to be assembled to a module and by that risk the loss of the module.

- Module 122 - One of the bottom side detectors is broken. This was detected during IV scan after assembly phase 1. The crack could have happen during the alignment of the module, as for this module the alignment was a little problematic. Another explanation could be dust or debris on the detector backplane. From the assembly of that detector on, an inspection of the backplane of the modules before sucking down the detectors on the miniature stages for the detector alignment was required.

- Module 131 - One detector has a too high current (8 microns at 500V). The reason is unknown, no visible damage was found.

- Module 420 - One of the top side detectors was scratched during the IV scans while removing the cover of the probe station. The vacuum pipe moved and scratched the grounding ring of the detector. The readout current after that was high but still within the limits, however we decided to abort the production of the module.

- Module 544 - One of the top side detectors is broken.

- Module 598 - High current in one of the bottom side detectors. No visible damage is identified. The detector draws a current of up to 10 mA at 350V with a tendency to drift to a higher current.

'Pass' modules:

- Module 10 - some glue needed to be added under the bottom fan-in of this module. during this operation, while the module was sucked on the bonding jig, a trapped glass debris that was on the teflon surface of the bonding jig damaged one of the detectors. The leakage current of this detector deteriorated after the hybrid assembly and was higher than the module leakage current limits (3 mA at 150V). Learning from this incident, some cleaning actions of the jigs and assembly tools and further precautions were added to the assembly operation.

- Module 18: The z profile exceeds specifications by 9 microns from the bottom side.

- Module 36: z profile parameter 'ZminF' outside the limits by 28 microns.

- Module 123: The z profile exceeds specifications by 6 microns from the top side.

- Module 571: 'msy' metrology parameter out of specs by 3 microns.

- Module 602: 16 bad channels, exceeds the limit of 15 bad ones (1%).

- Module 467: outside z profile specifications.

- Module 485: outside z profile specifications.
- Module 371: outside specifications for the z profile.
- Module 313: outside z profile specifications, msy exceeds limits by 2 microns.
- Module 277: 'mhy' metrology parameter outside the specified limits.

2.13 Module Production - Conclusion and Summary

There are three main criteria that are essential for modules produced in each assembly site:
good survey metrology results, good detector and module current behavior and, finally, a satisfactory module readout with a low number of defective channels.

The Geneva assembly system proved its ability to deliver the necessary yield of good modules within the time expected by the ATLAS SCT collaboration. Many efforts were put into improving the production procedure, infrastructure, equipment, manpower and tools as more experience was gained and new problems were encountered.

Overall, the module production for the ATLAS SCT in the different institutes have produced more than 2380 SCT Endcap modules with a yield of 93% (See Table 2.3). 'Good' and 'pass' modules could be used anywhere on an Endcap disk. There was no selection for more or less demanding locations. The flow of components and the tight schedule have been the main difficulties to overcome in order to keep continuous production while always preserving quality. Although the delivery of the module components has not been constant, the production was never stopped for that reason, mainly because of the close cooperation of all groups participating in the project.

Classification	Inner	Middle (Short + Long)	Outer	All
Module assembled	495	772	1113	2380
Good	394	665	995	2054
Pass	39	60	61	160
Hold/rework	46	42	23	111
Fail	16	5	34	55
Good+Pass	433	725	1056	2214
Good+Pass required to equip Endcaps	400	640	936	1976

Table 2.3 Statistics of the SCT Endcap module production.

With an excellent yield of 97%, 655 outer Endcap modules were produced at the University of Geneva, out of which 634 were qualified to be assembled onto the ATLAS

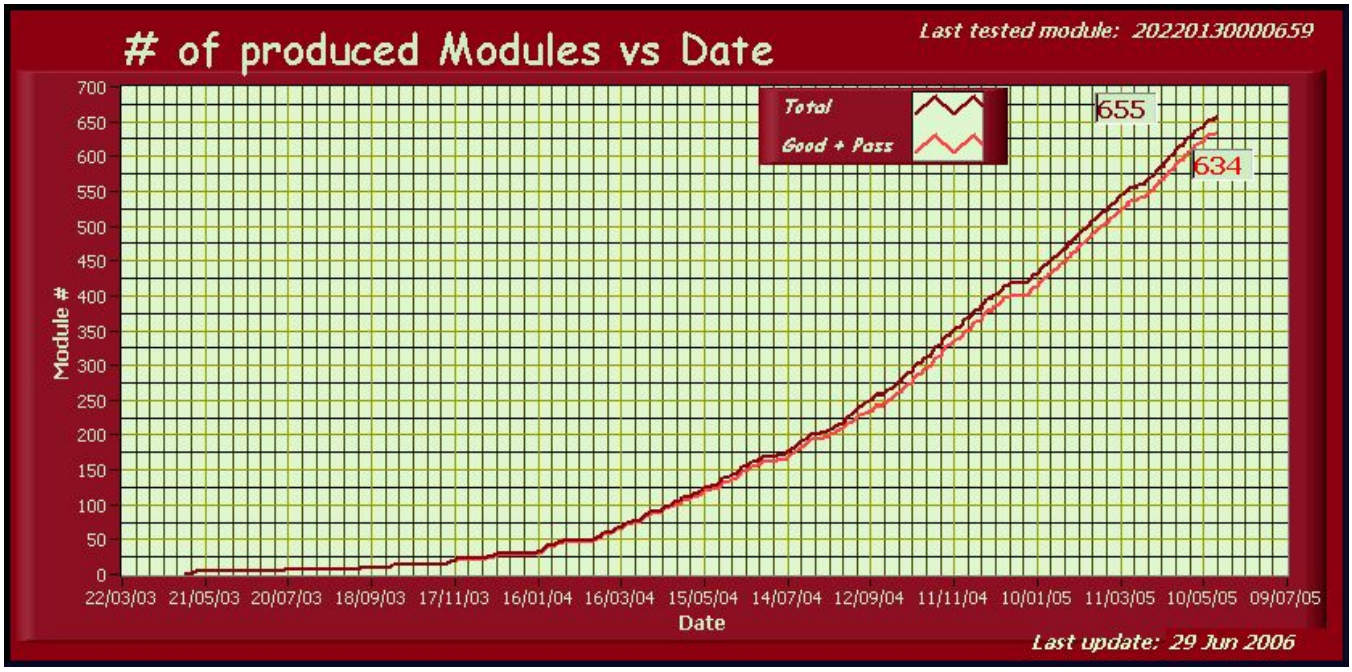

Figure 2.26 Number of produced modules versus date during the production period (May 2003 - June 2005) at the University of Geneva.

Total	Aborted at phase 1	# of complete modules	Good	Pass	Good + Pass	Failed
655	6	649	622	12	634	15
	0.9 %	100.0 %	95.8 %	1.8 %	97.7 %	1.4 %

Figure 2.27 A summary of the total module production divided into the different module acceptance categories.

SCT Endcap disks and be used as part of the ATLAS tracking system. The production overview given in thesis, the production summary shown in Figures 2.26, 2.27 together with the statistical presentation of the mechanical and electrical performance of the modules clearly demonstrates that the University of Geneva has done its best to reach a high quality module production, reliably satisfying the requirements for modules operating in the LHC environment.

Chapter 3

W helicity in Top Quark Decays

3.1 Top Production

In $p\bar{p}$ collisions the energies of the p and $\bar{p}$ are divided among partons, and the energy available in a partonic collision to create top quarks is only a fraction of the center-of-mass energy of the $p\bar{p}$ system.

There are two ways to produce pairs of top quarks: either via $q\bar{q}$ annihilation or gluon fusion. Figure 3.1 shows the leading order diagrams for $t\bar{t}$ production. At the Tevatron, the main contribution to the $t\bar{t}$ yield is from $q\bar{q}$ annihilation. This is purely the result of the fact that the *parton distribution functions* (PDFs) favor this channel at $\sqrt{s} = 1.96$ TeV. In fact, about 90% of the top quarks are produced through the quark interaction. This rate changes with the energy of the collision, developing more gluon fusion with higher energy. Single top quarks can also be produced at the Tevatron through an electroweak process, which has yet to be confirmed (the single top final state is very difficult to distinguish from background). The $t\bar{t}$ cross section can be calculated using pertubative methods, and the result depends on the mass of the top quark. A measurement of both parameters can check the validity of QCD calculations. The current measured values of the top mass and cross section are:
$M_t = 171.4 \pm 2.1$ GeV; (CDF+D0 July 2006 combination)
$\sigma_{t\bar{t}}(M_t = 175\ GeV) = 7.3 \pm 0.5\ (stat) \pm 0.6\ (syst) \pm 0.4\ (lumi)$ pb; (CDF, winter 2006)

At the Tevatron, with $\sqrt{s} = 1.96$ TeV, only about 1 event in a 10^{10} produces a pair of top quarks!

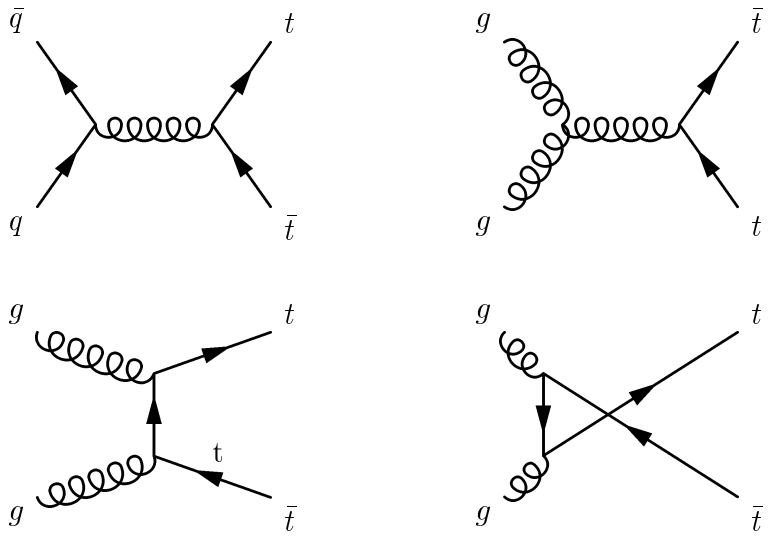

Figure 3.1 Leading order Feynman diagrams for $t\bar{t}$ production via the strong interaction: upper left - $q\bar{q} \to t\bar{t}$ s-channel, upper right - $gg \to t\bar{t}$ s-channel, lower left - $gg \to t\bar{t}$ t-channel, lower right - $gg \to t\bar{t}$ u-channel.

3.2 Top Quark Decay

The top quark decays via the weak interaction, which does not conserve flavor. Although is has not been measured directly, the coupling of W to tb can be inferred to be close to unity ($V_{tb} \simeq 0.999$) [28]. Therefore, the produced top (anti-top) quarks decay rapidly into W^+b ($W^-\bar{b}$). This is followed by the W^+ (W^-) decay into "hadronic" $u\bar{d}$, $c\bar{s}$ ($\bar{u}d$, $\bar{c}s$) or leptonic $l^+\nu$ ($l^-\bar{\nu}$) channels. The final states of the $t\bar{t}$ system have different topological classifications that depend on the decay of the W. There are three channels:

- **Dilepton** - both W bosons decay leptonically. Since τ leptons are difficult to identify this channel refers only to the ee, $e\mu$, and $\mu\mu$ combinations. This channel has the smallest branching ratio (4/81), as well as the smallest background rate. Although there are two neutrinos in the final state, given the six kinematic constraints (two M_t, two M_W, and conservation of transverse momentum), it is possible to fully reconstruct the three momenta of the two neutrinos and the entire $t\bar{t}$ system.

- **Lepton+jets** - one W decays leptonically, while the other W decays hadronically. The initial system is overconstrained, and can be fully reconstructed with only one neutrino in the final state. This channel has a branching fraction of 8/27 (without taking τs into account), but the amount of background is substantially larger than in the dilepton channel. **Our analysis relies on this channel**.

- **Fully hadronic** - both W bosons decay hadronically in this channel. The branching fraction is the largest (36/81). The major problem is that the amount of background

from multijet production makes it very challenging to analyze.

Table 3.1 lists all the tree-level $t\bar{t}$ final states and their respective branching ratios.

	$W \to e\nu_e$ 1/9	$W \to \mu\nu_\mu$ 1/9	$W \to \tau\nu_\tau$ 1/9	$W \to q\bar{q}$ 2/3
$W \to e\nu_e$ 1/9	1/81	1/81	1/81	2/27
$W \to \mu\nu_\mu$ 1/9	1/81	1/81	1/81	2/27
$W \to \tau\nu_\tau$ 1/9	1/81	1/81	1/81	2/27
$W \to q\bar{q}$ 2/3	2/27	2/27	2/27	4/9

Table 3.1 $t\bar{t}$ decay branching ratios for different channels. The factor of 2/3 for $q\bar{q}$ reflects the two hadronic channels and the three colors for all quarks: $2 \times 3 \times 1/9 = 2/3$

3.3 Helicity of W bosons

Among the known fundamental particles the top quark stands out as the heaviest, with its mass being of order of the electroweak symmetry breaking (EWSB) scale. Fundamental particles have spin and this internal degree of freedom plays an important role in their interactions. The knowledge of these interactions is required in order to discriminate mechanisms of EWSB. The tree-level $t \to Wb$ decay width of the top quark, with the general tWb vertex can be obtained by the helicity amplitudes of the W boson in the final state of the top decay: there are three modes in the $t \to Wb$ decay, depending on the polarization state of the W boson. Each mode is associated with a fraction, F_0, F_R (F_+) or F_L (F_-), that corresponds to the longitudinal, right-handed or left-handed polarization, respectively. The fractions are constrained to satisfy $F_0 + F_R + F_L = 1$. The SM makes definite predictions for the three W helicity fractions.

Currently, the only missing ingredient of the SM is the Higgs boson. This is the agent that causes the breaking of the electroweak symmetry, and LEPII searches have concluded that its mass must be greater that 114.4 GeV if such a particle exists [29]. This still leaves the SM with many important questions unanswered - what is the real origin of the fermion masses? what is the explanation for a significant cancellation of higher order corrections to the Higgs mass?

As a result, other theories of EWSB are given attention in particle physics. Theories like the Minimal Supersymmetric Standard Model ($MSSM$), the Technicolor models, and theories with new top quark interactions suggest some of the answers, but so far no indication of their validity has been found. Within the SM, the top quark decays via the weak interaction and therefore, like all fermions, has a V-A coupling which allows

the W boson to couple to left-handed fermions only. The V-A nature of interaction, together with conservation of angular momentum, result in the fact that production of right-handed W bosons in the final state of the top decay is highly suppressed. The right-handed W fraction becomes zero when neglecting the mass of the b quark. Observing a non-zero fraction of right-handed W bosons (beyond the very small prediction of the SM) would indicate a non-zero anomalous V+A coupling which would suggest non-SM physics. However, studies of the electroweak model in nuclear beta decay [30] and the measurements of rare decay processes such as $b \to s\gamma$ by the CLEO collaboration [31], [32], as well as precision data of LEP and SLC, already test the elctroweak V-A nature and put tight bounds on the V+A current. For instance, the measurement of $b \to s\gamma$ alone, though it measures indirectly the V-A current, sets a constraint of less than 0.5% for the possible strength of right-handed tWb coupling - this level of precision cannot be tested even at the LHC.

Measuring the W helicity fractions in top decays provides a direct search for a V+A current, and, with larger data samples than those available today, can be used as a test of various beyond the SM physics models.

3.4 W Helicity Fractions in the SM

The angular distribution ω of the W boson decay products with weak isospin $I_3 = -1/2$ (charged lepton, down quark, or strange quark) in the rest frame of the W boson can be described by introducing the angle θ^* with respect to the W flight direction in the top quark rest frame. The angular distribution has the general form [33]

$$\omega(\theta^*) = f_0 \cdot \omega_0(\theta^*) + f_- \cdot \omega_-(\theta^*) + f_+ \cdot \omega_+(\theta^*), \tag{3.1}$$

with

$$\omega_0(\theta^*) = \frac{3}{4}(1 - \cos^2\theta^*), \tag{3.2}$$

$$\omega_-(\theta^*) = \frac{3}{8}(1 - \cos\theta^*)^2, \tag{3.3}$$

$$\omega_+(\theta^*) = \frac{3}{8}(1 + \cos\theta^*)^2. \tag{3.4}$$

Figure 3.2 illustrates the definition of θ^* and Figure 3.3 shows angular distributions for longitudinal, right-handed and left-handed W boson decays as well as the distribution expected in the Standard Model.

The SM top decays almost exclusively to a W boson and a b quark. Because of the way the weak interaction maximally violates parity, the coupling of the top quark to a

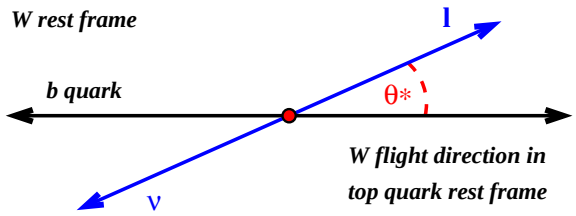

Figure 3.2 The decay angle θ^* in top decays is defined as the angle between the down-type particle from the W decay and the W boson flight direction in the top quark rest frame.

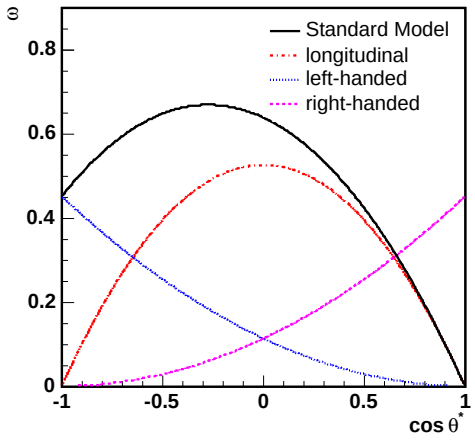

Figure 3.3 The plot shows the angular distribution $\omega(\theta^*)$ for longitudinal, right- and left-handed W boson decays as well as the distribution expected in the Standard Model [33].

left-handed W is different from that to a right-handed W: whereas t ($\bar{t}$) has a non-zero coupling to a left-handed (right-handed) W, its coupling to a right-handed (left-handed) W is almost zero (the suppression factor is of the order of $\frac{m_b^2}{M_W^2} \sim 0.5\%$). The coupling strength to a longitudinal W is proportional to m_t^3, ($\frac{1}{2}\frac{m_t^2}{M_W^2}$ times that to a left-handed W). This indicates an enhancement of the production of W bosons with longitudinal polarizations in the SM. This behaviour is representative of the models usually considered in particle physics. In these models, the longitudinal mode of the W boson, as generated through spontaneous symmetry breaking, has a coupling which increases with the fermion mass[1].

The quantitative expression for the branching fraction of the top to W's of various helicity states and a b quark is as follows:

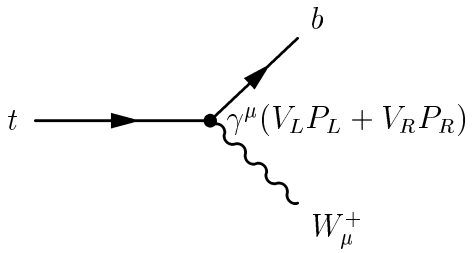

Figure 3.4 The tWb vertex includes both left (SM) and right (beyond the SM) components in the coupling.

$$\mathcal{M} = [\bar{u}_b \gamma^\mu (V_L P_L + V_R P_R) u_t] \epsilon_{W_\mu} \tag{3.5}$$

$$|\bar{\mathcal{M}}|^2 = \frac{1}{2}\frac{1}{3}\, Tr[(\not{p}_b + m_b)\gamma^\mu (V_L P_L + V_R P_R)(\not{p}_t + m_t)(V_L P_L + V_R P_R)\gamma^\nu] \epsilon_\mu^W \epsilon_\nu^{W^*} \tag{3.6}$$

V_L is the coupling constant for V-A interaction, V_R is the coupling constant for V+A interaction and $P_R = \frac{1}{2}(1+\gamma_5)$, $P_L = \frac{1}{2}(1-\gamma_5)$.

Summing over the b spin and averaging over the top spin and color:

$$\begin{aligned} |\bar{\mathcal{M}}|^2 = {} & \tfrac{1}{2}\tfrac{1}{3}\epsilon_\mu^W \epsilon_\nu^{W^*} \cdot 2[(p_b^\nu p_t^\mu + p_b^\mu p_t^\nu - (p_b \cdot p_t) g^{\mu\nu} - i\epsilon^{\alpha\beta\mu\nu} p_{b\alpha} p_{t\beta}) V_R^2 \\ & + (p_b^\nu p_t^\mu + p_b^\mu p_t^\nu - (p_b \cdot p_t) g^{\mu\nu} + i\epsilon^{\alpha\beta\mu\nu} p_{b\alpha} p_{t\beta}) V_L^2 + (2 m_b m_t g^{\mu\nu}) V_L V_R] \end{aligned} \tag{3.7}$$

Expressing the 4-vector in the top rest frame:

[1]It is not difficult to find the origin of that enhancement, by using the Goldstone boson equivalence theorem . In the gauge theory of weak interactions, the top quark obtains its mass from its coupling to the Higgs sector. The top quark can be heavy only if this coupling Λ_t is large. But then the amplitude for the top quark to decay to a Goldstone boson will be enhanced by the factor $\frac{\Lambda_t^2}{g^2} = \frac{m_t^2}{2M_W^2}$.

$$\begin{aligned} p_t^\mu &= (m_t, 0, 0, 0) \\ p_W^\mu &= (E_W, 0, 0, p_W) \\ p_b^\mu &= (E_b, 0, 0, -p_b) \end{aligned} \tag{3.8}$$

$$\begin{aligned} p_W &\equiv \sqrt{E_W^2 - M_W^2} \\ p_b &\equiv \sqrt{E_b^2 - M_W^2} \simeq E_b \\ E_W &= \tfrac{1}{2m_t}(m_t^2 - m_b^2 + M_W^2) \\ E_b &= \tfrac{1}{2m_t}(m_t^2 - M_W^2 + m_b^2) \end{aligned} \tag{3.9}$$

The polarization vectors of the W boson are then:

$$\begin{aligned} \epsilon_W^- &= (0, \tfrac{1}{\sqrt{2}}, -\tfrac{i}{\sqrt{2}}, 0) \\ \epsilon_W^+ &= (0, -\tfrac{1}{\sqrt{2}}, -\tfrac{i}{\sqrt{2}}, 0) \\ \epsilon_W^0 &= (\tfrac{p_W}{M_W}, 0, 0, \tfrac{E_W}{M_W}) \end{aligned} \tag{3.10}$$

Because of gauge invariance $p_W^\mu \epsilon_\mu^W$ is zero. If one uses $p_b^\mu = p_t^\mu - p_W^\mu$:

$$\begin{aligned} |\bar{\mathcal{M}}|^2 &= \tfrac{1}{3}\epsilon_\mu^W \epsilon_\nu^{W^*}[(2p_t^\mu p_t^\nu - (p_b \cdot p_t)g^{\mu\nu} - i\epsilon^{\alpha\beta\mu\nu}p_{b\alpha}p_{t\beta})V_R^2 \\ &+(2p_t^\mu p_t^\nu - (p_b \cdot p_t)g^{\mu\nu} + i\epsilon^{\alpha\beta\mu\nu}p_{b\alpha}p_{t\beta})V_L^2 + (2m_b m_t g^{\mu\nu})V_L V_R] \end{aligned} \tag{3.11}$$

In this case all polarization vectors are orthogonal and therefore there is no interference:

For the right-handed Ws -

$$\begin{aligned} |\bar{\mathcal{M}}|^2{}_+ &= \tfrac{1}{3}[(0 - (m_t E_b)(-1) - 1\epsilon^{3012}(-p_b(m_t)(\tfrac{-1}{\sqrt{2}} \times \tfrac{i}{\sqrt{2}} - \tfrac{-1}{\sqrt{2}} \times \tfrac{-i}{\sqrt{2}})))V_R^2 \\ &+(0 + m_t E_b + i(+1)(-p_b m_t i(-\tfrac{1}{2} - (+\tfrac{1}{\sqrt{2}}))))V_L^2 + 2m_b m_t(-1)V_L V_R] \\ &= \tfrac{1}{3}[m_t(E_b + p_b)V_R^2 + m_t(E_b - p_b)V_L^2 - 2m_t m_b V_L V_R] \end{aligned} \tag{3.12}$$

So - in the SM $V_R = 0$, $p_b \to E_b$ in the limit of $m_b \to 0$ and the amplitude above is zero! No right-handed Ws.

For the left-handed Ws -

$$\begin{aligned} \epsilon_W^- &= (0, \tfrac{1}{\sqrt{2}}, -\tfrac{i}{\sqrt{2}}, 0) = -\epsilon_W^{+\,*} \\ |\bar{\mathcal{M}}|^2{}_- &= \tfrac{1}{3}[m_t(E_b - p_b)V_R^2 + m_t(E_b + p_b)V_L^2 - 2m_t m_b V_L V_R] \end{aligned} \tag{3.13}$$

For the longitudinal Ws -

$$|\bar{\mathcal{M}}|^2{}_0 = \tfrac{1}{3}[(2m_t^2 \tfrac{p_W^2}{M_W^2} + m_t E_b)V_R^2 + (2m_t^2 \tfrac{p_W^2}{M_W^2} + m_t E_b)V_L^2 - 2m_t m_b V_L V_R] \tag{3.14}$$

Since all three polarizations have the same phase space factor:

$$BR^{helicity} = \frac{|\bar{\mathcal{M}}|^2_{helicity}}{|\bar{\mathcal{M}}|^2_0 + |\bar{\mathcal{M}}|^2_- + |\bar{\mathcal{M}}|^2_+} \tag{3.15}$$

$$BR(t \to W_- b) = \frac{1 + \frac{|\vec{b}|}{E_b}}{1 + 2\Big(\frac{E_W}{M_W}\Big)^2\Big(1 + \frac{|\vec{b}|^2}{E_b E_W}\Big)} \tag{3.16}$$

$$BR(t \to W_+ b) = \frac{1 - \frac{|\vec{b}|}{E_b}}{1 + 2\Big(\frac{E_W}{M_W}\Big)^2\Big(1 + \frac{|\vec{b}|^2}{E_b E_W}\Big)} \tag{3.17}$$

$$BR(t \to W_0 b) = \frac{1 + 2(\frac{m_t}{M_W})^2\frac{|\vec{b}|^2}{m_t E_b}}{1 + 2\Big(\frac{E_W}{M_W}\Big)^2\Big(1 + \frac{|\vec{b}|^2}{E_b E_W}\Big)} \tag{3.18}$$

In these formulae, $\vec{b}$ is the b quark momentum vector, and E_b and E_W are the b and W energies, all in the top quark rest-frame. In the top quark rest frame the quantities below are fixed, and can be expressed in terms of the t,W and b masses:

$$E_W = \frac{m_t^2 + M_W^2 - m_b^2}{2m_t} \tag{3.19}$$

$$E_b = \frac{m_t^2 + m_b^2 - M_W^2}{2m_t} \tag{3.20}$$

$$|\vec{b}| = \sqrt{E_b^2 - m_b^2} \tag{3.21}$$

The same expressions hold for $\bar{t} \to W^- \bar{b}$ when swapping left and right.
Taking $m_t = 175$ GeV, $M_W = 80.4$ GeV and $m_b = 4.7$ GeV, the branching fractions in the SM are:

$$BR(t \to W_-^+ b) = 0.297 \tag{3.22}$$

$$BR(t \to W_+^+ b) = 0.00043 \tag{3.23}$$

$$BR(t \to W_0^+ b) = 0.703 \tag{3.24}$$

Within the SM: $V_L = 1$, $V_R = 0$, and in the limit $m_b \to 0$:

$$\begin{aligned} &|\bar{\mathcal{M}}|^2_+ \to 0 \\ &|\bar{\mathcal{M}}|^2_- \to \tfrac{2}{3} m_t E_b \\ &|\bar{\mathcal{M}}|^2_0 \to \tfrac{1}{3}(m_t E_b + \tfrac{2m_t^2 p_W^2}{M_W^2}) \end{aligned} \tag{3.25}$$

The fraction of longitudinally polarized Ws is therefore:

$$F_0 = \frac{m_t E_b + 2m_t^2 \frac{p_W^2}{M_W^2}}{3m_t E_b + 2m_t^2 \frac{p_W^2}{M_W^2}} = \frac{m_t^2}{m_t^2 + 2M_W^2} \simeq 70\% \tag{3.26}$$

From Eq. 3.26 and assuming SM physics - the possibility of using the measured fractions of longitudinal Ws in order to measure the mass of the top quark looks like something which might deserve a further study. The current uncertainties on F_0, when translated into uncertainties on the top mass, give a large (> 10 GeV) uncertainty for the mass measurement. However, F_0 might be used in order to further constrain the top mass.

3.5 Possible modifications of the W helicity fractions - beyond the SM scenarios

New interactions at higher energies may manifest themselves in the form of effective couplings of the SM fermions. In new physics models, departures from the SM expectations are possible [34, 35], as well as new radiative contributions to the tWb vertex (loop effects) [36, 37]. To describe all possible effects from any physics beyond the SM we look at the most general Lagrangian consistent with the SM gauge symmetry ($SU(2)_L \times U(1)_Y$) and that contains all possible effects coming from the physics at higher energy scale [38]. The most general tWb vertex containing terms up to dimension five can be written with this effective Lagrangian[2]:

$$\mathcal{L} = \frac{-g}{\sqrt{2}} \bar{b} \gamma^\mu (V_L P_L + V_R P_R) t W_\mu^- - \frac{g}{\sqrt{2}} \bar{b} \frac{i\sigma^{\mu\nu} q_\nu}{M_W} (g_L P_L + g_R P_R) t W_\mu^- + h.c. \tag{3.27}$$

where $q = p_t - p_b$, $P_R = \frac{1}{2}(1 + \gamma_5)$, $P_L = \frac{1}{2}(1 - \gamma_5)$, $i\sigma^{\mu\nu} = \frac{1}{2}[\gamma^\mu, \gamma^\mu]$.

The four couplings need to be constrained using precision data. These parameters are not expected to be large, their absolute value would be at most of order one.

At the tree level in the SM, V_R, g_L, g_R vanish, while a non-zero $g_R = -0.0077$ is generated at one loop level [39]. Additional contributions to V_R, g_L, g_R are possible in the

[2]The most general tWb vertex (up to dimension five) involves ten couplings, but at the level of precision we anticipate, either at the Tevatron or at the LHC, it is an excellent approximation to consider the top on-shell. With b also on-shell and $W \to l\nu, jj$, six couplings can be eliminated. The additional couplings would also vanish in the case where the off-shell W boson couples to massless on-shell fermions [33]. The resulting Lagrangian can be further restricted assuming CP conservation. The couplings can then be taken to be real, of either sign.

SM extensions, without spoiling the agreement with low-energy measurements. The size of a V_R term is constrained by the measured rate of $\mathrm{Br}(b \to s\gamma)$. A right-handed coupling $|V_R| \geq 0.004$ would, in principle, give too large a contribution to this decay [40], which, however, might be (partially) canceled with other new physics contributions (couplings to particles heavier than the top). Hence, the bound $|V_R| \leq 0.004$ is model dependent and does not substitute a direct measurement of this coupling. Similar arguments applied to the $\sigma^{\mu\nu}$ terms do not set relevant constraints on g_R because its contribution is suppressed by the ratio $\frac{q_\nu}{M_W}$ for small q_ν (as in $b \to s\gamma$).

The polarization of the W bosons emitted in the top decay is sensitive to deviations from the SM values of these couplings [33]. The three partial widths can be calculated for a general tWb vertex as parametrized in Eq. 3.27, yielding [41]:

$$\begin{aligned}\Gamma_0 = \tfrac{g^2|\vec{q}|}{32\pi}\Big(&\tfrac{M_t^2}{M_W^2}[|V_L|^2+[|V_R|^2](1-x_W^2-2x_b^2-x_W^2x_b^2+x_b^4)-4x_bReV_LV_R^*+\\ &[|g_L|^2+[|g_R|^2](1-x_W^2+x_b^2)-4x_bReg_Lg_R^*\\ &-2\tfrac{M_t}{M_W}Re[V_Lg_R^*+V_Rg_L^*](1-x_W^2-x_b^2)\\ &+2\tfrac{M_t}{M_W}x_bRe[V_Lg_L^*+V_Rg_R^*](1+x_W^2-x_b^2)\Big)\end{aligned} \tag{3.28}$$

$$\begin{aligned}\Gamma_{R,L} = \tfrac{g^2|\vec{q}|}{32\pi}\Big(&[|V_L|^2+[|V_R|^2](1-x_W^2+x_b^2)-4xReV_LV_R^*\\ &+\tfrac{m_t^2}{M_W^2}[|g_L|^2+[|g_R|^2](1-x_W^2-2x_b^2-x_b^2x_W^2+x_b^2)-4x_bReg_Lg_R^*\\ &-2\tfrac{m_t}{M_W}Re[V_Lg_R^*+V_Rg_L^*](1-x_W^2-x_b^2)\\ &+2\tfrac{m_t}{M_W}Re[V_Lg_L^*+V_Rg_R^*](1+x_W^2-x_b^2)\Big)\\ &\pm\tfrac{g^2m_t^3}{64\pi M_W^2}(-x_W^2[|V_L|^2-|V_R|^2]+[|g_L|^2-|g_R|^2](1-x_b^2)\\ &+2x_WRe[V_Lg_R^*-V_Rg_L^*]+2x_Wx_bRe[V_Lg_L^*-V_Rg_R^*])\\ &\times(1-2x_W^2-2x_b^2+x_W^4-2x_W^2x_b^2+x_b^4),\end{aligned} \tag{3.29}$$

with $x_W = M_W/m_t$, $x_b = m_b/m_t$ and

$$\vec{q} = \frac{1}{2m_t}(m_t^4+M_W^4+m_b^4-2m_t^2M_W^2-2m_t^2m_b^2-2m_b^2M_W^2)^{1/2} \tag{3.30}$$

the modulus of the W boson three-momentum in the top rest frame. The total top width is:

$$\begin{aligned}\Gamma = \tfrac{g^2\vec{q}m_t^2}{32\pi M_W^2}\Big(&[|V_L|^2+|V_R|^2](1-x_W^2-2x_b^2-sx_W^4+x_W^2x_b^2+x_b^4)\\ &-12x_W^2x_bReV_LV_R^*+2[|g_L|^2+|g_R|^2](1-\tfrac{x_W^2}{2}-2x_b^2-\tfrac{x_W^4}{2}-\tfrac{x_W^2x_b^2}{2}+x_b^4)\\ &-12x_W^2x_bReg_Lg_R^*-6x_WRe[V_Lg_R^*+V_Rg_L^*](1-x_W^2-x_b^2)\Big)\end{aligned} \tag{3.31}$$

Finite corrections for the top and the W width have a negligible influence on the distribution and hence Eq. 3.27-3.31 can be used to make a general analysis of the effective

tWb vertex.

If we substitute in the two equations above the SM values (g_R, g_L, V_R set to zero) and at the limit where $m_b \to 0$, we get exactly the results shown in section 3.4.

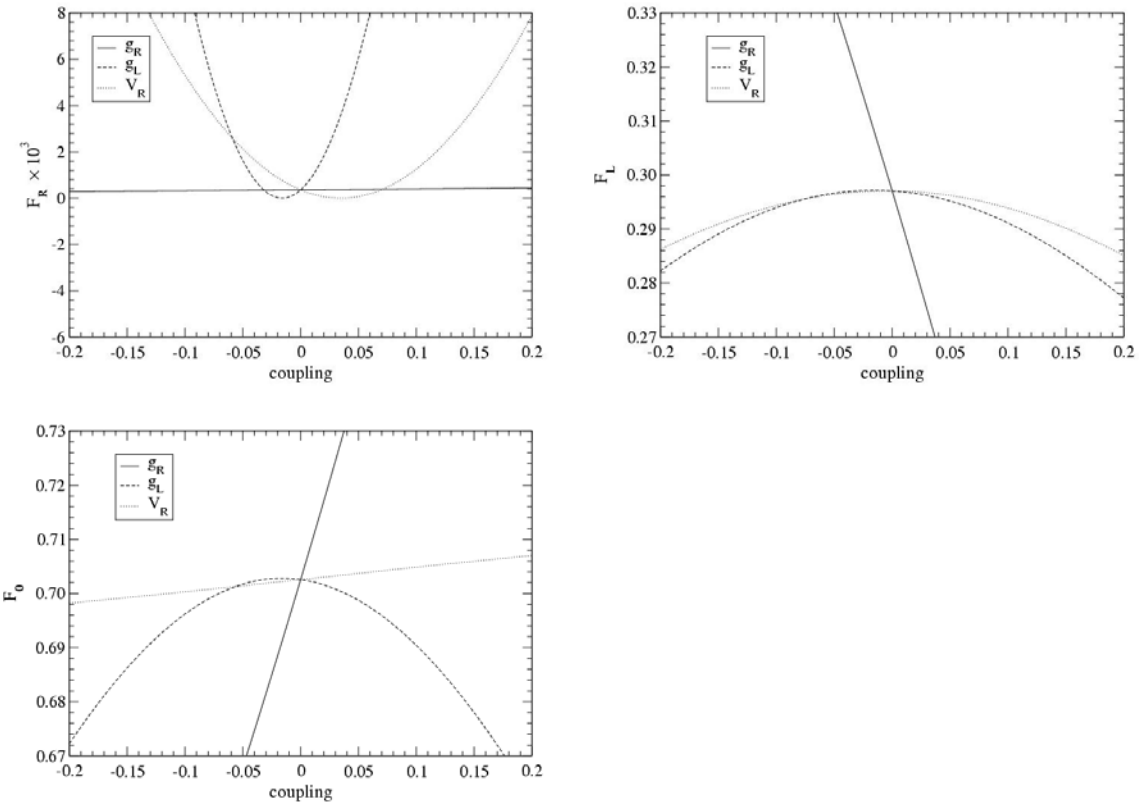

Figure 3.5 Dependence of the helicity fractions F_i on the anomalous coupling in Eq. 3.27 (plots taken from reference [41]).

In the presence of anomalous couplings induced by heavy new physics effects, the helicity fractions F_i are modified with respect to their SM values quoted in section 3.4. Their variation is shown in Figure 3.5, considering the CP-conserving case of real V_R,g_R and g_L, and that only one coupling is different from zero at a time. However, theoretical analyses described in [40] and [42] show that these couplings could be large, even of order 1, but in a correlated manner. A similar conclusion can be drawn from the partial wave unitarity bounds [43]. The LEP precision data imposes some constraint but only in correlation with similar neutral current anomalous ttZ couplings. These correlations predict that if one of the coupling is not zero, the others are forced to be of about the same order of magnitude [40]. These constraints assume there are no other sources of new physics that could cancel the effects of these couplings on the data.

One can see that F_L and F_0 are much more sensitive to g_R than to g_L and V_R. This is due to the interference term $V_L g_R^*$, which is not suppressed by the bottom quark mass

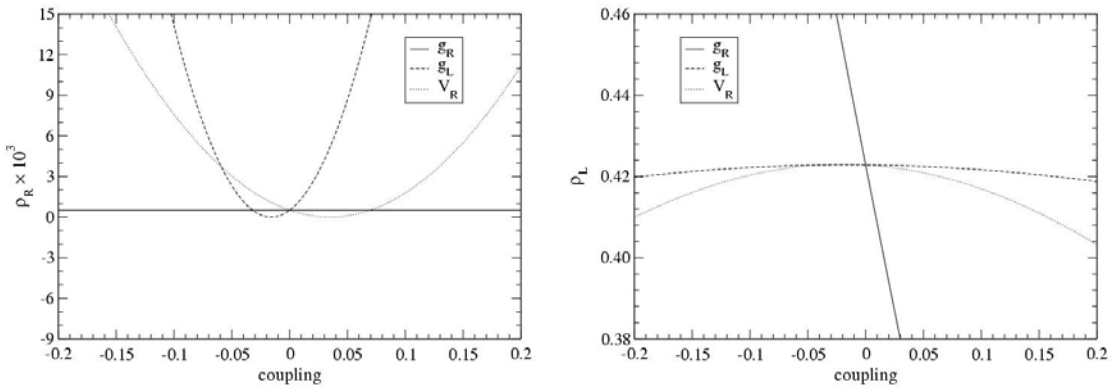

Figure 3.6 Dependence of the helicity ratios $\rho_{R,L} = \Gamma_{R,L}/\Gamma_0$ on the anomalous coupling in Eq. 3.27 (plots taken from reference [41]).
.

as for the g_L and V_R couplings. This linear term dominates over the quadratic one and makes the helicity fractions (and related quantities) very sensitive to g_R. The phases of anomalous couplings influence the helicity fractions through the interference terms which depend on the real part of V_R, g_L and g_R. The effect of complex phases is especially relevant for g_R, where the interference term dominates. In any case, the maximum and minimum deviations of the helicity fractions are found for real, positive and negative, values of V_R, g_R and g_L. Looking at anomalous couplings given the SM central values for the helicity fraction ($F_0 = 0.703$, $F_R \simeq 4.3 \cdot 10^{-4}$, $F_L = 0.297$) it is found that F_0 and F_L have a similar sensitivity to g_R, while the dependence on F_R sets the strongest bounds on V_R and g_L.

The sensitivity achieved for non-standard couplings may be greater from measuring the helicity ratios $\rho_{R,L} \equiv \Gamma_{R,L}/\Gamma_0 = F_{R,L}/F_0$ where the decay fractions can be used to determine the four independent couplings that define the tWb vertex (see Figure 3.5). These ratios can be directly measured from a simultaneous fit to the $\cos(\theta^*)$ distributions of two of the fractions.

In order to demonstrate the valuable information that lies in this analysis once the desired sensitivity is reached, we look as an example on the effect of two different models of physics beyond the SM:

- The Minimal Supersymmetric Standard Model ($MSSM$) with $\tan\beta > 1$ [36].
- The Topcolor assisted Technicolor (TC2) [37].

As discussed in the references, for W polarization in $t \to Wb$ in the case of $MSSM$, electroweak supersymmetry and QCD-SUSY corrections are of order of a few percent

and tend to cancel each other. The overall effect is to **increase the left-handed decay mode at the expense of reducing the longitudinal mode**.

For the Topcolor model, the TC2 scalars that couple strongly to the top quark will modify the tWb vertex in a way that **reduces F_L in favor of F_0**.

From the above discussion we can see that these two models predict opposite effects on the fractions.

If the total integrated luminosity from the Tevatron reaches 8 fb^{-1}, the statistical uncertainties on the measured fractions could be reduced to the order of 2-4%. The leading source of systematic uncertainties when measuring the W helicity fractions is the background model. Systematic uncertainties can be further reduced as well with a better background model, which can be achieved with more data. A larger signal MC sample will also reduce these uncertainties.

With the possible improvements of the analysis and the larger datasets it should be possible for CDF to be able to exclude some of the EWSB beyond SM models.

Performing a fit to extract the W helicity fractions in top decays can provide a determination of the four couplings of the tWb vertex and make an analysis that could test the different models of EWSB.

Because of the diversity of models proposed for possible new physics, it is necessary to be able to study these possible new interactions in a model independent approach. Due to the limited size of the available datasets, previous Tevatron analyses measured one of the W helicity fractions while fixing the other one to its SM value. A first simultaneous measurement of the longitudinal and right-handed fractions, making no assumptions on the W helicity, is presented in this thesis [44], but the statistical uncertainties of this particular measurement are too large to draw any conclusion concerning beyond SM physics.

We hope that the increasing total integrated luminosity delivered by the Tevatron will bring us to the region where we become sensitive to new physics effects and can distinguish between different EWSB models.

Chapter 4

Experimental Design

4.1 FNAL - the Fermi National Accelerator Laboratory

The Fermi National Accelerator Laboratory (or in short 'Fermilab') is located about 35 miles west of Chicago, Illinois. Fermilab, originally named the National Accelerator Laboratory, was commissioned by the U.S atomic energy under a bill signed by president Lyndon B. Johnson on November 21st, 1967. On May 11th 1974 the laboratory was renamed in honor of 1938 physics Nobel price winner Enrico Fermi, one of the greatest physicists of the atomic age.

The laboratory is currently the home of a large diversity of projects mostly related to high energy physics, including CDF, D0, Dark Energy Survey, Pierre Auger Observatory, Sloan Digital Sky Survey, MINERvA, MiniBooNE, MINOS, NOvA and NuTeV among them. Many of these experiments take advantage of the Fermilab Tevatron accelerator - the world's highest energy particle accelerator today.

4.2 Accelerator Complex

The accelerator complex at Fermilab [45] consists of several components, that can be conceptually separated into a series of accelerators preparing the protons, producing and storing anti-protons and finally accelerating both protons and antiprotons to $\sqrt{s}$ =1.96 TeV to make the collisions. The schematic view of the accelerator chain is shown in Figure 4.1.

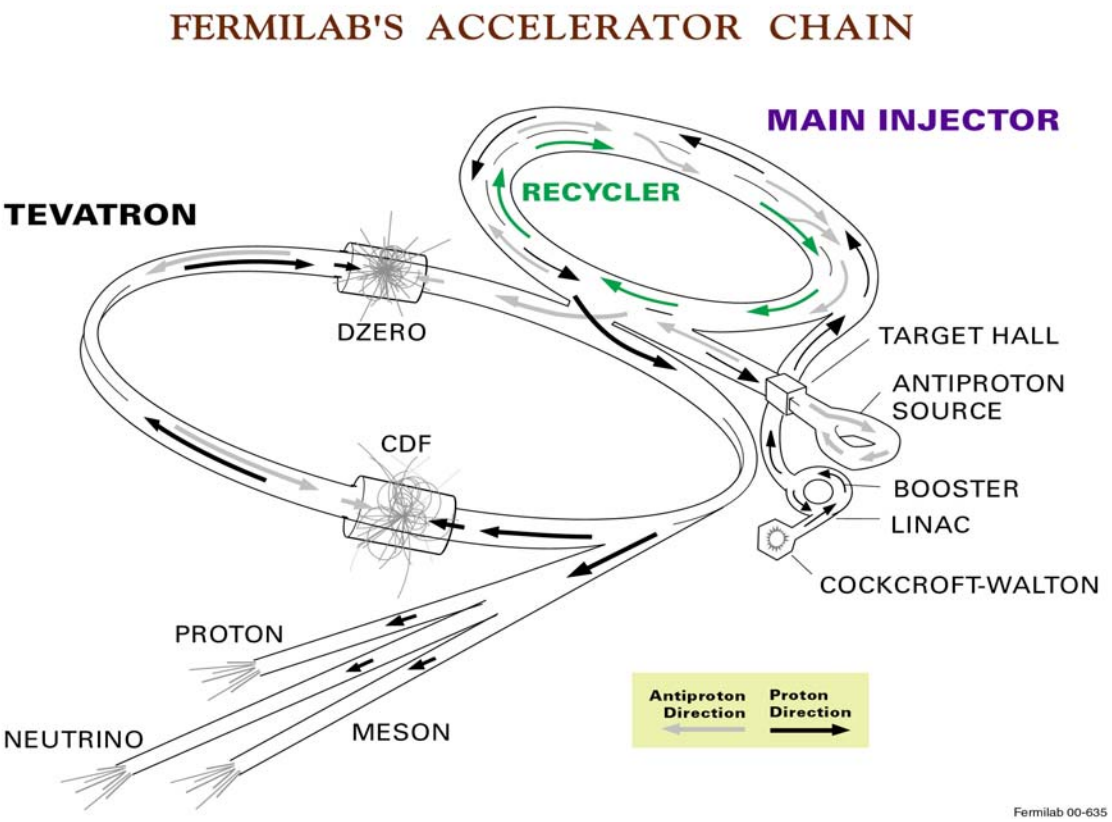

Figure 4.1 A schematic drawing of the Fermilab accelerator complex. the diagram shows the paths taken by protons and antiprotons at the Fermilab's five accelerators. The beam of particles begins as negative hydrogen ions at the right in the Cockcroft-Walton accelerator. They continue down the short, straight section, the Linac. As the beam of negative hydrogen ions enters the third accelerator, the circular Booster, both electrons are stripped off leaving a proton beam. The protons are injected into the Tevatron. In fixed target mode, the proton beam is extracted and sent down the Fixed Target beamline to the experimental areas. When the accelerator is run in colliding beam mode, antiprotons are collected in the triangle behind the Booster, the Antiproton Storage Rings. The antiprotons are injected into the Main Ring traveling in an opposite direction with respect to the protons. The protons and antiprotons collide inside the two detectors - CDF and Dzero (D0).

4.2.1 Proton Source

The Pre-accelerator is a linear accelerator that produces negative hydrogen ions and accelerates them to 750 keV by applying the electric field to the ionized hydrogen. The output frequency is 15 Hz and the resulting H^- ions then enter the Linac or Linear Accelerator [46]. The Linac is the next step in the acceleration process. It accelerates negatively charged hydrogen ions from 750 keV to 400 MeV. The Linac operates with a frequency of 15 Hz. The modes of operation include feeding the beam to the Booster, feeding the beam to the Nuclear Therapy Facility or dumping the beam into a concrete block. The Booster [47] is the first circular accelerator in the proton accelerator chain. It has a radius of 75 meters and consists of alternating magnets and RF cavities. The Booster strips electrons of the H^- ions and accelerates the protons from 400 MeV to 8 GeV with a period of 0.033 second. The RF cavities apply the accelerating field while the magnets apply the bending field to keep the protons in the circular orbit, and ramping it up in accordance with the instantaneous energy of the beam. The proton beams travel around the Booster about 20,000 times before they undergo the next acceleration step - acceleration in the main injector.

The Main Injector (MI) [48] is a circular accelerator that serves several purposes. One of its functionalities is to accelerate the protons transported from the Booster from 8 GeV to 150 GeV. In another mode of operation the MI stacks the antiprotons and accelerates them to 120 GeV. The circumference of this machine is seven times that of the Booster. The ramp up process takes about 1.5 seconds.

4.2.2 Antiproton Source

The production of antiprotons is a technologically challenging task and thus the antiprotons production and storage capacity is the main limiting factor for the luminosity of the colliding beams. The antiprotons are produced at the Target station when the 120 GeV proton beam coming from the Main Injector hits a nickel target. In this process different particles are being produced. A system of magnets is used to separate 8 GeV antiprotons and direct them to the next stage accelerator. The purpose of the Debuncher, a triangular synchrotron [1] machine, where antiprotons are directed after being produced, is not to accelerate them but rather to make the momentum of the particles inside the beam more uniform - this process is normally referred to as "cooling" [2]. The mean radius of the Debuncher is 90 meters. The resulting 8 GeV beam of antiprotons is then delivered

[1] A circular accelerator in which both magnetic field and accelerating electric field are varied synchronously as the particles are accelerated, in order to maintain the same particle orbit.

[2] Another way of looking at it is to consider cooling as a process of increasing particle density in momentum phase-space.

into the Accumulator. The Accumulator is located in the same tunnel as the Debuncher and is also a triangular synchrotron. It is used for storage and further cooling of the antiprotons.

The Recycler is a relatively recent addition to the Fermilab accelerator chain. It resides in the same tunnel as the Main Injector and is used to decelerate and cool down the antiprotons left at the TEVATRON after the store. Several different cooling techniques are used in the Recycler which serves an important purpose of improving the antiproton utilization efficiency.

4.2.3 TEVATRON

The Tevatron [49] is the final stage in the acceleration process. It receives 150 GeV (anti)protons from the Main Injector, and then accelerates them to the final energy of 980 GeV. The Tevatron ring is an underground circular beam tube with a radius of one kilometer buried about 6 meters deep. Its total circumference is about 6.3 km and it holds 816 dipolar superconducting magnets. These magnets are kept at a temperature of 4.3K by what is currently the largest cryogenic system in the world. At 980 GeV energy the magnetic field of the dipolar magnets is 4.2 Tesla, the current draw of the coils being 4000 A.

In addition to the dipole magnets there are 204 quadrapole pairs that focus the beam to achieve peak luminosity.

The RF system of the Tevatron consist of an array of 8 RF cavities running at a frequency of 53.03 MHz. This frequency does not need to be changed during the ramping since the very small velocity difference of the protons at 150 GeV and 980 GeV. It takes 9 cycles to fill the Tevatron with 36 bunches of protons (or antiprotons), and takes about 40 seconds to ramp the energy from the 150 GeV to 980 GeV. The typical number of protons (antiprotons) in a bunch is about $27 \cdot 10^{10}$ ($33 \cdot 10^{9}$).

During RunII the Tevatron is operated in 36x36 mode, which refers to the number of bunches of protons and antiprotons respectively. The bunch crossing occurs every 396 nsec.
The instantaneous luminosity is given by:

$$\mathcal{L} = \frac{N_B N_p N_{\bar{p}} f}{2\pi \sigma_p^2 \sigma_{\bar{p}}^2}, \tag{4.1}$$

where the N_B is the number of bunches in the machine, $N_{p,\bar{p}}$ is the number of protons/antiprotons in a bunch, f is the bunch revolution frequency and $\sigma_{p,\bar{p}}^2$ is the effective width of the proton/antiproton beams.
There are two detectors along the Tevatron ring located at the B0 and D0 points. The

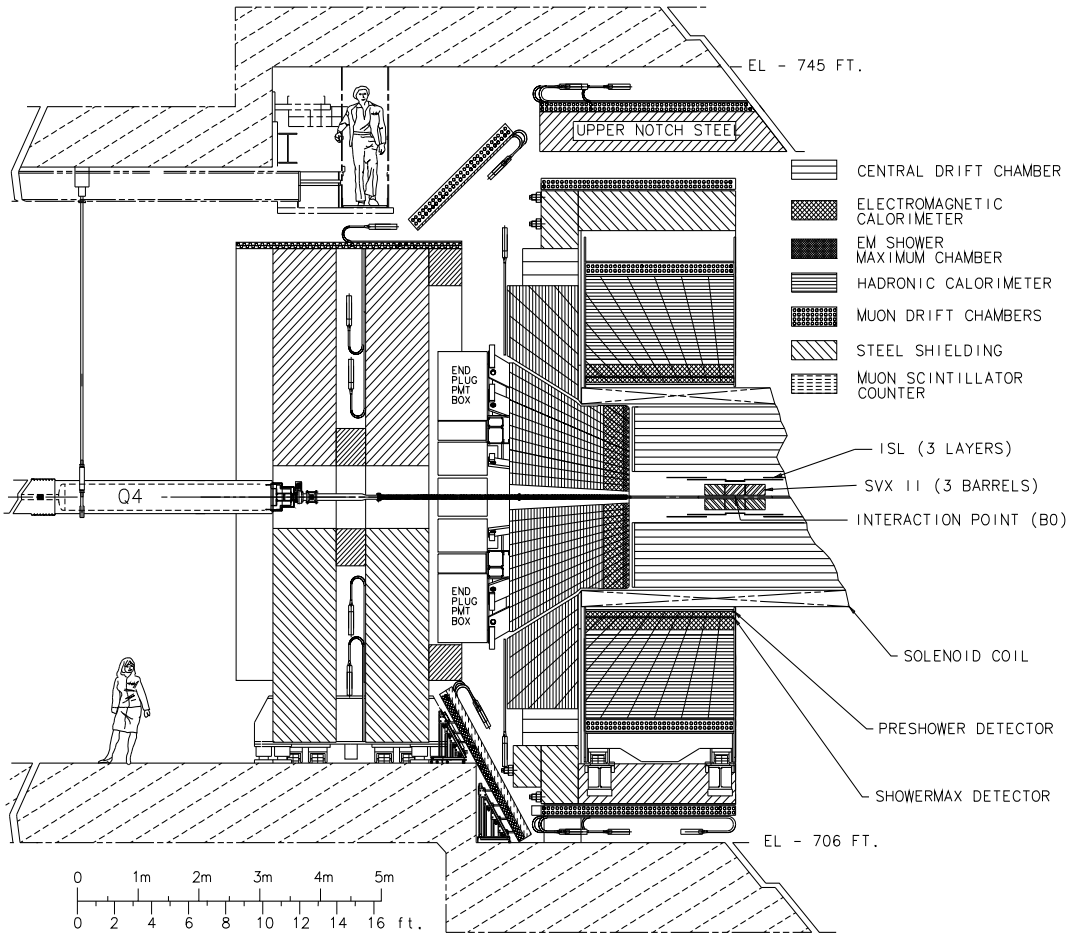

Figure 4.2 Elevation view of one half of the CDF II detector.

data used for the analysis reported in this thesis were collected by the detector located at B0 - the **C**ollider **D**etector at **F**ermilab (CDF).

4.3 The CDF II Detector

The Collider Detector at Fermilab (CDF) [50, 51], is a multipurpose particle detector built around the TEVATRON B0 interaction point. It is approximately 15 meters long and 10 meters high and maintains approximate axial and forward-backward symmetries. The associated Cartesian coordinate system is defined as a right-handed basis with the z-axis set by the colliding beams and the protons moving in the positive z-direction. The x-axis points radially outwards and the y-axis vertically upwards. Occasionally it is convenient to work in cylindrical (r, z, ϕ) or polar (r, θ, ϕ) coordinates, where the azimuthal angle ϕ is the (xy) plane angle measured from the direction of x-axis. Another coordinate system is

commonly used in collider physics where the polar angle θ is replaced by pseudo-rapidity:

$$\eta = -\ln\tan\frac{\theta}{2}. \tag{4.2}$$

The utility of the (r, θ, ϕ) coordinate system stems from the axial symmetry of the experiment and from the nature of proton-antiproton collisions. The latter manifests itself in the fact that the interactions of colliding partons often result in considerable longitudinal momentum of the collision products. The rapidity of the system:

$$y = \frac{1}{2}\ln\frac{E + p_z}{E - p_z}, \tag{4.3}$$

transforms under boosts along the z-axis as $y' = y + \tanh^{-1}\eta$ and thus Δy are invariant under such transformations. The pseudo-rapidity is the relativistic or massless approximation to the real rapidity of the system:

$$\eta = \frac{1}{2}\ln\frac{p + p_z}{p - p_z} = -\ln\tan\frac{\theta}{2}. \tag{4.4}$$

Many detector components are segmented uniformly in η and ϕ . Typically the pseudo-rapidity η refers to "detector η" is determined with respect to the center of the detector coordinate system. The η can also be determined with respect to the interaction point. (in that case it is called "event η").

The particles produced in each collision transverse through various detector subsystems. The first system to be encountered is the tracking system, then calorimetry and finally the muon sub-detectors. These are the basic components that provide the data that serve as the foundation of our measurement. The schematic overview of the CDF detector is shown in Figure 4.2.

4.3.1 Tracking System

The trajectory of particles can give valuable information about the kinematics of physical process, including charge sign and good momentum resolution if magnetic fields are present. The process of reconstructing a particle trajectory is known as *tracking*. In this section we describe the sub-detectors that form the integrated tracking system of the CDF detector as shown in Figure 4.3, followed by a brief overview of the basics in tracking reconstruction.

Solenoid:

All the tracking systems are enclosed inside a superconducting solenoid of 1.5m in radius and 4.8m in length. The solenoid provides a very homogeneous magnetic axial field of

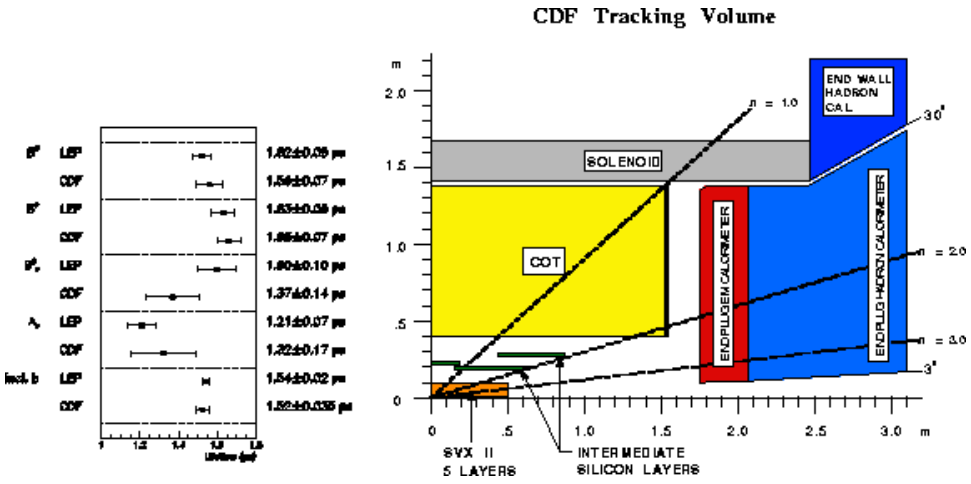

Figure 4.3 Longitudinal view of the CDF tracking volume. its main components are the solenoid, the central outer tracker (COT), which is a gas drift chamber, and the silicon micro-strip detectors - ISL, SVX and L00.

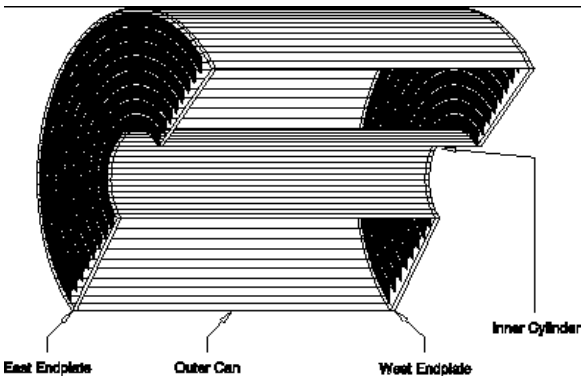

Figure 4.4 Cross section of the COT tracker.

1.4 Tesla inside a volume of 2.8m in diameter and 3.5m along the z direction. In normal operating conditions its current consumption is about 4650 A. Inside the solenoid and in direct contact with it the central outer tracker is located.

Central Outer Tracker (COT)

The COT position defines the global CDF reference frame and it is the main component of the tracking system. It is located inside the solenoid in the region of $|z| < 155$ cm between radii of 44 and 132 cm. The COT is a cylindrical multi-wire open-cell drift chamber. It consists of 8 super-layers, each made of a large number of cells (varies between 168 cells in the inner-most layer and 480 cells in the outer-most layer), Figure 4.4.

Each cell is either an 'axial' or 'stereo' cell. Each cell has an approximate size of about 2 cm by 10 cm and with a length of 310 cm spans the whole longitudinal direction of the COT.

When a charged particle passes through the gas it leaves a trail of ionization electrons.

These electrons drift towards the sense wire by virtue of the electric field created by the field panels and potential wires. Close to the sense wires the electrons are strongly accelerated because of the local $1/r$ electric field, producing more ionization in a process known as avalanche. The signal of this wire is further analyzed and depending on the charge collection (passing a threshold) the wire is said to be 'hit'. The time it takes from the moment the collision was expected to occur to the time the signal was detected gives information about the distance between the particle trajectory and the sense wire. The high voltage applied to the COT is such that the electric field drift is about 1.9kv/cm. The drift velocity is about 54 $\mu m/ns$.

The single 'hit' position resolution of the COT has been measured to be 140 μm, resulting in a transverse resolution of :

$$\frac{\Delta_{P_T}}{P_T} = 0.15\% \frac{P_T}{GeV/c} \tag{4.5}$$

Silicon vertex detector

The silicon tracking and vertex subdetector of CDF consists of three independent detectors named L00, SVX and ISL. They differ in size, radius and number of active elements, but they all use silicon micro-strip technology. They enable the measurement of the position of secondary vertices, like those produced in the decay of long lived hadrons such as B mesons, with excellent resolution - 10 times better than the resolution obtained using the COT only. Silicon micro-strip detectors were used for the first time in a hadronic accelerator by CDF during Run I of data taking.

SVX The silicon is supported with a rohacell foam in assemblies called ladders. Each ladder supports double-sided silicon modules, where in each side lies a string of four modules connected to each other by wire bonds, thus quadruplying the length of the strip. Twelve of these ladders are set in a semi-circular configuration to form a layer that surrounds the beam pipe at a given radius. The ladders are supported by two beryllium bulkheads, Figure 4.5.

The bulkhead provides support for 60 ladders in 5 concentric layers, confirming a 29 cm long SVX barrel. The SVX is built by placing three barrels along the beampipe. Layers are numbered from 0 (innermost) to 4 (outermost). Layers 0,1 and 3 combine $(\rho - \phi)$ modules on one side with 90° stereo on the other side. Layers 2 and 4 combine $(\rho - \phi)$ modules on one side with a small angle stereo on the other. The single hit resolution of the SVX is about $12\mu m$. The large number of channels require that much of the electronics is mounted close to the modules. This results in a better signal-to-noise ratio but also in additional multiple scattering due to the extra material in the volume.

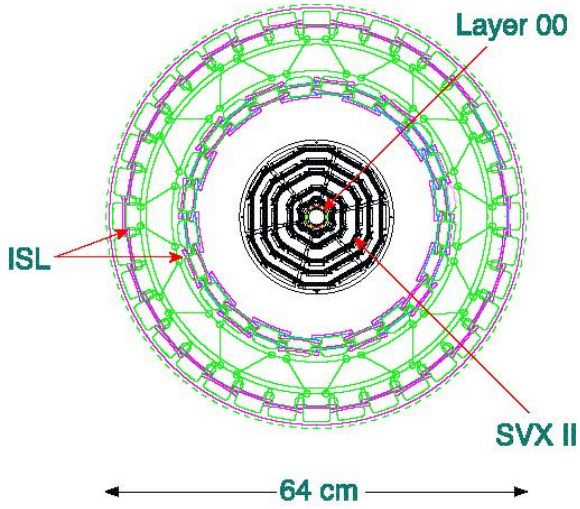

Figure 4.5 An overview of the CDF SVX.

The **ISL** consists of three layers. In the central region ($\eta \leq 1$) a single layer is placed at a radius of 22 cm. Two more layers are located in the region $1 \leq \eta \leq 2$ at a radii of 20 cm and 28 cm. The layers are double sided with $(\rho - \phi)$ on one side and a small stereo angle on the other side. To reduce the total number of channels to 268,800 only one out of two channels is read. The ISL single hit resolution is about $20\mu m$.

The **L00** consists of a single sided layer of 12 ladders, shown in Figure 4.6. Six of the ladders lie at a radius of 1.35 cm and the other six at 1.62 cm from the beamline. Each ladder is made out of six sets of two wire-bonded modules, spanning 95 cm in the $\hat{z}$ direction. The layer is supported by a carbon fiber structure.
In addition, L00, SVX and ISL have dedicated cooling lines running at a nominal temperature of $-6°C$. Special effort was made to accurately align the silicon detectors with respect to the beam, as opposed to the COT. This is because a small misalignment of the COT, while not significantly changing the track information obtained with it, can effect the impact parameter of the tracks[3]. which is obtained using silicon hit information and is used for triggering purposes, introducing a dependence on the ϕ coordinate.

Tracking and pattern recognition

Tracking Parameterization: In a plane perpendicular to a homogeneous magnetic field, such as the one provided by the CDF solenoid, the trajectory of a charged particle follows a circular pattern to the limit of energy loss due to the traversed material. The

[3]Distance to closest approach of the track to the beam, explained later

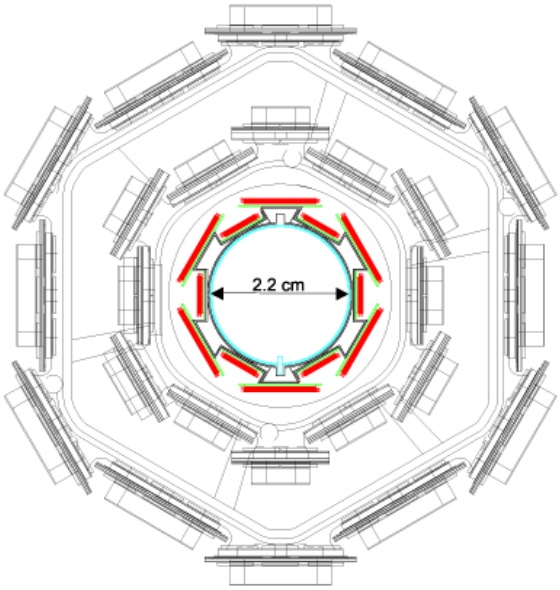

Figure 4.6 End view of the L00 detector

longitudinal component of the particle's momentum is not modified by the axial magnetic field, thus in three spacial dimensions the trajectories of charged particles are helices. The helices can be parametrized with five parameters chosen to be:
C: the signed helix curvature defined as $C = sign(q)/2R$, where R is the radius of the circle in the transverse plane and q is the charge of the particle.
z_0: The position of the point along the $\hat{z}$ axis at the point of closest approach.
d_0: a signed quantity defined as $d_0 = sign(q)(r_C - R)$, where r_C is the position of the center of the circle in the transverse plane, and its magnitude is the distance from z_0 to the closest point in the track.
ϕ_0: the direction of the transverse momentum of the particle at the point of closest approach.
$\cot(\theta)$: the ratio of the longitudinal and the transverse momentum (P_z/P_T).

4.3.2 The Calorimetry

Charged particles with energies greater than 350 MeV may leave the tracking volume and propagate beyond the solenoid magnet that surrounds it. Neutral particles, both photons and neutral hadrons, leave the tracking volume undetected. Even if they were seen by the tracking system, no information about their momenta would be available for a quite obvious reason – their trajectories do not bend in magnetic field. In many cases the measurement of their momenta is essential for understanding the observed events.

The calorimetry subsystem serves the purpose of filling this gap and is based on the fact that as particles that have reasonably high electromagnetic or hadronic interaction cross sections propagate through matter they transfer their energy to the medium, until eventually all of it is absorbed. Some media produce measurable response to such energy depositions by emitting light in amounts dependent on the amount of energy lost by the particles.

The CDF calorimetry system[52, 53] consist of alternating layers of scintillator and absorber material. As particles interact with absorber they produce cascades of particles or "showers" that penetrate the scintillator. The light from the latter is guided into photomultipliers. Their response is in turn digitized and with the help of relevant calibrations converted into the measurement of the deposited energy.

All the calorimeters are divided into segments or "towers" in such a way that the division boundaries between them point at the interaction point. The entire calorimetry system consists of two regions, central and forward; the later is also known as the "plug". The central calorimeters cover the region of 2π in ϕ and as far as $|\eta| < 1.0$ in pseudo-rapidity. They are segmented into the "towers" of $0.11 \times 15^\circ$ in $\eta \times \phi$. The Central ElectroMagnetic (CEM) part consists of alternating layers of lead absorber and polystyrene scintillator, while the Central HAdronic part (CHA) uses thicker steel plates as the absorber. The CEM is $18X_0$ radiation lengths thick, while the CHA is around $4.5\lambda_0$ attenuation lengths thick. The energy resolution of the CEM is estimated to be:

$$\frac{\sigma_E}{E} = \frac{13.5\%}{\sqrt{E_T}} \oplus 2\%, \tag{4.6}$$

where the notation $\oplus$ means that the constant part is added in quadrature. The CHA resolution is estimated to be:

$$\frac{\sigma_E}{E} = \frac{50\%}{\sqrt{E_T}} \oplus 3\%. \tag{4.7}$$

Other parts of the calorimeter system are the the CEntral Shower-maximum (CES) and Central Pre-Radiator (CPR) detectors. The CES is a gas multiwire proportional chamber with cathode strips that provide measurements of the z-position and anode wires that allow a measurement of the ϕ of the energy deposition. The chamber is embedded into the CEM at about $5.9X_0$ where the maximum of electromagnetic energy deposition occurs. The position resolution in both directions is around 2 mm. The CPR consists of proportional chambers placed between the solenoid and the calorimeter. These two subsystems, CES and CPR, provide both position measurement that helps in matching energy depositions to tracks and in shower profile measurements (information used in particle identification to distinguish between $e^{\pm}/\gamma$ and γ/π_0).

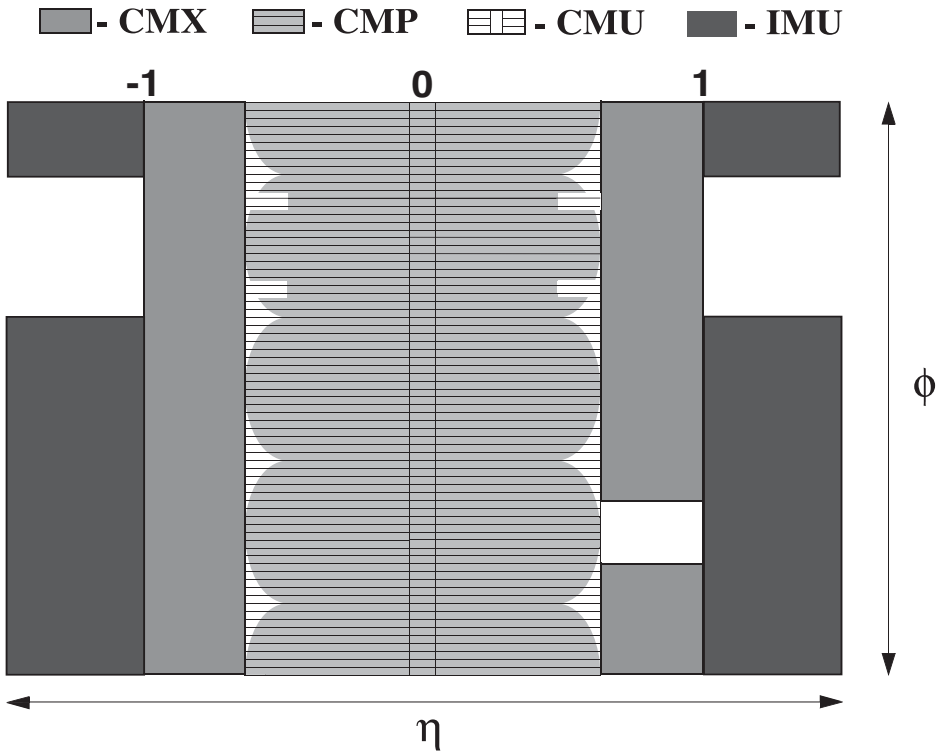

Figure 4.7 η and ϕ coverage of the CDF muon system.

It should be noted that the segmentation of the calorimeters is rather large and thus it is quite possible that the energy measured by a particular tower was contributed to by multiple particles. Occasionally this poses a problem as the energies of the individual particles can not be determined. In other cases, most notably when a "jet" of particles that results from hadronization of a quark or gluon coming directly from hard scattering hits the calorimeter, the total energy of all the particles in the jet is exactly the information that is needed.

4.3.3 The Muon System

Muons are 207 times heavier than electrons, so they loose substantially less energy due to electromagnetic interactions as they travel through the calorimeter material. This allows the muons to pierce through the calorimetry subsystem after they exit the tracking volume. The CDF muon subsystem consists of several chambers located outside the calorimeters and includes Central MUon detector (CMU), Central Muon uPgrade (CMP), Central Muon eXtension (CMX) [54, 55]. Due to space and design constraints, the muon coverage is incomplete. Figure 4.7 shows the ϕ-η regions that are instrumented. The CMU is comprised of series of rectangular drift cells four layers deep. The hits registered

in at least 3 out of 4 layers form a "stub", which after being properly matched with the corresponding COT track suggests the presence of a muon. The CMP sub-detector consists of both drift chambers and scintillator plates and functions similar to the CMU by providing a "stub" that is used in muon reconstruction. The coverages of CMU and CMP partially overlap, refer to Figure 4.7. The CMP is placed behind additional 60 cm of steel and thus is less sensitive to remnant hadrons that penetrate through CHA(punch-through hadrons). The CMX subsystem, like the CMP, combines drift cells and scintillator plates arranged in semi-conical arches that cover the pseudo-rapidity region of $0.6 < |\eta| < 1.0$.

4.3.4 The Cherenkov Luminosity Counter

The CLC (Cerenkov Luminosity Counter) is placed at the sides of the detector, in the 3° gap between the plug calorimeter and the beam pipe. It spans from 184 cm to 405 cm in the $\hat{z}$ axis.

It measures the average number of interactions per bunch crossing (μ), which allows the calculation of the instantaneous luminosity L from: $\mu f_{bc} = \sigma_{p\bar{p}}\mathcal{L}$, where f_{bc} is the frequency of bunch crossing at the Tevatron and $\sigma_{p\bar{p}}$ is the total $p\bar{p}$ cross section of about 100mb at the Tevatron's $\sqrt{s} = 1.96TeV$.
To measure μ the CLC takes advantage of Cerenkov radiation - the light emitted when particles travel in a medium with a velocity higher than the speed of light. This light is radiated in a fixed angle (δ) with respect to the particle's momentum. The angle δ depends on the refraction index of the medium (n) and the particle's velocity - $cos(\delta) = 1/n\beta$ where $\beta = v/c$.

The CLC is composed of an array of Cerenkov counters in the shape of long cones (cone-modules). More detailed information about the CLC is found in [56, 57].

4.4 Data Acquisition and Trigger

A schematic view of the CDF Data Acquisition(DAQ) and trigger system is given in Figure 4.8. The trigger plays an important role to efficiently extract the most interesting physics events from the large number of minimum bias and background events and to reduce the amount of data to a reasonable volume. The CDF trigger is a three level system. The time available for event processing increases in each level of the trigger, which permits the use of an increasing amount of information to either accept or reject an event. While Level-1 and Level-2 triggers are based only on parts of the detector information, the Level-3 triggers makes use of the complete event data. A signal is defined

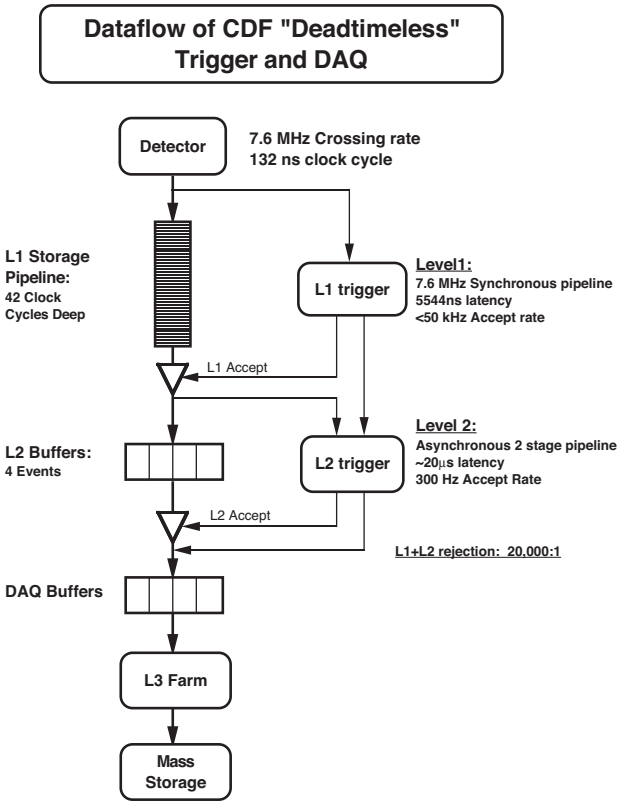

Figure 4.8 Data flow schematic of the three level pipe-lined and buffered trigger system.

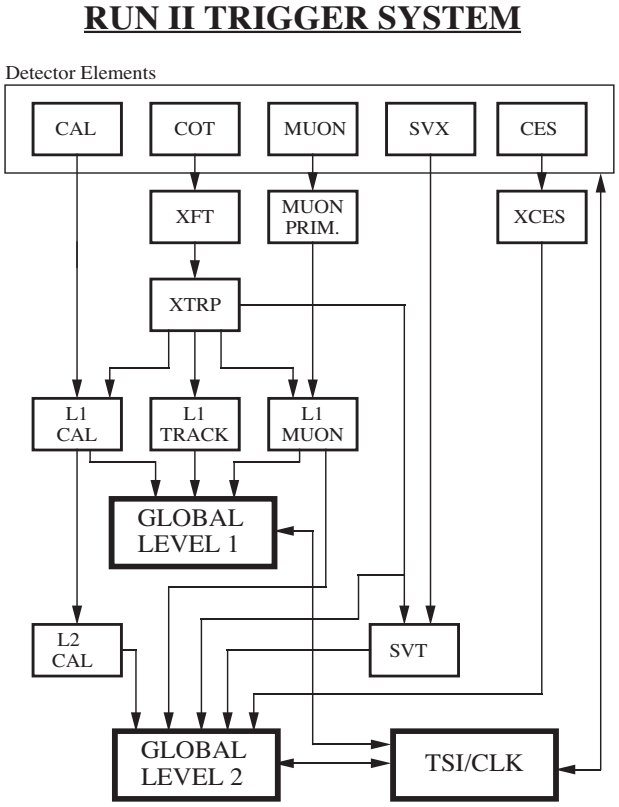

Figure 4.9 Functional block diagram of the CDF L1 and L2 trigger system.

as an event where a variable (for instance the energy in the calorimeter) lies above a certain trigger threshold. A list of quantities that can be cut on at the different trigger levels is given in [59]. L1 and L2 are hardware triggers while L3 is a software trigger. An optimized version of the reconstruction executable is running on a Linux PC farm with about 100 nodes. The design processing rates for Level-1, 2 and 3 are 50 kHz, 300 Hz and 50 Hz respectively. The typical event size is about 250-300 kB. The L1 triggers base their decisions on information of the calorimeters, the muon system, the forward detectors and the drift chamber(see Figure 4.9). The eXtremely Fast Tracker(XFT) reconstructs r/ϕ tracks in the COT in time to take part in the Level-1 decision making process. It has a transverse momentum resolution of $\delta P_T/P_T^2 = 0.01651$ GeV^{-1} and an angular resolution of 5.1 mrad. An important feature of Level 2 is the Silicon Vertex Tracker(SVT). It adds silicon r/ϕ hits to the L1 XFT tracks. This allows to select events with two tracks having an impact parameter larger than 120 μm in order to identify secondary vertices. This makes a large number of important processes involving the hadronic decays of bottom hadrons accessible. The SVT calculates the impact parameter with respect to the nominal z axis. Some misalignment and time variations of the beam position are possible, sometimes of the order of 100μm. The beam position in the transverse plane can be calcu-

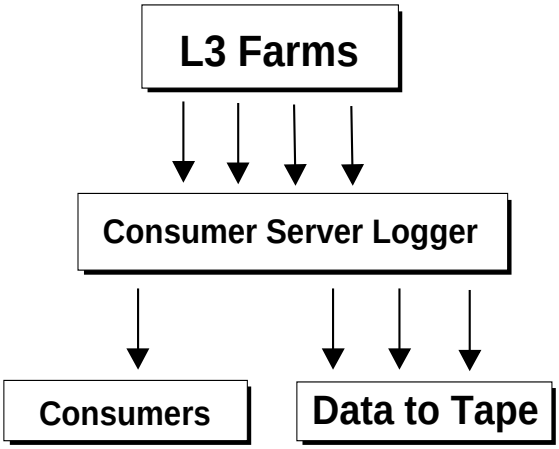

Figure 4.10 Data flow after L3 triggers.

lated using the impact parameter and the azimuthal angle ϕ [58]. The SVT continuously fits the transverse beam position and corrects the fitted value of the impact parameter. The corrected value is the output to the Level2 to be used in the event selection. The determination of the beam position is done on a run by run basis. Full event reconstruction takes place on the L3 trigger farm and hence a wide variety of requirements can be imposed on the events passing L3 [60]. Events passing the final trigger level belong to a certain trigger path. Each "path" is a unique combination of L1, L2 and L3 triggers. The trigger decisions are combined via a logical "AND". Many paths combined by a logical "OR" can be used to feed a single data set. The data is written to approximately 20 streams and stored on tape. After reprocessing the events they are split up into more specific data sets. During measurements the data quality is monitored online [61].

4.5 Online Monitoring

After passing L3 triggers, the data is saved in storage systems. Some of the data stream are picked up by online data validation programs, what is called "Consumer" [62] as shown in Figure 4.10. The data streams are arranged by Consumer Server Logger (CSL) [63, 64] to meet hardware and software requirements from up and down streams. The consumer programs consist of 13 subprograms which are meant to verify the condition of the dif-

ferent sub-detectors and the quality of data when data taking is performed. Information about the consumers is found at [65]-[77].

Chapter 5

Data Sample and Event Selection

This chapter describes the data sample and the event selection used in this analysis to achieve a top-enriched data sample in the lepton+jets channel. Estimations of the background content of this sample are presented, on the basis of models of signal and background used in this analysis.

5.1 Lepton+jets event selection

A top quark's production and decay vertices are expected to be separated by O(10^{-16}) m, which exceeds the spatial resolution of any detector by many orders of magnitude. Detection of a top quark therefore proceeds through identification and reconstruction of its daughter particles. Fortunately, the large top mass dictates that it is not produced highly relativistically. Consequently, its much lighter decay products have good angular separations and high momenta in the laboratory frame. Most end up in the central region of the detector, with P_T, the transverse momentum, exceeding 20 GeV in magnitude.

The event selection for the lepton+jets sample is well described elsewhere [78]. With this selection, events consist with the lepton+jets signature of $t\bar{t}$ decays are identified. From data corresponding to an integrated luminosity of 955 pb^{-1} used for the measurement reported here, 220 events passed the selection described in the following sections.

5.1.1 The data sample

The datasets used in this analysis were collected with the inclusive high-P_T lepton triggers, which select leptons with P_T above 18 GeV in the central part of the CDF detector. The samples are **bhel0d, bhel0d and bhel0i** for central electrons and **bhmu0d, bhmu0d and bhmu0i** for muons. The DQM v13 GoodRun list was used with bits (1,1,4,1) to

include silicon information. Table 5.1 summarizers the integrated luminosity of the data samples.

lepton	0d	0h	0i	total
CEM/CMUP	333.04	363.01	258.65	954.7 ± 57.28
CMX-Arches	319.64	363.01	258.65	941.3 ± 56.48
CMX-MiniSkirt+KeyStone	0	363.01	258.65	621.66 ± 37.3

Table 5.1 Luminosity using GoodRun list v13.

5.2 Event Reconstruction

The event data read out by the CDF detector has to undergo event reconstruction which, roughly speaking, converts tracking system hits, calorimeter energy deposition measurements and muon chamber stubs into physics objects that are associated with certain particles. The physics objects that are important to $t\bar{t}$ events in the lepton+jets final state are jets, high P_T electrons or muons and large missing transverse energy (missing E_T or $\not\!\!E_T$), which is the imbalance of transverse energy measurement and is assigned as a transverse energy due to undetected neutrinos. Thereby, jets, electrons, muons and missing E_T have to be reconstructed. The reconstruction of these objects is discussed below.

5.2.1 Electron identification

High energy electrons can be identified by a high P_T track in the drift chamber and large energy depositions in the electromagnetic calorimeters. The geometry of the CDF detector imposes the categorization of electrons to two types according to the calorimeter in which the deposition takes place - 'central electrons', which are described in details in the following section, and 'plug electrons'. Plug electron candidates deposit energy in the plug calorimeter, which covers the pseudorapidity η in the range of 1.1-3.5. Electron candidates with $|\eta| > 2$ have a large charge misidentification rate and the cut $|\eta| < 2.0$ is required. This requirement has a small effect on the acceptance of $t\bar{t}$ events since these are mostly central.

Our analysis does not treat plug electrons, only central electrons are considered.

Central electrons

Central electrons traverse the central part of the detector, $\eta \leq 1.1$, leaving a high-P_T track in the COT and depositing their energy in the CEM calorimeter. To identify central

electrons the following requirements are applied:

- $E_T = E \cdot sin(\theta) \geq 20GeV$
  The total electromagnetic energy deposited by the electron in the CEM (E) multiplied by $sin(\theta)$ of the COT track pointing to the seed tower of the cluster. The electron cluster is formed of a seed EM tower defined as the tower where most of the energy is deposited, and a number of shoulder towers which are added to the seed tower until the maximum cluster size is reached. The largest cluster spans two towers in pseudorapidity and one tower in azimuth. The energy E is corrected to account for non-linear effects and known differences in response between the different towers, as measured from $Z \rightarrow e^- e^+$ candidates.

- $P_T > 10GeV/c$
  The transverse momentum of the COT track. The resolution of the track is improved by constraining the track to originate from the beamline position.

- $E_{had}/E_{EM} < 0.055 + 0.00045 \times E_{total}$
  The ratio of the energy deposited in the hadronic calorimeter cluster to that deposited in the electromagnetic cluster. The second term on the right hand side compensates for inefficiencies of the cut at very high energies, as the electron shower leaks into the hadronic calorimeter.

- $E/p < 2$
  The ratio of the electromagnetic calorimeter to the momentum of the track as measured from the COT track. This cut helps reduce the number of jets that fake electrons. These jets typically contain a π^0 that deposits its energy in the electromagnetic calorimeter. This cut also helps discards those electrons that radiate a high energy photon. The photon is typically collinear with the electron track and generally deposits its energy in the same calorimeter tower and therefore the cluster energy does not differ much from the original energy of the electron. However, the P_T of the track significantly changes and the ratio E/P can be much larger than 1.

- $L_{shr} < 0.2$
  This quantity uses the lateral shower profile and compares it to what is expected from electromagnetic showers. It is defined as

$$L_{shr} = 0.14 \sum_i \frac{E_i^{measured} - E_i^{expected}}{\sqrt{(0.14\sqrt{E})^2 + \sigma^2_{E_i^{Expected}}}} \tag{5.1}$$

Where the index i runs over towers, $E_i^{measured}$ is the energy measured in tower i and $E_i^{expected}$ is the energy expected from testbeam data. The error in the energy measurement is represented by $0.14\sqrt{E}$ and $\sigma^2_{E_i^{Expected}}$ is the uncertainty of the energy estimate. Typically L_{shr} is a two-tower sum. Any extra particles accompanying that responsible for the main EM shower will tend to add to the energy in adjacent towers and make L_{shr} a larger number.

- $-3.0cm < Q \cdot \Delta x < 1.5cm$; $|\Delta z| < 3cm$
  The distance between the COT track extrapolated to the CES and the best matching CES cluster is represented by Δx and Q. This requirement imposes a close match between the two. The cut on Δx has been multiplied by the charge of the track, Q, and it is asymmetric in $r - \phi$ to account for possible photon bremsstrahlung in the direction of the outside of the track.

- $\chi^2_{strp} < 10$
  This quantity compares the shower profile in the shower maximum detector, CES, with the shower profile obtained from test beam electrons.

- $|z_{vertex}| < 60cm$
  The position in z of the primary vertex interaction. The z_{vertex} is determined by the intersection of the track with the beam axis. The longitudinal spread of the event vertex about the nominal interaction point $z = 0$ is a Gaussian with $\sigma = 26cm$. The vertex position is required to be within 2σ to exclude tracks from passing through uninstrumented regions of the detector.

- Track quality cuts
  A well reconstructed track should have at least seven hits in each of three axial and three stereo superlayers in the COT.

- Fiduciality
  This variable requires that the electron is reconstructed in a region of the CDF detector that is well instrumented.

- non-conversion electron
  The interaction of photons with the detector material can result in the conversion to electron-positron pairs. These conversions can be identified by the presence of another electron candidate. If two tracks with small $\Delta\phi$ are present at the point of conversion the event is flagged as conversion and is rejected.

- Calorimeter isolation - $E_T^{iso}/E_T^{cluster} < 0.1$.
  The ratio of transverse energy in the electromagnetic and hadronic calorimeter in a

cone of radius $\Delta R = \sqrt{(\Delta\eta)^2 + (\Delta\phi)^2} \leq 0.4$. This cut rejects electrons that are not isolated from hadronic activity, including those coming from semi-leptonic quark decays.

The efficiency of the central electron identification cuts is determined from $\gamma/Z^* \rightarrow e^+e^-$ data sample. Events are required to have oppositely charged electrons with an invariant mass of the electron pair in a $\pm 15 GeV/c^2$ range from the nominal Z mass. One electron is required to pass all the tight cuts while the other is used to obtain the efficiency of the cuts. The central identification efficiency is found to be 79.3%. To correct for differences acceptance at the reconstruction level between data and MC a scale factor of $\epsilon_{data}/\epsilon_{MC} = 89.1\%$ is applied [80].

5.2.2 Muon Identification

Muons are minimum ionizing particles which penetrate matter with little energy loss. Their passage through the detector is characterized by a track in the COT, little energy deposition in the calorimeter and hits in the muon chamber.

Muons at CDF are categorized by the detector region through which they pass. For the analysis presented here only the CMU, CMP and CMX sub-detectors are used. Muons reconstructed in the CMU detector are called CMU muons and similarly for the other subdetectors. Muons reconstructed both in the CMU and CMP are called CMUP muons. In particular, central tracks that are not expected to pass through any of the muon detectors are called Central Minimum Ionizing Objects or CMIO muons. They are called stubless muons to indicate that no stub was reconstructed in the muon detector.

The following requirements are applied to muon candidates:

- $P_T > 20 GeV/c$ - the transverse momentum of the COT beam-constraint track.
- $|z_0| < 60cm$ - the z position of the track.
- $d_0 < 0.2cm$ for tracks with no silicon hits. $d_0 < 0.02cm$ for tracks with silicon hits. The impact parameter d_0 is the distance of z_0 from the closest point of the track. This selection is of course used for the default muon track, i.e that is with no beam constraint. This cut requires the muon to originate from the nominal interaction point and substantially reduces cosmic muons that entered the detector in the time window of the collision.
- Track quality cuts - identical to electron track quality tracks.

- $E_{em} \leq 2GeV + max[0.0, 0.0115(p - 100GeV/c)]$ - requires the energy deposited in the electromagnetic calorimeter to be very small. A small change is introduced for muons with $p > 100GeV$.

- $E_{had} \leq 6GeV + max[0.0, 0.028(p - 100GeV/c)]$ requires the energy deposited in the hadronic calorimeter to be smaller than that of strongly interacting jets.

- $E_{em} + E_{had} > 0.1GeV$ for stubless muons only.
  Stubless muons are required to have non-zero energy deposition in the calorimeter to limit background from hadrons escaping the detector through non-instrumented regions of the calorimeter.

- $|\Delta X|_{CMU} \leq 3cm$, $|\Delta X|_{CMP} \leq 5cm$ and $|\Delta X|_{CMX} \leq 6cm$
  The distance in the $r - \phi$ plane between the COT track extrapolated to the stub segment and the position of the reconstructed stub for the muons in different sub-detectors. The requirements are weaker for CMP and CMX since the muons traverse more material and suffer greater deflections due to multiple scattering.

- Fiduciality
  This variable requires that the track of the muon candidate extrapolates to the proper muon chamber. For stubless muons the track is required to pass through well instrumented regions of the CDF detector and through no muon sub-detector.

- $\rho_{COT} > 140cm$
  The radius at which the track leaves the COT. This requirement is needed to make the offline selection consistent with the trigger, demanding the track to pass several superlayers of the COT.

- Isolation $E_T^{iso}/P_T < 0.1$
  The quantity E^{iso} is the energy of calorimeter towers in the cone $\Delta R = 0.4$ without including the tower associated with the track.

- non-cosmic muon.
  Muons coming from cosmic background are identified as dimuon events with an angular separation close to 180° in ϕ. Cosmic rays enter the detector at random times and random locations. As cosmic muons traverse the detector they leave energy in the calorimeter, traverse through the COT leaving a single track that is reconstructed as two tracks and energy in the calorimeter as it exits. The time difference between the energy deposited in the both ends of the hadronic calorimeter can be analyzed to identify cosmic muons. In addition, a cut on the impact parameter of

the track efficiently identifies cosmic muons. Events for which a cosmic muon is tagged are rejected.

Central muons at CDF are identified with about 90% efficiency.

5.2.3 Jet reconstruction

In a typical $p\bar{p}$ collision quarks and gluons are created. These carry color charge and are therefore subjected to hadronization processes. After these processes the original parton results in a stream of colorless particles. These particles are collimated along the direction of the original parton and, after traversing the tracker, deposit their energy in a cluster of towers in the calorimeter detector. This stream of particles is called a *jet*.

The jets are reconstructed from the energy deposited in the calorimeter towers with an algorithm called *jet clustering*. This algorithm starts by identifying the seed tower as that one with the largest calorimeter energy. The cluster of towers within the cone $\Delta R = \sqrt{(\Delta\eta)^2 + (\Delta\phi)^2} = 0.4$ from the center of the seed tower is identified. The cone size $\Delta R = 0.4$ is chosen to include most of the jet energy without a large contribution from other jets or tracks.

After the cluster is formed, the shower center in the plane (η, ϕ) of the calorimeter is determined as follows:

$$\eta_{centroid} = \frac{\sum_i E_T^i \eta^i}{\sum_i E_T^i} \tag{5.2}$$

$$\phi_{centroid} = \frac{\sum_i E_T^i \phi^i}{\sum_i E_T^i} \tag{5.3}$$

Where the sum runs over the towers in the cluster and $\eta^i, (\phi^i)$ represent the $\eta, (\phi)$ coordinate of the center of the tower. After the position of the shower is calculated a new cone is defined, centred in the new coordinates, and the calculation is repeated for the new cluster. This process is then iterated until the cluster is remained unchanged.
The traverse energy of the jet is determined as:

$$E_T^{raw} = \sqrt{(\sum_i E_i sin(\theta_i) cos(\phi i))^2 + (E_i sin(\theta_i) sin(\phi_i))^2} \tag{5.4}$$

where E_i is the total energy in tower i. This quantity represents the energy deposited in the cluster, and does not include corrections to account for detector effects or other physics processes and is thus referred to as *raw*.
The corrected value of the jet E_T is derived from the raw value E_T^{raw} using a set of multiplicative and additive correction factors resulting in corrected values that are close to

the energy of the initial parton. The correction are given by the following relation:

$$E_T = (E_T^{raw} \times f_{rel} \times f_{time} \times f_{scale} - E_T^{MI}) \times f_{abs} - E_T^{UE} + E_T^{OC} \tag{5.5}$$

The seven factors are briefly explained below (more detailed information can be found in [81]).

- Relative correction f_{rel}.
  this factor takes into account the relative tower-to-tower differences in the calorimeter response (level1 jet energy scale (JES) correction).

- Time dependent correction, f_{time}
  The calorimeter response decreased with time. This correction factor depends on the date the event was recorded and a multiplicative factor to account for that is assigned (level 2 JES correction).

- Energy scale correction f_{scale}. This factor accounts for the non-linear response of the calorimeter (level 3 JES correction).

- Multiple interaction E_T^{MI}. The energy of minimum bias events may fall in the jet clustering cone and must be subtracted. This is calculated on an event-by-event basis (level 4 JES correction).

- Absolute energy correction, f_{abs}.
  This factor corrects the energy of the jet to that of the original particle that generated it. It includes nuclear absorption and particle leakage effects that can reduce the total energy measured in the jet cluster (level 5 JES correction).

- Underlying event correction, E_T^{UE}.
  Extra energy that doesn't come from the original parton may be deposited in the jet cluster. This energy can originate from spectator partons, beam-beam soft interactions or beam remnants (level 6 JES correction).

- Out of cone corrections, E_T^{OC}.
  A fraction of the energy of the initial parton may fall outside the cone resulting in

an underestimation of its energy. This quantity is obtained from MC simulation of the physics process under study (level 7 JES correction).

Each level of correction has a systematic error associated with it, and the combination of them results in the total systematic uncertainty of the jet E_T measurement.

5.2.4 Missing Transverse Energy

The so called "missing transverse energy" or $\not\!\!E_T$ is a reconstructed object that is not directly related to a single particle produced in a collision. Considered as a two-component vector that lies in the plane transverse to the beam direction it is simply the negative of the sum of all transverse momenta in the event. More precisely, the uncorrected $\not\!\!E_T$ is the negative of the vector sum of all calorimeter tower depositions projected on the transverse plane. The missing energy is often thought of as a measure of the sum of the momenta of the particles that escape detection, most notably neutrinos. In order to be more readily interpretable as such the raw $\not\!\!E_T$ needs to be corrected:

$$\not\!\!E_T^{\rm corr} = \not\!\!E_T^{\rm raw} - \sum_{\rm jets} \left(E_{T\rm jet}^{\rm corr} - E_{T\rm jet}^{\rm raw} \right), \tag{5.6}$$

where $E_{T\rm jet}^{\rm corr}$, $E_{T\rm jet}^{\rm raw}$ are transverse energy of jets before and after the jet energy correction, $\not\!\!E_T^{\rm raw}$ is a raw level missing E_T defined as:

$$\not\!\!E_T^{\rm raw} = - \sum_{i \in {\rm tower}} E_T^{(i)}, \tag{5.7}$$

where $E_T^{(i)}$ is transverse energies of any calorimeter towers.

5.2.5 b-Tagging - Displaced Secondary Vertex algorithm

Physics processes that have jets in the final state have a huge amount of QCD light flavor jet background. Since the SM top quark decays to a W boson and a b quark the ability to identify jets originating from a b-quark is critical for the background reduction. The b-tagging algorithm used in this analysis, SecVTX [82], exploits the long lifetime of the b quark by identifying decay vertices significantly displaced from the primary interaction point.

The relatively long b-lifetime means that the B hadrons formed during the hadronization of the initial b-quark can travel a significant distance before decaying into a collection of lighter hadrons. This distance is given by $L = \beta c \tau'$, where β is the velocity $\beta \sim 1$ and τ' is the proper life time ($\tau' = \tau\gamma$).

The average transverse distance traveled by the B hadron is $L_T \sim 6.8$ mm at Tevatron energies. The decay point can be reconstructed in the micro-strip silicon detector by identifying tracks which form a secondary vertex significantly displaced from the primary $p\bar{p}$ interaction point (primary vertex).

SecVTX b-tagging is performed per jet for all of the jets in an event by using only the tracks which are within a jet cone of $\Delta R = 0.4$ for each jet. Poorly reconstructed tracks[1] are not used for SecVTX finding. To find secondary vertices, at least two tracks with good quality are necessary. Displaced tracks in jets, which are determined by impact parameter significance defined as $|d_0/\sigma_{d_0}|$ where d_0 and σ_{d_0} are the impact parameter and the total uncertainty from tracking and beam position measurements, are used for the SecVTX reconstruction. Secondary vertices are looked for and reconstructed by a two-pass approach.

Pass 1: At least three tracks are required to pass loose selection criteria ($P_T > 0.5$ GeV/c, $|d_0/\sigma_{d_0}| > 2.0$), and the secondary vertex is reconstructed out of the selected tracks. One of the tracks used in the reconstruction is required to have $P_T > 1.0$ GeV/c^2.

Pass 2: Exactly two tracks are required to pass tight selection criteria ($P_T > 1.0$ GeV/c, $|d_0/\sigma_{d_0}| > 3.5$. the tracks must have $P_T > 1.5$ GeV/c). The secondary vertex is reconstructed from the two tracks.

Only when **Pass 1** fails, **Pass 2** is applied. If either attempt is successful, the transverse distance L_{xy} from the primary vertex of the event is calculated along with the associated uncertainty on L_{xy}, which we denote $\sigma_{L_{xy}}$. Finally jets are tagged positively or negatively depending on $L_{xy}/\sigma_{L_{xy}}$ (L_{xy} significance)[83]:

$$L_{xy}/\sigma_{L_{xy}} \geq 7.5 \quad \text{(positive tag)} \tag{5.8}$$

$$L_{xy}/\sigma_{L_{xy}} \leq -7.5 \quad \text{(negative tag)} \tag{5.9}$$

The sign of L_{xy} indicates the position of the secondary vertex with respect to the primary vertex along the direction of the jet as illustrated in Figure 5.1. If the angle between the jet direction and the vector pointing from primary vertex to the secondary vertex is less than $\pi/2$, L_{xy} is positively defined. Otherwise, it becomes negative. If L_{xy} is positive, the secondary vertex points towards the direction of the jet. This is consistent with a B hadron traveling from the primary vertex in the direction of the jet. Positive L_{xy} is preferred in realistic B hadron decays. For negative L_{xy}, the secondary vertex points away

[1] Transverse momentum, the number of silicon hits attached to the tracks, quality of those hits, and $\chi^2/N_{\rm DOF}$ of tracks are used to determine if the track is good or poor.

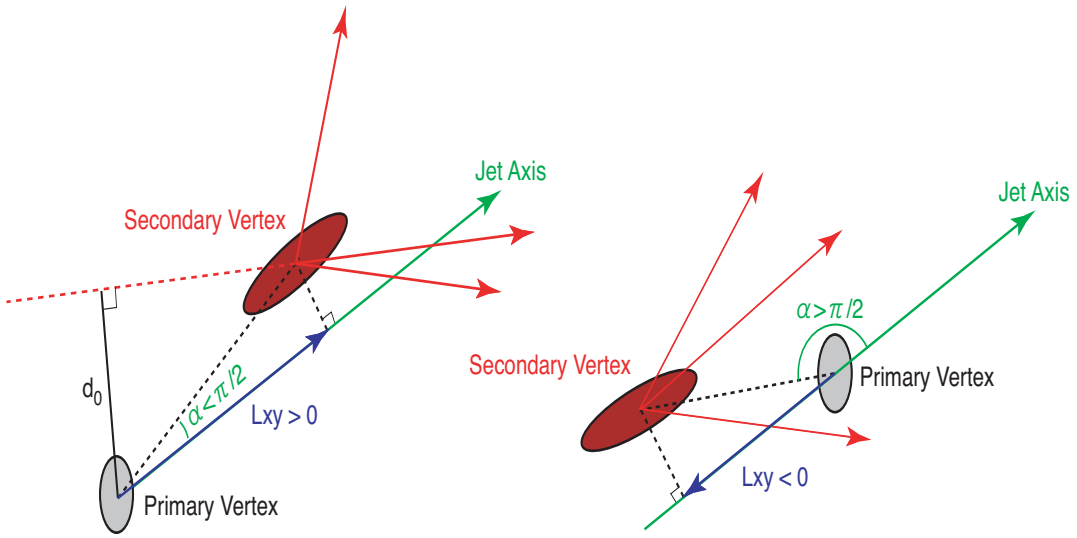

Figure 5.1 Cartoon showing true reconstructed secondary vertex ($L_{xy} > 0$, left) and fake one ($L_{xy} < 0$, right).

from the jet which may only happen by coincidence or as a result of mis-measured tracks. Additionally, in order to reject secondary vertices resulting from material interaction, secondary vertices must satisfy the following requirements:

- **Pass 2** vertices found between 1.2 and 2.5 cm from the center of SVX[2] are vetoed.
- All vertices with a radius greater than 2.5 cm with respect to the center of the SVX are vetoed.

The negative tags are useful for evaluating the rate of false positive tags, which is denoted as "mistag" in this thesis.

The SECVTX tag efficiency depends strongly on the jet kinematics (E_T and η). These jet properties will clearly vary depending on the physics process one considers. b-tagging efficiencies are calculated as functions of the E_T and η of the jets using $t\bar{t}$ Monte Carlo(MC) sample as shown in Figure 5.2. MC b-jets are not guaranteed to perfectly match data b-jets. So it is necessary to construct a data-to-Monte Carlo scale factor for tag efficiency, which encapsulates the discrepancies between b-jet tagging in MC and in data.

$SF_{\rm btag} = \epsilon_{\rm data}/\epsilon_{\rm MC}$. The scale factor is obtained as [106] :

$$SF_{\rm btag} = 0.89 \pm 0.07. \tag{5.10}$$

[2]Some care must be taken since CDF origin is taken to be the center of the COT which is not the origin of the SVX (the SVX center is shifted approximately (-1mm,+1mm) with respect to the COT origin.)

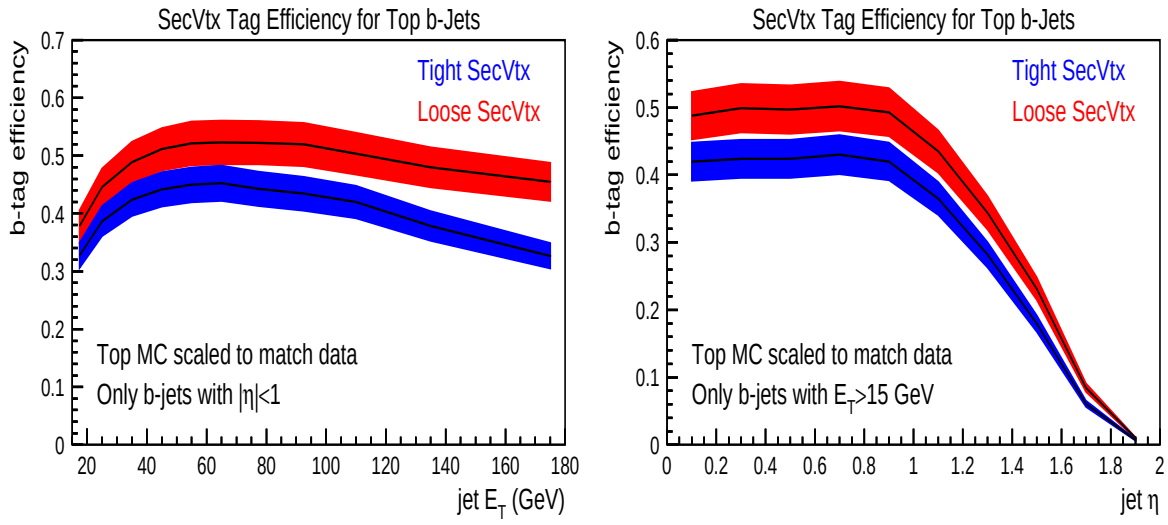

Figure 5.2 b-tagging efficiencies as functions of E_T(left) and η(right) of jets. Only jets which were b-quarks at the parton level are used for the calculation. Two SecVTX tagging conditions, "Tight" and "Loose" are shown. The bands associated with black lines show the total systematic uncertainty.

The tagging criteria used in this thesis is called "Tight SecVTX" [84]. A "Loose" tagging also exists, which requires looser criteria on the tagging variables.

5.3 Event Selection

The final event selection for the W helicity measurement is based on the $t\bar{t}$ cross section measurement [85]. In order to minimize the backgrounds a cut on the scalar sum of the transverse energies of all reconstructed objects in the event ($H_t > 200$ GeV) is required. The lepton+jets signature in the detector requires the reconstruction of at least four energetic jets, one isolated lepton and missing E_t due to the neutrino coming from the leptonic decay of the W boson. High P_T electron and muon triggers are used and additional offline selection criteria are imposed.

5.3.1 Triggers

High-P_T Electron Trigger

At the Level 1 trigger, calorimeter towers are gathered in pairs so that the effective $\eta \times \phi$ segmentation is $0.2 \times 15°$. At least one trigger tower is required to have $E_T > 8$ GeV with $E_{\rm HAD}/E_{\rm EM} < 0.125$. At least one XFT track with $P_T > 8$ GeV/c is also required

to point to this tower. At Level 2, a clustering algorithm combines the energy deposited in neighboring towers. Towers adjacent to the seed tower found at Level 2 with $E_T >$ 7.5 GeV are added to the cluster. The total E_T of the cluster must be larger than 16 GeV. At Level 3, the full event reconstruction and electron identification are performed. A three dimensional COT track of $P_T > 9$ GeV must point to a cluster of $E_T > 18$GeV with $E_{\mathrm{HAD}/E_{\mathrm{EM}}} < 0.125$. This trigger is denoted by "`ELECTRON_CENTRAL_18`".

High-P_T Muon Trigger

CMUP : At Level 1, hits in the CMP to match hits in the CMU are required. An XFT track with $P_T > 4$ GeV/c must point to the CMU and CMP hits. At Level 2, an XFT track with $P_T > 8$ GeV/c, which does not necessarily match the muon hits, must exist. At Level 3, a fully reconstructed COT track with $P_T > 18$ GeV/c must match a stub in the CMU($|\Delta x|_{\mathrm{CMU}} < 10$ cm) and in the CMP($|\Delta x|_{CMP} < 20$ cm). This trigger is called "`MUON_CMUP18`".

CMX : At Level 1, CMX hits must match the central muon extension scintillator hits and an XFT track with $P_T >$8 GeV/c. At Level 2, no requirement is imposed. At Level 3, a fully reconstructed COT track with $P_T > 18$ GeV/c must match a stub in the CMX($|\Delta x|_{\mathrm{CMX}} < 10$ cm). This trigger is called "`MUON_CMX18`".

5.3.2 Offline Selection

To select candidate $t\bar{t}$ events in the lepton+jets channel, the following criteria are imposed:

- Data quality:
  Data collected using the silicon detector components must be of good quality [86], based on the conditions of each component of detectors.

- Trigger:
  Data must be triggered by the specific triggers discussed in the previous section.

- Presence of exactly one primary lepton($e^{\pm}/\mu^{\pm}$):
  The leptonic decay of the W boson produces exactly one high P_T lepton, which must be identified by the criteria discussed in Sections 5.2.1 and 5.2.2. If there exist more than one lepton such events are vetoed.

- Distance between the primary vertex and the vertex of lepton track:
  · $|z_{\text{lepton track}} - z_0| < 5$ cm
  If the lepton comes from the interaction point(primary vertex, z_0), the vertex position of the lepton track($z_{\text{lepton track}}$) should be close to primary vertex.

- Z^0 removal:
  If a lepton is not identified correctly, for example isolated tracks, $Z^0 \to \ell\bar{\ell}$ events still remain. To remove such events, the invariant mass of the lepton and other objects(X) must not be in the Z^0-boson mass window($76 < m_{\ell X} < 106$ GeV/c^2).

- Significant missing E_T:
  $\cdot \not\!\!E_T > 20$ GeV
  The neutrino from W-boson decay is expected to have large missing transverse energy.

- Jet:
  $\cdot E_T > 15$ GeV
  $\cdot |\eta| < 2.0$
  The target process considered in this thesis contains at least four energetic jets in the central part of the detector. Thus the jets are expected to have large transverse energy and they are required to be in the SVX coverage for SecVTX b-tagging.

- $H_t > 200\ GeV$:
  In order to further reduce the QCD background, the scalar sum of transverse energies of the reconstructed objects has to be greater than 200 GeV.

- b-tagging:
  To increase the purity of b-tagged events, at least one SecVTX b-tagged jet is required.

5.4 Top Quark Reconstruction

Once the full selection is applied and events with a typical characteristic of $t\bar{t}$ production in the lepton+jets channel remain, the final objects can be reconstructed - one isolated lepton, four or more energetic jets and missing E_t. The task now is to choose the correct assignment between those reconstructed objects and the partons from which they originate. In total there are 24 different ways to assign these objects to the partons - 12 different ways of matching the four leading jets to the four partons times the two possible solutions for the z-component of the neutrino. We do not know with certainty which combination is correct.

The first step in order to reduce the number of possible combinations is to be consistent with the b-tagging information we have. Since we require that at least one of the jet we find is tagged as a b-jet, we can assign it only to the b-quarks. This reduces the number of possibilities from 24 to 12.

To further reconstruct the top quarks a kinematic fitter is used. It is the same fitter used in the CDF top mass analysis [87] where the following χ^2 is minimized using the Minuit package [88]:

$$\chi^2 = \sum_{i=l,4\ jets} \left(\frac{P_T^{i,fit} - P_T^{i,measured^2}}{\sigma_i} + \frac{M_{jj} - {M_W}^2}{\Gamma_W^2} + \frac{M_{l\nu} - {M_W}^2}{\Gamma_W^2} + \frac{M_{bjj} - {M_t}^2}{\Gamma_t^2} + \frac{M_{bl\nu} - {M_t}^2}{\Gamma_t^2}\right) \tag{5.11}$$

where σ_i are the P_T resolutions of the lepton and the four leading jet in the event, which are P_T dependent functions [89]; M_{jj} is the sum of the jet 4-vectors, M_t is a free parameter taken as the reconstructed top mass after the χ^2 is minimized. The widths of the W and the top are fixed to be $\Gamma_W = 2.5\ GeV$ and $\Gamma_t = 1.5\ GeV$. The mass of the t-quark and the and the mass of the $\bar{t}$-quark are required to be identical. The jet energy corrections described in 5.2.3 are applied to the jets used by the kinematic fitter. In addition, several special corrections - "top specific corrections" [90], are applied. The top specific corrections take into account the flavor and topology of $t\bar{t}$ events. They strongly depend on the P_T spectrum of the jets and yield a better resolution performance in the reconstruction of W and top mass by folding in the information of the P_T spectrum of the jets from $t\bar{t}$ events. For example - the final state of $t\bar{t}$ events always include b-jets, which contain muons and neutrinos that can be partially undetected. Thus the b-jet energy is underestimated.

With the corrected jet energies, all jet-parton assignments consistent with the b-tagging information are tried and the combination which yield the lowest kinematic fit χ^2 is used. No χ^2 requirement is made. Studies using pseudo-experiments indicated that there was no significant gain in statistical sensitivity from applying such a cut.

To quantify the performance of the kinematic fitter, we defined the correct permutation, by constructing the distance, $\Delta(R)$, between tree-level information and reconstructed objects. We use the sum of the distances of partons and leptons to the reconstructed jets and leptons. The neutrino is not considered. The permutation which is closest to its tree-level objects is called the "best match". The distribution of $\Delta(R)$ for the best match is shown in Figure 5.3.

In this analysis we select the permutation with the lowest χ^2 solution and sort a vector of all permutation according to their χ^2. In this way, each permutation has an index, its place in the vector. The "best χ^2" permutation always has index=0. The two plots in Figure 5.4 show the index of the "best match". The ratio of entries in the first bin to all entries gives the efficiency of finding the best match. We get an efficiency of 33.2% to find the best match and an efficiency of 36.4% to find the best match when the best match of the lepton and the b on the leptonic side of the decay is required.

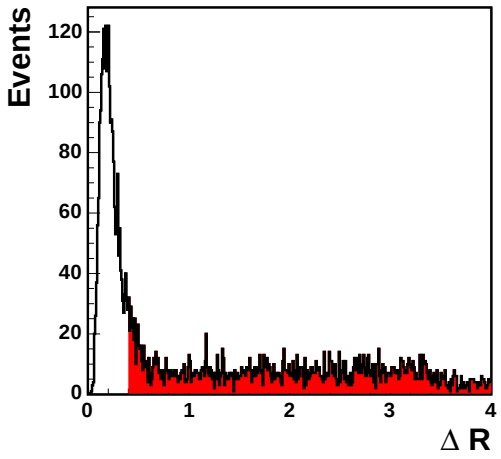

Figure 5.3 Distance between tree-level information and reconstructed object. For events with $dR > 0.4$ no correct match can be assigned.

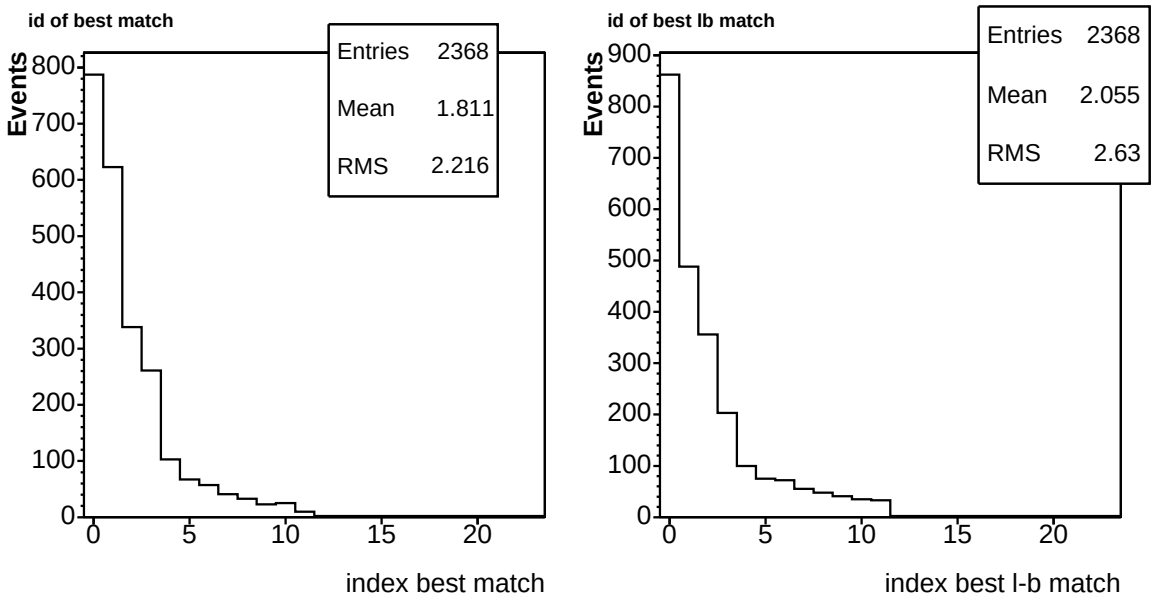

Figure 5.4 The performance of the top-quark reconstruction. The left plot shows the index of the best combination in a list of combinations sorted by χ^2 for the permutation chosen as the "best match". The plot on the right shows the performance when sorting by χ^2 the list of the "best lepton-b match" combinations.

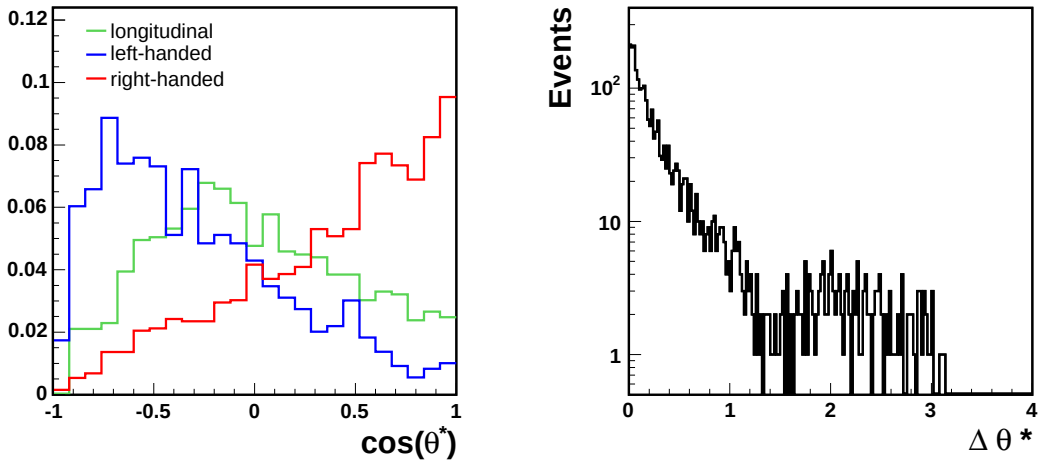

Figure 5.5 Reconstructed $\omega(\theta^*)$ distribution for longitudinal, right- and left-handed W boson decays (left). The absolute value of the difference between tree level value and the reconstructed value for θ^* in a Standard Model $t\bar{t}$ sample is shown in the right plot.

We fully reconstruct the $cos\theta^*$ from the four vectors of the lepton, jets and missing transverse energy returned by the kinematic fitter. Figure 5.5 shows the reconstructed $\omega(\theta^*)$ distribution for longitudinal, right- and left-handed W boson decays. Also shown is the difference between the tree level value and the reconstructed value for θ^* in a Standard Model $t\bar{t}$ sample.

Other analyses for a determination of the W helicity fractions and searches for a V+A current have been performed in CDF, using other discriminating variable like the P_T spectrum of the charged lepton from the W decay or the invariant mass of the charged lepton and the b quark in the laboratory [91, 92].

Those analyses do not require a full reconstruction of the event and therefore are 'simpler'. We chose to pursue this method, which requires a full reconstruction of the event, because we thought it would offer particular advantages over others that would offset the drawbacks.

The reason we chose for this measurement a method which requires a full reconstruction of the event is that it makes the most efficient use of all the inforamtion in the event.

in particular, although less-simple, it does make better use of the information available - this is evident in the fact that while the analysis using the invariant mass of the lepton and the b quark (M_lb) [92] uses about three times more events than we do, we have the same expected statistical uncertainty on the right-handed fraction. The second reason we use it is that it has a very reduced dependence on the top mass and jet energy scale

(JES). The reason is that this analysis calculates a real angle, determined (roughly) by ratios of jet-energies. So changes in jes and top mass only matter to the extent that they make the kinematic fitter choose a different combination. This is an important point, for this analysis the top mass has a second order effect. The left-handed, right-handed, and longitudinal templates are the same for all top masses - they're driven by the W helicity. This makes sense because the matrix elements themselves are independent of top mass. The top mass only dictates how these 3 templates get mixed together. For the $M_l b$ analysis the effect is much bigger. Our JES systematics are also smaller 0.010 when being conservative (we verified this sysatematic is indepent of f+, we get something around 0.003 for most values we checked for f_+ and round to 0.01), while the $M_l b$ method has a JES systematic of 0.033.

Chapter 6

Background

There could be different processes which would result with the same final state signature in the detector as the signature of the target process. Understanding the different background sources and estimating their contribution is crucial in order to correctly interpret what is observed in the measurement. The final state of the Lepton+Jets sample in $t\bar{t}$ events includes four or more energetic jets, one isolated lepton and missing E_T.

The contribution of background processes is estimated mainly from W+jets production. The different sources and their contributions in the selected data sample used in this analysis are based on the measurement of the $t\bar{t}$ production cross-section in SECVTX tagged lepton+jets events [78], and are discussed below.

6.1 Background Categories

The background consists of all possible physics processes except the target process. In order to estimate the number of $t\bar{t}$ events in the selected sample the following background processes have been considered:

- Non-W QCD:
  Events where the lepton is faked by a QCD jet or comes from semileptonic decay of heavy flavor jet.

- Mistag:
  Events that have jets falsely b-tagged by SECVTX due to vertex and track resolution and reconstruction errors.

- W+ heavy flavor:
  $Wb\bar{b}$, $Wc\bar{c}$ and Wc processes at parton level where a c or b jet is tagged by the SECVTX.

- Events originating from single top and diboson ($WW/WZ/ZZ$) processes.

In the following subsections, each of the contributions to the background is discussed in detail.

6.1.1 Non-W QCD

Jet events sometimes mimic the W-boson signature when a jet passes the lepton selection criteria based on calorimeter information, or a heavy flavor jet produces leptons via semileptonic decays. Also a large $\not\!\!E_T$ derived from mismeasurements of energy or semileptonic decays of heavy flavor jet can be obtained. It is difficult to model and produce such an event in detector simulation since the heavy flavor content cannot be well predicted. Generally, non-W events mainly come from a non-isolated lepton[1] and small $\not\!\!E_T$. Such an event is used to extrapolate the expected non-W contribution in signal region, e.g. good lepton isolation and large $\not\!\!E_T$. Accordingly, the lepton isolation vs. $\not\!\!E_T$ plane is divided into 4 sectors (shown in Figure 6.1)[93, 94]:

- region A: Isolation > 0.2 and $\not\!\!E_T <$ 15 GeV
- region B: Isolation < 0.1 and $\not\!\!E_T <$ 15 GeV
- region C: Isolation > 0.2 and $\not\!\!E_T >$ 20 GeV
- region D: Isolation < 0.1 and $\not\!\!E_T >$ 20 GeV

Region D is the signal region. The $\not\!\!E_T$ vs. isolation distribution obtained from high-P_T electron and muon samples are shown in Figure 6.2. For an extraction of non-W background from data, we make two assumptions:

- The lepton isolation and $\not\!\!E_T$ are uncorrelated in non-W events
- The b-tagging rate does not depend on missing E_T in non-W events

The lepton and the missing E_T in non-W events are not real, therefore there is no reason to apply corrections for them.

With the first assumption, the number of non-W events($N_D^{\text{non}-W}$) and its fraction($f_{\text{non}-W}$) in the signal region before requiring b-tagging are obtained as:

$$N_D^{\text{non}-W} = \frac{N_B \times N_C}{N_A}, \tag{6.1}$$

$$f_{\text{non}-W} = \frac{N_D^{\text{non}-W}}{N_D} = \frac{N_A \times N_B}{N_C \times N_D}, \tag{6.2}$$

[1] Object that passes all of the lepton identification criteria except for isolation requirement.

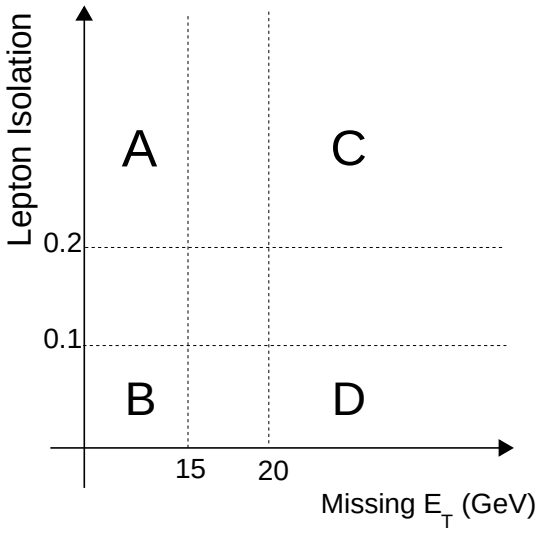

Figure 6.1 Missing E_T and lepton isolation plane divided into four sectors for non-W background estimation.

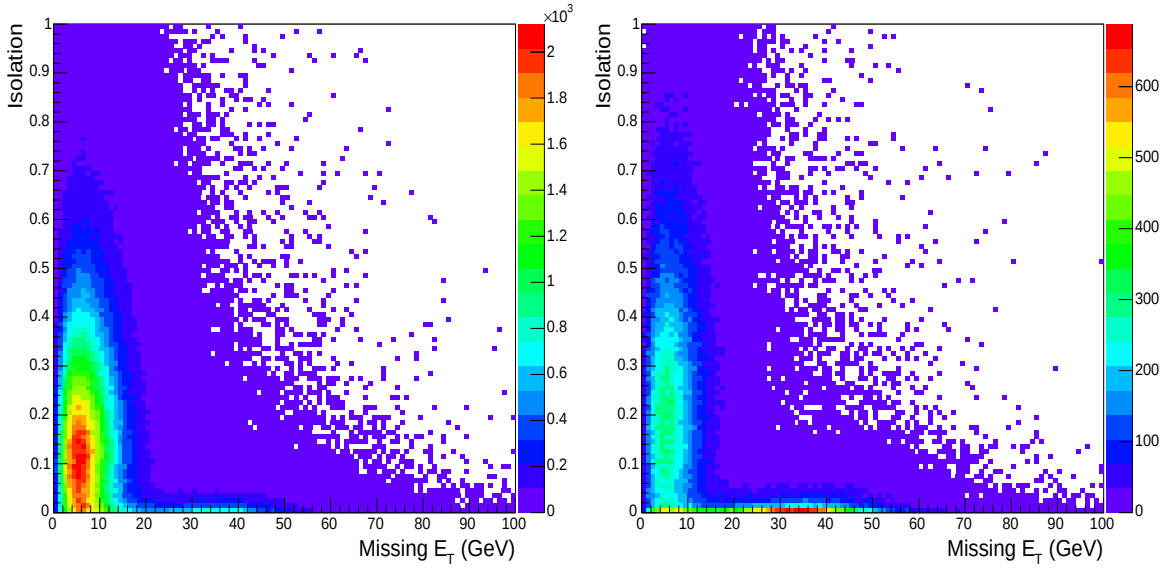

Figure 6.2 $\not\!\!E_T$ vs lepton isolation distributions in high-P_T electron(left) and muon(right) samples associated with at least one jet before applying SECVTX b-tagging.

where N_i $(i = A, B, C, D)$ are the number of pre-tag[2] events in each side-band region. In accordance with the second assumption, the SECVTX b-tagging efficiency obtained in region B can be applied to the signal region D. Here we define an event tagging efficiency per taggable jets as:

$$r_B = \frac{N_B^{(\text{tagged event})}}{N_B^{(\text{taggable jet})}}, \tag{6.3}$$

where $N_B^{(\text{tagged event})}$ and $N_B^{(\text{taggable jet})}$ are the numbers of tagged events and taggable jets in region B respectively. Then the number of non-W background in region D after SECVTX b-tagging($N_D^{+\text{non}-W}$) is obtained by the relation:

$$N_D^{+\text{non}-W} = f_{\text{non}-W} \times r_B \times N_D^{(\text{taggable jets})}. \tag{6.4}$$

This procedure is called "Tag Rate Method" since it uses the tag rate in region B. It is also possible to estimate non-W contribution directly from the SECVTX tagged sample as:

$$N_D'^{+\text{non}-W} = \frac{N_B^+ \times N_C^+}{N_A+}, \tag{6.5}$$

where $N_X^+(X = A, B, C, D)$ denotes positive SECVTX b-tagged events, and this method is called the "Tagged Method". These methods are data-based techniques, so the estimates could also contain other background processes. Subtracting the known backgrounds should result in a better non-W QCD estimate. The contributions from $t\bar{t}$ and W+jets events to each sideband region are studied in [93, 94], and their contributions from $t\bar{t}$ and W+jets events to each side band region are subtracted.

For a validation and estimation of systematic uncertainties of the four sector method, the following sectors are considered:

- region A: Isolation > 0.2 and $\not\!\!E_T <$ 15 GeV
- region E: $0.1 <$ Isolation < 0.2 and $\not\!\!E_T <$ 15 GeV
- region C: Isolation > 0.2 and $\not\!\!E_T >$ 20 GeV
- region F: $0.1 <$ Isolation < 0.2 and $\not\!\!E_T >$ 20 GeV
- region A'': Isolation > 0.1 and $\not\!\!E_T <$ 10 GeV
- region A' : Isolation > 0.1 and $10 < \not\!\!E_T <$ 20 GeV
- region B'': Isolation < 0.1 and $\not\!\!E_T <$ 10 GeV

[2]Pre-tag means before b-tagging

- region B' : Isolation < 0.1 and $10 < \not\!\!E_T < 20$ GeV

These regions are slightly different and are used as a check of the stability and systematic uncertainty when boundaries of the four sectors are varied. The ratios of $G = (N_E \cdot N_C)/(N_A \cdot N_F)$ and $G' = (N_{B''} \cdot N_{A'})/(N_{A''} \cdot N_{B'})$ are calculated for both the pretag and the tagged samples. Here region F and B' are the isolation and missing E_T side band region. If the extrapolations from isolation and missing E_T are valid, the fractions of G and G' should be equal to unity. The deviations from unity is assigned as a systematic uncertainty. For both of pretag and tagged estimate, a 25% systematic uncertainty is assigned.

After obtaining the estimates independently with the tag rate method and tagged method, the two results are combined by making a weighted average. At first the estimates over the different detector components for each method are added, then these two methods are combined.

6.1.2 Mistag

The rate of SECVTX mistag or false tagged jets is derived from generic jet sample varying bins of η, ϕ, jet E_T, track multiplicity within an event[95]. Tag rate probabilities are summed for all of the taggable jets in the event. Since the double mistag rate is small, this sum is a good approximation of the single-tag event rate. Negative mistags, tags with unphysical negative decay length due to finite tracking resolution or reconstruction errors, are calculated as an estimate of falsely tagged jets, independent to first order of the heavy flavor content in the generic jet sample. A systematic uncertainty of 8% is assigned to this estimation [98]. The positive mistag rate is enhanced relative to the negative tag rate by light-flavor secondary vertices and material interactions in the silicon detectors. As a result, the positive mistag rate is estimated by multiplying the negative mistag rate by a factor of 1.37 ± 0.15 [97]. For data collected after December 2004, an additional correction factor of 1.05 ± 0.03 is applied [98]. The final mistag estimate is corrected for the non-W QCD fraction and $t\bar{t}$ contribution to the pretag sample.

6.1.3 W+Heavy Flavor

The $Wb\bar{b}$ and $Wc\bar{c}$ states are other sources of background of b-tags in the lepton+jets channel. Their contributions are estimated primarily from Monte Carlo, but their overall rates are normalized to data, because MC generators predict W+jets events only to leading order diagrams. As a result, large theoretical uncertainties exist for overall normalization. The contribution from true heavy flavor production in W+jet events is

determined from measurements of the heavy flavor event fraction in W+jet events and the tagging efficiency for these events.

These heavy flavor fractions have been studied extensively [99] using ALPGEN + HERWIG Monte Carlo[100, 101]. Heavy flavor fractions measured in ALPGEN have been calibrated using a jet data sample. A scaling factor of 1.5 ± 0.4 is found to be necessary in order to match the heavy flavor production in Monte Carlo and in the data.

For the tagged W+HF background estimate, the heavy flavor fractions and tagging rates are multiplied by the number of pre-tag events in the data, after the number of pretag events have been corrected for the non-W contribution. The W+HF background must also be corrected for the contribution of $t\bar{t}$ events to the pretag sample.

The number of events estimated to be W+HF background is obtained by the following relation:

$$N_{W+HF} = f_{HF} \cdot \epsilon_{\text{tag}} \cdot [N_{\text{pretag}} \cdot (1 - f_{\text{non}-W}) - N_{\text{EWK}}], \tag{6.6}$$

where f_{HF} is the heavy fraction, ϵ_{tag} is tagging efficiency and N_{EWK} is the expected number of $t\bar{t}$, single top and diboson events.

6.1.4 Single top and diboson

Other small contributions (see table 6.2) come from diboson events and single top production. The normalization of the diboson and single top backgrounds are based on the theoretical cross sections listed in Table 6.1 [102–105], the measured luminosity and the acceptance and b-tagging efficiency derived from MC. The MC acceptance is corrected for lepton identification, trigger efficiencies and the z vertex cut. The tagging efficiency is always corrected by the scale factor (MC/data) of $0.89 \pm 0.01(stat) \ \pm 0.07(syst.)$ [106] . The expected number of events is obtained by:

$$N = \int \mathcal{L}dt \times \epsilon \times \sigma, \tag{6.7}$$

where ϵ is the total detection efficiency corrected by all of the scale factors.

6.2 Summary of Background Estimate

The individual background sources to the final background estimate have been described above. The observed data and the Standard Model background expectations are consistent. In order to measure the W boson helicity in top quark decay, events that fall in the bin of 4 or more jets were analyzed. Figure 6.3 summarizes the results of the $t\bar{t}$ lep-

Theoretical Cross Sections	
WW	12.40 $\pm$ 0.8 pb
WZ	3.96 $\pm$ 0.06 pb
ZZ	1.58 $\pm$ 0.02 pb
Single Top s-channel	0.88 $\pm$ 0.05 pb
Single Top t-channel	1.98 $\pm$ 0.08 pb
$Z \to \tau\tau$	320 $\pm$ 9.0 pb
$t\bar{t}$	$6.7\ ^{+0.7}_{-0.9}$ pb

Table 6.1 Theoretical cross sections and errors for the electroweak and single top backgrounds, along with the theoretical cross section for $t\bar{t}$ at (m_t = 175GeV/c^2). The cross section of $Z^0 \to \tau\tau$ is obtained in the dilepton mass of $m > 30$ GeV/c^2 together with k-factor(NLO/LO) of 1.4.

ton+jets cross section measurement [78] in the different jet bins, where the background content of each been is shown. These estimates are for events with at least one b-tagged jet and a cut on $H_t > 200\ GeV$. This cross section measurement was performed using 695 pb^{-1} of data, the background content of the $N_{jets} \geq 4$ is listed in table 6.2. To get an estimation of the backgrounds for the 955 pb^{-1} data set, each of these background estimations was scaled according to the method used to extract it. The background estimations for the 955 pb^{-1} are listed as well in table 6.2.

	Sample Size	
	695 pb^{-1}	955 pb^{-1}
source	N($\geq$ 4 jet)	N($\geq$ 4 jet)
Mistag	6.6 ± 1.0	9 ± 1.4
W+h.f.	5.2 ± 1.5	6.4 ± 1.9
Single top	0.4 ± 0.1	0.6 ± 0.2
Diboson	1.0 ± 0.2	1.4 ± 0.3
QCD	4.1 ± 0.8	5.5 ± 1.1
Total	17.2 ± 1.9	22.8 ± 2.5
Data	158	220

Table 6.2 Expected number of background events and the number of observed events in the 695 pb^{-1} data set and the scaling to the 955 pb^{-1} data set, using the selection criteria described in reference [85], including the H_T requirement and demanding at least four tight jets.

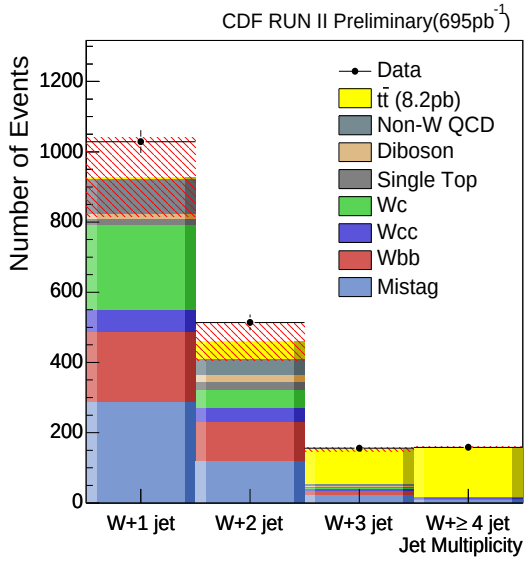

Figure 6.3 The expected number of W+jets events with at least one SECVTX b-tagged jet and a $H_t > 200\ GeV$ cut.

Chapter 7

$cos\theta^*$ templates

The measurement of the longitudinal and right-handed fractions of W boson helicity in top quark decays is made via the analysis of the angular distribution of $cos\theta^*$ - the angle between the charged lepton coming from the W decay and the W flight direction in the rest frame of the top quark. Due to background, reconstruction and acceptance effects the measured distribution of $\cos\theta^*$ differs from $\omega(\cos\theta^*)$ presented in chapter 3. However, the shape of the reconstructed $\cos\theta^*$ distribution depends on f_0, f_- and f_+ and can therefore be used to extract these helicity state fractions. The strategy of the measurement presented here is to fully reconstruct $t\bar{t}$ events and determine the $\cos\theta^*$ distribution, and then to use a template method to determine the longitudinal and right-handed fractions.

The templates are constructed from a fit to the $cos\theta^*$ distributions in fully reconstructed MC events, after applying all selection criteria described in chapter 5.

The samples used as signal MC and background MC in which we look at the $cos\theta^*$ shape are also described in this chapter.

7.1 Signal samples

7.1.1 GGWIG - a modified version of HERWIG

Currently, all MC generators used to study $t\bar{t}$ events at CDF assume SM coupling of the tWb vertex. We used a modified version of the Herwig Monte Carlo called *GGWIG*, which allows one to change the W helicity fractions [107].

Samples of $t\bar{t}$ production with a top mass of 175 GeV and a fixed helicity for the leptonic decay were generated[1]. Data set names, sample sizes and the acceptances for

[1]Studies have shown that the fixed top mass for constructing the templates does not have a significant effect on this measurement. See Section 9.2

the event selection are listed in table 7.1.

process	sample	generator	size	acceptance
$t\bar{t}$ $M_t = 178\ GeV$	ttopel	pythia	1.2M events	0.0273 ± 0.0004
$t\bar{t}$ $M_t = 175\ GeV$	ttopvl	pythia	1M events	0.0296 ± 0.0002
W^+ left handed $M_t = 175\ GeV$	utop0i	GGWIG	92500 events	0.073 ± 0.002
W^+ right handed $M_t = 175\ GeV$	utop1i	GGWIG	0.1M events	0.097 ± 0.002
W^+ longitudinal $M_t = 175\ GeV$	utop2i	GGWIG	90000 events	0.088 ± 0.002
W^- left handed $M_t = 175\ GeV$	utop4i	GGWIG	95000 events	0.083 ± 0.002
W^- right handed $M_t = 175\ GeV$	utop3i	GGWIG	0.1M events	0.106 ± 0.003
W^- longitudinal $M_t = 175\ GeV$	utop5i	GGWIG	85000 events	0.097 ± 0.003

Table 7.1 Summary of the Monte Carlo $t\bar{t}$ signal samples used in the analysis.

7.1.2 Pythia samples

To validate the GGWIG samples, as well as the likelihood fitter performance, generic $t\bar{t}$ Pythia Monte Carlo samples, listed in table 7.1, were used. In these samples the W helicity fractions are these of the SM.

7.1.3 GGWIG validation

The GGWIG samples were validated both in comparison to data and to Pythia Monte Carlo. The samples were simulated and reconstructed using the 5.3.4 CDF offline version. Figures 7.1 and 7.2 show the distributions of some kinematic variables in the data and the GGWIG MC. In these plots GGWIG is a mix of events from the samples of left-handed and longitudinal W bosons in proportion to the SM expectations. Figure 7.3 shows the comparison of GGWIG and PYTHIA.

7.2 Background samples

The processes used to model the background in the analysis are listed in Table 7.2 together with the data set names, the total number of events, and the acceptance after all of the selection criteria.

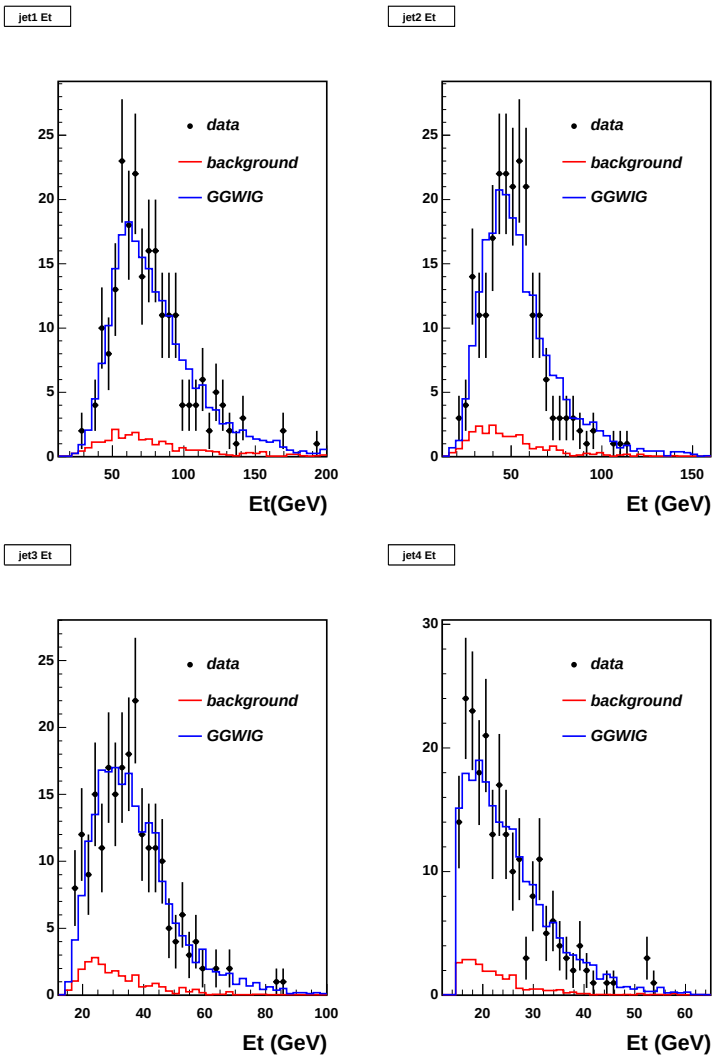

Figure 7.1 Jet E_T distributions for events passing the selection for data together with SM signal and background. The four plots refer to the four leading jets in the event. The upper-left plot is for the leading jet, the upper-right plot for the second leading jet and the bottom plots show the E_T distribution for the third (left) and fourth (right) leading jets.

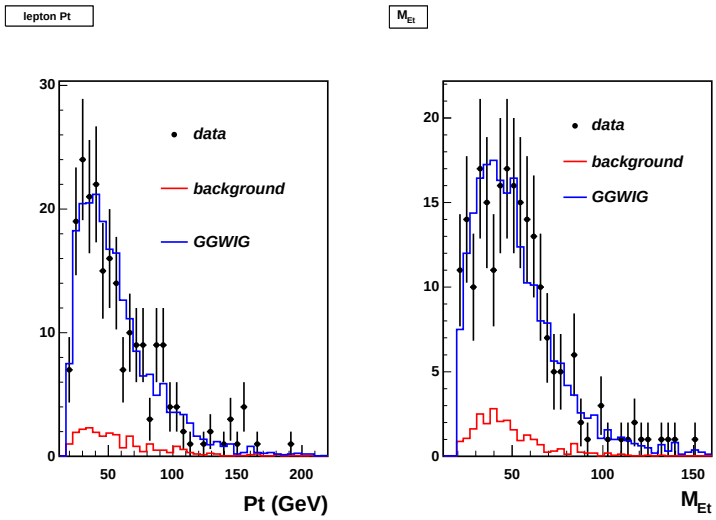

Figure 7.2 The left plot shows the P_T of the lepton for data in the signal region and for MC. The right plot shows the distribution of the missing E_T.

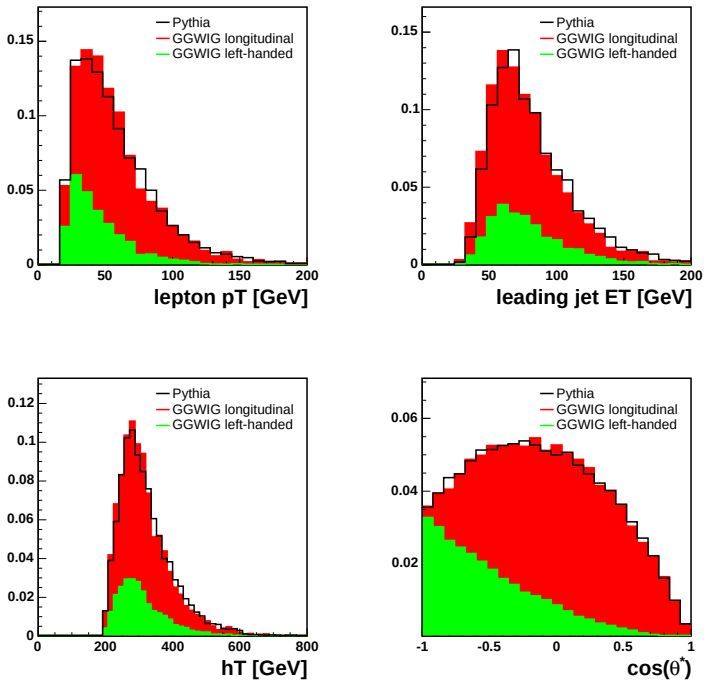

Figure 7.3 SM mixture of the GGWIG samples in comparison with Pythia: the P_T of the lepton (up left), E_T of the leading jet (up right), H_t (bottom left) and the $cos\theta^*$ distribution at the particle level (HEPG).

process	sample	generator	size	acceptance
$W(e)4p$	atop7a	Alpgen+Herwig	0.2M events	$0.00040 \pm 4 \cdot 10^{-5}$
$W(e)4p$	ltop4n	Alpgen+Herwig	0.5M events	$0.00040 \pm 4 \cdot 10^{-5}$
$W(\mu)4p$	atopfb	Alpgen+Herwig	0.2M events	$0.00044 \pm 8 \cdot 10^{-5}$
$W(\mu)4p$	ltop4m	Alpgen+Herwig	0.5M events	$0.00065 \pm 7 \cdot 10^{-5}$
$W(e)b\bar{b}+2p$	ltop2b	Alpgen+Herwig	0.5M events	0.0054 ± 0.0001
$W(\mu)b\bar{b}+2p$	ltop5b	Alpgen+Herwig	0.5M events	0.0038 ± 0.0001
WW	wtop1w	Pythia	0.4M events	$(7 \pm 1) \cdot 10^{-5}$
WW	wtop2w	Pythia	0.5M events	$(2 \pm 0.4) \cdot 10^{-5}$

Table 7.2 Summary of the Monte Carlo samples used to model the background.

7.3 Constructing the Templates - Fit Parameterizations of the $\cos\theta^*$ Distributions

The reconstructed $\cos(\theta^*)$ distributions for signal and background are parameterized ($\omega_{par}(\theta^*)$) using a 3rd degree polynomial times exponential of the following form

$$\omega_{par}(\theta^*) = (\sum_{i=1,2,3} p_i \cdot cos^{i-1}(\theta^*)) \cdot e^{p_4 \cdot cos(\theta^*)}. \quad (7.1)$$

The fit results are summarized in Table 7.3. Figure 7.4 shows the reconstructed $\omega(\theta^*)$ distribution and the fitted parameterizations for longitudinal, right- and left-handed W-boson decays and for background. The background includes W+4jets events, W+$b\bar{b}+2p$ events and WW events in their correct proportions. We use the W+4jets contribution to model the shape of the non-W background component and ignore single top contributions, which are negligible in comparison to the other background sources. Figure 7.5 overlays the full set of parameterizations for comparison. The normalized fits shown in Figure

sample	p_1	p_2	p_3	p_4
longitudinal	-32 ± 13	-45 ± 3.6	49 ± 11	0.13 ± 0.2
left-handed	67 ± 11	52 ± 16	25 ± 7	-3.2 ± 0.2
right-handed	19 ± 21	-9 ± 32	21 ± 11	0.6 ± 0.4
background	2.4 ± 14	18 ± 11	62 ± 7	-0.86 ± 0.2

Table 7.3 Summary of the resulting fit parameters used to parameterize the signal and background $\cos\theta^*$ distributions.

7.5 are the templates used by the likelihood fitter.

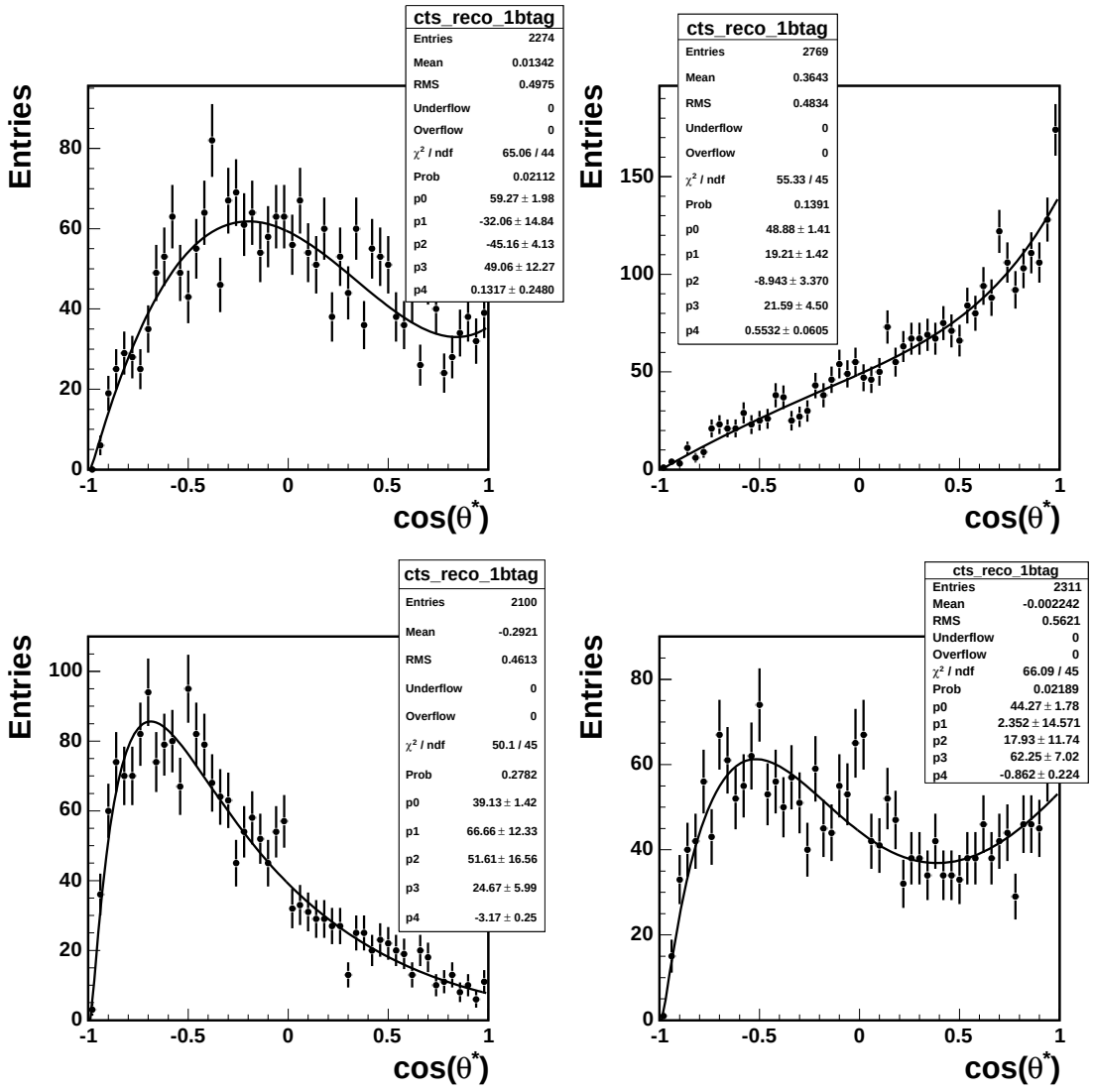

Figure 7.4 The reconstructed $\cos\theta^*$ distribution and the fitted parameterization for longitudinal (up-left) , right- (up-right) and left-handed (low-left) W-boson decays and for W+jets background (low-right).

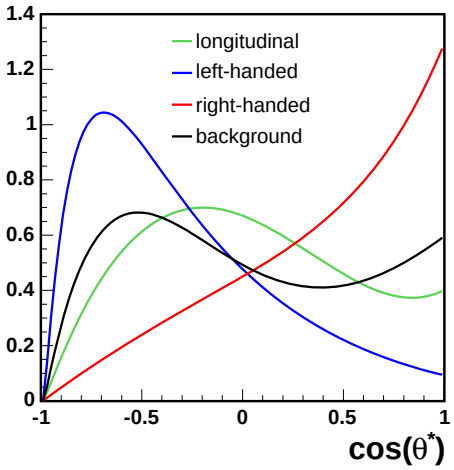

Figure 7.5 A comparison of the parameterizations of the reconstructed $\cos\theta^*$ distributions for signal and the dominant background sources.

Chapter 8

The Likelihood Fitter

8.1 The Extended Likelihood Function

We use an unbinned extended likelihood fitter to extract the uncorrected longitudinal and right-handed fractions, F_0, and F_+, from the data sample by comparing the $\cos(\theta^*)$ distribution for all selected events to parameterized MC templates for longitudinal, right-, and left-handed signal events, plus the parameterized background template. For a sample of N_s selected events, the likelihood function is defined as:

$$\mathcal{L} = G(b|\mu_b, \sigma_b) \cdot P(s+b|\mu_s + \mu_b) \cdot \prod_{i=1}^{N_s} (f_b p_b(\cos\theta_i^*) + (1-f_b) p_s(\cos\theta_i^*)) \tag{8.1}$$

and

$$p_s = F_0 \cdot p_0 + F_+ \cdot p_+ + (1 - F_0 - F_+) \cdot p_- \tag{8.2}$$

The term $G(b|\mu_b, \sigma_b)$ is a Gaussian constraint on b, the mean number of expected background events in the sample. The Gaussian mean, μ_b, and width, σ_b, are the a priori estimate of the background content of the lepton+jets sample as determined from Table 6.2. The term $P(s+b|\mu_s+\mu_b)$ is the Poisson probability that the total number of signal+background events is $s+b$ given the mean expected number of signal+background events is $\mu_s+\mu_b$. Since we use the observed cross-section as an estimate of μ_s, $\mu_s+\mu_b = Ns$, the background fraction, f_b, is taken to be $b/(s+b)$. The probability density function of the background, $p_B(\cos\theta^*)$, is taken from the fit in Figure 7.4. Similarly for the signal, p_0, p_+, and p_- are also taken from the fits of Figure 7.4. In all cases the probability density functions are each required to satisfy the normalization condition $\int_{-1}^{+1} p(\cos\theta^*) dcos\theta^* = 1$. From equation 8.2 it can be seen that, at most, there are two free polarization fractions determined from the fit, F_0 and F_+. Given the limited statistics of the data sample used here, these parameters are allowed to float anywhere in the range $(-1.5, 1.5)$. As

will be demonstrated in Section 8.3, this range is sufficiently wide to yield well-behaved pull distributions, even for pseudo-experiments constructed with one of the polarization fractions near the physical boundaries of 0 or 1.

We have performed several checks of the fitter. First, we use a toy Monte Carlo (toyMC) to construct large statistics pseudo-experiments to verify that the fitter itself is unbiased and accurately estimates the statistical uncertainties. For this test the toyMC pulls signal events from the idealized $\omega(\theta^*)$ distribution of equation 3.1 and models the background as a flat distribution. The probability densities used in the unbinned likelihood fitter are taken from equations 3.2-3.4 for the signal and a flat line for the background. We construct pseudo-experiments with various polarization fractions, f_0, and f_+. In the pseudo-experiments the mean background fraction is 20%, comparable to the expectation using the selection described in chapter 5. The mean number of signal-plus-background events is taken to be 1000 per pseudo-experiment but signal and background are both allowed to fluctuate according to Poisson statistics. No selection requirements are made so that the $F_{0,+}$ determined from the fit should correspond the generated polarization fractions $f_{0,+}$. The results are shown in Table 8.1. In all cases the fitter is unbiased and yields Gaussian pull distributions with widths consistent with unity (within 3%). We also constructed pseudo-experiments with background fractions at ± 1 and ± 2 standard-deviations away from the mean expectation used in the fitter. These also yielded unbiased determinations of the polarization fractions and pull widths consistent with unity (within 3%).

toyMC input $(f_0,\ f_+)$	fit results $(F_0,\ F_+)$
(0.3, 0.0)	$(0.308 \pm 0.013,$ fixed$)$
(0.5, 0.0)	$(0.485 \pm 0.012,$ fixed$)$
(0.65, 0.0)	$(0.647 \pm 0.012,$ fixed$)$
(0.7, 0.0)	$(0.696 \pm 0.011,$ fixed$)$
(0.75, 0.0)	$(0.732 \pm 0.011,$ fixed$)$
(0.9, 0.0)	$(0.904 \pm 0.010,$ fixed$)$
(0.7, 0.0)	$($fixed$,\ -0.001 \pm 0.006)$
(0.7, 0.05)	$($fixed$,\ 0.045 \pm 0.006)$
(0.7, 0.1)	$($fixed$,\ 0.101 \pm 0.006)$
(0.7, 0.15)	$($fixed$,\ 0.141 \pm 0.006)$
(0.7, 0.2)	$($fixed$,\ 0.201 \pm 0.006)$
(0.70, 0.1)	$(0.689 \pm 0.017,\ 0.106 \pm 0.010)$

Table 8.1 Test of the unbinned likelihood fitter using simple toy Monte Carlo pseudo-experiments constructed as described in the text.

As a second check, we construct signal-only pseudo-experiments but use tree-level information from standard $t\bar{t}$ MC samples to construct each experiment. Only lepton-plus-jets events are used where the lepton is an electron or muon from a $W^{\pm}$. No other selection requirements are made. Again the probability densities used in the likelihood fitter are taken from equations 3.2-3.4. There is no background used in this check. We fit both Pythia and Herwig samples for a couple different top-quark masses. We construct 100 pseudo-experiments for each sample, varying the number of events per pseudo-experiment depending on the statistics of the MC sample. The results are shown in Table 8.2. In all cases the fit is unbiased and the pull widths are well described by a Gaussian distribution with unit width.

sample		expected f_0	fitted F_0
ttopel	Pythia $m_t = 178$	0.710	0.705 ± 0.003
ttop0z	Pythia $m_t = 175$	0.703	0.705 ± 0.004
ttophl	Herwig $m_t = 175$	0.703	0.703 ± 0.002

Table 8.2 Test of the unbinned likelihood fitter using pseudo-experiments constructed from tree-level Monte Carlo information as described in the text.

At this stage we have sufficient confidence in the fitter itself that we proceed to more sophisticated tests using fully reconstructed events and including acceptance effects.

8.2 Acceptance Corrections

The lepton P_T spectrum is correlated with the helicity of the W from which it originates.

- In the rest frame of a left-handed (spin -1) W^+ boson (allowed by a $V-A$ SM interaction) that decays via $W^+ \to l^+\nu$, angular momentum conservation implies that the left-handed neutrino momentum must be anti-parallel to the direction of the W^+ spin. Therefore, the anti-lepton momentum is parallel to the direction of the W^+ spin. As the left-handed W^+ boson has spin anti-parallel to its momentum, the anti-lepton momentum in the lab-frame is decreased by the W boost.

- In the rest frame of a right-handed (spin 1) W^+ boson (highly suppressed by the SM $V-A$ interaction) that decays into $W^+ \to l^+\nu$, angular momentum conservation implies that the left-handed neutrino momentum must be anti-parallel to the direction of the W^+ spin. Therefore the anti-lepton momentum must be parallel to the direction of the W^+ spin. As the right-handed W^+ boson has spin parallel to

its momentum, the anti-lepton momentum in the lab-frame is increased by the W boost.

- In the rest frame of a right-handed W^- boson (allowed by $V-A$ SM interaction), that decays as $W^- \to l^-\bar{\nu}$, angular momentum conservation implies that the right-handed anti-neutrino momentum must be parallel to the direction of the W^- spin. Therefore the lepton momentum is anti-parallel to the direction of the W^- spin. As the right-handed W^- boson has spin parallel to its momentum, the lepton momentum in the lab frame is deceased by the W boost.

- In the rest frame of a left-handed W^- boson (highly suppressed within the SM) that decays via $W^- \to l^-\bar{\nu}$, angular momentum conservation implies that the right-handed anti-neutrino momentum must be parallel to the direction of the W^- spin. Therefore the lepton momentum is anti-parallel to the direction of the W^- spin. As the left-handed W^- boson has spin anti-parallel to its momentum, the lepton momentum is the lab frame is increased by the W boost.

Consequently the selection requirements yield different acceptances for longitudinal, right-, and left-handed W decays. Since the lepton P_T spectrum is softest (hardest) for left-handed (right-handed) decays, the acceptance is smaller (larger) relative to the acceptance for longitudinal decays. The lepton isolation requirement also effects the relative acceptances of the three polarization samples. These acceptance effects are most important near $\cos\theta^* = -1$ and are the reason the left-handed template in Figure 7.4 falls instead of rises at that edge. However, the probability density functions used by the likelihood fitter are all normalized to 1 and the difference in the acceptances is not taken into account. We therefore correct for this effect on average using the acceptances calculated from the `GGWIG` samples and given in Table 8.3:

$$F_0 = \frac{\alpha_0 f_0}{\alpha_+ f_+ + \alpha_0 f_0 + \alpha_- f_-} \tag{8.3}$$

where F is the measured fraction returned by the fitter and needs to be corrected, and f is the true fraction:

$$f_0 = F_0 + correction \tag{8.4}$$

We perform two fits on the data. In the first we will constrain $f_+ = 0$ and determine F_0. For this fit the acceptance correction has a simple analytic form:

$$R = \frac{Acc.(left-handed\ Ws\ sample)}{Acc.(longitudinal\ Ws\ sample)} = \frac{\alpha_-}{\alpha_0} \tag{8.5}$$

$$Correction(F_0) = \frac{F_0(R-1)(1-F_0)}{1+F_0(R-1)} \tag{8.6}$$

The correction versus the measured fraction is shown in Figure 8.1.

In the second fit, we will constrain $f_0 = 0.70$, the Standard Model expectation for $m_t = 175$ GeV/c^2, and determine F_+. In a similar way to correcting F_0, for this second fit the acceptance correction to determine the true polarization fraction, f_+, is very small (~ 0.01 for $f_+ < 0.10$ and lower than that around the expected region of $F_+ \sim 0$) compared to the present statistical sensitivity (~ 0.10). The acceptance correction itself has an uncertainty since it is derived from MC samples with a limited size. For simplicity then, it is omitted and we take the fitted F_+ to be the true f_+. The linearity checks discussed in the next section will verify that for the present data-sets this is an adequate approximation. As a cross-check of the GGWIG samples, we show in Table 8.4

sample		acceptance
left-handed	utop0i+utop4i	0.078 ± 0.002
longitudinal	utop2i+utop5i	0.092 ± 0.002
right-handed	utop1i+utop3i	0.101 ± 0.002

Table 8.3 The acceptance as a function of the W-boson polarization determined using the $t\bar{t}$ GGWIG samples. These numbers are used to correct the fitted fractions $F_{0,+}$ to determine the true polarization fractions $f_{0,+}$ as described in the text. The uncertainties are statistical only.

the acceptance of a Standard Model sample (ttopvh) and compare to a mixture of GGWIG samples (utopXX) which have been weighted according to the Standard Model value of f_0. The acceptances are in good agreement.

sample		acceptance
Standard Model	ttopvh	0.086 ± 0.002
Standard Model	leptonic utop	0.088 ± 0.002
Standard Model	hadronic utop	0.090 ± 0.002

Table 8.4 The acceptance for a Standard Model $t\bar{t}$ PYTHIA sample and a mixture of $t\bar{t}$ GGWIG samples which have been weighted according to the Standard Model predictions of f_0. The row marked "leptonic" ("hadronic") utop corresponds to GGWIG samples in which the leptonic (hadronic) decaying W boson is forced to a specific helicity while the other W boson decays with SM helicity fractions.

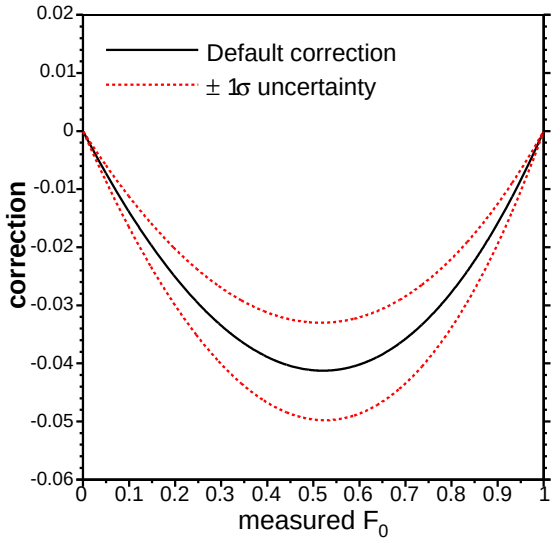

Figure 8.1 The acceptance correction necessary to determine the true polarization fraction f_0 as a function of the fitted fraction F_0.

8.3 Linearity Study and Expected Statistical Uncertainty

To test the full method, including reconstruction and acceptance effects, we generate 1000 pseudo-experiments for arbitrary values of f_0 and f_+. The mean number of background events is taken from Table 6.2. The number of signal events for a given pseudo-experiment is then chosen to yield 220 total events. We generate 1000 pseudo-experiments for arbitrary values of f_0, f_+, and f_-, randomly drawing from the appropriate `GGWIG` samples and mixing them in the appropriate ratios to form the signal sample. The background events are randomly drawn from the $W + 4p$, $W + b\bar{b} + 2p$ and WW samples with the correct ratio. We find that the corrected fit results are consistent with the input helicity fractions as shown in Table 8.5. Some representative pull distributions are shown in Figure 8.2 and demonstrate that the fitter is accurately determining the statistical uncertainty. Using the pseudo- experiments constructed with the Standard Model values $(f_0, f_+) = (0.70, 0.00)$ we estimate that the expected statistical uncertainty is $\delta f_0(\text{stat}) = 0.12$ and $\delta f_+(\text{stat}) = 0.06$ for the determination of the longitudinal and right-handed W-polarization fractions, respectively.

Tests of the method using pseudo-experiments in which the signal is drawn from other Monte Carlo samples (e.g. the default Pythia and Herwig $t\bar{t}$ samples) are discussed in Section 9.0.5.

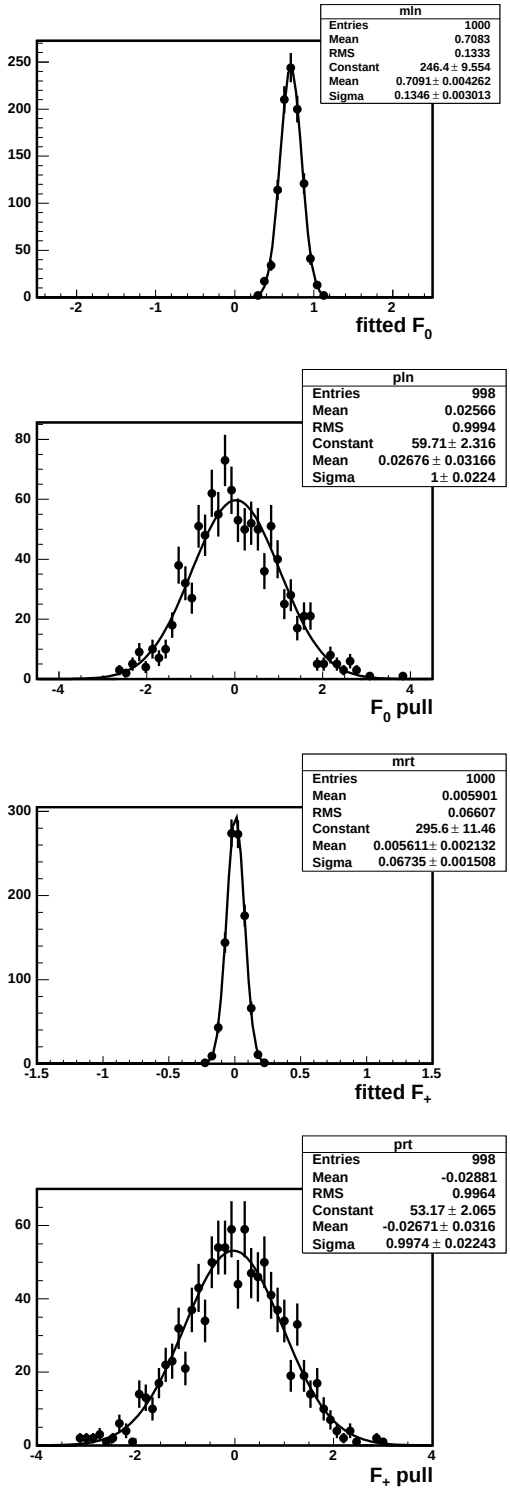

Figure 8.2 Representative pull distributions for the realistic signal-plus-background pseudo-experiments constructed with $(f_0, f_+) = (0.70, 0.00)$. The top two plots are the fitted f_0 and its pull when f_+ is constrained to 0. The bottom two plots are the fitted f_+ and its pull when f_0 is constrained to 0.70.

MC input (f_0, f_+)	corrected fits (f_0, f_+)
(0.3, 0.0)	$(0.314 \pm 0.025$, fixed)
(0.5, 0.0)	$(0.514 \pm 0.025$, fixed)
(0.7, 0.0)	$(0.709 \pm 0.025$, fixed)
(0.9, 0.0)	$(0.901 \pm 0.025$, fixed)
(0.7, 0.0)	(fixed, 0.006 ± 0.012)
(0.7, 0.1)	(fixed, 0.103 ± 0.012)
(0.7, 0.2)	(fixed, 0.202 ± 0.012)
(0.7, 0.0)	$(0.687 \pm 0.052, 0.012 \pm 0.025)$
(0.6, 0.1)	$(0.581 \pm 0.052, 0.113 \pm 0.025)$

Table 8.5 Linearity tests of the unbinned likelihood fitter using realistic, fully simulated, signal-plus-background Monte Carlo pseudo-experiments.

Chapter 9

Systematic Uncertainties

Aside from the statistical uncertainty on the measurement which arises due to the finite size of the data sample, the systematic uncertainties associated with the measurement of f_0 and f_+ must also be considered. In almost all cases the systematic uncertainty was determined by constructing pseudo-experiments with signal and/or background templates affected by the systematic under study but fit using the default parameterizations and normalizations described above. The resulting shifts in the mean fitted longitudinal and right-handed fraction are used to quantify the systematic uncertainty. The pseudo-experiments were all performed using the default Pythia sample (`ttopel`) as signal, which has the Standard Model values $(f_0, f_+) = (0.70, 0.00)$, and our background model as described in Sections 7.1 and 7.2, unless otherwise noted. The following sources of systematic uncertainties have been considered:

- Jet Energy Scale
- Background
- Initial State Radiation
- Final State Radiation
- Parton Distribution Functions
- Monte Carlo Modeling
- Monte Carlo Statistics
- Acceptance Correction
- Instantaneous Luminosity

These are each discussed in more detail in the following sections.

9.0.1 Jet Energy Scale

Changes in the Jet Energy Scale (JES) have two effects on the analysis. They can change the acceptance and the $\cos(\theta^*)$ shapes. We investigate each of these separately. First, we re-evaluate the acceptances for `GGWIG` samples when we vary the JES by $\pm 1\sigma$ and propagate those changes into the acceptance correction. We find that in the ratio relevant for the correction shown in Figure 8.1 the effects of changing JES are largely canceled. The resulting change in the correction is $<< 0.01$ and is neglected. Second, we construct pseudo-experiments in which the signal and background are constructed from events reconstructed with $\pm 1\sigma$ shifts in their jet energies. The differences between the mean fitted value of f_0 (f_+) from pseudo-experiments from the GGWIG samples and the mean fitted value of f_0 (f_+) from pseudo-experiments from the GGWIG samples when the JES is varied by $+\sigma$ and $-\sigma$ are calculated. The average between these two differences is taken to the JES systematics for f_0 (f_+). We find this uncertainties to be ± 0.013 for f_0 and ± 0.010 for f_+.

9.0.2 Background

Uncertainties in the background normalization are already accounted for in the fit by inclusion of the Gaussian constraint. Remaining sources for systematic uncertainties are the background sample composition and the uncertainty of the shape for each sample.

To assess the uncertainty in the background sample composition we construct two sets of pseudo-experiments for the extreme cases that the background is entirely from mistags or entirely from 'W + heavy flavour'. The full difference in the mean fitted f_0 and f_+ is taken as the systematic uncertainty. We find ± 0.02 and ± 0.01 for f_0 and f_+, respectively.

The shape uncertainty for the W background is assessed by testing samples generated with different q^2. We constructed pseudo-experiments were the background was replaced by the modified W sample and find ± 0.023 and ± 0.013 for f_0 and f_+, respectively.

W+jets MC events have been used to model the shape of QCD background shape. To gain confidence in the background model, a multi-jet sample has been studied, in which jets with large electromagnetic fraction (emf) are selected as electron candidates. The selection criteria are $0.8 <$ emf < 0.95 and ntracks > 3. The sample was used and added with a background fraction of 25% to the total background samples. Pseudo-experiments show a systematic uncertainty of ± 0.022 and ± 0.002 for f_0 and f_+, respectively. Figure 9.1 shows the $\cos(\theta^*)$ distribution for the multi-jet sample together with a parametrization (left) and all background parameterizations (right).

This results in a total background systematic uncertainty of ± 0.038 and ± 0.017 for

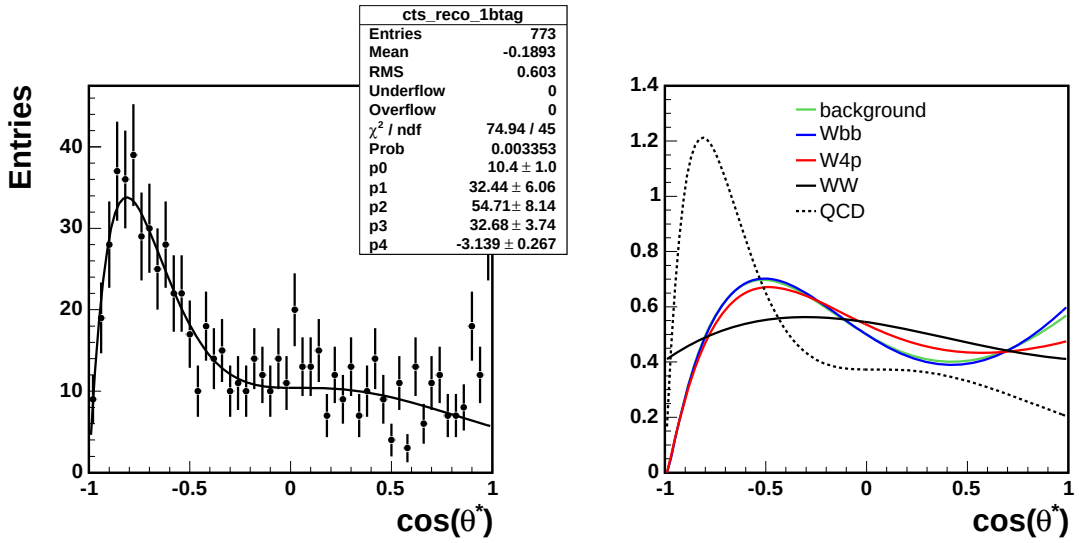

Figure 9.1 The $\cos(\theta^*)$ distribution for the multi-jet sample together with a parametrization (left) and all background parametrisations (right)

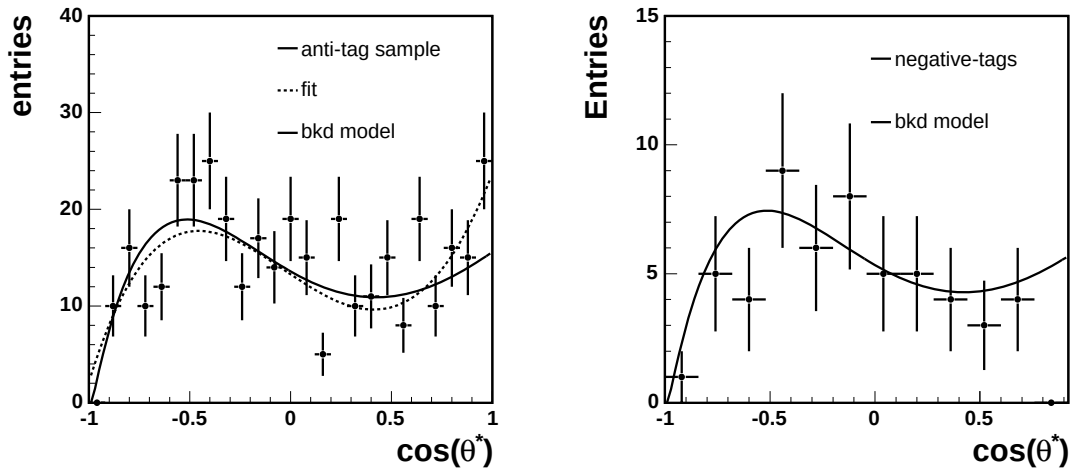

Figure 9.2 Zero-tag sample is shown together with a fit and the background model (left). The negative-tag sample is shown together with the background model (right).

f_0 and f_+, respectively.

Further tests have been performed to show the agreement of the background model with the data. Using events without b-tag, we create a sample dominated by W+jets and QCD events. The $\cos(\theta^*)$ distribution is shown in Figure 9.2 (left). Similarly, we select a sample with negative tagged jets. The $\cos(\theta^*)$ distribution is shown in Figure 9.2 (right). Both samples show good agreement with our background model, which gives us confidence that it is a reasonable description of the background in the signal region.

9.0.3 Initial State Radiation

We compare the mean fitted f_0 and f_+ when using the ISR more/less samples, `ttopdr` and `ttopbr`, for the signal events in pseudo-experiments. In these samples the strong coupling constant α is varied according to theoretical uncertainties and the quarks and gluons radiate more/less. We take half the full difference between these two samples as the symmetrized systematic uncertainty, ± 0.01 and ± 0.005 for f_0 and f_+, respectively.

9.0.4 Final State Radiation

We compare the mean fitted f_0 and f_+ when using the FSR more/less samples, `ttopkr` and `ttopfr`, for the signal events in pseudo-experiments. In these samples the strong coupling contant α is varied according to theoretical uncertainties and the quarks and gluons radiate more/less. We take half the full difference between these two samples as the symmetrized systematic uncertainty, ± 0.01 and ± 0.005 for f_0 and f_+, respectively.

9.0.5 Signal Monte Carlo

We construct pseudo-experiments using events from the default Pythia sample as signal and compare the mean fitted f_0 and f_+ to the mean fitted values when using the default Herwig sample for the signal events. We take the full observed difference as a systematic uncertainty of ± 0.02 and ± 0.01 for f_0 and f_+, respectively.

9.0.6 Monte Carlo Statistics

The templates shown in Figure 7.4 have an uncertainty associated with them due to the finite statistics of the MC samples used to construct them. To assess the systematic on f_0 and f_+ associated with this uncertainty, we re-fit the templates 1000 times, each time letting the bins Poisson-fluctuate around their central values. We then drew pseudo-experiments from these re-fits, and assigned the resulting increase in the RMS of the fitted $f_{0,+}$ values as a systematic: ± 0.02 for f_0 and ± 0.01 for f_+.

9.0.7 Acceptance Correction

The statistical uncertainty on the acceptance correction is propagated to an uncertainty in the measured f_0 of ± 0.01. We assign a systematic of ± 0.01 to the measured f_+ to account for the missing acceptance correction, which is < 0.01 in the region of small f_+.

9.0.8 Parton Distribution Functions

The effect of PDFs is studied using the re-weighting technique [108]. The PDF we used are:

- CTEQ5L - the default PDF. The relative weight for every event is 1.
- MRST72 - Leading order PDF. If a difference relative to the default PDF is found it should be taken as a systematic.
- MRST75 - Same as the previous, but using a different value of α_s, corresponding to $\Lambda_{QCD} = 300\ MeV$ vs. $\Lambda_{QCD} = 228\ MeV$ for MRST72. The difference between the two PDFs is taken as a systematic.

In order to assign a systematic uncertainty due to differences between the MRST72 PDF and the default CTEQ5L PDF we parametrize the re-weighted histograms of $\cos\theta^*$ fitting to the same function we used for getting the parameterizations for out default fitter. From the parameterizations of the re-weighted histograms we generate pseudo-data to construct pseudo-experiments. We then perform 1000 pseudo-experiments, each of 220 events, for fitting f_0 while f_+ is fixed and 1000 pseudo-experiments for fitting f_+ while f_0 is fixed, using our default fitter. The difference between the fitted values we get from the pseudo-experiments constructed according to the parameterizations derived from the different re-weighted histograms is taken as a systematic uncertainty. Only the parameterizations of the signal shapes (longitudinal, left handed and right handed) were changed with respect to the default ones. The background parameterization is untouched. The uncertainty is found to be 0.0009 for f_0 and 0.001 for f_+. We repeat the same procedure to estimate the differences between the MRST75 PDF and the MRST72 PDF. We get an uncertainty of 0.0007 for f_0. Fitting f_+ for pseudo-experiments constructed from the parameterizations of the reweighted histograms according to MRST75 and according to MRST75 give exactly the same fitted values.

Another source for a PDF related systematic uncertainty are the variations of the 20 CTEQ6M eigen-vectors. We plot 40 different re-weighted histograms of $\cos\theta^*$ corresponding to $\pm 1\sigma$ variation of the 20 free PDF parameters in the CTEQ6 global PDF fit. For each event we normalize the weights of the 40 CTEQ6M variations with respect to the weight we get from the CTEQ5L PDF. We apply our fitter to extract the W-helicity fractions for each set of reweighted histograms. A systematic uncertainty for f_+ and f_0 is assigned [109]:

$$\Delta F = \frac{1}{2}\left(\sum_{i=1}^{20}[F(S_i^+) - F(S_i^-)]^2\right)^{1/2} \tag{9.1}$$

Where F is either f_+ or f_0 and $F(S_i^{\pm})$ are the values correspond to $\pm 1\sigma$ variation of the 20 eigen-vectors returned by the fitter. This yields uncertainties of 0.0083 and 0.0059 for f_0 and f_+ respectively,which dominate the total PDF systematic uncertainty. The PDF eigenvectors are described in [110] and [109]. Table 9.1 and Figure 9.3 show the uncertainty associated with the variation of each independent eigenvector. The dominant contribution to the (still very small) total pdf uncertainty comes from eigenvector 15. This is not a surprise - here the input functional form related to the gluon is varied. This is expected to affect high P_T jet production at the Tevatron and LHC.

Even though the pdf systematic uncertainty is small, we performed two different cross checks to verify that different fractions of $t\bar{t}$ pairs produced from quark annihilation versus $t\bar{t}$ pairs produced from gluon fusion does not have a significant impact on our results:

- We performed two fits for the helicity fractions: a fit to a large number of events (as one pseudo-experiment) from a Herwig SM sample (ttopvh) with $M_t = 175$ GeV, where 85% of the events are produced via $q\bar{q}$ annihilation and 15% of the events are produced via gluon fusion, and a second fit to a Herwig sample (ttop0q) with the same top mass were 15% of the events are produced via $q\bar{q}$ annihilation and 85% of the events are produced via gluon fusion.
  The central value for the W helicity fractions returned by the fitter in both cases are almost identical.

- We compared the $\cos(\theta^*)$ distributions in a sample where the gg (gluon fusion) fraction is 5% and in a sample where the gg fraction is 15% (see Figure 9.4). These distribution are in a very good agreement.

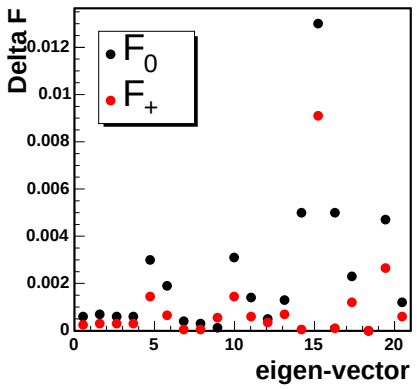

Figure 9.3 Systematic uncertainties for f_+ and f_0 for each of the 20 PDF eigen-vectors.

eigen vector	Δf_0	Δf_+
1	0.0006	0.00025
2	0.0007	0.00030
3	0.0006	0.00030
4	0.0006	0.00030
5	0.0030	0.00145
6	0.0019	0.00065
7	0.0004	0.00005
8	0.0003	0.00005
9	0.0002	0.00055
10	0.0031	0.00145
11	0.0014	0.00065
12	0.0005	0.00035
13	0.0013	0.00070
14	0.0050	0.00005
15	0.0130	0.00910
16	0.0050	0.00010
17	0.0023	0.00120
18	0.0000	0.00000
19	0.0047	0.00265
20	0.0012	0.00060

Table 9.1 The systematic uncertainties of the 20 PDF eigen-vectors for f_+ and f_0.

9.0.9 Instantaneous Luminosity

With larger instantaneous luminosity the number of multiple interaction per event increases. To study the effect we perform pseudo-experiments using `ttop5v` and `ttop7v` as signal samples. These are Pythia samples with one and two additional min-bias events. The default MC sample we use include only the hard scattering process. We assign a systematic uncertainty of ± 0.0061 and ± 0.0015 for f_0 and f_+, respectively.

9.1 Summary of Systematic Uncertainties

The systematic uncertainties from each of the sources given above are summarized in Table 9.2. The total systematic uncertainty is taken to be their quadrature sum.

Figure 9.5 shows a projection of the statistical uncertainties for performing this analysis with up to 8 fb^{-1} of total integrated luminosity, assuming no improvements or changes in the analysis. One can see that with 4 fb^{-1} of data the statistical uncertainties and the systematic ones become of the same order.

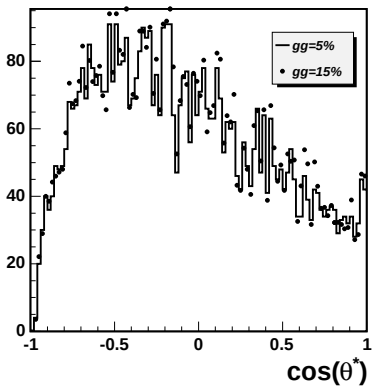

Figure 9.4 $\cos^{\theta^*}$ distribution in events with different gluon fusion/$q\bar{q}$ annihilation ratios.

source	δf_0	δf_+
Jet Energy Scale	± 0.013	± 0.010
Background	± 0.038	± 0.017
ISR/FSR	± 0.010	± 0.005
Signal Monte Carlo	± 0.020	± 0.010
MC statistics	± 0.020	± 0.010
Method	± 0.010	± 0.010
PDF	± 0.009	± 0.006
Instantaneous Luminosity	± 0.007	± 0.002
Total Systematic	± 0.053	± 0.027
Statistical	± 0.120	± 0.063
Total Uncertainty	± 0.131	± 0.069

Table 9.2 The sources of systematic uncertainty and their related estimate. The total systematic uncertainty is taken as the quadrature sum of the individual sources.

9.2 Top Mass dependence

As a decision of the CDF top working group, results are quoted at a given top mass. At the time of this analysis the convention is to use a top mass of 175 GeV. However, the dependency of the result on the mass of the top was studied and is presented here for completeness.

Before discussing how the result of the analysis changes with the real value of the top mass, it has to be clarified that no constraint of the top mass was used in the kinematic fit.
Where does the top mass enter the analysis?

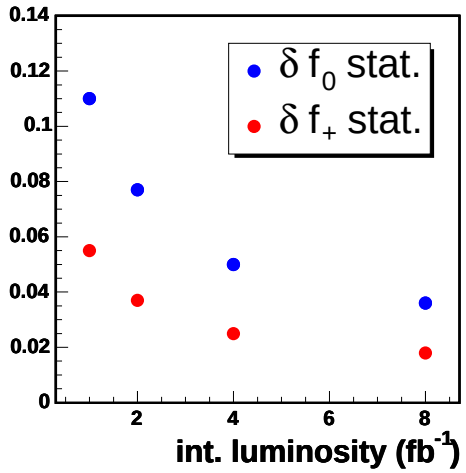

Figure 9.5 Projection plot for the expected statistical uncertainty for measuring the right-handed and longitudinal W helicity fractions assuming no improvements or changes in the current method.

1. the templates for longitudinal, left- and right-handed W's in top decays are made from a sample of $M_t = 175$ GeV. Fitting a top sample of different mass with those templates can result in a bias.

2. when fitting for F_+, we constraint F_0 to its SM value. This value is top mass dependent and therefore our result of F_+ is dependent on the top mass. We can also quote the result of F_+ as a function of F_0.

Concerning 1):
Top MC samples at different top masses were studied as shown in the following plots:

There is no significant mass dependence in the f_0 measurement. A 1σ variation of the top mass results in a 0.5% correction on the result, well below the sensitivity of the measurement.

The same pseudo-experiments have been used to measure f_+:

There is a moderate top mass dependence in measuring f_+. A 1σ variation of the top mass results in a 0.5% correction on the result, well below the sensitivity of the measurement.

In summary, studying samples with different top mass we find variations for f_0 of up to 4%. However, each sample has an uncertainty of 2%. We fit a linear function, and find a 0.5% correction for a 1σ variation of the top mass (+/-3GeV). Similarly, the variation

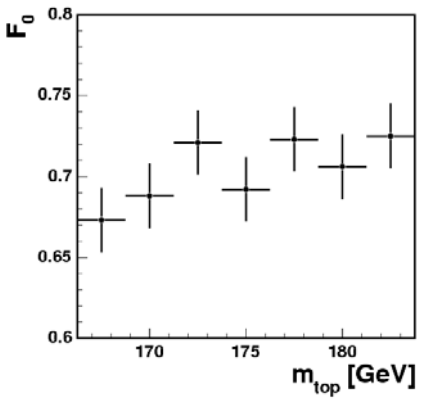

Figure 9.6 The measured fraction of longitudinal Ws from MC samples with different top masses

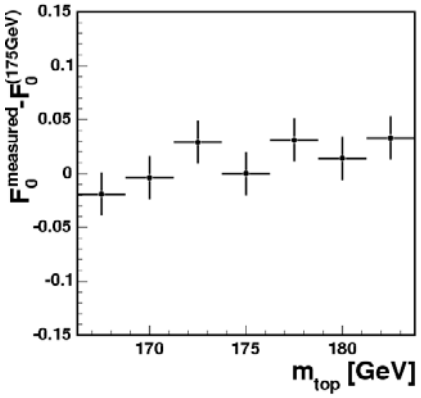

Figure 9.7 The difference between the measured longitudinal fraction f_0 from different top mass MC samples and the measured fraction at $M_t = 175$ GeV

of the measured value of f_+ with the top mass is consistent with variations expected from the sample statistics.

Concerning 2):

Showing the measured f_+ as a function of the top mass. The dependency enters the game through the value of f_0. As one can see in Figure 9.13, the value of f_+ hardly changes.

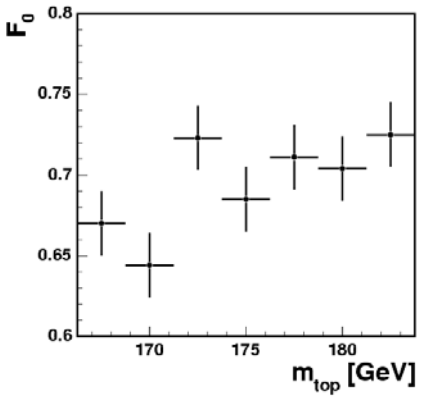

Figure 9.8 The measured fraction of longitudinal Ws from MC samples with different top masses - results with signal events only using the full sample, but only one pseudo-experiment

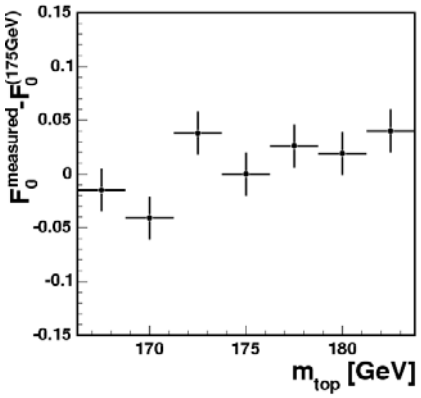

Figure 9.9 The difference of the measured value of f_0 and the value at 175 GeV in the signal only sample.

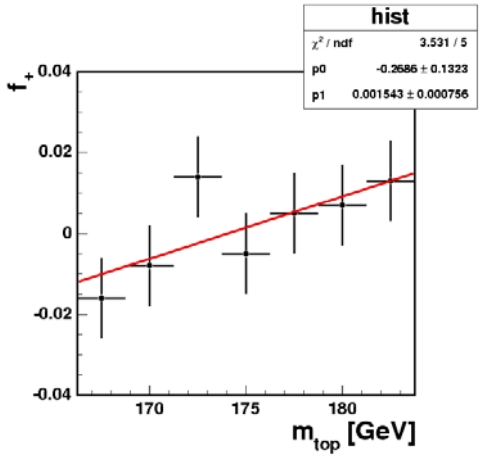

Figure 9.10 The measured fraction of right-handed Ws from MC samples with different top masses. f_0 is fixed to 0.703

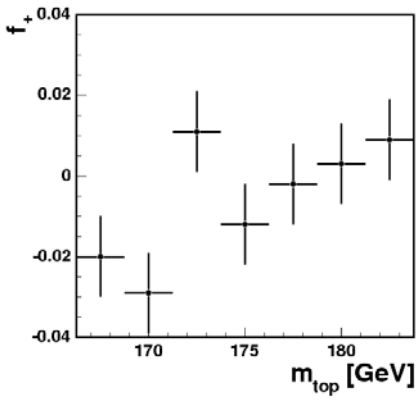

Figure 9.11 The measured fraction of right-handed Ws from signal only MC sample with different top masses. f_0 is fixed to 0.703

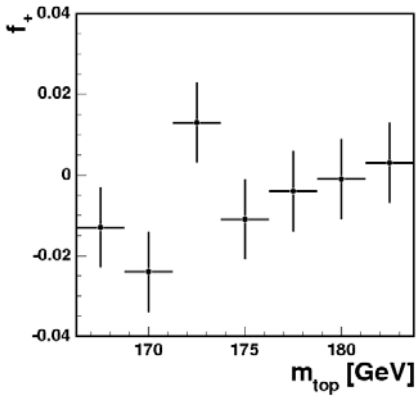

Figure 9.12 The measured fraction of right-handed Ws from signal only MC sample with different top masses. f_0 is fixed its expected value.

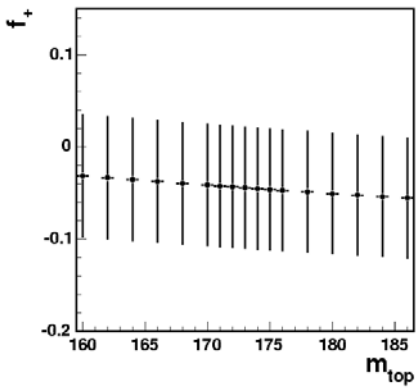

Figure 9.13 The measured fraction of right-handed Ws from MC sample with different top masses.

Chapter 10

Results

10.1 Fitting the Data - separate measurement of f_0 and f_+

The $\cos(\theta^*)$ distribution measured from the data is shown in Figure 10.1. We use the templates described in chapter 7 to fit the observed data distribution, fixing $f_+ = 0$, to obtain $F_0 = 0.645 \pm 0.12$. After making the acceptance correction we estimate the true fraction of longitudinal polarized W-bosons to be $f_0 = 0.606 \pm 0.12$. Since the result is consistent with the Standard Model expectation, we then fit for f_+ while fixing the longitudinal fraction to the expected value assuming $m_t = 175$ GeV/c^2, $f_0 = 0.70$: $f_+ = -0.056 \pm 0.056$. The statistical uncertainties are reported here, while the systematic uncertainties are discussed in chapter 9. The likelihood curves for the two fits are shown in Figure 10.2.

10.1.1 Limit on f_+

As our measurement of f_+ is consistent with the SM expectation of zero, we proceed to set an upper limit on f_+ following a Bayesian prescription. We multiply the f_+ likelihood returned by the fit by a flat prior to arrive at a posterior probability density distribution for f_+, and then integrate this distribution out to the point where 95% of the area is captured; see Figure 10.3.

We incorporate the effect of systematic uncertainties in the determination of the limit by modeling them as a Gaussian with mean zero and width equal to the total systematic uncertainty on f_+ (see Sec. 10.2.4). We have verified that the systematic uncertainties on f_+ reported in Table 9.2 are independent of the f_+ value used in the pseudo-experiments used to quantify them.

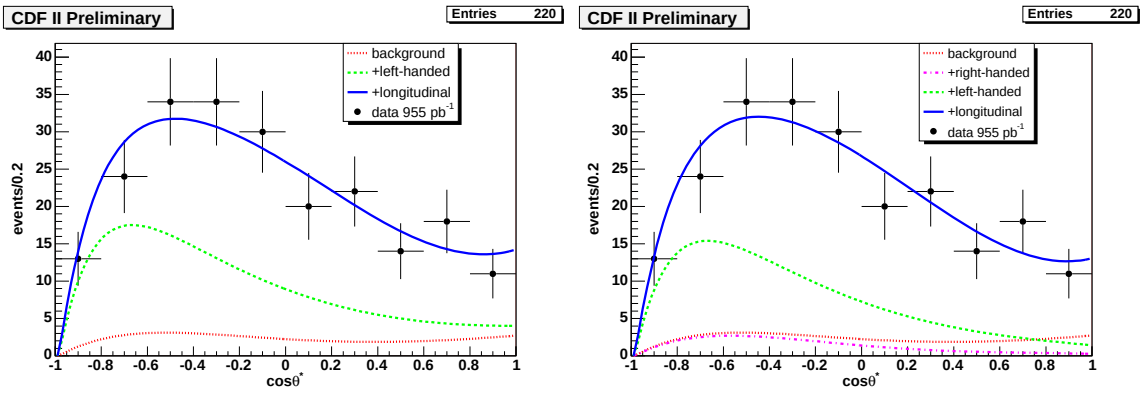

Figure 10.1 On the left - the observed $\cos(\theta^*)$ distribution in the data (points) overlaid with the background (dotted), background + left-handed (dashed), and background + left-handed + longitudinal (solid) distributions as determined by the fit for F_0. On the right - the observed $\cos(\theta^*)$ distribution in the data (points) overlaid with the background (dotted),background + right-handed (dash-dot), background + right-handed + left-handed (dashed), and background + right-handed + left-handed + longitudinal (solid) distributions as determined by the fit for F_+.

We then convolute the f_+ likelihood with this Gaussian before multiplying by the prior. Since the total f_+ uncertainty is still statistics dominated, the systematics have only a very small effect on the posterior probability distribution; see Figure 10.4. The 95% CL upper limit on f_+ determined from this procedure is 0.11.

10.2 First Simultaneous Measurement of f_0 and f_+

Chapter 3 explains the importance of determining the W helicity fractions in top quark decays in a model independent way.

Fixing one of the fractions to its SM value while fitting for the other one is a special case of a general measurement where both f_+ and f_0 float and the likelihood fitter extracts these two fractions simultaneously. Chronologically, however, the simultaneous fit was done later due to the limited statistics of the data sample. This analysis reports the results of such a simultaneous fit, performed for the first time using the full available CDF 955 pb^{-1} of data. The statistical uncertainties of this fit are rather large, but hopefully with the increasing integrated luminosity provided by the Tevatron, a better precision will be achieved.

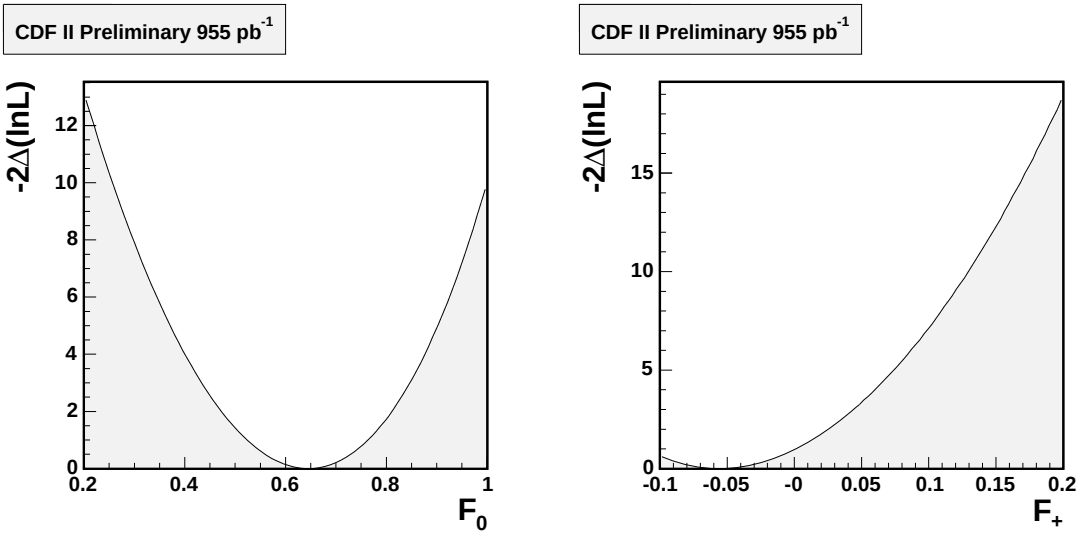

Figure 10.2 Distributions of $-2\Delta \ln \mathcal{L}$ for F_0 (left plot) and F_+ (right plot) from the fits to the data.

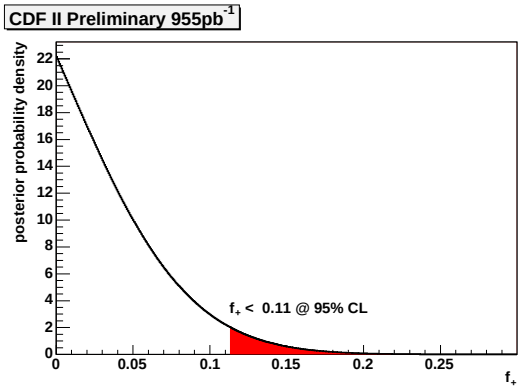

Figure 10.3 Posterior probability distribution for and 95% CL upper limit on f_+.

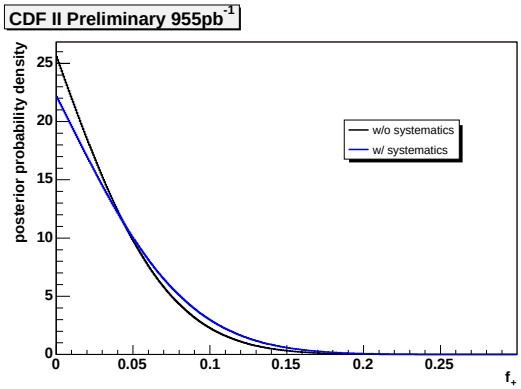

Figure 10.4 f_+ posterior probability with (blue) and without (black) folding in systematic uncertainties.

10.2.1 Method

In the measurement of the right-handed and longitudinal fractions of W bosons the strategy, tools, MC samples, etc. are identical to whatever has been used for measuring the fractions separately. The only difference is that in the likelihood fitter none of the two fractions is fixed to a constant value, instead they are both measured simultaneously. The relevant studies, as described in the following sections, were done and taken into account when quoting the final results.

10.2.2 Linearity Studies

Pseudo experiments have been used to study the performance of the analysis with different input values for f_0 and f_+. For each pair of values (f_0, f_+) ensembles of pseudo experiments have been generated. The results are displayed in Figure 10.5 to Figure 10.7 and in Table 10.1.

The left plot in Figure 10.5 shows the measured longitudinal fraction f_0 while the right-handed fraction has been varied from 0-30%. A wrong assumption on the value of f_+ results in a bias on the measurement of f_0, when f_+ is fixed in the fit to the Standard Model value (standard fit). The combined fit for f_0 and f_+ shows a linear behavior. Similarly, the measured right-handed fraction is shown in the right plot as a function of the input value of the longitudinal fraction f_0.
Figure 10.6 shows the measured longitudinal fraction f_0 as a function of input value of f_0. Both, the standard fit and the combined fit show a linear behavior, when the right-handed fraction is fixed to zero. As shown in Figure 10.7, a linear behavior can also be observed for the fits of the right-handed fraction, when the longitudinal fraction is fixed to the Standard Model value. Pull distributions from the 2D fit for two different

F_0	F_+	fitted F_0	fitted F_+
0.8	0.0	0.794 ± 0.008	0.004 ± 0.004
0.8	0.1	0.780 ± 0.008	0.110 ± 0.004
0.8	0.2	0.780 ± 0.008	0.210 ± 0.005
0.7	0.0	0.690 ± 0.008	0.006 ± 0.004
0.7	0.1	0.681 ± 0.008	0.106 ± 0.004
0.7	0.2	0.693 ± 0.008	0.205 ± 0.005
0.6	0.0	0.592 ± 0.008	0.005 ± 0.004
0.6	0.1	0.582 ± 0.008	0.109 ± 0.004
0.6	0.2	0.583 ± 0.008	0.210 ± 0.004

Table 10.1 Results of combined fits for the longitudinal and right-handed helicity fractions in ensembles with pairs of input values (F_0, F_+).

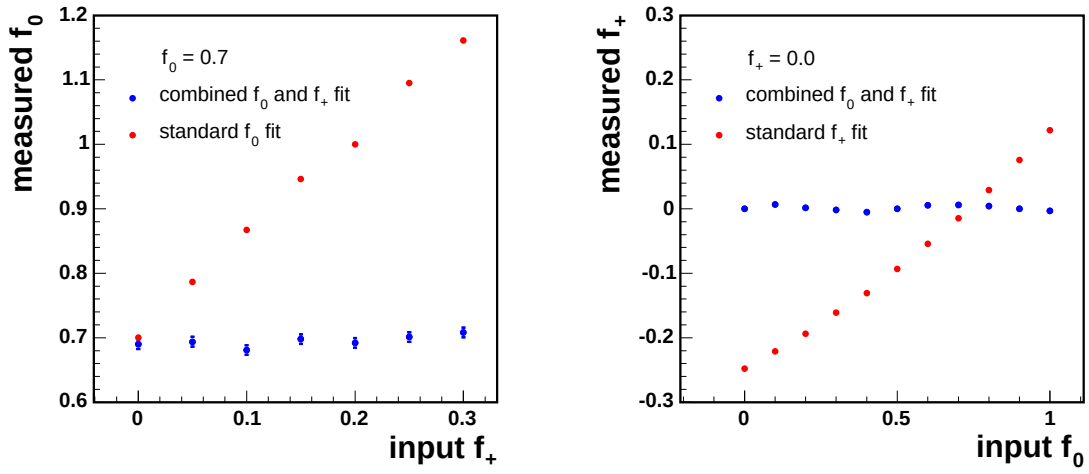

Figure 10.5 Standard and combined fit results as function of the input polarization fraction. The left plot shows the measured longitudinal fraction f_0 as a function of the input right-handed fraction f_+, while the input longitudinal fraction is set to $f_0 = 0.7$. The right plot shows the measured right-handed fraction as a function of the input longitudinal fraction f_0, while the input right-handed fraction is set to $f_+ = 0.0$.

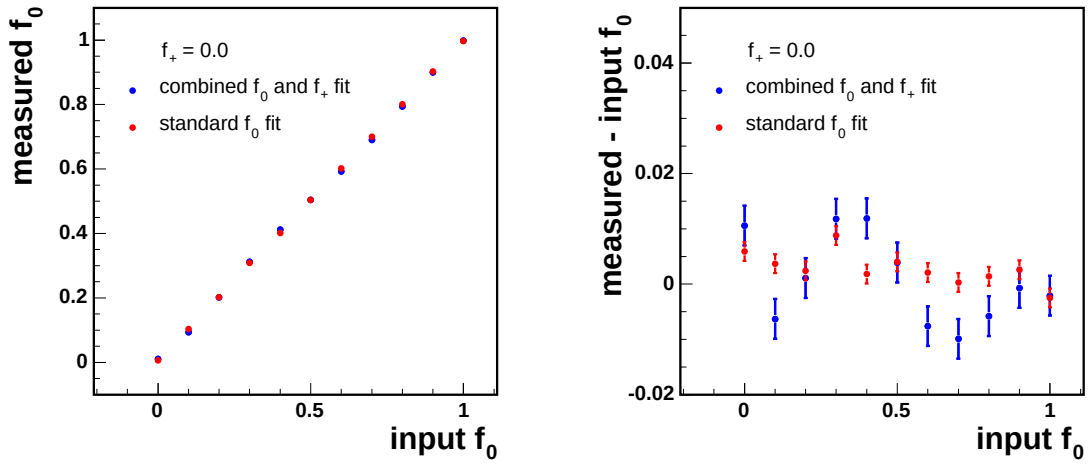

Figure 10.6 Standard and combined fit results as function of the input polarization fraction. The plot show the measured longitudinal fraction f_0 as a function of the input longitudinal fraction, while the input right-handed fraction is set to $f_+ = 0.0$.

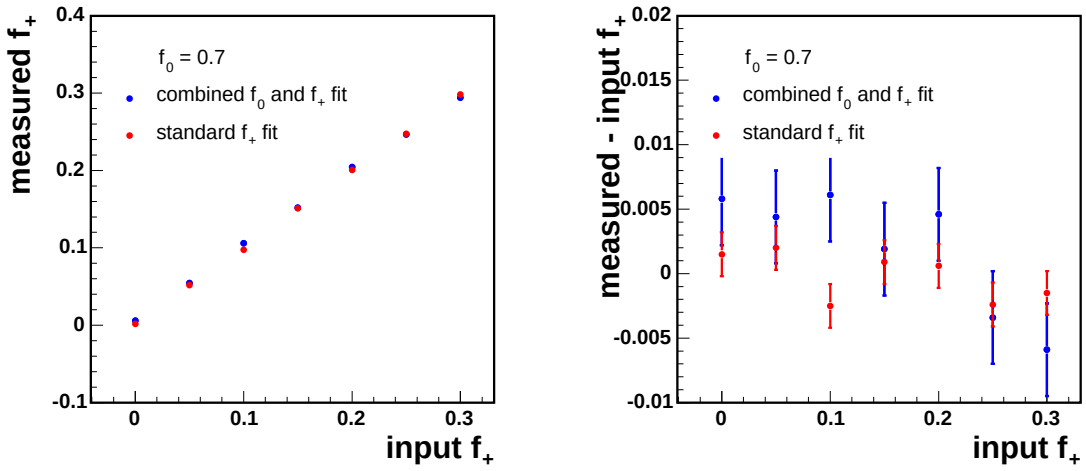

Figure 10.7 Standard and combined fit results as function of the input polarization fraction. The plot show the measured right-handed fraction f_+ as a function of the input right-handed fraction, while the input longitudinal fraction is set to $f_0 = 0.7$.

ensembles of pseudo-experiments are shown in Figure 10.8 — one is for an ensemble with SM W helicity fractions and the other is an example of an ensemble with non-SM helicity fractions. In either case, the pull distributions have mean zero and unit width.

10.2.3 Acceptance Correction

The measured fractions have to be corrected for acceptance effects, see Section 8.2. When measuring the fractions separately, the correction was either negligible (f_+), or had a very simple form (f_0). In the simultaneous measurement the corrections are applied to both fractions and are given by:

$$f_0(F_0, F_+) = \frac{F_0 \cdot R_0}{1 + F_0(R_0 - 1) + F_+(R_+ - 1)} \tag{10.1}$$

$$f_+(F_0, F_+) = \frac{F_+ \cdot R_+}{1 + F_0(R_0 - 1) + F_+(R_+ - 1)} \tag{10.2}$$

where $R_0(R_+)$ is the ratio of the left-handed acceptance to the longitudinal (right-handed) acceptance (taken from Table 8.3).

10.2.4 Systematic Uncertainties

In a similar way to what is described in chapter 9 we estimate the systematic uncertainties for the simultaneous fit of f_+ and f_0. As can be seen in Table 10.2, there is no significant

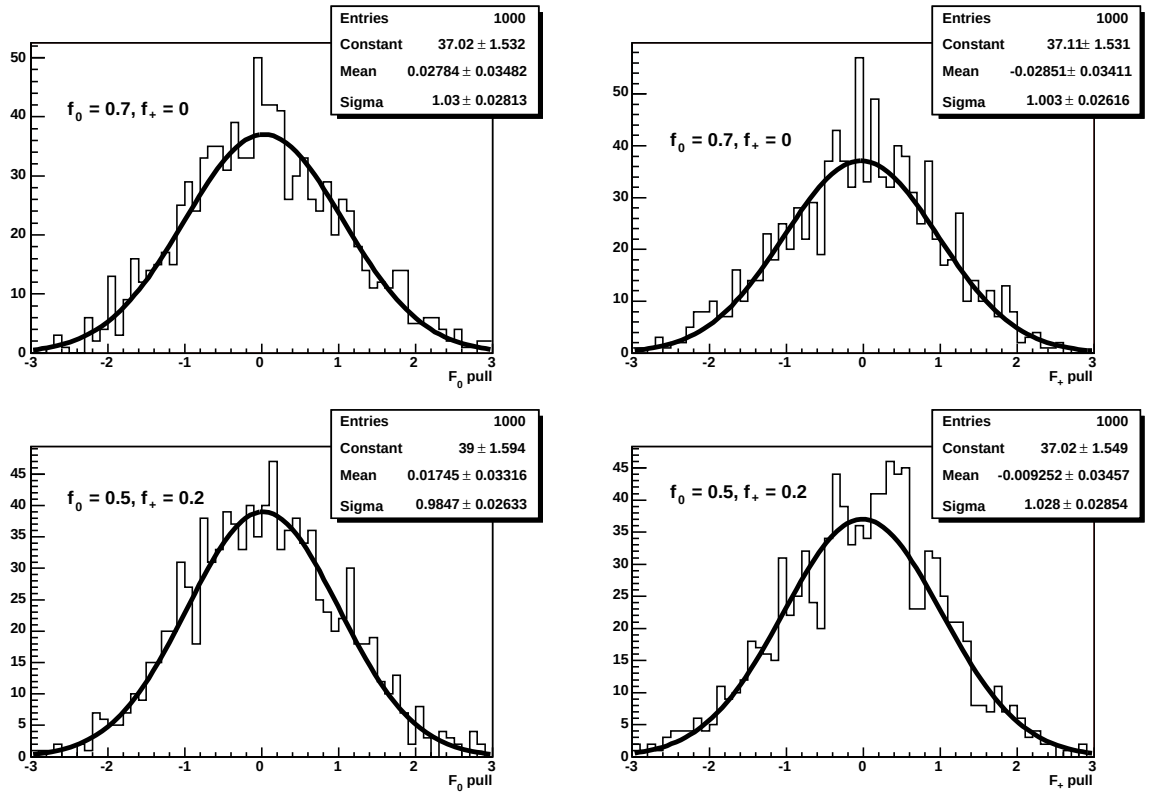

Figure 10.8 Pull distributions for F_0 (left) and F_+ (right) for the 2D fit. The upper pair is an ensemble of pseudo-experiments with SM W helicity fractions; the lower pair is an ensemble with non-SM W helicity fractions.

change in the systematic uncertainties and the total systematic uncertainty is almost identical to that estimated before.
The expected statistical uncertainty, however, is larger.

source	δf_0	δf_+
Jet Energy Scale	± 0.015	± 0.008
Background	± 0.037	± 0.015
ISR/FSR	± 0.010	± 0.005
Signal Monte Carlo	± 0.020	± 0.010
MC statistics	± 0.020	± 0.010
Method	± 0.010	± 0.010
PDF	± 0.009	± 0.006
Instantaneous Luminosity	± 0.007	± 0.002
Total Systematic	± 0.053	± 0.026
Statistical	± 0.246	± 0.096
Total Uncertainty	± 0.252	± 0.099

Table 10.2 The sources of systematic uncertainty and their related estimate when measuring f_+ and f_0 simultaneously. The total systematic uncertainty is taken as the quadrature sum of the individual sources.

10.2.5 Results from the Data

The $\cos(\theta^*)$ distribution observed in the data is shown in Figure 10.10. We perform a fit to the data to extract both, the fraction of longitudinal and right-handed polarized W bosons. We obtain $F_0 = 0.78 \pm 0.24$ and $F_+ = -0.07 \pm 0.1$. Shown in Figure 10.9 are distributions of the statistical uncertainty on F_0 and F_+ from 1000 SM pseudo-experiments; the result observed in the data is seen to be quite likely. After correcting for acceptance effects, we estimate the true fraction of longitudinal polarized W bosons to be $f_0 = 0.74 \pm 0.25$ and $f_+ = -0.06 \pm 0.10$. Only the statistical uncertainties are reported here while the systematic uncertainties are discussed in the previous sections. The likelihood as a function of f_+ and f_0 is shown in Figure 10.11. We construct a posterior probability density in the (f_+, f_0) plane by multiplying the likelihood by a prior that is flat in the physical region defined by $f_+ \geq 0$, $f_0 \geq 0$, $f_0 + f_+ \leq 1$ and is zero everywhere else. We then set an exclusion at 95% CL in this plane by finding the contour of constant probability density that captures 95% of the volume under the probability surface. This is shown in Figure 10.12. This procedure does not explicitly incorporate the effects of the systematic uncertainties on f_+ and f_0; however, the fact that the systematics are about a factor of four less than the statistical uncertainties (see Section 10.2.4) renders their contribution to the exclusion limit negligible.

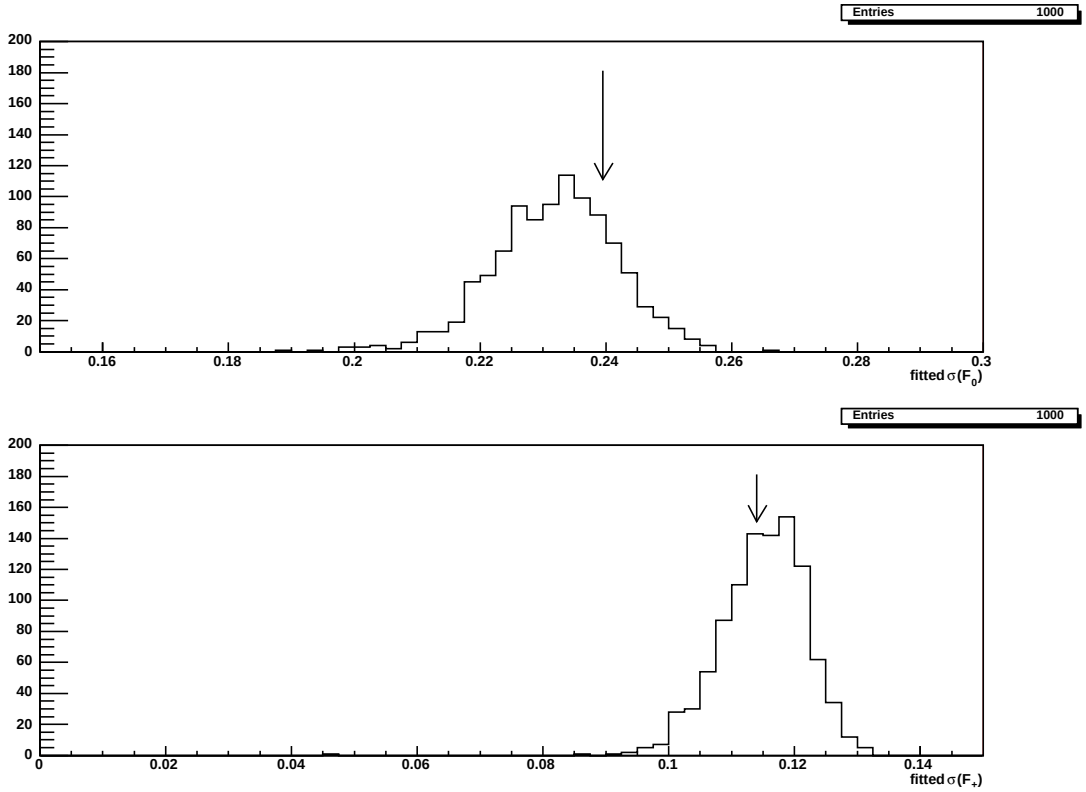

Figure 10.9 The distribution of the statistical uncertainty on F_0 (top) and F_+ (bottom), from 1000 SM pseudo-experiments. The arrows indicate the result from the CDF data.

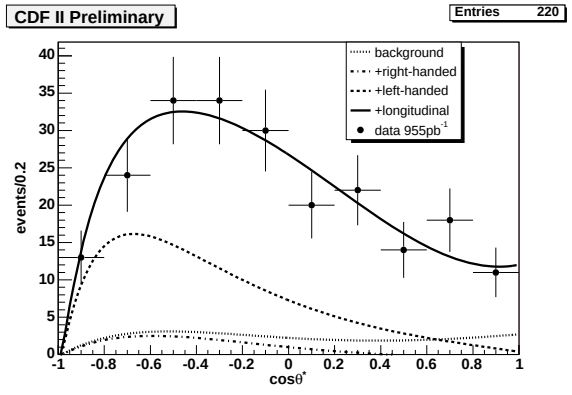

Figure 10.10 The observed $\cos(\theta^*)$ distribution in the data (points) overlaid with the background (dotted),background + right-handed (dash-dot), background + right-handed + left-handed (dashed), and background + right-handed + left-handed + longitudinal (solid) distributions as determined by the fit for F_+.

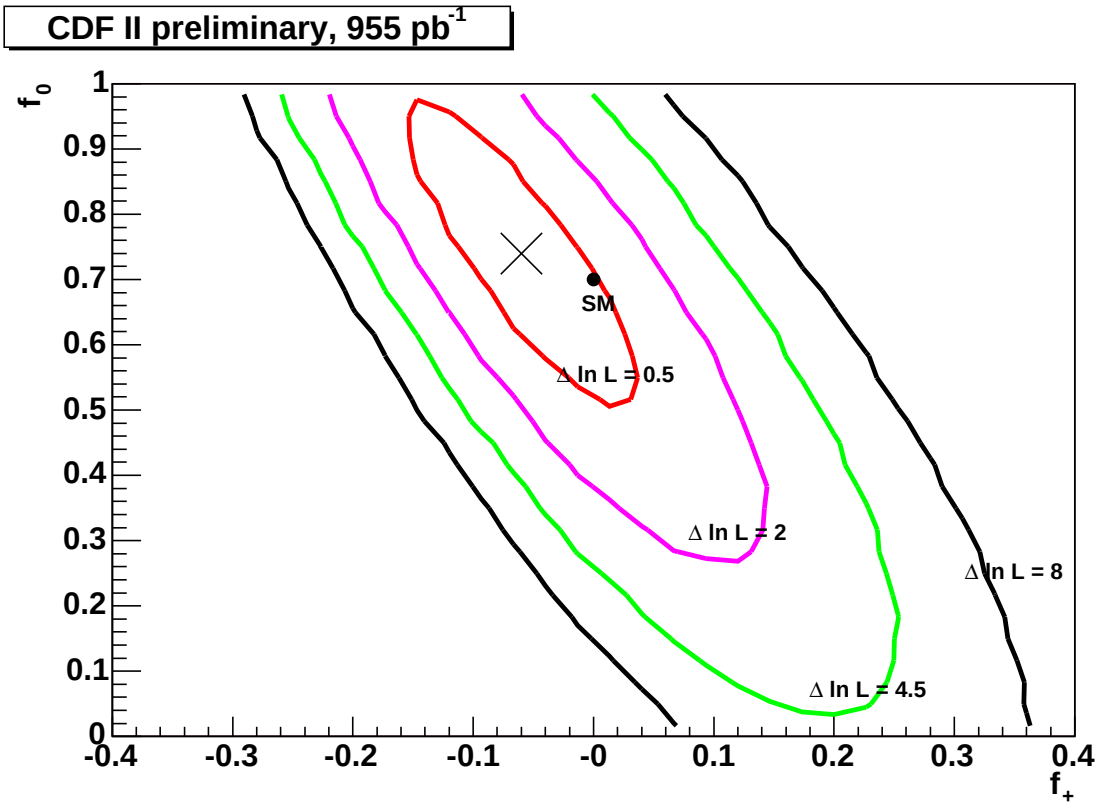

Figure 10.11 Contours of constant ln-likelihood in the (f_+, f_0) plane from the fit to the data. The X shows the minimum of the ln-likelihood, *i.e.* our result.

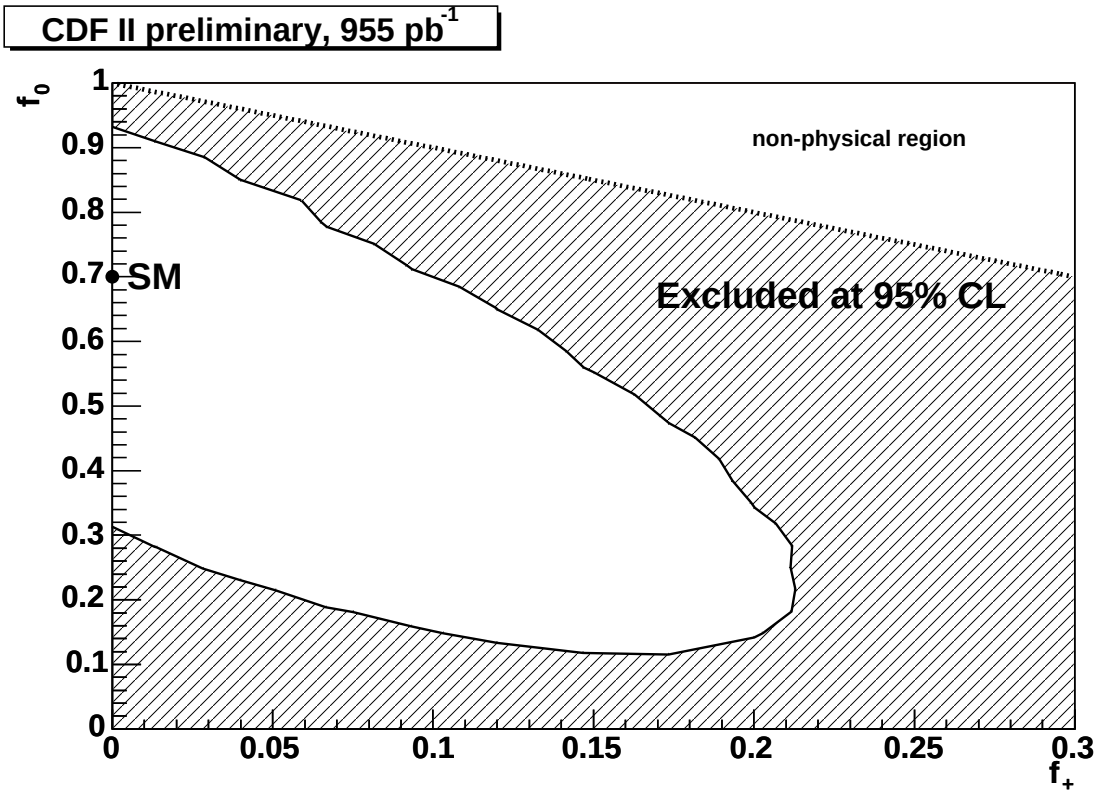

Figure 10.12 The area of the (f_+, f_0) plane excluded by the data is shown as the hatched region. The unhatched region in the upper right is unphysical.

10.3 Determination of W helicity fractions - conclusions

Measurements of the mass of the top quark and its production cross section have indicated that these general parameters agree with expectations of the SM. More detailed and interesting questions remain to be answered, that may be especially sensitive to new physics. In particular, the top quark couples to a W boson and a b quark almost 100% od the time and has a V-A coupling. The helicity of the W boson offers a way to learn about this coupling.

In this analysis we used a template method to measure the fraction of longitudinal (f_0) and right-handed (f_+) Ws in top decay. We constructed angular distributions of the angle between the W boson and the charged lepton of its decay products ($\cos\theta^*$) and extracted the helicity fractions using an unbinned maximum likelihood fitter. This method offers the possibility of reducing sensitivity to the main source of systematic uncertainties (jet energy scale), while making the most efficient usage of information per event, therefore increasing the statistical sensitivity.
Applying this method to $955pb^{-1}$ of data we obtained:

$$f_+ = -0.056 \pm 0.06 \pm 0.03 \text{ , while fixing } f_0 \text{ to its SM value (0.7).}$$
$$f_0 = 0.606 \pm 0.12 \pm 0.06, \text{ while fixing } f_+ \text{ to zero.}$$

In the absence of an observed signal, we set an upper limit on the fractions of right-handed W bosons:

$$f_+ < 0.11 \text{ @95\% C.L}$$

In addition, for the first time, a simultaneous measurement of both the longitudinal and the right-handed fractions was performed. Using the same data sample we obtained:

$$f_+ = -0.06 \pm 0.10 \pm 0.03$$
$$f_0 = 0.74 \pm 0.25 \pm 0.06$$

These results assume a top mass of 175 GeV. Our sample contains 220 candidates in the lepton+jets channel, which contains about 90% $t\bar{t}$ signal events.

For the higher statistics anticipated some improvements, like dividing the sample according to the number of b-tagged jets or adding the dilepton channel, may be considered, and the method shown here offers one of the best ways to measure the helicity properties of the W boson in $t\bar{t}$ events.

Chapter 11

Summary

This thesis summarizes the work I've been involved in for the past four years, both taking part in constructing the ATLAS detector, that will operate soon when the LHC is turned on, and analyzing data collected with the CDF detector at the Tevatron.
The construction of silicon modules for the ATLAS SCT demonstrates the complexity of building HEP experiments, that need to meet the tight requirements for high quality performance for a long period of time. This cannot be achieved without sharing knowledge and experience and collaborating closely among the different institutes taking part in the project. Designing a detector that will stand years of hard radiation while providing efficient event tracking and reconstruction is a real challenge. This work shows how tedious, thought-through and time-consuming the process is, and how every piece involved finally has an effect on the detector performance.
Moving from construction to data taking and analysis, this thesis has shown the importance of a semiconductor tracker to the variety of different analyses that rely on track and vertex reconstruction in order to obtain a high purity data sample.
The determination of the W boson helicity fractions in top decays is a test of the SM V-A nature of interaction, as well as its description of electroweak symmetry breaking. It uses b-tagging information to achieve enriched $t\bar{t}$ data samples. However, although this measurement is now a factor of two better in precision than previous measurements, it is still statistically limited.
Figure 11.1 shows a projection of the expected statistical uncertainty for this measurement, when performed on larger data samples. This is done assuming no improvement in the analysis method. It shows then with a total integrated luminosity of about 4 fb^{-1} the statistical and systematic uncertainties become of the same order. Measuring the W helicity fractions with more data at the Tevatron and with the large data samples anticipated at the LHC can provide a more precise determination of these fractions, and therefore a better look at various models beyond the SM.

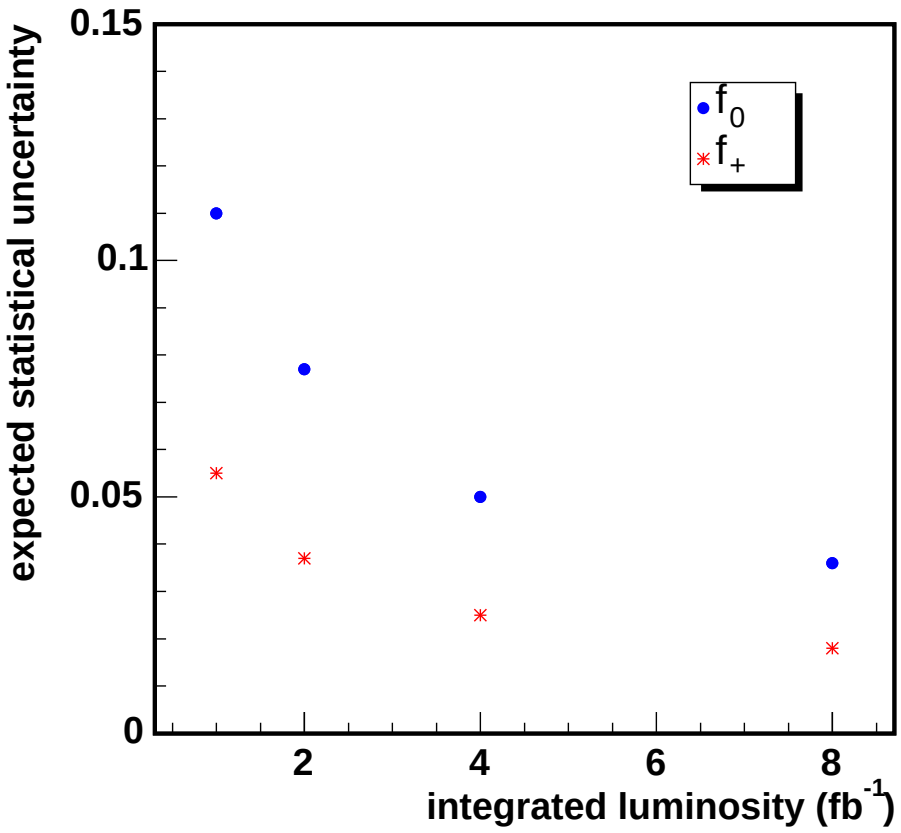

Figure 11.1 Expected statistical uncertainties for measuring the right-handed and longitudinal W fractions with larger datasets.

Bibliography

[1] The ATLAS collaboration, Technical proposal for a general-purpose pp experiment at the LHC at CERN; Technical report, CERN, LHCC 94-43

[2] The ATLAS Collaboration. ATLAS Inner detector technical design report. Technical report, CERN, LHCC 99-14/15, 1999.

[3] http://atlas.web.cern.ch/Atlas/TDR/caloperf/caloperf.html

[4] http://atlas.web.cern.ch/Atlas/TP/NEW/HTML/tp9new/node19.html

[5] Atlas muon spectrometer tdr: 2nd edition.
http://atlas.web.cern.ch/Atlas/GROUPS/MUON/newTDR/TDR_chapters.html.

[6] T. Kondo et al. Construction and performance of the atlas silicon micro-strip barrel modules. *Nucl. Instrum. Meth.*, A485:27–42., 2002.

[7] D. Robinson *et al.*, Silicon micro-strip detectors for the ATLAS SCT, Nucl. Instrum. Meth, A485, 84-88, 2002.

[8] L. Andricek *et al.*, "Design and test of radiation hard p+ n silicon strip detectors for the ATLAS SCT," Nucl. Instrum. Meth. A 439, 427 (2000).

[9] Semiconductor Radiation Detectors, Lutz Gerhard, Springer, copyr. 1999, Berlin.

[10] W. Dabrowski et al. "*Design and performance of the abcd chip for the binary readout of silicon strip detectors in the atlas semiconductor tracker*". *IEEE Trans. Nucl. Sci.*, 47, pages 1843–1850, 2000;
L. Andricek *et al* Nucl. Instrum. Meth A 439 (2000) 427; D. Robinson *et al* Nucl. Instrum. Meth A 485 (2002) 84.

[11] Hamamtsu Photonics Co. Ltd., 1126-1 Ichino-cho, Hamamtsu, Shizuoka, 431-3196, Japan

[12] The ATLAS Semiconductor Tracker Endcap Module;
http://www.uv.es/lacasta/ECpaper/NIM/ATLAS-SCT-Endcap-Module.pdf

[13] S. Snow, *Thermal and Mechanical specifications and Expected Performance of the Forward SCT Module*, ATLAS Internal Note ATL-IS-EN-0007 (1992)

[14] Micro-Vu Corporation, 7909 Conde Lane, Windsor CA 95492 U.S.A.
See http://www.microvu.com

[15] D. Ferrere, M. Weber, Glue dispensing tests,
http://dpnc.unige.ch/atlas/ferrere/assembly/Geneva/GlueTest/GlueTest-10min.jpg
and http://dpnc.unige.ch/atlas/ferrere/assembly/Geneva/GlueTest/GlueTestMay01.jpg

[16] Hesse and Knipps GmbH, Vattmannstr. 6, D-33100 Paderborn, Germany.
See http://www.hesse-knipps.com

[17] Status Report on the Construction of Mechanical Outer Forward Module Prototypes for the SCT. ATL-INDET-2000-008 12/04/2000,
see also http://dpnc.unige.ch/atlas/ferrere/assembly/Geneva/documents/Indet-2000-008.jpg.

[18] http://www.hep.man.ac.uk/atlas/module/surv3.ps

[19] A.G. Clark, D. Ferrere, R. Fortin, S. Roe, M. Weber, *Forward Modules - Assembly Procedure*,
ATLAS Internal Note ATL-IS-AP-0049 (2002).
http://dpnc.unige.ch/atlas/ferrere/assembly/documents/GeAssmSystem.pdf

[20] NIGraphite, Electrodnaya Street 2, 111524 Moscow, Russia. NIITAP, 1 May Street, 103681 Zelenograd, Russia.

[21] M. Ullan *et al, High Pitch Metal-on-Glass Technology for Pad Pitch Adaptation Between Detectors abd Readout Electronics*, IEEE Trans. Nucl. Science 51 (2004) 968.

[22] L. Feld, *Forward Module Compoenta*,ATL-IS-EN=0009,
see also https://edms.cern.ch/document/3161211/1.

[23] A. Clark *et al, The ATLAS SCT Production Database*, ATLAS Internal Note ATL-INDET-2002-015 (2002).

[24] http//www.ph.man.ac.uk/atlas/module/specs.html, SCT-BM-FDR-4 Barrel module FDR document;

[25] http://sct-testdaq.home.cern.ch/sct-testdaq/sctdaq/sctdaq.html

[26] http://dpnc.unige.ch/users/moed/sct-stat.html

[27] ROOT - An Object Oriented Data Analysis Framework, http://root.cern.ch

[28] Particle Data Group. http://pdg.lbl.gov (2006)

[29] R. Barate *et al.* [LEP Working Group for Higgs boson searches], "Search for the standard model Higgs boson at LEP," Phys. Lett. B 565, 61 (2003) [arXiv:hep-ex/0306033].

[30] Nathal Severijns and Marcus Beck, Tests of the standard electroweak model in nuclear beta decay, reviews of moderm physics, volume 78, 2006.

[31] S. Eidelman *et al.* Phys. Lett. B592 (2004) 1

[32] K. Fujikawa and A. Yamada, Tests of the Chiral structure of the top-bottom charged current by the process $b \to s\gamma$, Phy. Rev. D49 (1994)

[33] G.L Kane, G.A. Ladinski and C.P Yuan, Phys. Rev. D 45, 124 (1992).

[34] J.A. Aguilar-Saavedra, Phys. Rev. D 67 (2003)

[35] F. del Aguila and J. Santiago, JHEP 0203 (2002) 010

[36] J. Cao, R.J. Oakes, F. Wang and J.M. Yang, Phys. Rev. D 68 (2003) 054019

[37] X. Wang, Q. Zhang and Q. Qiao, Phys. Rev. D 71 (2005) 015035

[38] H. Georgi, Annu. Rev. Nucl. Part. Sci. 43 (1993) 209 and references therein.

[39] H.S. Do, S. Groote, J.G. Korner and M.C Mauser, Phys.Rev. D 67 (2003) 091501

[40] F. Larios, M.A. Perez and C.P. Yuan, Phys. Lett. B 457 (1999) 334; G. Burdman, M.C. Gonzalez-Garcia and S.F. Novaes, Phys. Rev. D 61 (2000) 114016; K. Whisnant, J.M. Yang, B.L. Young and X. Zhang, Phys. Rev. D 56 (1997) 467.

[41] Probing anomalous Wtb couplings in top pair decays; J.A.Aguilar-Saavedra,J. Carvalho, N. Castro, F. Veloso, hep-ph/0605190

[42] E. Malkawi and C.P. Yuan Phys. Rev. D.50, 4462 (1994); Phys. Rev. D52 472 (1995), F. Larios, E. Malkawi and C.P. Yuan, hep-ph/9704288

[43] M. Hosch, K. Whisnant and Bing-Lin Young, Phys. Rev. D55, 3137 (1997).

[44] CDF internal note 8449.

[45] Fermilab beam division, Run II handbook,
http://bdnew.fnal.gov/pbar/run2b/Documents/RunII_handbook.pdf

[46] Fermilab beam division, Fermilab Linac Upgrade. Conseptual Design.,
http://www-lib.fnal.gov/archive/linac/fermilab-lu-conseptualdesign.pdf,1998

[47] Fermilab beam division, The Booster rookie book,
http://www-bdnew.fnal.gov/operations/rookie_books/Booster_PDF/Booster_TOC.html

[48] The Main Injector rookie book,
http://www-bdnew.fnal.gov/operations/rookie_books/Main_Injector_PDF/Main_Injector.html

[49] Fermilab beam division, The Tevatron rookie book,
http://www-bdnew.fnal.gov/operations/rookie_books/Tevatron_PDF/TeV_Rookie_Book.htm

[50] F. Abe *et al.*, Nucl. Instrum. Meth. A271, 357 (1988).

[51] The CDF Collaboration, FERMILAB-Pub-96/390-E (1996).

[52] L. Balka and others., Nucl. Instrum. Meth. A267, 272 (1988).

[53] S. Bertolucci *et al.*, Nucl. Instrum. Meth. A267, 301 (1988).

[54] A. Artikov *et al.*, Part. Nucl. Lett. 114, 25 (2002).

[55] A. Artikov, J. Budagov, and G. Bellettini, Nucl. Instrum. Meth. A538, 358 (2005).

[56] CDF Collaboration, *"Luminosity Monitor Based on Cherenkov Counters for a P Anti-P Colliders "*,Nucl. Instr. & Meth. A, 441, 366-373, 2000

[57] CDF Collaboration, The CDF RunII Luminosity Monitor, Nucl. Instr. & Meth. 2001, A, 461, 540-544, 2001

[58] SVT TDR, CDF internal note 3108

[59] Trigger and dataset working Group,
http://www-cdf.fnal.gov/internal/upgrades/daq_trig/twg/tools/trigopts.ps.

[60] K. Anikeev *et al.*, CDF internal note 5051 (1999).

[61] K. Maeshima *et al.*,
http://www-cdfonline.fnal.gov/internal/mon/consumer/home/consumer_home.html

[62] H. Wenzel *et al.*,
http://www-cdfonline.fnal.gov/internal/mon/consumer/framework/index.html.

[63] B. Kilminster *et al.*, CDF internal note 4794 (1998).

[64] B. Kilminster *et al.*, CDF internal note 5292 (2000).

[65] J. Han *et al.*,
http://www-cdfonline.fnal.gov/internal/mon/consumer/ymon/YMon_Home.html

[66] C. Plager *et al.*,
http://www-cdfonline.fnal.gov/internal/mon/cdfdaq/XMon/xmon.html

[67] M. Worcester *et al.*,
http://www-cdfonline.fnal.gov/internal/mon/consumer/trigmon/trigmon.html

[68] S. M. Wang *et al.*,
http://www.phys.ufl.edu/ ming/WWW/cdf/lummon/lummon.html

[69] H. Stadie *et al.*,
https://www-cdfonline.fnal.gov/internal/mon/consumer/BeamMon

[70] H. Bachacou *et al.*,
http://fcdfhome.fnal.gov/usr/bachacou/SVXMon/svxmon.html

[71] G. Manca *et al.*,
http://www-cdfonline.fnal.gov/internal/mon/consumer/silimon/new/Intro.html

[72] V. Khotilovich *et al.*,
http://www-cdfonline.fnal.gov/internal/mon/consumer/objectmon/objectmon.html

[73] J. Paul *et al.*,
http://www-cdf.fnal.gov/internal/people/links/KevinA.Burkett/COT/stage0.html

[74] W. Badgett *et al.*,
http://www-cdfonline.fnal.gov/internal/mon/consumer/daqmon

[75] W. Badgett,
http://www-cdfonline.fnal.gov/daq/hardware/daqerrmon.html

[76] M. Rescigno *et al.*,
http://www-cdfonline.fnal.gov/internal/ops/svt/spymon/consumer.html

[77] S. Levy *et al.*,
http://hep.uchicago.edu/cdf/physmon/physmon.html

[78] R. Erbacher *et al.*,Event Selection and $t\bar{t}$ Signal Acceptance of the Winter 2005 Top Lepton + Jets Sample, CDF note 7272, 2005

[79] J. Goldstein *et al*, Silicon Tracking for Plug Electrons, CDF note 5970, 2002

[80] CDF note 8274

[81] F. Canelli, and A. Bhatti, "Generic Jet Corrections for Run II", CDF note 7358; see also
http://www-cdf.fnal.gov/internal/physics/top/jets/corrections.html.

[82] D. Glenzinski *et al.*, CDF notes 2925,2955,6417

[83] Christopher Neu and others, *"SecVtx Optimization Studiesfor 5.3.3 Analysis"*, CDF note 7578, 2005

[84] C. Neu, E. Thomson, H. Williams, Ultratight SECVTX Tagging Efficiency and Purity Studies, CDF note 7932, 2006

[85] S. Budd, *et al.*, Measurement of the t-tbar Production Cross Section in SecVtx-Tagged Lepton+Jets Events, CDF note 8037

[86] Data Quality Monitoring Home Pgae, Matteo Cavalli and others,
http://www-cdf.fnal.gov/internal/dqm/dqm.html

[87] A. Abulencia *et al.* (CDF Collaboration), Phys. Rev. D 73, 032003 , 2006

[88] http://seal.web.cern.ch/seal/work-packages/mathlibs/minuit/home.html

[89] CDF internal note 6845

[90] J.F. Arguin and P.K Sinervo, Revisiting the Top Specific Jet Energy Corrections, CDF note 6404

[91] A. Abulencia, *et al.*, (CDF Collaboration), "Measurement of the Helicity of W Bosons in Top-Quark Decays", submitted to *Phys. Rev. Lett.* (CDF note 7761).

[92] CDF note 8229; CDF note 8250.

[93] H. Bachacou, J. Nielsen, and W. Yao, CDF-6569 v1.0 (2004).

[94] H. Bachacou, J. Nielsen, and W. Yao, CDF-6569 v2.0 (2004).

[95] J. Guimaraes and C. S. Rappoccio, CDF-7326 (2006).

[96] CDF internal note 8072.

[97] D. Sherman, S. Rappoccio, and J. G. da Costa, CDF-7585 (2005).

[98] S. Budd, T. Junk, and C. Neu, CDF-8072 (2006).

[99] H. Bachacou *et al.*, CDF-7007 (2004).

[100] M. L. Mangano *et al.*, arXiv:hep-ph/0206293 (2003).

[101] G. Corcella *et al.*, arXiv:hep-ph/0201201 (2002).

[102] J. M. Campbell and R. K. Ellis, Phys. Rev. D 65, 113007 (2002).

[103] D. Acosta *et al.*, Phys. Rev. Lett. 94, 091803 (2005).

[104] M. Cacciari *et al.*, arXiv:hep-ph/0303085 (2005).

[105] B. W. H. Laenen *et al.*, Phys. Rev. D 66, 054024 (2002).

[106] CDF internal note 8025.

[107] G. Guillian, M.Campbell, A.Amidei, A modified version of Herwig for studying the spin properties of the top quark, CDF note 4261, 1997.

[108] http://www-cdf.fnal.gov/internal/physics/top/run2mass/topmass_systematics.html

[109] J. Pumplin, D.R Stump, J. Huston, H.L. Lai, P. Nadolsky, W.K Tung "New Generation of Parton Distributions with Uncertainties from Global QCD Analysis", hep-ph/0201195

[110] J. Huston "PDF uncertainties and their meaning", talk at Joint physics meeting May 5, 2006